CARDIFF UNIVERSITY

KINETICS OF GaAs (001) SURFACES INVESTIGATED BY LEEM-MBE

Daniel Gómez Sánchez

A thesis submitted as partial fulfilment for the degree of

Doctor of Philosophy

School of Physics and Astronomy

26th September 2019

A mi tío Jose

Abstract

Understanding the physical mechanisms behind epitaxial growth of semiconductors is crucial for the comprehensive control of the interfaces and ultimately for the fabrication of state-of-the-art optimised optoelectronic devices i.e. single-photon emitters or quantum computing. The current in-situ characterisation techniques have certain limitations in analysing dynamic processes during growth. Our unique III-Vs LEEM-MBE system at Cardiff, allows us to resolve dynamical processes on III-Vs under MBE conditions i.e. nucleation of nanostructures, with atomic resolution in the vertical axis and 5 nm in the XY plane at video rate. We have developed a new technique: Selective Energy Dark-Field Low Energy Electron Microscopy (SEDFLEEM), which conjoins the advantages of Dark-Field LEEM with the accuracy of the I-V curve of diffracted spots for identification of complex structures generated at GaAs(001) surfaces. This technique provides a very useful tool for the investigation of atomic arrangements and nanostructures nucleation. Studies on the c(8×2) and the (6×6) phase reconstructions for GaAs(001) using SEDFLEEM revealed a metastable (6×6) within the stable c(8×2) regime that is present in the surface at temperatures above 570°C. Using the principles of droplet epitaxy, we have from used a Gallium droplet, to generate a monotonically decreasing Gallium chemical potential (μ_{Ga}) profile over a flat trail and we have utilised SEDFLEEM to map qualitatively different phase reconstructions around liquid gallium droplets at a fixed temperature. We have also analysed the coexistence of the c(8×2) and the (6×6) for GaAs(001) between 520°C and 570°C using SEDFLEEM. These discoveries have revealed that this transition is a first order transition and the theory of transitions for monoatomic systems can be applied to complex binary systems. The implementation of this knowledge is a key point for the growth of high-purity crystalline structures and will pave the way for the development of high-technology optoelectronic devices.

Acknowledgments

Firstly, primarily and foremost, I would like to thank my supervisor Juan Pereiro for teaching me how NOT to use all these connectors. I thank you sincerely for all your patience, attention, dedication and human care that you have shown in these years. This thesis would have been nothing without our endless discussions or our hours-long meetings.

Second, I want to thank Yuran Niu, for all his support throughout the years and for all his good advices and his infinite patience and help.

To Hugh, because without him things in the lab would not function properly and because he has always been willing to help me every time.

I want to thank David Jesson, for all the dedication that he has always shown with me and with the group. I wish you the very best in your new life, and I really hope Chelsea does well this season (although they have not started particularly well…).

To David Westwood, for his "last minute" support and for all his help during my demonstrating years.

To everyone from uni (whether they are still at uni or not), all the people from astro, Suzanne, Sara, Adam, Val, Penny, Dani, Max, Ruth…and a long etc.

To everyone in my group, Deb, Kennet and Matyo, I want to thank them all they have done for me during all these years, specially Kennet, who has had to bear with me for quite some time now.

To all my special assholes whom with I have shared so many memories (Cardiff, India…) Greg, Chinu, and Aris. Oh! and by the way Aristeidis, you owe me three beers 😉.

To my family in Cardiff…all the people that have made this possible, I thank them all.

To my dearest family, whom I love to death and have always made sure this thesis goes well.

To my parents and my brother, for they will always be there, and this thesis contains a bit of each of them. This thesis would have never been possible without your countless patience that you have always shown with me.

Last, but definitely, not least, to my dearest girlfriend. I want to thank you specially because no one will ever know how much dedication I have put into this, and because this is certainly our thesis, and you deserve everything, just to have been able to stay with me, to withstand discussions, misbehaviours and just because you have all the patience of the world. Without you I would have never accomplished this much. I really love you.

This thesis has received the support from EPSRC research grants No. EP/P023452/1 and No. EP/N022661/1 and the European Union's Horizon 2020 research and innovation programme under the Marie Sklodowska-Curie grant agreement No. 701246. I want to thank them all for the funding granted to my supervisor.

Agradecimientos

Quiero volver a agradecer a Juan una vez más por su incansable apoyo y su infinita paciencia que ha mostrado conmigo durante casi 4 años. Soy todo un privilegiado por haberte tenido como supervisor.

Quiero agradecer a toda la gente importante de mi vida en Cardiff. A Eli (por fin, he acabado maja…), a Laia (que, aunque haya pasado tiempo, nunca podré olvidar que en los primeros años siempre estuviste ahí) a Iria, a Carlitos, a Cristina…y a todos los que en algún momento me hayáis acompañado en este arduo camino.

A Kennet, por todas esas conversaciones de la vida en general, de la uni, de países, y de todo un poco, y por hacerme más amena esta tesis.

A Beatriz y a todos los del barrio por su incansable afán de darme ánimos desde la distancia y porque sin esos ánimos todo sería mucho más difícil.

A toda mi gente de la uni que me habéis entretenido como nunca. A Rodri, Álvaro y Kike porque los memes que has habéis currado me han hecho llorar como nunca, especialmente durante mi escritura. A Pablo, Laura, Iso y Vivi porque siempre se han preocupado de mi a su manera y siempre han intentado apoyarme y animarme.

A Jorge y a Andrea, por supuesto, porque son mi familia de Cardiff y sin ellos Cardiff nunca hubiera sido lo mismo.

A mi familia en general, por haberme siempre apoyado y empujado para que todo esto saliera adelante, y por estar siempre ahí.

Quiero agradecer en especial a Rosario y a mi abuela, porque sé lo orgullosas que están de mí y porque esta tesis también lleva una parte vuestra.

A mis padres y a mi hermano porque siempre han sido un pilar fundamental en mi vida y nunca han dejado de apoyarme. La educación que he tenido el privilegio de disfrutar es gracias a vosotros. Hoy acaba mi etapa de formación académica por la que tanto habéis sufrido y por la que tantos esfuerzos habéis dedicado.

Nada de esto hubiera sido posible sin vosotros. No obstante, me gustaría decir que lo más importante que he aprendido en todos estos años es que lo importante es la vida, y por eso tenemos que disfrutar de cada minuto que tenemos de ella.

A Sophia, que, aunque no pueda entender esto, nunca habrá un idioma para expresar lo agradecido que estoy de haber encontrado a alguien como tú. Me has ayudado como nadie y siempre te has preocupado por muchísimo por mí.

Ya por último, quiero agradecer de manera muy especial a mi tío Jose. Nadie más que tú y yo sabemos lo orgulloso que me siento de haber compartido toda esta tesis contigo. Nunca podré olvidar los esfuerzos que has puesto siempre en intentar entender mi investigación, en aprender inglés, y el cariño que siempre has mostrado hacia mí durante todo este tiempo. Ahora, eres eterno. Esta tesis doctoral, va por ti.

Publications & Conferences

Publications

[1] Y. R. Niu, J. Pereiro, D. Gomez, and D. E. Jesson, "Selected energy dark field imaging using low energy electrons for optimal surface phase discrimination" *Ultramicroscopy*, vol. 200, no. February, pp. 79–83, 2019.

My contribution to this publication was the acquisition of experimental data using LEEM-MBE together with Yuran Niu and the development of the SEDFLEEM technique.

[2] K. Hannikainen, D. Gomez, J. Pereiro, Y. R. Niu, and D. E. Jesson, "Surface Phase Metastability during Langmuir Evaporation" *Phys. Rev. Lett.*, vol. 123, no. 186102, pp. 1-5, 2019.

My contribution to this publication was the acquisition of experimental data using LEEM-MBE. All the experimental images were taken by me as well as part of the data analysis.

[3] C. X. Zheng *et al.*, "Mapping Surface Free Energy of GaAs(001) during Droplet Epitaxy," *Phys. Rev. Mater.*, vol. 3, no. 124603, pp. 1–9, 2019.

My contribution to this publication was the acquisition of experimental data using LEEM-MBE together with Yuran Niu using SEDFLEEM.

Conferences

[4] D. Gomez, Y. R. Niu, K. Hannikainen, J. Pereiro, and D. E. Jesson, "Low Energy Electron Microscopy (LEEM) at Cardiff University" in *Poster Conference Cardiff University*, 2017.

[5] D. Gomez, "Low Energy Electron Microscopy (LEEM) of GaAs (100) surfaces" in *Postgraduate Conference Cardiff University*, 2018.

[6] D. Gomez, Y. Niu, J. Pereiro, and D. Jesson, "Selected energy dark-field imaging using low energy electrons for optimal surface phase discrimination by LEEM-MBE" in *UK-MBE Workshop*, 2019.

[7] D. Gomez, Y. R. Niu, K. Hannikainen, J. Pereiro, and D. E. Jesson, "Selected energy dark field imaging using low energy electrons for optimal surface phase discrimination on GaAs(001) by LEEM-MBE" in *UK Semiconductors*, 2019.

Table of Contents

List of figures

Chapter 1

Chapter 2

Chapter 3

Chapter 4

Chapter 5

Chapter 6

Chapter 7

Chapter 8

Chapter 1: Introduction

In the world we live in, the use of new technology has become a necessity. According to a GlobalWebIndex study, the typical digital consumer owns 3.64 devices (from smartphones, laptops and tablets to streaming sticks, wearables and consoles) [1]. In order to improve the development of devices, deep understanding of the fabrication processes results crucial.

For optoelectronic devices, the fabrication of high-quality materials, with competitive properties is being the subject of research in the last decades. These materials: semiconductors, have many different processes of fabrication. The purest technique for the growth of semiconductors, it is Molecular Beam Epitaxy (MBE).

Low Energy Electron Microscopy is an analytical surface science technique that allows real time imaging of surface processes at a video. Ernst Bauer invented this innovative characterisation technique in 1962 [2].

In this thesis, an overview on the importance of this technique and its combination with other characterization techniques for the observation of different critical phenomena is going to be given.

Following this introduction, an outline on the fundamentals of MBE, and Low Energy Electron Microscopy will be presented. Together, these two techniques constitute a unique tool for the analysis of physical processes happening at the surface of different semiconductors: LEEM-MBE. A thorough description of these surface physical processes will also be introduced.

In chapter 3, a detailed description of the unique LEEM-MBE equipment will be provided. Novel technical implementations on the system critical for surface science investigations will be outlined.

A new technique for in-situ characterization allowing phase discrimination at the surface of semiconductors at video rate will also be introduced. This new

technique, Selective Energy Dark-Field Low Energy Electron Microscopy (SEDFLEEM) has been used throughout the thesis for the analysis of different dynamical processes on GaAs (001). The description of this technique will be provided in chapter 4.

In the next chapter 5, an insight on the kinetics of Gallium and Arsenic utilising SEDFLEEM technique under MBE conditions will be provided. An update on the GaAs (001) phase diagram will be pointed out using a Ga droplet and As-flux.

Chapter 6 will review work on the evolution of two surface reconstructions (c(8×2) and (6×6)) for GaAs for a range of temperatures. Coexistence in the thermodynamically stable regime between 520°C and 570°C for both phases have been analysed using SEDFLEEM. Subsequently, a more detailed analysis on the evaporation from GaAs surfaces will be presented and compared with the Si surface. The aforementioned two surface phases will be further described in chapter 7, introducing a metastability regime of the (6×6) phase above 570°C. It has been discovered that for a large range temperature, the (6×6) is metastable which was thought to be the c(8×2) stable regime.

Future work will be presented in chapter 8. Here, different approaches for the study of the nucleation of nanostructures will be reviewed. Some of these approaches include Droplet Epitaxy (DE), Local Droplet Etching (LDE), as well as the development of an anodisation cell built up for Al anodisation, which generates porous alumina. All these techniques hold promising potential for the site-controlled growth of nanostructures.

Last but not least, the main conclusions of this thesis will be outlined.

Fundamentals of epitaxy

Introduction to epitaxy:

Silicon technology is well established, and the fabrication techniques are cheap and accessible for planar integrated circuit manufacturing due to their great development over the past decades. However, Si is a semiconductor with indirect band gap, which makes it difficult to implement as light emitter in photonics [3].

III-V semiconductor technology has been widely developed for the fabrication of emitters since the 70's. Among the III-Vs, GaAs and GaN and their combination with Al and In: (Al, In, Ga)As and (Al, In, Ga)N have been of interest due to their direct band gap and their possibilities in terms of emission creating devices with band gap energies ranging from 0.354 eV of InAs to 6.026 eV of AlN as can be observed in Figure 1 [4][5][6].

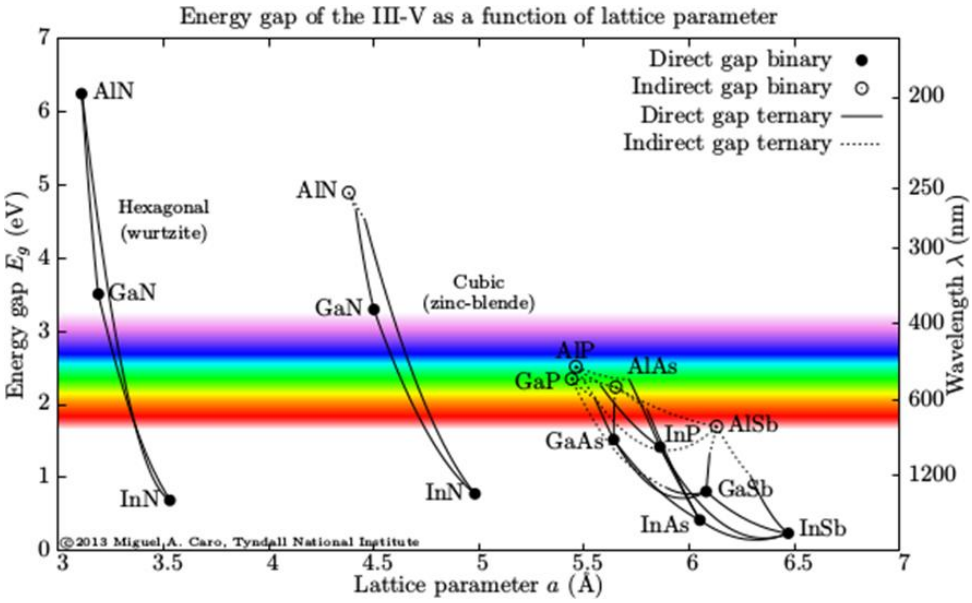

Figure 1. Band Gap energy as a function of the lattice parameter for the III-V semiconductor compounds. (Figure adapted from [7] with permission from publisher).

Si and GaAs possess very similar lattice parameters, like some other III-V compounds like AlAs. This property makes them good candidates to be adequate substrates, which results of high interest for the epitaxial growth of thin films based on these materials. GaAs is a semiconductor with a direct band gap of 1.441 eV at room temperature. The GaAs structure is zinc-blende. A representation of the GaAs crystalline structure is shown in Figure 2. Apart from a direct band gap, GaAs has a high dielectric constant and a high electron mobility. All these characteristics make GaAs a very suitable material for optoelectronic applications.

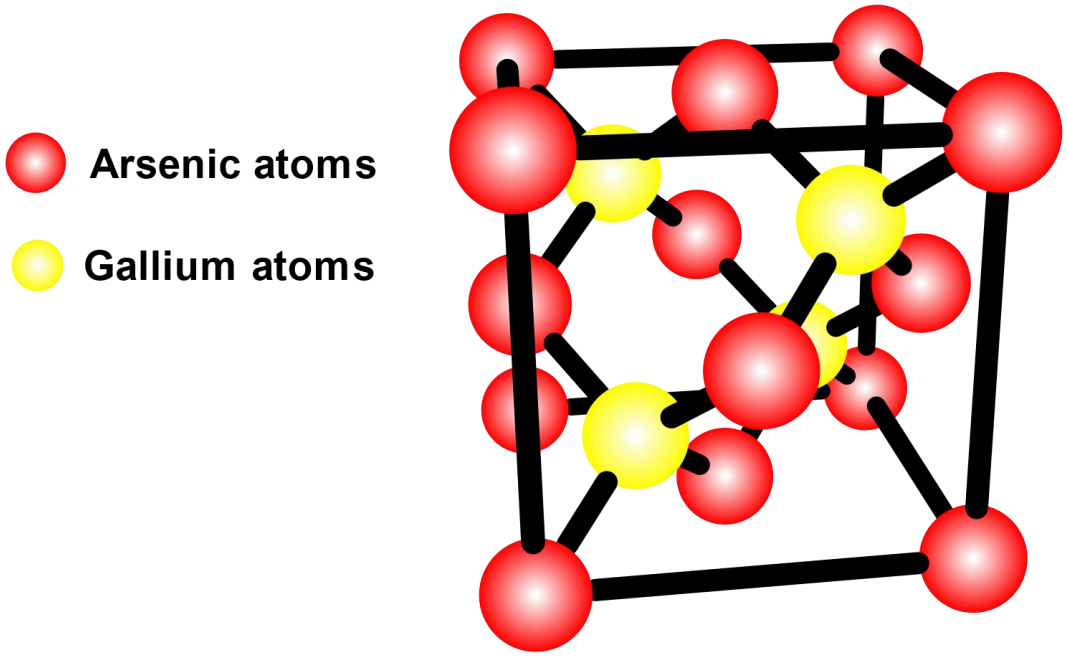

Figure 2. Schematic representation of GaAs zinc-blende structure.

Epitaxy refers to the deposition of a crystalline overlayer on a substrate with a crystallographic relationship. Two types of epitaxy can be distinguished: homoepitaxy, when the thin film deposited is of the same chemical composition

or lattice parameter as the substrate; and heteroepitaxy, when the chemical composition or lattice parameter of the material deposited are different than the substrate. The mismatch between the crystal lattices of the substrate and the materials deposited, generate structural defects. The concentration of these defects plays a role for the electrical and optical properties of the device. Homoepitaxy reduces the concentration of growth defects as there is no mismatch between the substrate and the material grown. For heteroepitaxy, it is important to find substrates to grow onto with a similar lattice parameter than the material to be deposited to reduce the concentration of defects. The strain (ε) associated with heteroepitaxial of a layer with lattice constant a_L onto a substrate of lattice parameter a_S, is described in Eq. 1. This strain will be present on the substrate material along the growth direction up to a critical thickness d_c. The critical thickness has a value of roughly $d_c \approx \frac{a_S}{2|\varepsilon|}$ [8].

$$\varepsilon = \frac{a_L - a_S}{a_L} \qquad \text{Eq.1}$$

Following this principle, the epitaxial growth can be performed under strain. The strain during growth, lowers the energy of the interfacial atoms at the expense of stored strain energy within the epitaxial layer [9]. This mechanism will reduce the lattice mismatch between two layers and therefore widening the range of variety of semiconductors that can be used in heteroepitaxy. Additionally, strain-engineering allows changes in the band structure, which leads to tailoring of the optoelectronic properties of the devices [10]–[13].

Growth of nanostructures:

The growth of nanostructures-based optoelectronic devices enables confinement of electrons when reducing the size and the physical properties can be tailored by modifying the dimension of the nanostructure. There are several techniques for

investigating the growth of nanostructures. Here, we review the growth mechanisms for different nanostructures:

- **Nanowires (NWs):** NWs, are nanostructures of one-dimensional electron confinement, can be grown Self Assembled (SA), when their nucleation occurs in random positions of the surface. Alternatively, we can control the position where the NWs grow, which is Selective Area Growth (SAG). Attending to the nucleation mechanisms, the growth of NWs could be classified in two different techniques.

    - With catalyst: Vapour-Liquid-Solid (VLS) is a process for the growth of one-dimensional nanostructures which introduces a catalytic liquid alloy phase which can rapidly adsorb a vapor to supersaturation levels, and from which crystal growth can subsequently occur from nucleated seeds at the liquid–solid interface. In the case of GaAs, Au or Ga droplets can be used as a catalyst. In the case of liquid catalyst, the growth takes place by VLS mechanism. There is a debate about this technique. It is still not clear whether Au droplets are fully liquid or not, and the nucleation mechanisms have not been completely understood yet [14]. The NWs grow right under the droplet in presence of Ga and As fluxes. An example of this mechanism can be observed in Figure 3.

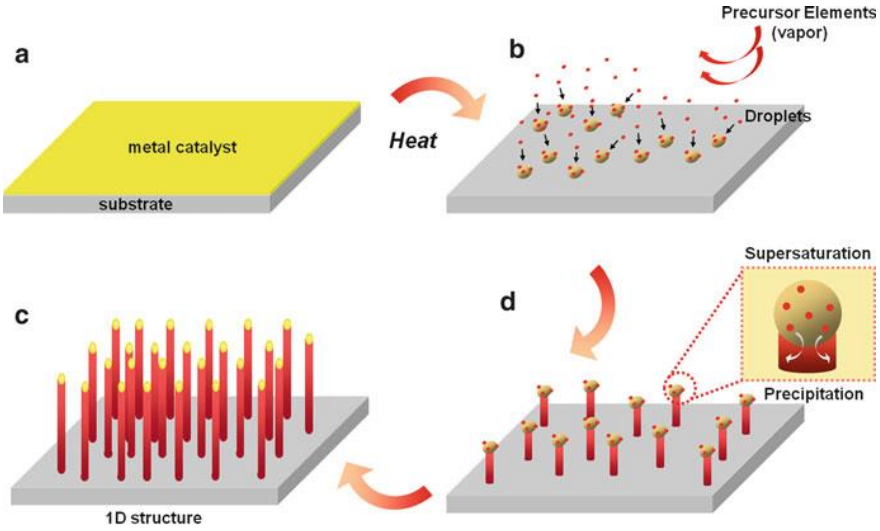

Figure 3. Growth of NWs via VLS mechanism. (Figure adapted from [15] with permission from publisher).

- Without catalyst: This method permits the growth of nanowires without the use of a catalyst. An example of this phenomenon is displayed in Figure 4, where an array of SAG GaN nanowires were grown by MBE without any catalyst [16].

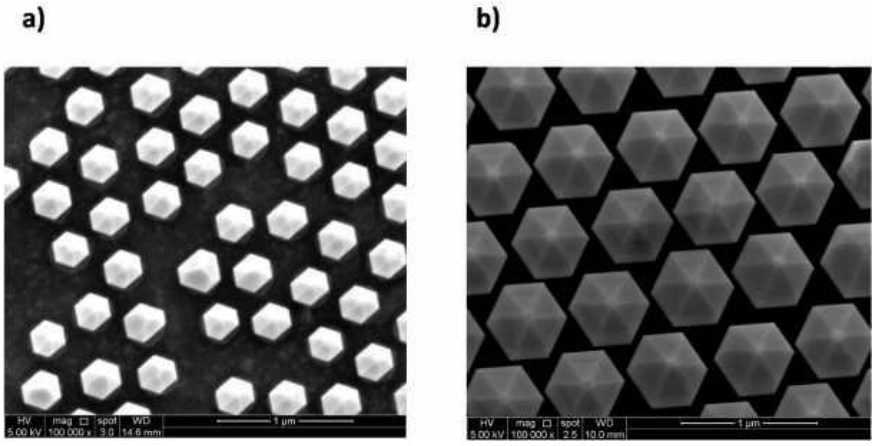

Figure 4. SAG GaN nanowires with different diameters and dispersions. The surface was prepared by colloidal lithography. (Figure adapted from [16] with permission from publisher).

- **Quantum Dots (QDs):** Quantum Dots are zero-dimensional nanostructures in which the electrons' wavefunction is confined in the three dimensions. I am going to discuss briefly two approaches for the QDs formation regarding the nucleation mechanisms:

    - Stranski-Krastanov (SK): This method is defined as layer + islands growth model. When the layer acquires a critical thickness, a transition from 2D to 3D growth occurs so that the self-assembled quantum dots are generated. A Wetting Layer (WL) is epitaxially grown onto the surface using a molecular beam epitaxy equipment and by the effect of the strain, the QDs formation takes place. A sketch of this process can be observed in Figure 5 [17][18]. This method will be developed further in chapter 2.

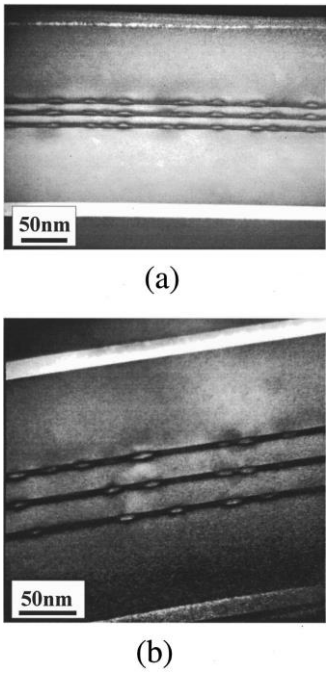

Figure 5. [110] cross section dark-field images of multiple QD layers grown by Stranski-Krastanov growth technique with (a) 10 nm and (b) 25 nm thick spacers. (Figure adapted from [18] with permission from publisher).

- Droplet epitaxy: is an alternative approach to Stranski-Krastanov that makes use of the deposition of liquid metal droplets on a semiconductor surface, for example a Ga metal on a GaAs surface. A further exposure to As flux provokes the reaction of the droplet material and forms a crystalline quantum structure as shown in Figure 6. This technique has been used to grow quantum dots [19][20][21] and quantum rings [22]. In comparison with SK technique, droplet epitaxy is more flexible regarding the choice of materials, and the fabrication of unstrained nanostructures is possible [23]. However, nucleation mechanisms are still a matter of study and the controllability of the process gets difficult because of the high sensitivity to growth parameters such as substrate temperature and As-flux.

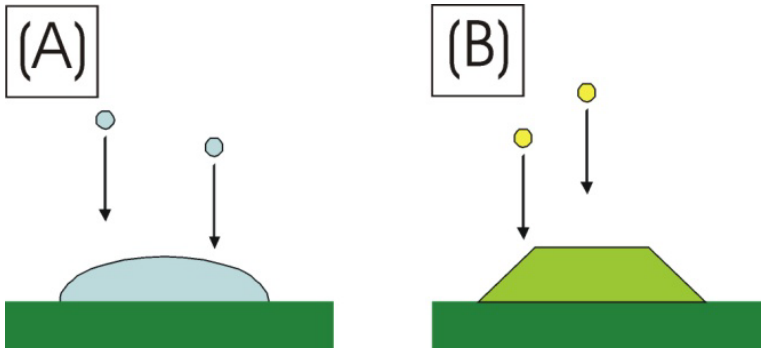

Figure 6. (A) First step of DE: generation of metallic droplet on the surface. (B) Second step: crystallization to create QD. (Figure adapted from [24] with permission from publisher).

Fundamentals of LEEM

LEEM has been proven to be a very powerful technique for morphological characterisation of surfaces [25]–[29]. The lateral resolution of Scanning Electron

Microscopy (SEM) is comparable to LEEM. A standard SEM, however, is not very sensitive to the surface. The high energy of the electrons impedes the visualisation of atomic steps by secondary electrons.

Scanning Probe Microscopies (SPM) such as Scanning Tunnelling Microscopy (STM) and Atomic Force Microscopy (AFM) are able to achieve atomic resolution, unlike LEEM. Nonetheless, LEEM has decisive advantages in imaging speed since it is a non-scanning characterisation technique that allows imaging of surfaces with atomic resolution in the vertical axis at video rate. LEEM can make observations in real-time while the surface is evolving, and it is capable of carrying out analysis of different dynamical processes at the surface, all within one instrument. The ability of video-imaging while changing the surface's state by varying different physical parameters (temperature, pressure, external fluxes, etc.) and the ability for fast real-space imaging combined with selected-area diffraction makes LEEM a unique technique [30].

Surface science in semiconductors

Introduction to surface science:

A surface corresponds to a discontinuity in the periodicity of the crystal in the direction perpendicular to it. This discontinuity may lead to atomic rearrangements. The epitaxial growth of high-purity crystalline structures relies on the accurate control of the growth parameters. In order to optimise these parameters, it is crucial to understand the physical mechanisms that take place on the surface of different semiconductors. During the last decades, the scientific community has realised the importance of the role of difference surface mechanisms (atoms desorption, phase reconstructions, atom diffusion, atomic steps, defects…) in growth processes by MOVPE or MBE on different semiconductors and a significant number of studies have been performed

addressing these phenomena. For the study of all these processes, flat surfaces are required.

Sample preparation

Native oxides form on the surfaces of all the semiconductors by the mere exposure to air. Prior to the epitaxial growth, one of the main phenomena to be aware of is the removal of this oxide on the surface of any semiconductor. The desorption of oxide for GaAs has been a matter of study in the past years [31], [32] and many of these studies report that after the oxide layer is desorbed, the surface appears to be rough [33]–[37]. Figure 7 has been created for the sake of clarity. This effect presumes a problem as flat surfaces are needed for epitaxial growth. To overcome this, normally a thick buffer layer of around 500 nm or higher is grown on the surface after oxide desorption. This way, the defects coming from the surface roughness are annihilated. LEEM-MBE technique does not allow growth for a long period of time, and alternatively, David Jesson et al. developed a method to achieve atomically flat surfaces by generating Ga droplets on GaAs (001) substrates. As the Ga droplet moves across the surface, the surface behind it gets planarized [38]–[40].

A different approach to overcome the roughness after the oxide desorption for GaAs is As-capping. This technique allows to cover the surface with a thick layer of arsenic using a low temperature deposition. The arsenic layer prevents the oxidation of the GaAs planar surface and facilitates the MBE-to-MBE transfer as it has been reported by several groups already and [41]–[45]. This way, once the arsenic layer is thermally desorbed at around 300 °C, the surface underneath is presented flat as it was prepared on an MBE equipment.

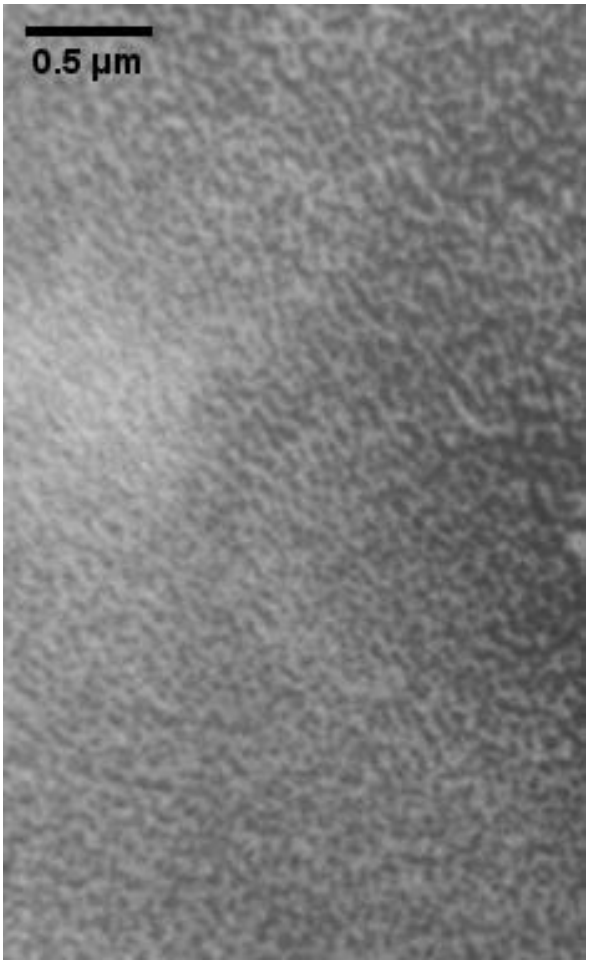

Figure 7. LEEM image of a rough GaAs (001) surface after oxide desorption.

Surface reconstructions:

Detailed knowledge of the atomic arrangement on the surface, results critical for the growth of different semiconductors by MBE for high speed electronic applications and optoelectronic devices. Different atomic arrangements on the surface of semiconductors correspond to different phase reconstructions.

In crystallography, surface reconstruction is a term that describes a change in the two-dimensional structure of the surface of a crystal led by energy minimisation [46]. A reconstruction can affect one or more layers at the surface.

Attending to the interaction of a given surface reconstruction with the medium, changes in surface reconstruction can also be induced or influenced by the adsorption of other species onto the surface since the interatomic interaction at surface level are altered. These changes depend on different factors such as temperature, pressure, or stoichiometry.

The nomenclature of the surface phase reconstructions is given with reference to the 2-D translations vectors $\vec{a}$ and $\vec{b}$ [46]. A surface phase reconstruction (7×1), will indicate that the unit cell at the surface is 7 times longer in direction $\vec{a}$ than in direction $\vec{b}$.

A common tool to determine the bulk structure of crystalline materials, is the analysis of Braggs peaks via X-Ray diffraction technique. Nevertheless, due to the low number of atoms involved, this technique is not viable for surface analysis, and more precise characterisation techniques such as STM, AFM, or LEED are demanded.

The Electron Counting Rule (ECR) is an accepted formalism based on the achievement of the same electron configuration as the noble gas in the period used for each element. Having an orbital full of electrons, results energetically favourable for the system. For the simple case of Silicon, since it belongs to the group IV of the periodic table, the state that would minimise its energy would be bonding with other atoms in order to "gain" four more electrons, what would fill up its orbitals reaching the electronic configuration of a noble gas. It is due to this reason, that on a pure Si lattice, each Si is bonded with another 4, sharing their electron in covalent bonds. ECR assumes surfaces are non-metallic so dangling bonds of electronegative atom are full and dangling bond on electropositive atoms are empty [47]. This tool can be very useful for classifying and predicting the electronic structure and bonding characteristics of different compounds and semiconductors [48]. In the bulk, most crystals follow these rules. However, at the surface the ECR is not always met, leading to dangling bonds and forcing the surface to minimise the energy to compensate for the missing bonds.

A very illustrative case of surface reconstruction can be exemplified in silicon. By cleaving Si along the (100) surface, its ideal diamond-like structure is disrupted and results in a 1×1 square array of surface Si atoms, as exposed in Figure 8 a). Each of these has two dangling bonds remaining from the diamond-like structure, therefore generating an unstable surface. The system then, will try to minimise the surface energy decreasing the number of dangling bonds. The dangling bonds will recombine generating pairs of atoms referred to as dimers. In the case of Si (001), the number of dangling bonds is decreased by a factor of two, bringing the reconstruction 2×1. This phenomenon is represented in Figure 8 b) [46].

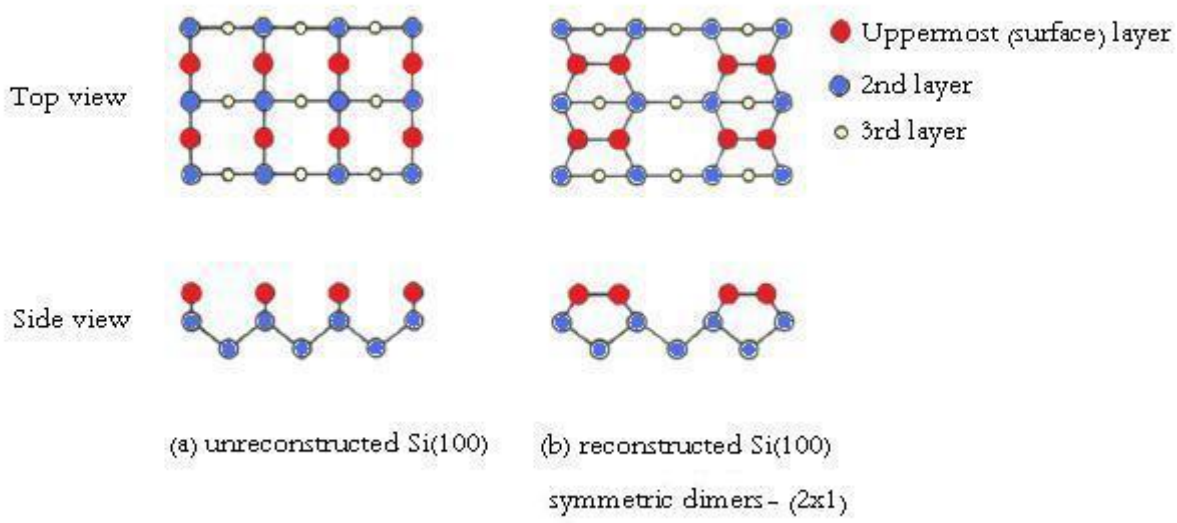

Figure 8. Description of (2x1) phase reconstruction for Si. (Figure adapted from [49] with permission from publisher).

The surface reconstruction plays an important role in the epitaxial growth on GaAs (001) too, however, GaAs is a more complex system where ECR is not always met. GaAs structure is the zinc-blende. Two hybridized orbitals, one for Ga and one for As, combine to form a bonding and antibonding orbital in bulk structures, some hybrid orbitals cannot form a bond at surfaces. The unreconstructed surfaces have partially filled dangling bonds, which are energetically

unfavourable. Figure 9 shows the surface of GaAs along the [001] direction. It is visible how the surface can be either Ga-terminated or As-terminated [50].

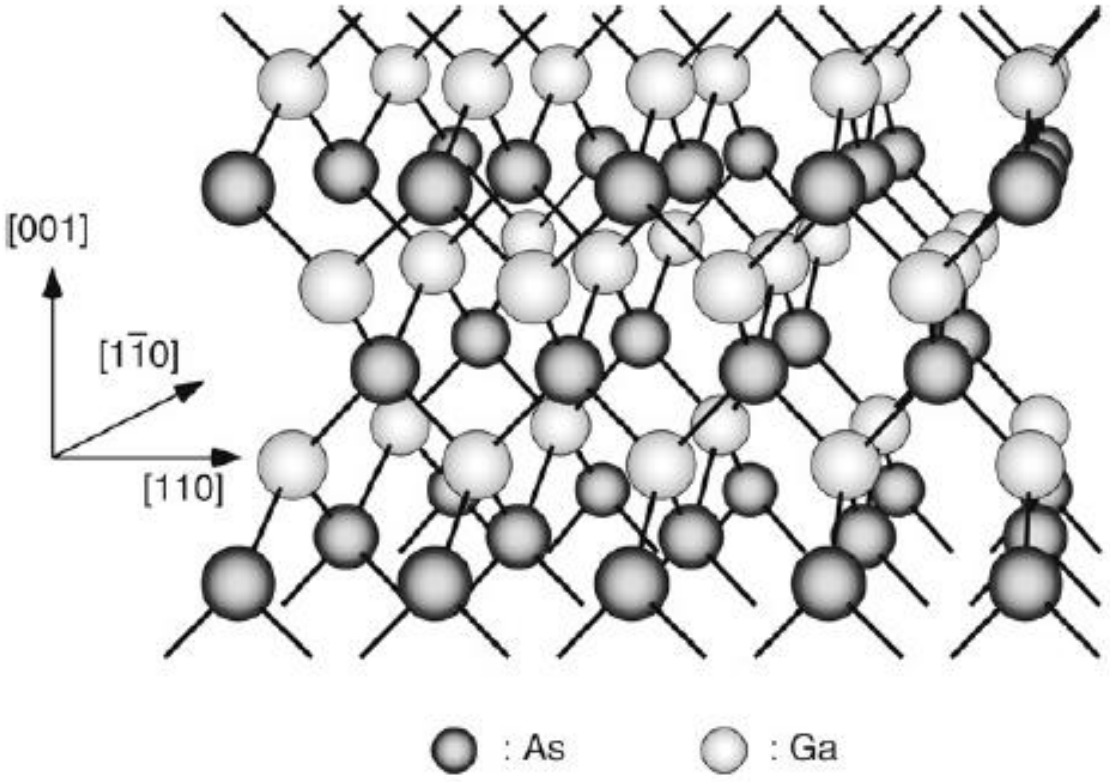

Figure 9. GaAs zinc-blende structure along the [001] direction. Different terminations for Ga or As are shown. (Figure adapted from [50] with permission from publisher).

To get rid of the energy unfavourable dangling bonds, the Ga and As atoms of the GaAs (001) surface reorganise into dimers, which lead to complex reconstructions. Depending upon the stoichiometry, the surface can be Ga-rich or As-rich. Most studied Ga-rich reconstructions are (4 × 6), (3 × 1), c(8 × 2) and (6 × 6), As-rich phases are (2 × 4) c(4 × 4); all ranging from Ga-rich to As-rich respectively. The "c" at the beginning of some reconstructions stands for centred.

Up to now, the MBE community has been referring to the phase diagram for GaAs presented by Däweritz et al. This diagram is shown in Figure 10. However, in the past years updates to this diagram has been presented and provide a much deeper knowledge on phase reconstructions on GaAs [41], [51]–[53]. Many of them, have

been devoted to the analysis of Ga-rich reconstructions [54]–[58]. A detailed insight on the different surface reconstructions is crucial for MBE growth for GaAs.

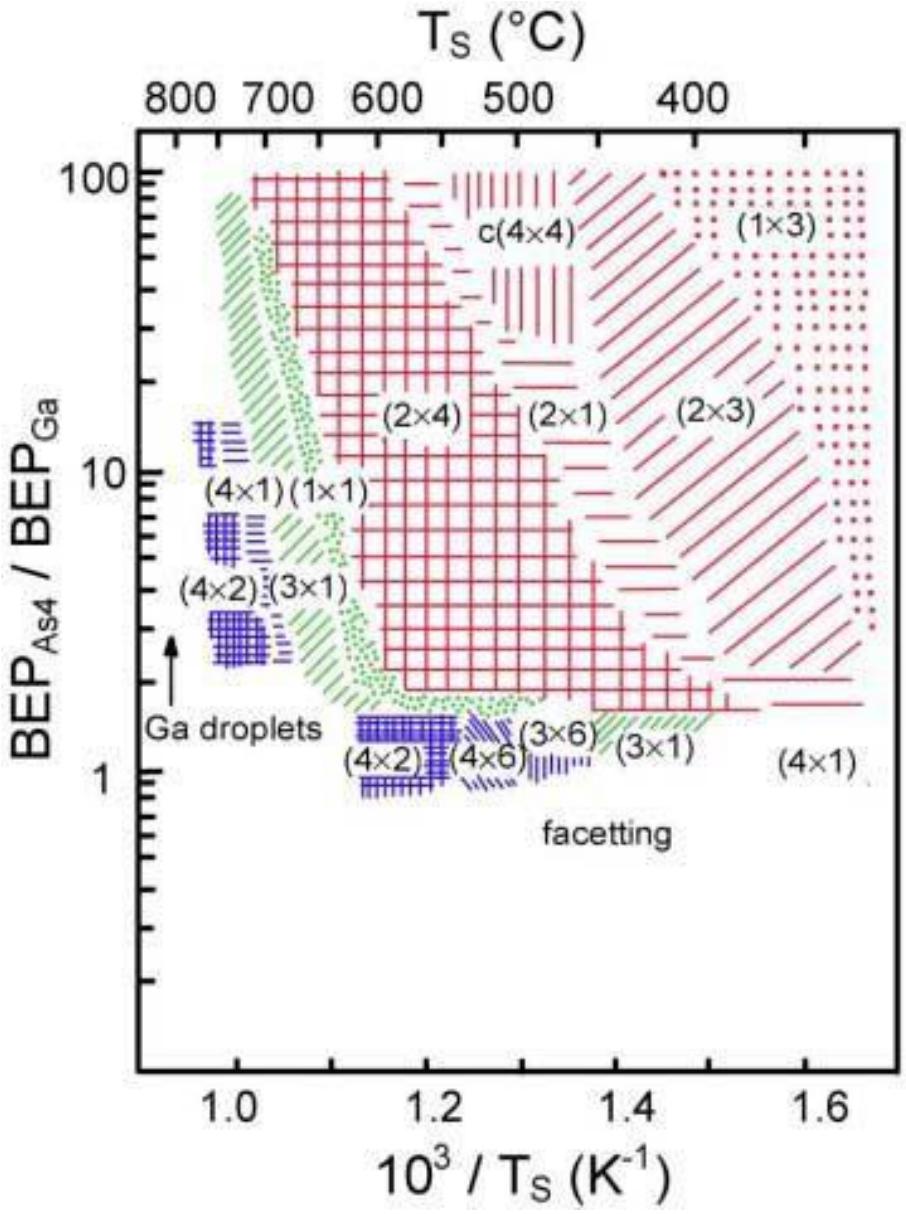

Figure 10. Phase diagram for GaAs (001) as a function of temperature, and ratio of the fluxes, expressed Beam Equivalent Pressure (BEP) for As_4 and Ga. (Figure adapted from [59] with permission from publisher).

At given temperature, the stable structure will always be the one with the lowest Gibbs free surface energy. The total surface energy for GaAs depends on the values

of the Ga and As chemical potentials individually. Surface chemical potential is thus a critical parameter for the stability of surface phases [52]. It is defined as the variation of Gibbs energy per variation of number of atoms [60]. The surface chemical potential will be expressed as reflected in Eq. 2. The stoichiometry at the surface therefore will ultimately determine the total chemical potential [61], [62].

$$\mu_i^S = \left(\frac{\partial G}{\partial N_i}\right)_{P,T,N_{j\neq i}} \qquad \text{Eq. 2}$$

Changes in the surface which imply the migration, incorporation, or motion of atoms; will lead to changes in the chemical potential and therefore may induce a local phase transformation. Phase transformation on surfaces have been object of study lately. Investigation on phase transitions on silicon [63]–[66] and GaAs [52]–[54], [67] have been reported. Some of these studies have been carried out using LEEM technique [29], [52], [68], [69]. Ab-initio calculations have also been developed to investigate the nature of the surface phases, although these studies are typically performed at 0K and they don't consider the effect of temperature [70].

Variations on the chemical potential of the species can be caused by desorption of atoms from the surface. The investigation on the desorption of species for GaAs has been reported by some groups who highlight the importance of these studies to optimise the control of the growth parameters [71]–[73]. Ploog et al. studied the desorption of As on GaAs (001). They demonstrated in 1997 that for the GaAs (001) surface, the As desorption commences at step edges and gradually continues on the terraces [74].

The analysis of atomic steps is also another phenomenon of high importance for the analysis of surface science for growth applications. Numerous studies have been devoted to the scrutiny of the generation of new terraces, the boundaries between phase domains and the nature of the atomic steps on the surface of Si

[64], [75]–[80], GaAs [81], [82], and other materials like GaN [83], [84] or sapphire [85]. Also, theoretical simulations and a Monte Carlo (MC) model have been carried out regarding atomic steps on different crystallographic directions [86], [87]. All these studies provide useful information on the evolution of the surface on different semiconductors. This information on the surface kinetics is of high importance for the optimisation of growth parameters. A number of these studies have been performed using the advantages of LEEM [76], [88]–[91]. We aim to provide a good insight on the dynamical processes at the GaAs (001) surface under MBE conditions using our unique LEEM-MBE equipment. This equipment holds substantial potential for the identification of dynamical processes during growth at video rate.

In this thesis, different phase reconstructions for GaAs (001) will be mentioned throughout different chapters. Deeper analysis has been taken out for four particular Ga-rich phases: c(8×2), (2×4), (6×6), and (3×6). Many different atomic arrangements have been proposed in the literature for these phases. For the first three, Figure 11 shows with detail the atomic models for each of the reconstructions.

The (2×4) and the c(8×2), are well established in the literature. For the (2×4) reconstruction, the most well-accepted model in the literature is the so-called β2(2×4)model, which contains two As dimers in the outermost atomic layer and a third As dimer situated in the third atomic layer, within the trench formed due to missing dimers [92].

The Ga-rich c(8×2) reconstruction, similar to the As-rich (2×4), in the c(8×2) reconstruction, the twofold periodicity in the [110] direction is due to the formation of surface Ga dimers. The recently proposed structure model contains 0.5 ML of surface As atoms at faulted positions, due to the presence of the Ga-Ga dimers in the second layer. The β model, which is one of the most accepted in the literature, has been supported in the literature by the I-V curve analysis of LEED for this phase [93].

The (6×6) reconstruction, has been a matter of debate during the years and some people have referred to it as (n×6), (1×6), (2×6) or even (2×6)/(3×6). It was suggested by Ohtake, that kinetics might play an important role in the formation of this phase due to the fact that the (6×6) has not been observed under As-flux [50]. The (6×6) reconstruction is generally achieved by cooling the c(8×2) surface and the coexistence of both phases has already been proved in the literature [94]. Ga subsurface dimers are believed to be present, which results in surface As atoms locating in faulted positions. In addition, the presence of a surface mixed Ga-As dimer has been suggested in the literature for the (6×6) reconstructions as the configuration more stable than the surface As-As dimers [54]. This model as it was originally proposed does not satisfy the ECR. The missing spots observed in some STM patterns may be attributed to missing As-As dimers. If 25% of the As-As dimers in the (6×6) unit cell are missing, the structure then satisfies the ECR. In principle, the minimum unit cell size that would satisfy this condition would be a (12×6) reconstruction [95], but recently this has been attributed to configurational entropy [96]. Seino et al. also concluded that the random sequence within the bright chains observed in some STM images can be explained by the energetic degeneracy of different arrangements of Ga-As mixed dimers explains. They reported that the (6×6) model seemed unstable and that it could be stabilised by creating larger reconstructions that allow for complying with ECR [95].

The (3×6) structure, however, has not yet been reported and there is very little information about it. Ohtake has already hypothesised that this phase might actually be a disordered form of the (6x6) [50], but no information with respect to its atomic structure has been provided. Figure 12 shows other atomic models presented for different (n×6) reconstructions. We hypothesise that the (3×6) atomic model, shares similar dimer positions with the periodicity of other (n×6) reconstructions, and that certain disorder must be involved [50].

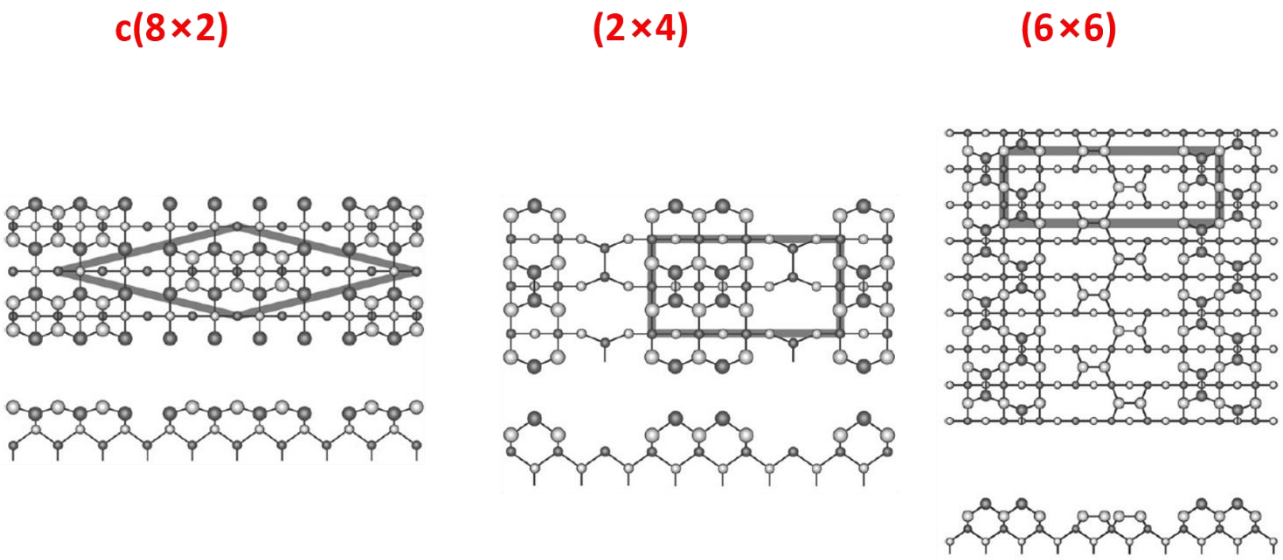

Figure 11. Atomic models for different phases, c(8×2) [97], (2×4) [98], (6×6) [99]. (Figures adapted with permission from publisher).

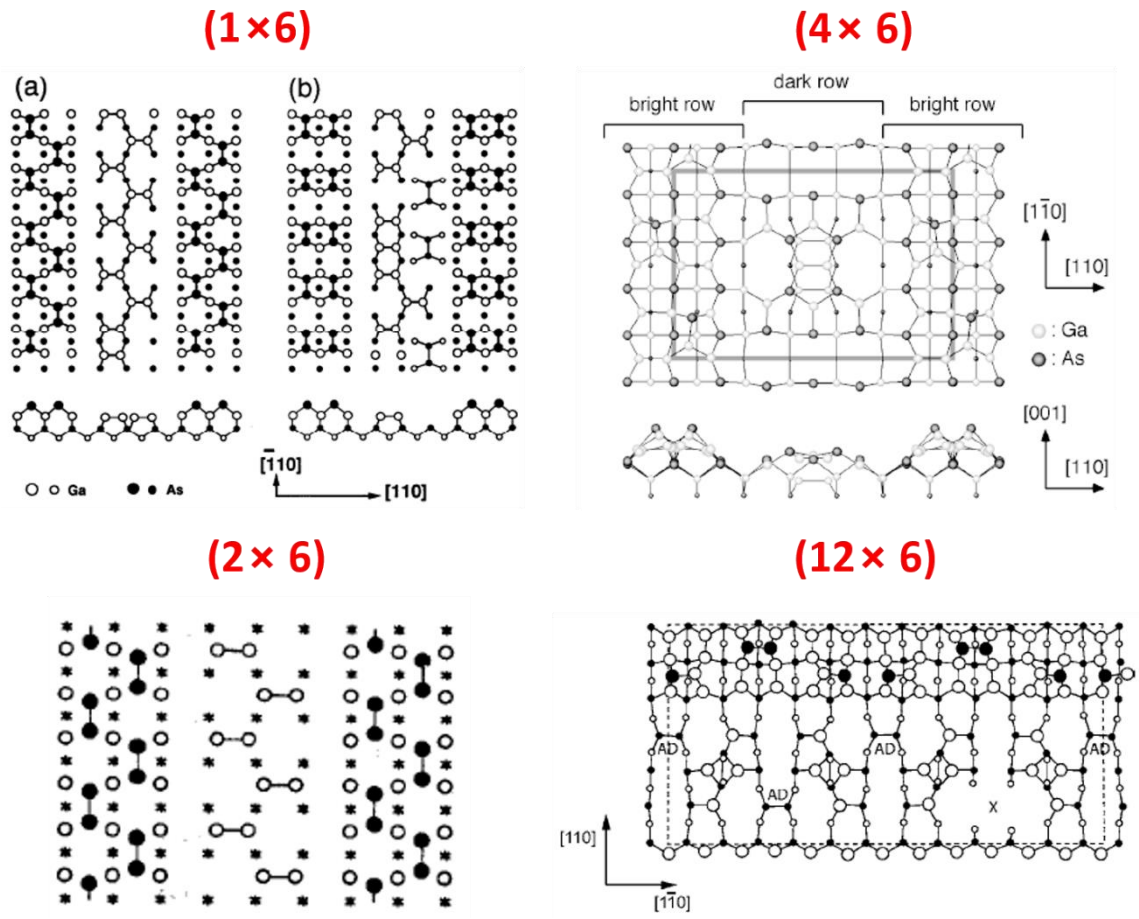

Figure 12. Atomic models for different (n×6) reconstructions: (1×6) [98] top left, (4×6) [56] top right, (2×6) [99] bottom left, and (12×6) [95] bottom right. (Figures adapted with permission from publisher).

References:

[1] C. Buckle, "Digital consumers own 3.64 connected devices," 2016. [Online]. Available: https://blog.globalwebindex.com/chart-of-the-day/digital-consumers-own-3-64-connected-devices/. [Accessed: 24-Jun-2019].

[2] E. Bauer, *Surface microscopy with Low Energy Electrons*. Springer, 2014.

[3] J. E. Bowers, J. T. Bovington, A. Y. Liu, and A. C. Gossard, "A Path to 300 mm Hybrid Silicon Photonic Integrated Circuits," *Ofc 2014*, pp. 1–3, 2014.

[4] V. Y. Aleshkin *et al.*, "Monolithically integrated InGaAs / GaAs / AlGaAs quantum well laser grown by MOCVD on exact Ge / Si (001) substrate," vol. 061111, no. 001, pp. 6–10, 2016.

[5] Y. Wan *et al.*, "Temperature characteristics of epitaxially grown InAs quantum dot micro-disk lasers on silicon for on-chip light sources," *Appl. Phys. Lett.*, vol. 109, no. 011104, pp. 1–5, 2016.

[6] A. Y. Liu, C. Zhang, A. C. Gossard, and J. E. Bowers, "Quantum Dot Lasers on Silicon," *Gr. IV Photonics (GFP), 2014 IEEE 11th Int. Conf.*, pp. 205–206, 2014.

[7] M. Á. Caro Bayo, "Theory of elasticity and electric polarization effects in the group-III nitrides," *Dr. Thesis. Univ. Coll. Cork*, 2013.

[8] K. Burak, "Epitaxy Epitaxial Growth," 2007.

[9] J. C. I. Bean, "Strained-Layer Epitaxy of Germanium-Silicon Alloys," *Science (80-.).*, vol. 230, no. 4722, pp. 127–131, 1985.

[10] V. Orsi Gordo *et al.*, "Band structure engineering in strain-free GaAs mesoscopic systems," *Nanotechnology*, vol. 31, no. 255202, pp. 1–9, 2020.

[11] J. G. Hao *et al.*, "Phase tailoring and wafer-scale uniform hetero-epitaxy of metastable-phased corundum α-Ga2O3 on sapphire," *Appl. Surf. Sci.*, vol. 513, no. 145871, pp. 1–6, 2020.

[12] T. P. Dash, S. Dey, S. Das, E. Mohapatra, J. Jena, and C. K. Maiti, "Strain-

engineering in nanowire field-effect transistors at 3 nm technology node," *Phys. E Low-Dimensional Syst. Nanostructures*, vol. 118, no. December 2019, p. 113964, 2020.

[13] Y. Chen *et al.*, "Strain engineering and epitaxial stabilization of halide perovskites," *Nature*, vol. 577, no. 7789, pp. 209–215, 2020.

[14] D. E. Perea, J. E. Allen, S. J. May, B. W. Wessels, D. N. Seidman, and L. J. Lauhon, "Three-dimensional nanoscale composition mapping of semiconductor nanowires," *Nano Lett.*, vol. 6, no. 2, pp. 181–185, 2006.

[15] H. Choi, "Vapor–Liquid–Solid Growth of Semiconductor Nanowires," in *Semiconductor Nanostructures for Optoelectronic Devices Processing, Characterization and Applications*, G.-C. Yi, Ed. Springer, 2012.

[16] Z. Gačević, D. Gómez Sánchez, and E. Calleja, "Formation mechanisms of gan nanowires grown by selective area growth homoepitaxy," *Nano Lett.*, vol. 15, no. 2, pp. 1117–1121, 2015.

[17] H. Zhang, Y. Chen, G. Zhou, C. Tang, and Z. Wang, "Wetting layer evolution and its temperature dependence during self-assembly of InAs/GaAs quantum dots.," *Nanoscale Res. Lett.*, vol. 7, no. 1, p. 600, 2012.

[18] J. X. Chen *et al.*, "Tuning InAs/GaAs quantum dot properties under Stranski-Krastanov growth mode for 1.3 μm applications," *J. Appl. Phys.*, vol. 91, no. 10 I, pp. 6710–6716, 2002.

[19] J. G. Keizer, J. Bocquel, P. M. Koenraad, T. Mano, T. Noda, and K. Sakoda, "Atomic scale analysis of self assembled GaAs/AlGaAs quantum dots grown by droplet epitaxy," *Appl. Phys. Lett.*, vol. 96, no. 062101, pp. 1–4, 2010.

[20] J. Bocquel, A. D. Giddings, T. Mano, T. J. Prosa, D. J. Larson, and P. M. Koenraad, "Composition profiling of GaAs/AlGaAs quantum dots grown by droplet epitaxy," *Appl. Phys. Lett.*, vol. 105, no. 153102, pp. 1–4, 2014.

[21] N. Ha *et al.*, "Droplet epitaxy growth of telecom InAs quantum dots on metamorphic InAlAs / GaAs (111) A," *Jpn. J. Appl. Phys.*, vol. 54, p. 04DG07, 2015.

[22] S. Huang, Z. Niu, Z. Fang, H. Ni, Z. Gong, and J. Xia, "Complex quantum ring structures formed by droplet epitaxy," *Appl. Phys. Lett.*, vol. 89, no. 3, pp. 10–13, 2006.

[23] C. Heyn, T. Bartsch, S. Sanguinetti, D. Jesson, and W. Hansen, "Dynamics of mass transport during nanohole drilling by local droplet etching.," *Nanoscale Res. Lett.*, vol. 10, p. 67, 2015.

[24] A. Nemcsics, "Quantum Dots Prepared by Droplet Epitaxial Method," in *Quantum Dots - Theory and Application*, 2015.

[25] E. Bauer, "Low-Energy Electron Microscopy," *Elsevier*, no. February 2015, pp. 1–14, 2016.

[26] E. Bauer, M. Mundschau, W. Swiech, and W. Telieps, "Low Energy Electron Microscopy of surface processes on clean Si (111) and Si (100)," *Mater. Res. Soc.*, vol. 159, no. 100, pp. 225–233, 1990.

[27] N. Rougemaille and A. K. Schmid, "Magnetic imaging with spin-polarized low-energy electron," *Eur. Phys. J. Appl. Phys.*, vol. 50, no. 20101, 2010.

[28] E. Bauer, "LEEM and UHV-PEEM : A retrospective," *Ultramicroscopy*, vol. 119, pp. 18–23, 2012.

[29] J. B. Hannon and R. M. Tromp, "Low-energy electron microscopy of surface phase transitions," *Annu. Rev. Mater. Sci.*, vol. 33, pp. 263–288, 2003.

[30] J. De Figuera and K. F. Mccarty, *Low-Energy Electron Microscopy*. 2013.

[31] A. J. SpringThorpe, S. J. Ingrey, B. Emmerstorfer, P. Mandeville, and W. T. Moore, "Measurement of GaAs surface oxide desorption temperatures," *Appl. Phys. Lett.*, vol. 50, no. 2, pp. 77–79, 1987.

[32] G. Britain, E. Engineering, and S. Received, "The thermal oxidation of GaAs," vol. 11, pp. 1451–1456, 1978.

[33] Y. Asaoka, "Desorption process of GaAs surface native oxide controlled by direct Ga-beam irradiation," *J. Cryst. Growth*, vol. 251, no. 1–4, pp. 40–45, 2003.

[34] O. A. Ageev, M. S. Solodovnik, S. V Balakirev, and M. M. Eremenko, "Effect of GaAs native oxide on the Ga droplets formation during GaAs MBE growth," no. 15, pp. 1–2, 2016.

[35] A. Guillén-Cervantes, Z. Rivera-Alvarez, M. López-López, E. López-Luna, and I. Hernández-Calderón, "GaAs surface oxide desorption by annealing in ultra high vacuum," *Thin Solid Films*, vol. 373, no. 1–2, pp. 159–163, 2000.

[36] Y. Asaoka, T. Kanebishi, N. Sano, and T. Kaneko, "In situ control of the desorption process of GaAs surface native oxide by direct Ga beam irradiation," *Molecular Beam Epitaxy, 2002 International Conference on*. pp. 111–112, 2002.

[37] J. J. D. Lee, K. W. West, K. W. Baldwin, and L. N. Pfeiffer, "Smoothness and cleanliness of the GaAs (100) surface after thermal desorption of the native oxide for the synthesis of high mobility structures using molecular beam epitaxy," *J. Cryst. Growth*, vol. 356, pp. 46–52, Oct. 2012.

[38] C. Zheng, W.-X. Tang, and D. E. Jesson, "Planar regions of GaAs (001) prepared by Ga droplet motion," *J. Vac. Sci. Technol. A*, vol. 34, no. 4, pp. 1–8, 2016.

[39] J. Tersoff, D. E. Jesson, and W. X. Tang, "Running Droplets of Gallium from Evaporation of Gallium Arsenide," *Science*, vol. 324, no. 5924, pp. 236–238, 2009.

[40] D. E. Jesson and W. X. Tang, "Surface Electron Microscopy of Ga Droplet Dynamics on GaAs (001)," *Microsc. Sci. Technol. Appl. Educ.*, no. 001, pp. 1608–1619, 2010.

[41] U. Resch-Esser *et al.*, "Surface quality and atomic structure of MBE-grown GaAs(100) prepared by the desorption of a protective arsenic layer," *Surf. Sci.*, vol. 352–354, pp. 71–76, May 1996.

[42] R. W. Bernstein and A. Borg, "Capping and decapping of MBE grown GaAs (001), $Al_{0.5}Ga_{0.5}As$ (001), and AlAs (001) investigated with ASP , PES , LEED , and RHEED," *Appl. Surf. Sci.*, vol. 58, no. 001, pp. 74–80, 2007.

[43] C. Heinlein *et al.*, "Patterned regrowth of n -GaAs by molecular beam epitaxy using arsenic passivation," *J. Vac. Sci. Technol. B*, vol. 17, no. 217, pp. 217–223, 1999.

[44] K. G. Eyink, Y. S. Cong, R. Gilbert, M. A. Capano, T. W. Haas, and B. G. Streetman, "In situ ellipsometric study of As capping and low temperature molecularbeam epitaxy GaAs growth and implications for the low temperature critical thickness," *J. Vac. Sci. Technol. B*, vol. 11, no. 1423, pp. 1423–1426, 1993.

[45] J. W. Dong, L. C. Chen, and C. J. Palmstrøm, "Molecular beam epitaxy growth of ferromagnetic single crystal (001) Ni2MnGa on (001) GaAs," *Appl. Phys. Lett.*, vol. 75, no. 10, pp. 1443–1445, 1999.

[46] M. Hanbucken and J.-P. Deville, *Stress and Strain in Epitaxy*. Elsevier, 2001.

[47] R. Cortés *et al.*, "Observation of a mott insulating ground state for Sn/Ge(111) at low temperature," *Phys. Rev. Lett.*, vol. 96, no. 12, pp. 1–4, 2006.

[48] S. C. Rasmussen, "The 18-electron rule and electron counting in transition metal compounds: theory and application," *ChemTexts*, vol. 1, no. 1, pp. 1–9, 2015.

[49] S. Mustafa, "Size–dependent structure parameter for silicon nanowires and nanoparticles," in *PhD Thesis*, no. October 2010, 2010.

[50] A. Ohtake, "Surface reconstructions on GaAs(001)," *Surf. Sci. Rep.*, vol. 63, pp. 295–327, 2008.

[51] W. G. Schmidt, F. Bechstedt, and J. Bernholc, "GaAs(001) surface reconstructions: geometries, chemical bonding and optical properties," *Appl. Surf. Sci.*, vol. 190, no. 1, pp. 264–268, 2002.

[52] C. X. Zheng, J. Tersoff, W. X. Tang, A. Morreau, and D. E. Jesson, "Novel GaAs surface phases via direct control of chemical potential," *Phys. Rev. B*, vol. 93, no. 19, p. 195314, 2016.

[53] V. V Preobrazhenskii, M. A. Putyato, O. P. Pchelyakov, and B. R. Semyagin, "Surface structure transitions on (001)GaAs during MBE," *J. Cryst. Growth*, vol. 202, pp. 166–169, 1999.

[54] M. Pristovsek *et al.*, "Gallium-rich reconstructions on GaAs(001)," *Phys. Status Solidi Basic Res.*, vol. 240, no. 1, pp. 91–98, 2003.

[55] S. Tsukamoto *et al.*, "Ga-rich GaAs[001] surfaces observed by STM during high-temperature annealing in MBE chamber," *MBE 2002 - 2002 12th Int. Conf. Mol. Beam Ep.*, vol. 251, pp. 113–114, 2002.

[56] A. Ohtake, P. Koćan, K. Seino, W. G. Schmidt, and N. Koguchi, "Ga-rich limit of surface reconstructions on GaAs(001): Atomic structure of he (4 × 6) phase," *Phys. Rev. Lett.*, vol. 93, no. 26 I, pp. 4–7, 2004.

[57] M. Kuball, D. T. Wang, N. Esser, M. Cardona, J. Zegenhagen, and B. O. Fimland, "Microscopic structure of the GaAs(001)-(6 x 6) surface derived from scanning tunneling microscopy," *Phys Rev B Condens Matter*, vol. 51, no. 19, pp. 13880–13882, 1995.

[58] A. Ohtake, S. Tsukamoto, M. Pristovsek, N. Koguchi, and M. Ozeki, "Structure analysis of the Ga-stabilized GaAs(001)-c(8x2) surface at high temperatures," *Phys. Rev. B*, vol. 65, no. 233311, p. 14, 2002.

[59] L. Daweritz, "Surface characterization by RHEED techniques during MBE growth of GaAs and $Al_xGa_{1-x}As$" *Superlattices Microstruct.*, vol. 9, no. 2, pp. 141–145, 1997.

[60] A. D. McNaught and A. Wilkinson., *IUPAC. Compendium of Chemical Terminology. Gold Book*. Oxford: Blackwell Scientific Publications, 1997.

[61] B. Bhushan, *Encyclopedia of nanotechnology*, vol. 50, no. 06. Colombus, OH, USA: Springer, 2013.

[62] C. Bermúdez-Salguero and J. Gracia-Fadrique, "The surface chemical potential from a surface equation of state versus Butler's equation," *Fluid Phase Equilib.*, vol. 375, pp. 367–372, 2014.

[63] M. K. T.Doi, "Investigation of Si(001) stable surfaces in alternating current heating," *Surf. Sci.*, vol. 653, pp. 226–236, 2016.

[64] H. Jeong and E. D. Williams, "Steps on surfaces : experiment and theory," *Surf. Sci. Rep.*, vol. 34, pp. 171–294, 1999.

[65] Sangyeob Lee, "Surface potential measurements of 2×1 reconstructed Si(001) using UHV Kelvin probe force microscopy," *Surf. Sci.*, vol. 641, pp. 16–22, 2015.

[66] S. J. White and D.P.Woodruff, "The surface structure of Si (100) surfaces using averaged LEED," *Surf. Sci.*, vol. 64, pp. 131–140, 1977.

[67] M. Pristovsek, T. Trepk, M. Klein, J.-T. Zettler, and W. Richter, "Dynamic study of the surfaces of (001) gallium arsenide in metal-organic vapor-phase epitaxy during arsenic desorption," *J. Appl. Phys.*, vol. 87, no. 3, p. 1245, 2000.

[68] L. Zhu *et al.*, "Coverage-driven phase transition of copper silicide monolayer on Si (111)," *Ultramicroscopy*, vol. 200, no. February, pp. 39–42, 2019.

[69] J. B. Hannon, F. J. Meyer zu Heringdorf, J. Tersoff, and R. M. Tromp, "Phase coexistence during surface phase transitions," *Phys. Rev. Lett.*, vol. 86, no. 21, pp. 4871–4874, 2001.

[70] B. Meyer, "Surface Phase Diagrams from Ab Initio Thermodynamics," *Comput. Nanosci.*, vol. 31, pp. 411–418, 2006.

[71] T. Ohachi, J. . Feng, and K. Asai, "Arsenic pressure dependence of Ga desorption from MBE high index GaAs substrates," *J. Cryst. Growth*, vol. 211, no. 1, pp. 405–410, 2000.

[72] Z. Y. Zhou, C. X. Zheng, W. X. Tang, D. E. Jesson, and J. Tersoff, "Congruent evaporation temperature of GaAs(001) controlled by As flux," *Appl. Phys. Lett.*, vol. 97, no. 121912, pp. 1–3, 2010.

[73] J. Tersoff, D. E. Jesson, and W. X. Tang, "Decomposition controlled by surface morphology during Langmuir evaporation of GaAs," *Phys. Rev. Lett.*, vol.

105, no. 3, pp. 1–4, 2010.

[74] J. Behrend, M. Wassermeier, and K. H. Ploog, "Different As desorption behaviour at step edges on InAs(001) and GaAs(001) surfaces," *Surf. Sci.*, vol. 372, no. 1–3, pp. 307–311, Feb. 1997.

[75] Y. Homma, M. Tomita, and T. Hayashi, "Atomic step imaging on silicon surfaces by scanning electron microscopy," *Ultramicroscopy*, vol. 52, pp. 187–192, 1993.

[76] M. Henzler, "Atomic Steps on Single Crystals: Experimental Methods and Properties," *Appl. Phys.*, vol. 9, pp. 11–17, 1976.

[77] C. Schelling, G. Springholz, and F. Schäffler, "Kinetic Growth Instabilities on Vicinal Si (001) Surfaces," *Phys. Rev. Lett.*, vol. 83, no. 5, pp. 995–998, 1999.

[78] H. J. W. Zandvliet, "Morphology of monatomic step edges on vicinal Si(001)," *Phys. Rev. B*, vol. 48, no. 19, pp. 14269–14275, 1993.

[79] A. L. Latyshev, A.V.; Litvin L.V.; Aseev, "Peculiarities of step bunching on Si 001 surface induced by DC heating," *Appl. Surf. Sci.*, vol. 130–132, pp. 139–145, 1998.

[80] K. Fujita and M. Ichikawa, "Size-scaling exponents of current-induced step bunching on silicon surfaces," *Phys. Rev. B*, vol. 60, no. 23, pp. 6–12, 1999.

[81] J. E. Van Nostrand, S. J. Chey, D. G. Cahill, and H. Morko, "Surface morphology of GaAs (001) grown by solid- and gas-source molecular beam epitaxy," *Surf. Sci.*, vol. 346, pp. 136–144, 1996.

[82] M. D. Johnson, J. Sudijono, A. W. Hunt, and B. G. Orr, "The dynamical transition to step-flow growth during molecular beam epitaxy of GaAs (001)," *Surf. Sci.*, vol. 298, pp. 392–398, 1993.

[83] Z. S. Gong Hua, Pan Guoshun, Zhou Yan, Shi Xiaolei, Zou Chunli, "Investigation on the surface characterization of Ga-faced GaN after chemical-mechanical polishing," *Appl. Surf. Sci.*, vol. 338, pp. 85–91, 2015.

[84] H. Gong, G. Pan, C. Zou, Y. Zhou, and L. Xu, "Investigation on the variation of

the step-terrace structure on the surface of polished GaN wafer," *Surfaces and Interfaces*, vol. 0, pp. 1–5, 2016.

[85] R. Wang, D. Guo, G. Xie, and G. Pan, "Atomic Step Formation on Sapphire Surface in Ultra-precision Manufacturing," *Sci. Rep.*, pp. 1–9, 2016.

[86] N. Akutsu, "Effect of the roughening transition on the vicinal surface in the step droplet zone," *J. Cryst. Growth*, no. October, pp. 1–6, 2016.

[87] J. Krug, V. Tonchev, S. Stoyanov, and A. Pimpinelli, "Scaling properties of step bunches induced by sublimation and related mechanisms," *Phys. Rev. B*, vol. 71, no. 045412, pp. 1–15, 2005.

[88] K. L. W. Lau, K. M. Yu, D. Luo, R. S. Ruo, and M. S. Altman, "High throughput scanning μ LEED imaging of surface structural heterogeneity : Defective graphene on Cu (111)," *Ultramicroscopy*, vol. 200, no. February, pp. 67–72, 2019.

[89] G. C. Robertson MacCallum, Yizheng Wu, Schmid, Andreas K., "Observation of surface step bunch induced perpendicular magnetic anisotropy using spin-polarized low energy electron microscopy," *Ultramicroscopy*, vol. 200, pp. 180–183, 2019.

[90] C. X. Zheng, W. X. Tang, and D. E. Jesson, "Relief of surface stress at steps during displacive adsorption of As on," *Appl. Phys. Lett.*, vol. 100, no. 201602, pp. 1–4, 2012.

[91] K. F. McCarty, J. a Nobel, and N. C. Bartelt, "Vacancies in solids and the stability of surface morphology.," *Nature*, vol. 412, no. August, pp. 622–5, 2001.

[92] A. Ohtake, T. Yasuda, and N. Miyata, "Anisotropic kinetics on growing Ge (001) surfaces," *Surf. Sci.*, vol. 603, no. 5, pp. 826–830, 2009.

[93] J. Cerda, F. J. Palomares, and F. Soria, "Structure of GaAs(100)-c(8 x 2)-Ga," *Phys. Rev. Lett.*, vol. 75, no. 4, pp. 665–668, 1995.

[94] P. Kocán, A. Ohtake, and N. Koguchi, "Structural features of Ga-rich

GaAs(001) surfaces: Scanning tunneling microscopy study," *Phys. Rev. B - Condens. Matter Mater. Phys.*, vol. 70, no. 20, pp. 4–7, 2004.

[95] K. Seino, W. G. Schmidt, and O. A., "Ga-rich GaAs(001) surface from ab initio calculations: Atomic structure of the (4x6) and (6x6) reconstructions," *Phys. Rev. B*, vol. 73, no. 035317, pp. 4–9, 2006.

[96] K. Hannikainen, D. Gomez, J. Pereiro, Y. R. Niu, and D. E. Jesson, "Surface Phase Metastability during Langmuir Evaporation," *Phys. Rev. Lett.*, vol. 123, no. 186102, pp. 1–5, 2019.

[97] I. Kamiya, D. E. Aspnes, L. T. Florez, and J. P. Harbison, "Reflectance-difference spectroscopy of (001) GaAs surfaces in ultrahigh vacuum," *Phys. Rev. B*, vol. 46, no. 24, pp. 15894–15904, 1992.

[98] Q. K. Xue, T. Hashizume, and T. Sakurai, "Scanning tunneling microscopy of III-V compound semiconductor (001) surfaces," *Prog. Surf. Sci.*, vol. 56, no. 1–2, pp. 1–131, 1997.

[99] L. K. Verheij, M. K. Freitag, and F. Wiegershaus, "Helium scattering study of clean and oxygen covered GaAs(100)," *Surf. Sci.*, vol. 334, no. 1–3, pp. 105–113, 1995.

Chapter 2: Experimental techniques

In this chapter the experimental techniques utilised in this thesis (except for the LEEM-MBE) will be reviewed.

Atomic Force Microscope

Scanning Probe Microscopy (SPM) provides the tools for observation of 3D objects at atomic resolution using the interaction between a probe and the sample. This technique does not require from vacuum and the probe-sample interaction can be utilised for the atomic manipulation of the sample surface, as IBM demonstrated in 1989 by printing their logo using SPM techniques [1].

AFM is a powerful morphological characterisation technique that allows surface mapping at atomic resolution in the Z-axis [2]. The AFM relies on the interaction between the sample, and a tip situated on a cantilever. The tip and the cantilever are usually made of Si or Si_3Ni_4. The tip scans the sample in 2-Dimensions, and the forces between the tip and the sample are recorded. In order to calculate this force, Hooke's law is used.

The deflection of the tip is measured using a laser and a photodetector. The laser impinges on the top surface of the tip. This laser is reflected and further detected on a photodetector. The photodetector is divided into four different quadrants. When there is no deflection, the laser is positioned so that the light is shined at the centre of the quadrants. Any deflection will cause the beam to move away from the centre of the photodetector. This is translated into different relative forces which are then translated into different contrast for each pixel in the image. An schematic representation of AFM is shown in Figure 1.

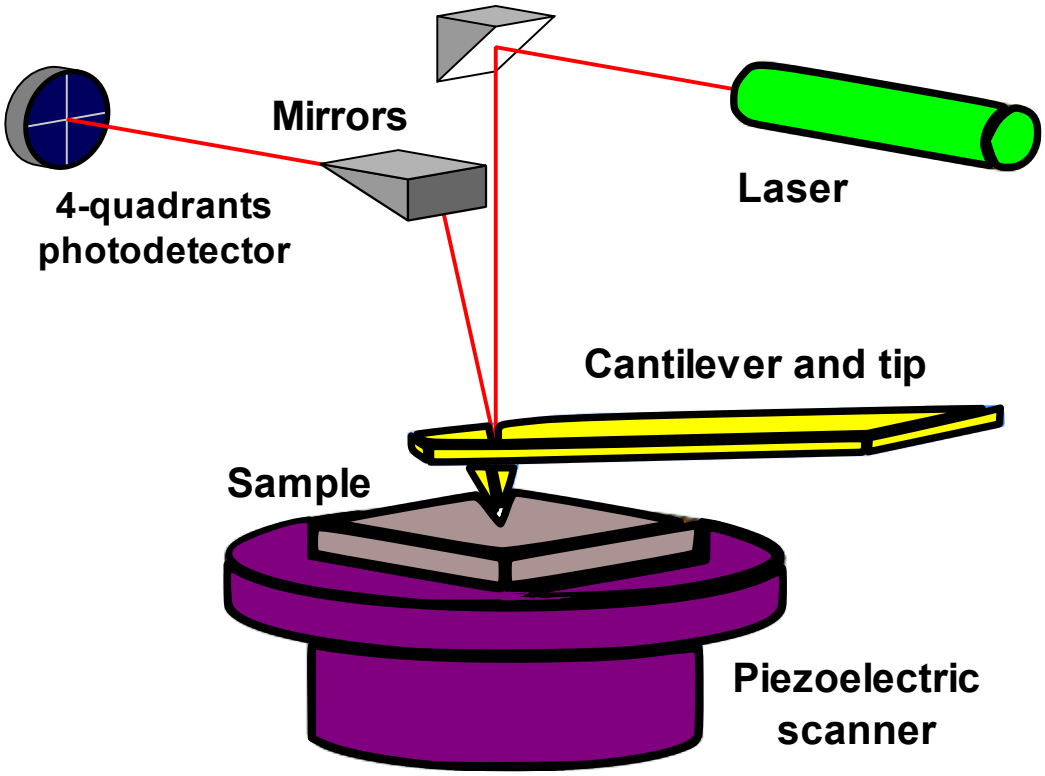

Figure 1. Schematics of Atomic Force Microscope.

There are three different modes the AFM can operate in:

- Contact mode: The tip is kept in contact with the sample and it is dragged across the surface, keeping the deflection constant. The tip works in the repulsive regime (red region of the graph, Figure 1). The tip is exposed to quick degradation and erosion.

- Non-contact: The tip is kept away from the sample and the Van der Waals forces are recorded using the attractive regime (blue region of the graph, Figure 1). The tip is safe from any mechanical damage and usually last longer.

- Tapping mode: This mode is the most commonly used. Also called intermittent contact mode or dynamic mode, this mode was developed to

overcome the stickiness of the liquid meniscus layer originated in most of the samples. The tip is oscillated vertically to a frequency close to the resonance frequency of the tip. As the tip oscillates near the surface, the intermolecular attraction generated between the tip and the surface causes the tip to move towards the sample. Once the tip touches the sample, repulsive forces come into play and this causes the tip (and cantilever) to spring away from the sample. The oscillation amplitude is enough to overcome the stickiness of the surface [2]. Slight variations of the resonance frequency are registered. Using a feedback electronic system, the cantilever sample distance is controlled by keeping either the amplitude or the phase of the oscillating cantilever constant. During the measurements carried out in this project, tapping mode was utilised.

Scanning Electron Microscopy

Electron microscopy uses electrons to form an image, improving the imaging resolution by a factor of 10^5 with respect to optical microscopy techniques. The typical resolution of a conventional SEM is on the range of nanometres.

SEM uses a cathode to generate high-energy electrons. There are several types of filaments that are commonly used: **a)** tungsten (W), which is the cheapest but provides the worst resolution of the three, **b)** lanthanum hexaboride (LaB_6) which provides around 10 times the brightness and 50 times the service life of tungsten cathodes [3]. As the tungsten filament, electrons are generated by thermionic emission; and **c)** FEG (Field Emission Gun) which is based on the application of a difference of potential to the cathode so that electrons are accelerated with a higher acceleration. The electrons are generated by an electron field, so their energy is well-defined, reducing the chromatic aberration. This filament is very efficient, and it is one of the most common filaments nowadays in technology of Electron Microscopy. FEG filament is the one that has been used in this project. A

visual representation of the different filaments for electron microscopy is shown in Figure 2.

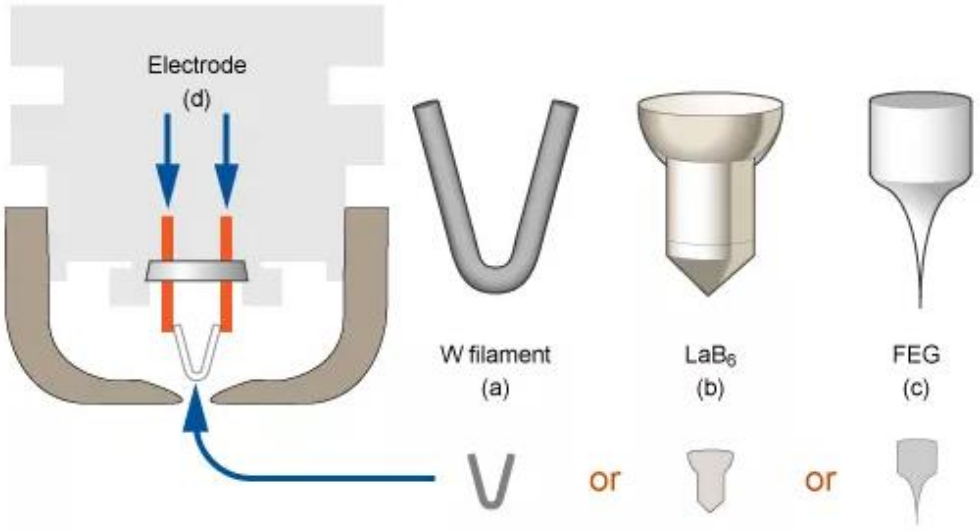

Figure 2. Schematics of different electron sources for electron microscopy a) Tungsten filament, b) LaB_6 c) FEG. (Figure adapted from [4], with permission from publisher).

The SEM is usually under high vacuum to increase the mean free path of the electrons and increase the resolution by reducing the scattering of the electrons with the particles between the emission filament and the sample. After the electrons are emitted, they are accelerated with an energy of between 1-30 KeV and guided through a set of magnetic lenses until they reach the sample [5]. A simple sketch of a conventional SEM equipment can be observed in Figure 3.

The magnetic lenses produce a convergent beam of electrons. Slight variations on the magnetic field of the lenses, will change the focus of the beam. The two condenser lenses control the amount of demagnification of the electron beam in the electron gun to provide a smaller beam size. The final lens aperture focuses the beam on the sample. The current in the final probe is controlled by the size of the aperture. There is an optimum aperture angle which minimises aberrations.

In SEM the probe current is maximised, and the electron beam should be converged, and its diameter should be as small as possible [6]. Due to the high current needed to generate the magnetic field, the lenses need to be refrigerated, typically with water.

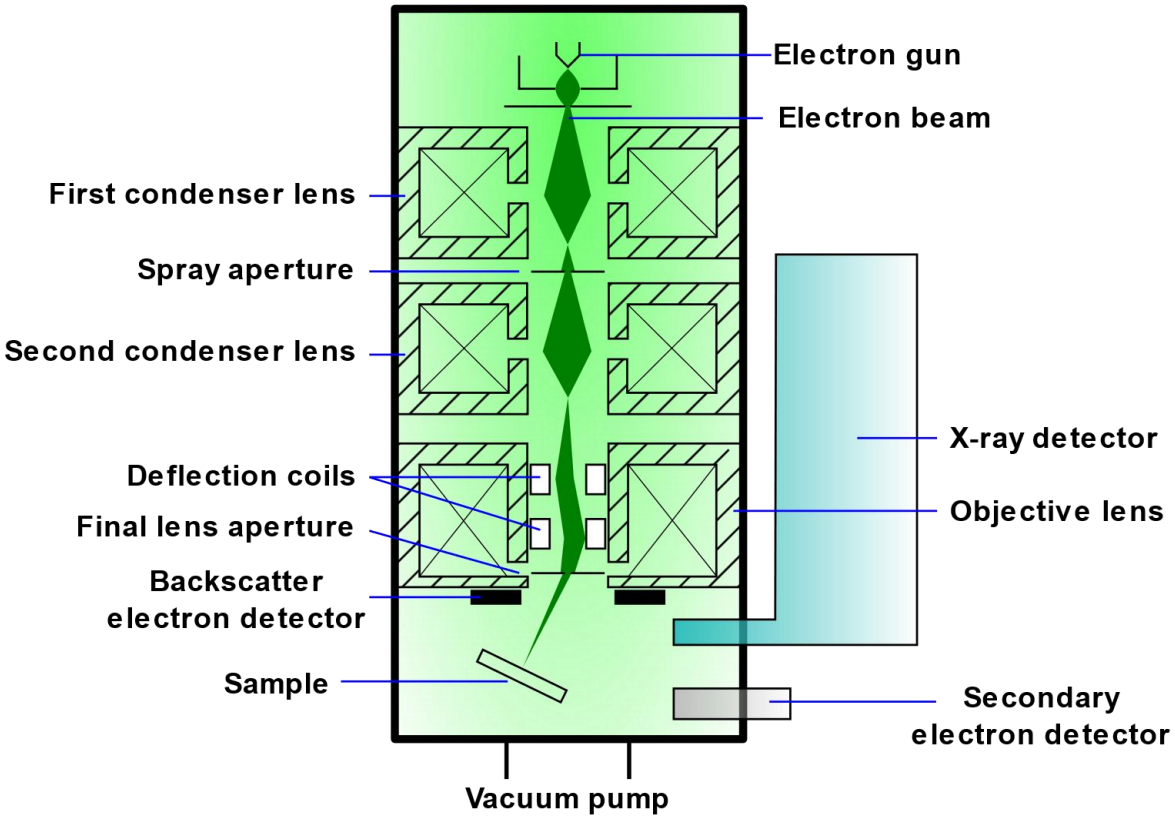

Figure 3. Schematics of a conventional SEM.

The electrons interact with the sample, and then they are detected depending on the nature of the interaction with the sample. The size of the interaction volume will determine the resolution of the optical system. The different types of interaction, as a function of the sample depth are described in Figure 4.

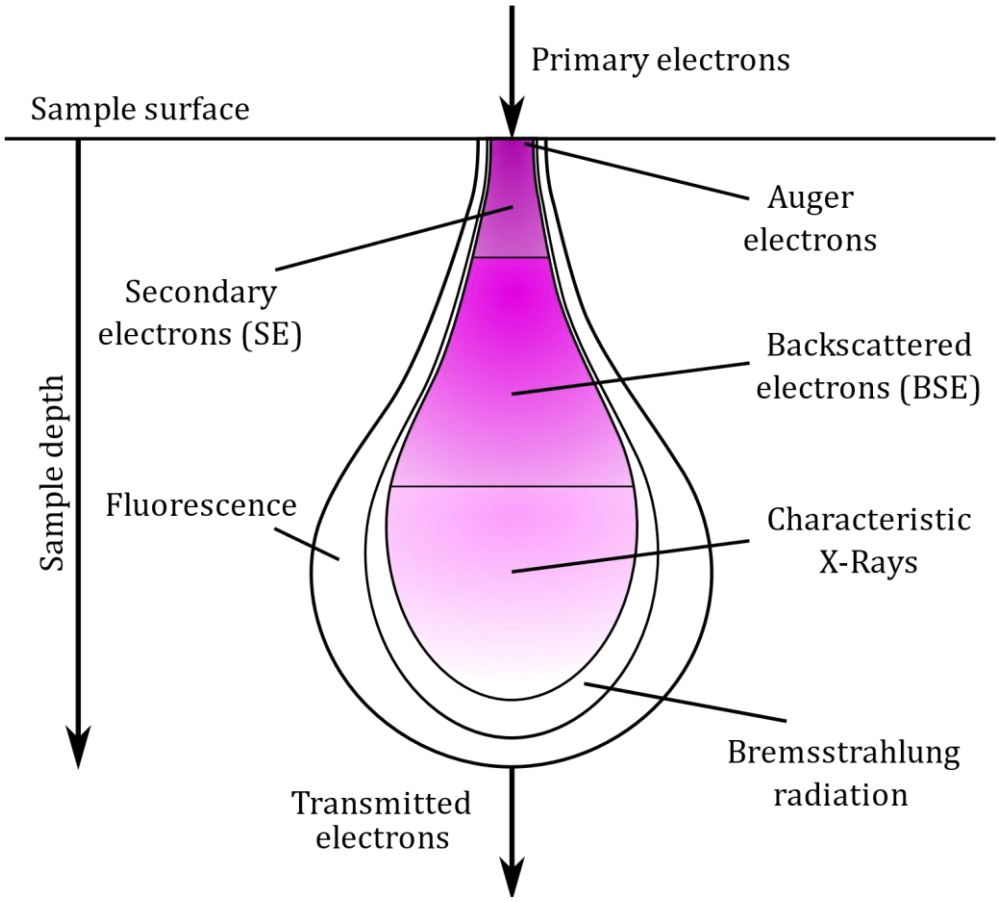

Figure 4. Electron-sample interaction volume as a function of the sample depth.

Usually for 2D imaging, secondary electrons (SE) and backscattered electrons (BSE) are detected. The BSE are primary electrons coming from the electron beam that after interacting with the sample, they are reflected with a very high angle (close to 180° with respect to the emitted beam). SE are electrons from the atoms from the sample. The electrons coming from the electron beam, expel some electrons from the outer shells of the atoms from the sample. Those electrons are expelled from the sample with a much lower angle (around 60° from the emitted beam) and further detected. A sketch of the generation of SE is represented in Figure 5.

Once the electrons have been detected, at a certain point of the surface, the process repeats where the intensity of every point is displayed as the intensity of

every pixel. The whole surface is mapped, and a representation of the surface is originated.

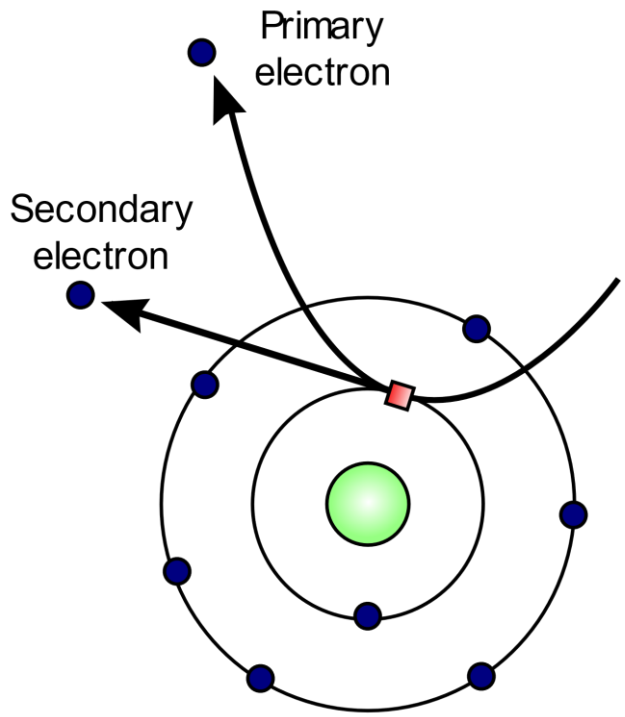

Figure 5. Sketch of SE generation for an isolated atom.

For the detection of electrons, there is no “imaging set of lenses” truly. The magnification of the image can be changed by reducing the current on the scanning coil. One consequence of this is that high magnifications are easy to obtain with the SEM, while very low magnifications may become burdensome. The completely different operation of the SEM compared to most other microscopes is possible because there are no imaging lenses, and any signal that comes from the action of the incident electron beam (electron reflection, electrons transmission or light emission) may be utilised to create an image [5].

Mass spectrometry

Mass spectrometry is a chemical characterisation technique that separates the components of a sample by their mass and electrical charge. In order to identify the chemical composition of a sample, the species evaporated from the sample are firstly ionised. The ionisation process is provoked by electrons produced by heating up a metal coil. These electrons collide with sample molecules, knocking off one or more electrons off to give a positive ion. The ions are accelerated through a potential difference and focused into a beam. The ion beam then is deflected using a magnetic field and sorted by their atomic mass. A time-of-flight analyser is generally used to accelerate ions to the same potential and then determines how long is required for the ions to hit the detector. Since the kinetic energy of the particles at the beginning is the same and all of them have the same charge, the velocity depends on the mass. Lighter components will therefore reach the detector first, whereas heavier elements will take longer [7]–[9].

Low Energy Electron Diffraction (LEED)

Low energy electron diffraction (LEED) is one of the most powerful techniques available for surface analysis. It is widely used in materials science research for the determination of the surface structure of materials via electron bombardment at low energies (20–200 eV) [10]. The structural information is obtained from the analysis of the particles and waves scattered by the crystal. The atomic arrangement within a unit cell is contained in the intensity of the diffracted beam. Assuming an incident wave vector $\boldsymbol{k_0}$ arriving to a crystal, the scattered wave vector $\boldsymbol{k}$ is directly related to the reciprocal lattice of the crystal with momentum conservation:

$$\boldsymbol{k} - \boldsymbol{k_0} = \boldsymbol{G_{hkl}} \qquad \text{Eq. 1}$$

Where $\boldsymbol{G_{hkl}}$ is the reciprocal lattice vector. For elastic scattering, the energy is conserved such as $|\boldsymbol{k}| = |\boldsymbol{k_0}|$**.** When electron waves interact with several obstacles at the surface, a 'cooperative effect' may occur. This interference could be constructive, leading to unexpectedly large fields, which is the case for interaction of electrons with a periodic arrangement of identical scatterers (crystal); or destructive, leading to unexpectedly small fields, which is typical from random arrangement of scatterers (amorphous) [11]. The coherent or incoherent nature of the interaction between electron waves in a crystal is determined by the Bragg's condition displayed at Eq. 2, where *d* is the interplanar distance, θ is the angle of incidence, λ corresponds to the wavelength of the incident wave and *n* is a positive integer.

$$2d \sin\theta = n\lambda \qquad \text{Eq. 2}$$

The Ewald sphere is a geometric way of visualising the events of constructive interference within a crystal. A schematic representation is provided in Figure 6 for the sake of clarity.

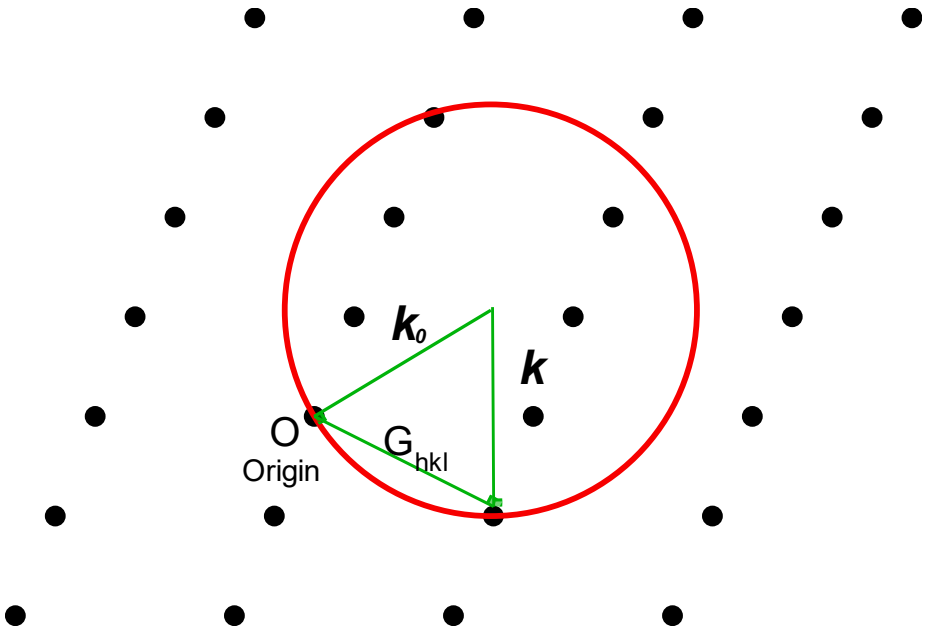

Figure 6. Representation of Ewald sphere (red circle) in reciprocal space for a single crystal.

Multiple scattering theory

For full apprehension of the interaction of electrons with the surface we ought to understand both the basic electron scattering mechanism and the nature of electron diffraction. The multiple-scattering procedure has been reported in the literature to be a valid method for the high-energy range [12]–[14]. Multiple scattering refers to the interaction of electrons with two or more scattering centres. These scattering centres deviate the electrons from their original path. The scattering as a result of the interactions between the electron beam and the surface, will deviate the electrons' path to any direction of the space. Electrons diffracting from a surface are scattered by all electric charges present in their paths: nuclei and electrons. The localized core electrons as well as the less localized valence electrons and conduction electrons must be included in this interaction [14]. We can classify as a function of the angle of deviation. According to this parameter, the scattering can be forward, when the electrons scatter with an angle lower than 90° with respect to the incident angle; or backward scattering,

when the electrons scatter with an angle higher than 90° with respect to the incident angle. We can distinguish between two types of scattering from an energetic point of view: elastic scattering and inelastic scattering. For an incident electron of energy E_0, the energy after collision with scatterers will be $E_F = E_0 - \Delta E$. Elastic scattering refers to the interaction of particles with scatterers without energy loss, assuming that $\Delta E \cong 0$. Inelastic scattering occurs when the interaction of the particle with scatterers implies an energy loss $\Delta E > 0$.

Low energy electrons interact strongly with matter. For electron diffraction at surfaces, scattering of the electrons with the atoms at the surface, tends to merge diffracted electrons in the forward direction, especially at higher energies. The strong (elastic and inelastic) scattering is responsible for the high surface sensitivity of LEED [13]. Nonetheless, at energies below 30-40 eV, where backward scattering has a similar strength to forward scattering [14] and the anisotropic parts of the atomic potentials are strongly effective, this method lacks accuracy and the analysis of the interaction between the electron and the surface to be analysed, result slightly more complicated [15]. At those energies, the process is referred to in the literature as Very-Low Energy Electron Diffraction (VLEED) [16]–[30].

In any periodic medium the Bloch waves are defined as the natural eigenfunctions of the Schrodinger equation. Those surfaces with two-dimensional periodicity parallel to the surface, and, therefore, Bloch waves with vectors k parallel to the surface will be considered [13], [14].

Assuming a plane wave with a certain energy and a specific direction such that a Bragg condition described in Eq. 1 is fulfilled; it is understood that constructive interference builds up more and more intensity in the diffracted waves as the incident wave penetrates deeper into the surface [14]. Subsequently, the incident wave will lose its intensity and will decay exponentially. At VLEED energies, the atomic scattering strength is quite large. The decay of the incident wave intensity may take place over only a few atomic layers, sometimes falling within the inelastic mean free path of the electron. This can be understood as a band gap, a

range of prohibited energies in which the incident wave cannot penetrate through the lattice, but is deflected into other directions, for example, back out of the crystal. Each band gap will correspond to a Bragg condition [31]. Multiple scattering needs to be taken into consideration, as this allows additional Bragg conditions between diffracted waves, not just between the primary incident wave and the diffracted wave [32]. Including the effects of the inelastic scattering, there are few changes that need to be considered. Multiple scattering is difficult to get rid of, and this effect will inevitably reduce the surface sensitivity [12], [14]. In order to overcome this, the concept of Bloch-wave procedures for very low electron energies was developed. This method is a much better approach for modelling the interaction between electrons and matter at low energies, although it requires additional theoretical adjustment [33].

Surface diffraction in 2D

LEED supply mainly information about the two dimensions of the surface perpendicular to the electron beam (sample surface). In the case of 2D diffraction, the conservation of momentum is as described in Eq. 3.

$$\boldsymbol{k}^{\parallel} - \boldsymbol{k_0}^{\parallel} = \boldsymbol{G_{hk}} \qquad \text{Eq. 1}$$

A 2D-lattice can be understood as a 3D-lattice whose perpendicular direction has infinite periodicity. In the reciprocal space, the points in the normal direction have an infinitesimally spaced and therefore Crystal Truncation Rods (CTR) are formed. The wave vector $\boldsymbol{k_0}$ ends at the CTR. The interception of the Ewald sphere with the CTR define the scattered wave vectors $\boldsymbol{k}$ for the diffracted beams [10]. An example of the diffraction for 2D surfaces is displayed in Figure 7.

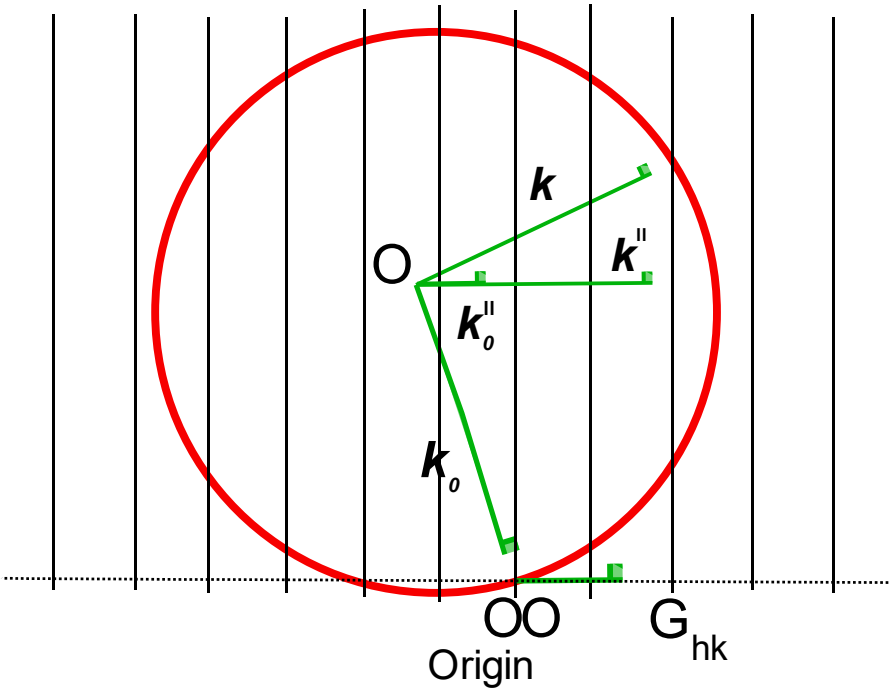

Figure 7. Representation of the Ewald sphere for 2D diffraction.

MBE

There exist different epitaxial growth techniques depending on the growth conditions and the precursor from which the material is deposited. One of the commonly used epitaxial techniques is Metal Organic Vapor Phase Epitaxy (MOVPE) which uses organic precursors to generate a chemical reaction and deposit the III-V compound onto a given substrate. The substrate temperature breaks the molecules from the precursors and controls the growth rate. Molecular Beam Epitaxy is a pure growth technique from sublimation of solid precursors, heated up in effusion cells (crucible or Knudsen cell), on top of a substrate. Both techniques are carried out under Ultra High Vacuum (UHV), with pressures ranging from 10-8-10-12 Torr. The main advantage of MBE over MOVPE relies on

the better control of the interfaces. MBE growth results in a purer crystalline structure. The number of atoms impinging on the sample controls the stoichiometry of the compound. In order to control this, the temperature of the cells and the shutter at the exit need to be monitored. A sketch of a conventional MBE is presented in Figure 8.

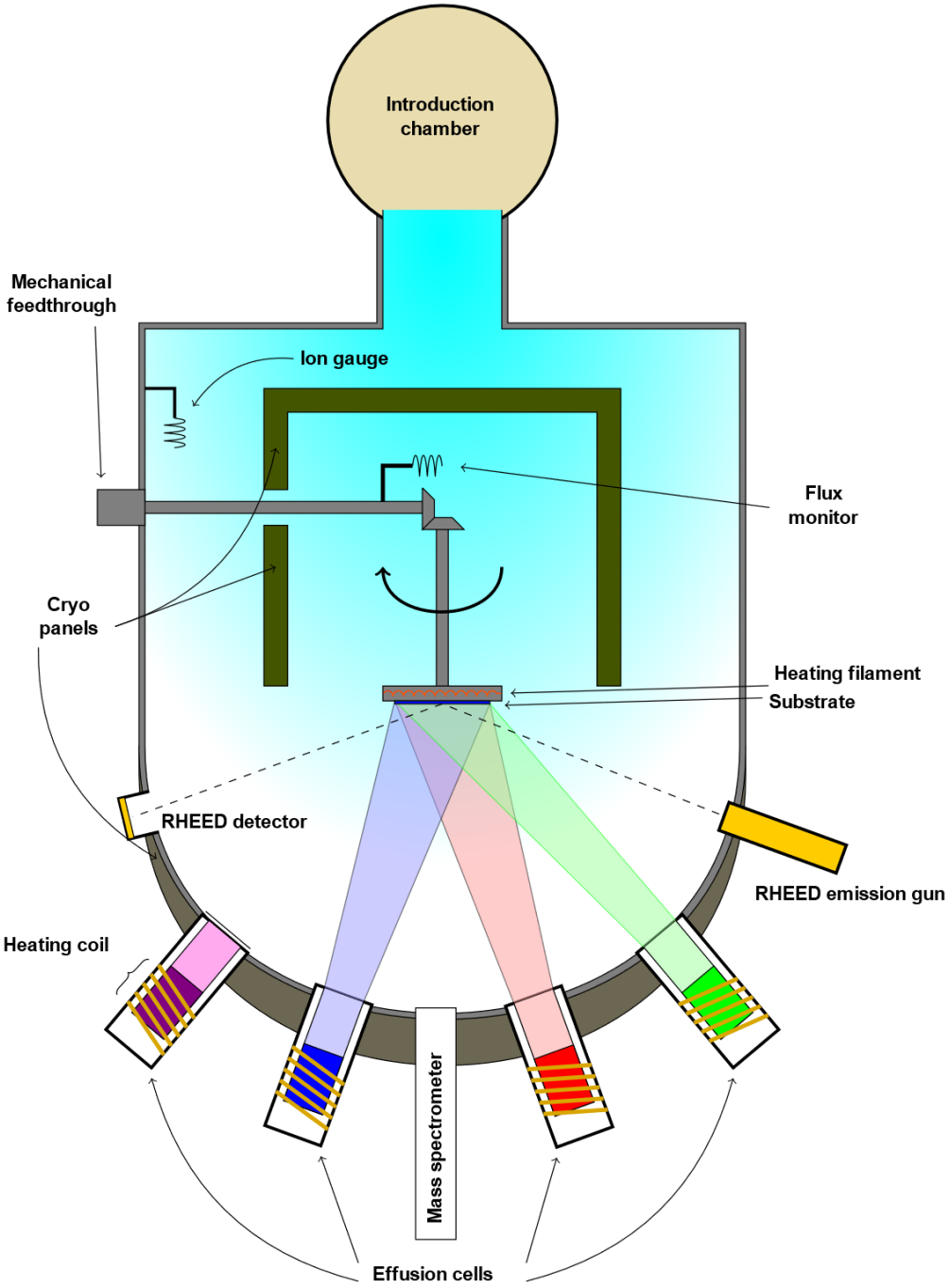

Figure 8. Descriptive sketch of a conventional MBE equipment.

For GaAs growth in MBE, Ga-flux and As-flux control the rate of impinging materials. Also, The substrate temperature and the background pressure, controls the growth kinetics, atom diffusion and desorption. [34] Depending on these parameters, three main growth modes are described for the growth of GaAs and other III-Vs. Each mode will develop different surface morphology. The different arrangement of atoms at the surface, lead to different surface structures. Each of the surface structures will have a different surface energy (γ) for the grown film, the substrate, and the interface between both as sketched in Figure 9.

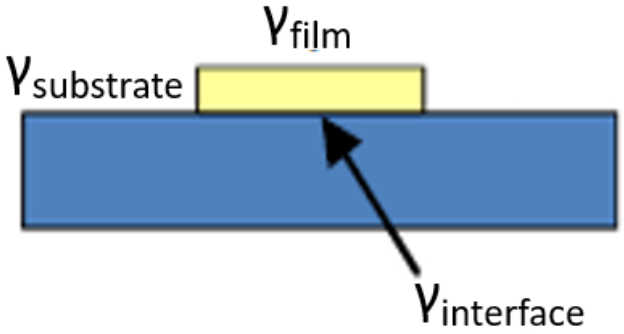

Figure 9. Representation of surface energy for MBE substrates.

1. **Volmer-Weber (VM):** Also known as 3D islands growth. In this growth mode, the interactions between adatoms are stronger than those of the adatom with the substrate, facilitating the formation of three-dimensional adatom islands. Eq. 1 shows the relation between different surface energies in the surface.

$$\gamma_{substrate} < \gamma_{film} + \gamma_{interface} \quad \text{Eq. 1}$$

2. **Frank Van-der-Merwe (FVM)**: Also referred to as 2D layer-by-layer deposition. In this mode, the atoms deposited are more attracted to the substrate than to each other. Therefore, Eq. 2 is met.

$$\gamma_{substrate} \geq \gamma_{film} + \gamma_{interface} \quad \text{Eq. 2}$$

3. **Stranski-Krastanov (SK):** Also accepted as layer-by-layer + islands growth. This heteroepitaxial growth mode is a combination of FVM and VM mode. Both equations 1 and 2 represent the conditions for the surface energy at the different stages of growth. Initially, the growth starts in FVM mode following Eq. 2. The effect of the strain on the surface, provokes a change in the surface energy of the substrate and the growth mode changes to VM. Eq. 1 is then met. Since heteroepitaxial structures are grown, typically the stress is caused by the lattice mismatch between the substrate and the material deposited.

Figure 10 has been presented for the sake of clarity. All the three growth modes are represented at different stages of growth.

In the microscopic growth process surface steps play a key role. On exactly oriented (001) planar surfaces, there exist no steps and they must be originated by small islands, which make the surface suitable for growth. Differently, if the substrate is misoriented, then steps are already present, and the surface is defined as vicinal [35].

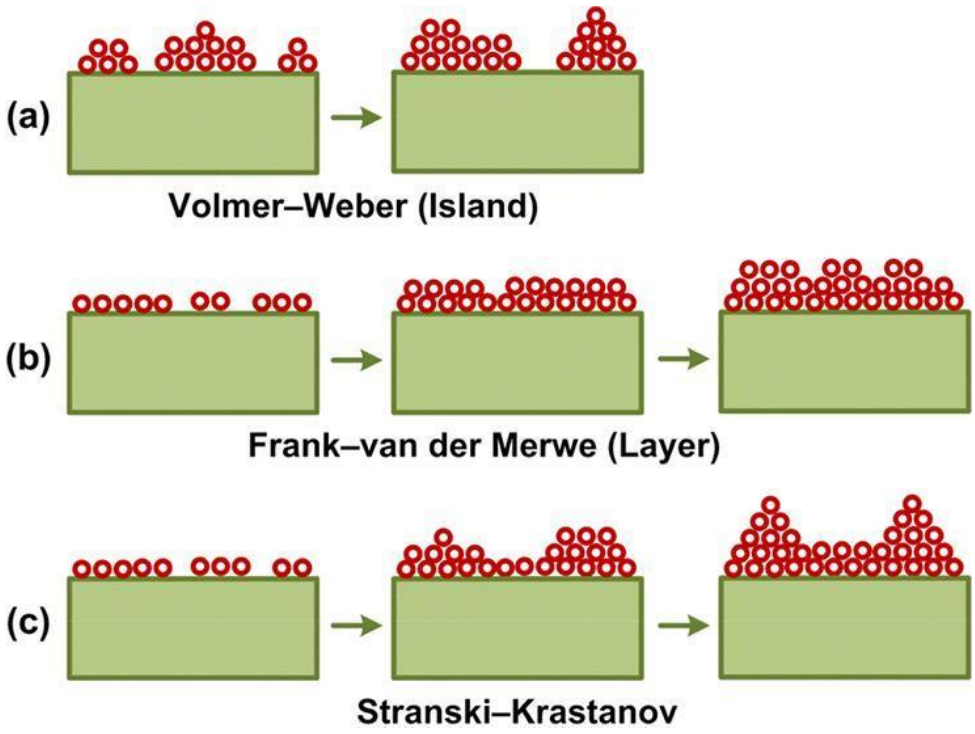

Figure 10. Representation of different growth modes in MBE. (Figure adapted from [36] with permission from publisher).

For in-situ analysis of the growth morphology, RHEED (Reflected High Energy Electron Diffraction) technique is used. This technique is based on the diffraction of electrons with a large scattering angle (close to 0°). The electrons are emitted by an electron gun at energies around 15KeV. The electron beam interacts with the sample and it is projected into a phosphorescent screen. The image collected contains information of the morphology of the surface of growth. The interpretation of these patterns is complicated. As a rule, dotted patterns correspond with a rough surface, whilst stripy patterns correlate with a more planar surface [37].

When the growth mode is closer to VM mode, the surface is rough with three-dimensional islands, and the electron beam penetrates through the islands and produces a transmission diffraction pattern, rather than a reflection pattern. When the islands are epitaxially grown on the surface, the reciprocal lattice is the same as the one of a three-dimensional crystal, which is three-dimensional array

of reciprocal spots. Facets on the side islands' wall, lead to small streaks around the diffraction spots [38].

On the FVM growth mode, an atomically flat surface with a perfect single-crystalline structure is obtained, the electron beam penetrates several atomic layers below the surface. The diffraction pattern is a reflection type in which all diffraction spots are on the Laue zones and have the same intensity. The intensity is modulated along the reciprocal rods, resulting in inhomogeneities in intensity due to interference between waves scattered from different atomic layers [38].

References:

[1] IBM, "'IBM' atoms," *Vintage Views*, 1989. [Online]. Available: https://ibm.co/2mcUTRY. [Accessed: 22-Jul-2019].

[2] Q. Thong and D. Inniss, "Fractured polymer / silica fiber surface studied by tapping mode atomic force microscopy," *Surf. Sci. Lett.*, vol. 290, pp. L688–L692, 1993.

[3] AP-Tech, "LaB6 cathode," *LaB6 cathode information*, 2019. [Online]. Available: http://www.a-p-tech.com/lab6-cathodes.html. [Accessed: 24-Jul-2019].

[4] Thememattic, "New year, new emitter," *The best science is mad science*, 2016. [Online]. Available: http://hackerfriendly.com/new-year-new-emitter/. [Accessed: 24-Jul-2019].

[5] O. J. and A. V. Samudra, "Scanning electron microscopy," in *Characterization of Solid Surfaces*, 1974.

[6] U. of C. Riverside, "SEM," *Scanning Electron Microscopy*, 2019. [Online]. Available: https://cfamm.ucr.edu/documents/sem-intro.pdf. [Accessed: 24-Jul-2019].

[7] ThoughtCO., "Introduction to Mass Spectrometry," *Mass Spectrometry - What It Is and How It Works*, 2019. [Online]. Available: https://www.thoughtco.com/definition-of-mass-spectroscopy-605331. [Accessed: 24-Jul-2019].

[8] M. S. University, "Mass Spectrometry," *William Reusch*, 2013. [Online]. Available: https://www2.chemistry.msu.edu/faculty/reusch/VirtTxtJml/Spectrpy/MassSpec/masspec1.htm. [Accessed: 24-Jul-2019].

[9] J. Clark, "The Mass Sectrometer," 2019. [Online]. Available:

https://www.chemguide.co.uk/analysis/masspec/howitworks.html. [Accessed: 24-Jul-2019].

[10] M. K. K. Oura, V.G. Lifshits, A.A. Saranin, A.V. Zotov, *Surface Science: An introduction*. 2003.

[11] P. A. Martin, "Multiple Scattering," in *Encyclopedia of Mathematics and its Applications*, 2006.

[12] T. Shirasawa and I. Science, *Surface Analysis: Low-energy Electron Diffraction*, Third Edit., vol. 9, no. February 2018. Elsevier, 2019.

[13] K. Heinz, "Structural analysis of surfaces by LEED," *Prog. Surf. Sci.*, vol. 27, no. 4, pp. 239–326, 1988.

[14] M. A. Van Hove, W. H. Weinberg, and C. M. Chan, *Low-Energy Electron Diffraction Experiment, Theory and Surface Structure Determination*, vol. 53, no. 9. 2013.

[15] W. Schattke, "Electron scattering states for low-energy spectroscopies," *Prog. Surf. Sci.*, vol. 64, no. 3, pp. 89–138, 2000.

[16] G. Held, H. Pfnür, and D. Menzel, "A LEED— IV investigation of the Ru (001)-p (2× 1)-H structure," *Surf. Sci.*, vol. 271, no. 1, pp. 21–31, 1992.

[17] J. C. Le Bosse, J. Lopez, B. J.M., and C. J.D., "A method for comparing measured and calculated VLEED fine structures," *Surf. Sci.*, vol. 137, pp. 361–372, 1984.

[18] V.N. Strocov, "On qualitative analysis of the upper band effects in Very-Low-Energy Electron Diffraction and Photoemission," *Solid State Commun.*, vol. 106, no. 2, pp. 101–105, 1998.

[19] C. Sun, "Oxygen-reduced inner potential and work-function in VLEED," *Vacuum*, vol. 48, no. 10, pp. 865–869, 1997.

[20] V. N. Strocov, P. Blaha, H. I. Starnberg, R. Claessen, J.-M. Debever, and J.-M. Themlin, "The 3D unoccupied band structure of graphite by very-low-

energy electron diffraction," *Appl. Surf. Sci.*, vol. 162–163, pp. 508–512, 2000.

[21] C. Q. Sun, "Time-resolved VLEED from the O-Cu(001): atomic processes of oxidation," *Vacuum*, vol. 48, no. 6, pp. 525–530, 1997.

[22] V. N. Strocov, H. I. Starnberg, and P. O. Nilsson, "Very-low-energy electron diffraction as a direct probe for unoccupied band structure: principles, results, implications in photoemission," *Appl. Surf. Sci.*, vol. 142, no. 1, pp. 311–315, 1999.

[23] I. Bartos, M. A. Van Hove, W. F. Chung, Z.Hec, and M. S. Altman, "Ag (111) electron band structure and channeling by VLEED," *Surf. Sci.*, vol. 402–404, pp. 697–700, 1998.

[24] S. Kawata, M. Oka, T. Takami, S. Mizuno, H. Nakane, and H. Adachi, "Atomic arrangement on ZrO/W(100) cathode surface - models for LEED intensity vs. voltage analysis," *Appl. Surf. Sci.*, vol. 146, no. 1, pp. 408–411, 1999.

[25] C. Q. Sun, "Coincidence in angular-resolved VLEED spectra: Brillouin zones, atomic shifts and energy bands," *Vacuum*, vol. 48, no. 6, pp. 543–546, 2003.

[26] J.Lopez, J. C. L. Bossé, C.Gaubert, R.Baudoing, and Y. Gauthier, "Dynamical Effects of the Surface Potential Barrier in Very Low Energy Electron Diffraction," *Surf. Sci.*, vol. 126, pp. 286–293, 1983.

[27] C. Sun, "Exposure-resolved VLEED from the O-Cu(001): Bonding dynamics," *Vacuum*, vol. 48, no. 6, pp. 535–541, 1997.

[28] H. Pfniir, M. Lindroos, and D. Menzel, "Investigation of adsorbates with low energy electron diffraction at very low energies (VLEED) In situ observation of oxidation and reduction of small supported copper particles using optical absorption and X-ray diffraction Real-time optical observation," *Surf. Sci.*, vol. 248, pp. 1–10, 1991.

[29] A. Dittmar-Wituski, A. Grudzinski, Ł. Lademann, A. Mikołajczyk, Ł.

Andraszyk, and M. Roszak, "Investigation of InSb(110) and InSb(111) surfaces by means of target current (VLEED) spectroscopy and LEED.," *Appl. Surf. Sci.*, vol. 256, pp. 4789–4795, 2010.

[30] M. N. Read, "Momentum dependence of the surface potential barrier for above-barrier electrons," *Appl. Surf. Sci.*, vol. 175–176, pp. 288–293, 2001.

[31] J. C. Le Bosse and L. J., "Subthreshold effects in vleed and the non-isotropy of absorption potential in metal," *Surf. Sci.*, vol. 162, pp. 953–960, 1985.

[32] R. M. Feenstra and M. Widom, "Low-energy electron reflectivity from graphene: First-principles computations and approximate models," *Ultramicroscopy*, vol. 130, pp. 101–108, 2013.

[33] M. Notomi, "Negative refraction in photonic crystals," *Opt. Quantum Electron.*, vol. 34, pp. 133–143, 2002.

[34] J. Orton and T. Foxon, "Molecular Beam Epitaxy," *Oxford Univ. Press*, 2015.

[35] T. Marek, C. Schür, and S. Kunsági-Máté, "Surface orientation as a control parameter for the growth of non-stoichiometric gallium arsenide," *Phys. Status Solidi Appl. Mater. Sci.*, vol. 202, no. 15, pp. 2980–2991, 2005.

[36] V. S. K. Channam, "Synthesis of strongly correlated oxides and investigation of their electrical and optical properties," 2017.

[37] M. Dabrowska-Szata, "Analysis of RHEED pattern from semiconductor surfaces," *Mater. Chem. Phys.*, vol. 81, pp. 257–259, 2003.

[38] S. Hasegawa, "Reflection High-Energy Electron Diffraction," *Charact. Mater.*, pp. 1925–1938, 2012.

Chapter 3: Low Energy Electron Microscopy combined with Molecular Beam Epitaxy (LEEM-MBE)

In this chapter, the development of the Cardiff LEEM-MBE system during this work as well as a description of the new implementations to the equipment will be presented.

Introduction to LEEM

Low-Energy Electron Microscopy (LEEM), was first invented by Ernst Bauer in 1962, and fully developed by Ernst Bauer and Wolfgang Telieps in 1985. LEEM is a very effective technique to image crystalline surfaces processes [1]. An electron gun emits a beam of high energy electrons. The electrons are guided through a set of electromagnetic lenses, and sent through a magnetic beam splitter, which bends the beam towards an electromagnetic objective lens. A large voltage difference is set between the objective and the sample, which decelerates the electrons to low energies (0-100 eV). When the electrons interact with the sample, they "bounce back" through the objective lens, reaccelerate, and pass through the beam splitter again (see Figure 1). Nevertheless, for detection the electrons travel in the opposite direction this time and the beam splitter guides them opposite to the electron gun, where the detector is placed. Projecting the back focal plane, this equipment also can look at the reciprocal lattice (Low-Energy Electron Diffraction, LEED). These capabilities allow imaging of the reciprocal space or the actual real image of the surface in real time, permitting to make movies of different surface processes [2]. One of the main advantages of LEEM is that stray magnetic fields are strongly suppressed. The electron beam is decelerated to the desired low energy only in the immediate, magnetically shielded vicinity near the sample of study. In the rest of the microscope, the beam is at high energy (typically around 20 KeV), for an easy manipulation by conventional electro-magnets [3]. Many surface mechanisms have been studied with LEEM, from Dark-field

diffraction contrast from adjacent terraces of the GaN (0001) surface [4], to the behaviour of thin indium films on Si (001) surfaces [5], or transformation of different oxides on W (110) surfaces at high temperatures [6].

The electrons are generated by a cathode. The types of cathodes used for electron emission are the same as the ones described for SEM. The most commonly used electron gun is FEG. The FEG electron gun possesses a lower both chromatic and spherical aberration. The reason for this relies on the fact that the electrons are generated from an electric field, which makes the electron beam more coherent. The resolution of the system depends upon the source of emission utilised. The broad energy distribution of the LaB_6 cathode limits the resolution to slightly better than 10 nm. With a Schottky Field Emission Gun (FEG) the limit is about 5 nm. Typically, it is around 5 nm on the XY plane for thermionic emission using LaB_6 and around 10 nm for FEG. LEEM typically has atomic resolution on the Z axis. The difference in contrast that allows to have this resolution is due to electron beam interference. Coherent waves satisfying Bragg's condition will interact constructively whereas other waves will interact destructively leading to lower illumination in the step edges.

Another possible form of excitation is photoemission. Integrated in the LEEM system, an external source of light can be implemented. The light is used to excite electrons from the sample which are further detected. This technique is named Photo Emission Electron Microscopy (PEEM). PEEM allows to achieve chemical contrast on materials with a suitable work function [7].

After the electrons are generated by the filament, a negative biased electrode named "Wehnelt" is used for focusing and control of the electron beam. By tuning the voltage of the Wehnelt (typically −200V to −300V relative to the emitter), a repulsive electrostatic field is created, suppressing emission of electrons from most areas of the cathode allowing emission from only the area of the tip. The Wehnelt bias voltage determines the emission area from the tip, which determines the beam current and effective size of the electron beam. Upon emission, the electrons are accelerated at 20 KeV.

The beam of electrons is further guided and focused by a set of magnetic lenses until they reach the objective lens (OL), which focalises the beam towards the sample. For the objective lens an electrostatic tetrode or a magnetic triode has been used. The set of lenses used by a LEEM system in the illumination part, is very similar to the one used on a SEM system, except for the fact that the lenses in LEEM need to be bakeable. There are three condenser lenses in the illumination column (C1, C2, C3), and a close-packed prism array beam splitter. Then the electrons are decelerated before they reach the sample. For that, the sample is mounted in a holder at 20kV with respect to the objective lens, which is located at around 2 mm from the sample. One can also modify the energy that the electrons have when they reach the sample by slightly modifying the 20kV between the sample and the objective. When the electrons have 0 eV or negative energy, they do not hit the sample and they are reflected to be detected, this mode is so called Mirror Electron Microscopy (MEM). If the electrons have a positive energy value at the surface (LEEM), they interact with the sample before they are accelerated back to be detected [8].

In the imaging column, there is a transfer lens (TL), a field lens (FL), an intermediate lens (IL), and two projective lenses (P1 and P2), in that order. The intermediate lens, together with the two projective lenses permits fast switching between diffraction and imaging over wide magnification range [8]. These lenses are respectively represented by circles in Figure 10. All lenses are also bakeable and equipped with magnetic deflection coils. Most LEEM instruments are also equipped with a magnetic diode with magnetic stigmator and deflectors. The illumination aperture is located between the C2 and C3 in the illumination column. When this aperture is used, the area of the sample which is shined by the electrons gets reduced, and therefore the energy dispersion of the electrons curtails. The back focal plane of the objective lens is imaged by a transfer lens after the beam separator into a field lens, where the contrast aperture is placed. The contrast aperture reduces the chromatic and spherical aberrations which permits to improve the contrast and the resolution of the image. Bright Field mode is achieved by placing the aperture in the (0,0) spot of the diffraction pattern. Dark Field is obtained by filtering different points of the diffraction pattern so that

different surface reconstructions can be distinguished. When the back focal plane is projected into the detector, information of the diffraction pattern on the surface is obtained, and this technique is called Low Energy Electron Diffraction (LEED).

The detection consists of a multi-channel plate (MCP) which multiplies the number of electrons for improving the intensity, and then these electrons are projected into a phosphor screen. A CCD (Charged Couple Device) camera records the image and send the information to the computer.

Every electron microscope needs vacuum in the chamber to increase the mean-free path of the electrons and avoid scattering of the electrons between the electron emitter and the sample. The LEEM system is not an exception, and it is under ultra-high vacuum. A sketch of a whole conventional LEEM equipment can be observed in Figure 1.

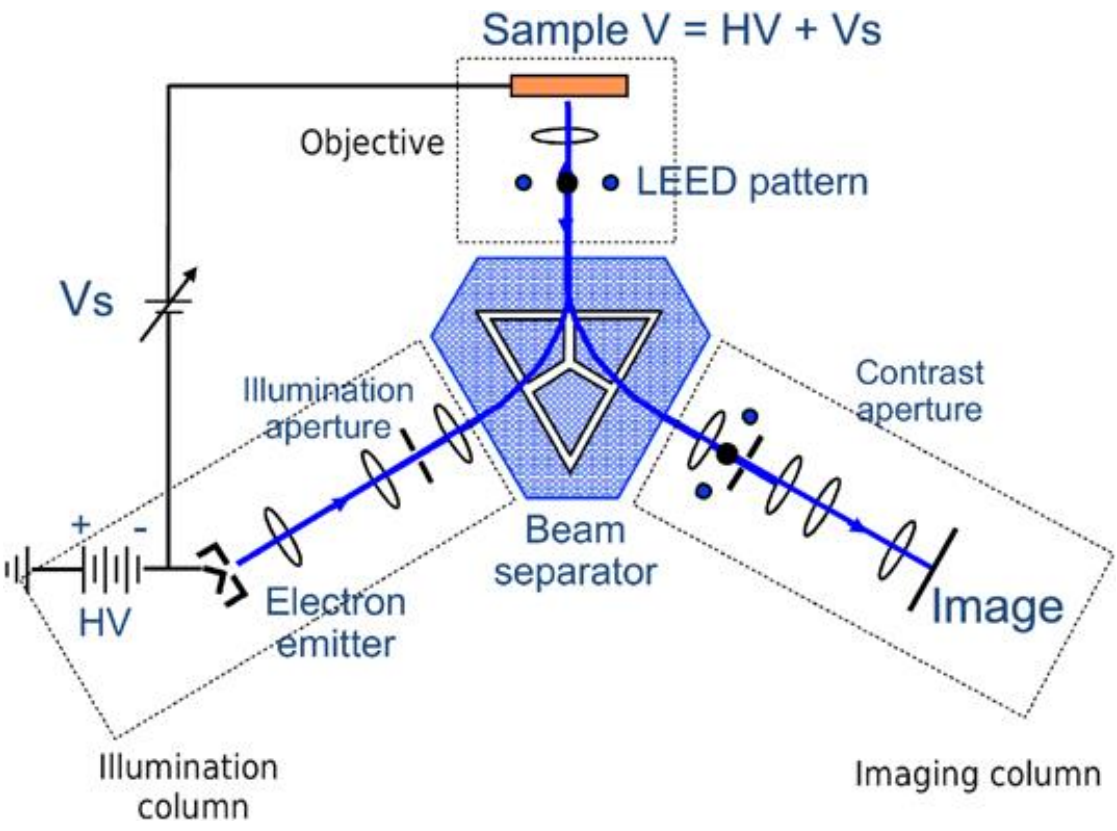

Figure 1. Schematics of a LEEM equipment. (Figure adapted from [9] with permission from publisher).

Typically, the sample holder possesses four pins connected with metallic springs. Two of the pins are connected to a heating filament which allows electron bombardment of the sample by applying a high voltage in between the filament and the sample, and two other pins are connected to a thermocouple (usually W-Re) to measure the temperature. An example of the sample holder for a conventional LEEM system is shown in Figure 2. Heating via electron bombardment allows reaching temperatures above 2000 K.

For temperature acquisition, apart from the thermocouple located within the sample holder, the equipment also includes a pyrometer or a band-IT which measures the temperature based on the sample radiation and near-edge band emission respectively.

Figure 2. Picture of a conventional LEEM sample holder. (Figure adapted from [10] with permission from publisher).

LEEM-MBE: motivation.

The growth of high-quality semiconductors is a crucial factor for the fabrication of the state-of-the-art optoelectronic devices. The full comprehension of the basic physical phenomena behind the growth of structures is an indispensable step for optimising the industrial processes of semiconductor devices fabrication. The

understanding of the dynamical mechanisms and the kinetic processes at the surface of the different semiconductors is therefore required and it has already been recognised in the scientific community, where many articles have been presented highlighting the importance of the study of kinetic processes. For example, Stanley et al. presented an interesting study about InGaAs and InGaN surface, in which they unveiled the activation energies for the In desorption [11]. Ageev et al. have also developed kinetic studies on GaAs island-growth, finding that the growth rate, has a dramatic influence in the island morphology and the Ga surface diffusion length [12]. They also found that an increase to the V/III ratio has similar influence upon island formation than decreasing the temperature [13]. Mao et al. also demonstrated that the islands density on GaAs depend mostly on the substrate temperature [14].

For the analysis of different processes happening at the surface of semiconductors, powerful characterisation techniques are required. The optimisation of these techniques will ultimately improve the capabilities of interpretation of the physical processes involved in growth. There exist plenty characterisation techniques which help in the understanding of such processes. Many different ex-situ characterisation techniques have been reported to investigate surface processes in semiconductors. Techniques such as Transmission Electron Microscopy (TEM), Scanning Electron Microscopy (SEM), Atomic Force Microscopy (AFM) or Scanning Tunnelling Microscopy (STM) have been widely used for ex-situ analysis of surfaces. This means that for the growth of semiconductors, the samples are characterised in a different chamber than the one used for growth, which influences the surface conditions. Using ex-situ methods of characterisation, different surface mechanisms such as atom diffusion, atomic arrangement at the surface, nucleation of structures during growth; could not be observed. For the thorough analysis of surface dynamical processes behind growth in-situ techniques are therefore required, to obtain useful information on dynamical processes during growth. These would imply the combination of some of these characterisation techniques with different growth techniques. For this reason, in-situ characterisation techniques offer a more accurate approach for the analysis of the surface kinetics [15], [16].

The growth of epitaxial structures can be carried out by different techniques, being MOCVD and MBE the two most used ones (see chapter 1 for further information). MOCVD, which the technique most used for industrial processes, relies mainly on the monitoring of the substrate temperature for control on the surface chemical reactions which will determine the growth rate and quality of the material grown. The surface processes involved in growth on this technique are mostly dominated by thermodynamics. MBE on the contrary, is a purer technique that relies a lot more on kinetical processes at the surface i.e. atoms diffusion, strain. Due to the relatively high pressures used for MOCVD growth, the implementation of in-situ techniques gets complicated. MBE growth pressures allow for different in-situ techniques to be implemented.

There are many in-situ characterisation techniques used in growth chambers, from X-Ray Photoelectron Spectroscopy (XPS), X-Ray Diffraction (XRD), Laser Interferometry, to Spectroscopic Ellipsometry, Synchrotron X-Ray Reciprocal Space Mapping (RSM), Reflectance Spectroscopy (RS), Auger Spectroscopy[17], LEED, or the most commonly used in-situ technique for growth which is Reflection High-Energy Electron Diffraction (RHEED).

In RHEED, an electron gun produces a beam of electrons which impinge the sample at a very low angle relative to the sample surface. The impinging electrons diffract from the atoms at the surface of the sample to be characterised. Then, a portion of the diffracted electrons interfere constructively at certain angles and form regular patterns on the detector. The interference of the electrons depends on the atomic arrangement at the surface. Normally, the RHEED diffraction pattern is difficult to interpret, and certain parameters such as atom diffusion, generation of new atomic terraces at the surface or metastable phases could be difficult to detect using this technique. The inability to image the real space, make the surface analysis incomplete. This effect motivated the generation of new in-situ techniques for a thorough analysis of surface mechanisms. In the 80s, the μ-RHEED combined with SEM imaging for real space imaging introduced by Ichikawa et al. allowed the observation of atomic-layer microstructures with a low angle resolution [18], [19]. Some of the work developed on micro-probe

RHEED included surface phase transitions on Si surfaces [20], [21], 2D nucleation on GaAs(111)B [22], estimations on the growth rate on GaAs (001) near the edge of (111)A direction [23], or calculations of inter-surface diffusion of Ga on GaAs surfaces [24]. Though this technique provides a very resourceful tool for the observation of semiconductor surface processes given its low spatial resolution and its ability to perform in-situ experiments, the fact that it is a scanning technique makes difficult the observation of various metastable processes that may occur on a very low scale.

One of the important techniques which combines the epitaxial growth of an MBE and the morphological characterisation of a surface microscopy, is SEM-MBE. This technique combines the capacity of an MBE to generate epitaxial growth of different species; with the ability of a SEM, in which nanometric-resolved images of the real space of different surfaces can be achieved. This technique allows the identification of different kinetical processes during growth to be observed, as demonstrated by Nishinaga et al. in their various studies applying this technique for the analysis of the surface diffusion of atoms in III-Vs [24]–[28]. Yamaguchi et al. also contributed to this technique analysing the time development of atomic steps on GaAs (111)A [29]. SEM-MBE, however, does not allow for the visualisation of the reciprocal lattice or the filter of specific surface reconstruction for phase discrimination. The fact that it is a scanning technique, makes impossible the simultaneous visualisation of the whole surface, affecting the time resolution of the system.

Another in-situ technique that combines an epitaxial growth technique and a powerful electron microscopy is the so called TEM-MBE. This technique allows the investigation of the surface kinetics and different dynamical processes during growth through the interpretation of the reciprocal lattice [30]. A high-energy beam of electrons is shone at the surface, where the electrons transmit, and are further detected. This equipment permits atomic resolution images and allows the interpretation of different surface processes without growth, as well as phase contrast for discrimination of different atomic reconstructions at the surface. One of the main requirements of this technique, is that the sample must be very thin

in order to favour electron transmission. The preparation of the samples is not trivial and sometimes this may induce problems in the epitaxy and may limit the number of epitaxial layers that can be grown or the physical processes that can be studied. Also, the processes for growth in this technique since only lateral imaging is allowed.

One of the most complete in-situ characterisation technique for growth, is STM-MBE. This technique allows the investigation of different kinds of physical processes at the surface of semiconductor during epitaxial growth with atomic resolution. The capabilities of this technique are quite impressive and they have led to breakthrough discoveries in surface science like the thermal desorption flux of cation adatoms in InAs [31], the evolution of the growth morphology at atomic level on Si and Ge systems [32], or different surface atomic arrangements on InGaAs alloys [33]. This characterisation technique has been also utilised for the observation of different surface mechanisms during growth on GaAs [34]–[44] and many of them have been devoted to understand the different atomic arrangements at the surface of GaAs (001) [45]–[54]. However, for these processes quenching of the sample was necessary in order to generate STM images of the surface right after growth, which did not quite work out as an "in-situ" technique. Tsukamoto et al. however, developed a "real" in-situ STMEMBE equipment able to scan the sample across at the moment of growth. This technique led to important discoveries on InAs and GaAs surface mechanisms [55]–[58]. This technique is based on the so-called tunnelling effect, for which a conductive sample is needed to favour the detection of electrons by the STM tip. The fact that it is a scanning technique, impedes simultaneous image acquisition over a certain area reducing therefore the time resolution to few seconds. Certain short-time processes i.e. metastable phases at the surface, may therefore not be appreciated. Even though this technique has an atomic spatial resolution, the formation of the images is not a straightforward process and requires certain modelling for the surface potential and the electrostatic interactions prior to image formation, which make complicate the interpretation of certain surface mechanisms. The reason for this is that under growth conditions, evaporated material also gets pinned to the STM tip, which needs to be accounted for.

In order to complement these techniques, there was a need of creating a technique with high resolution, able to image surface mechanisms involving growth [59], [60]. Different systems have been built around the world devoted to the study of growth dynamics of Si [61]–[63], GaN [64], [65], Ru [66], Au [67], or even Cu [68]. We have developed an Arsenides' system which consists of a Low Energy Electron Microscope (LEEM) and an MBE system which allows us for real-time imaging of surface processes at video rate under growth conditions.

LEEM-MBE at Cardiff University

In this work, the development of a LEEM-MBE equipment for the study of the growth physics of (In/Ga)As will be presented. This system is equipped with 2 Knudsen cells (Ga and In), an As cracker and a Hydrogen ion gun. This unique LEEM-MBE enables real space imaging of the surface of complex semiconductor binaries with a theoretical spatial resolution around 5 nm in the XY plane, and atomic resolution in the vertical axis; and 0.1 s of time resolution. Realistically, the lateral resolution of the system tends to be of around 20 nm, with a transfer width in diffraction of around 10 nm. This novel system combines the advantages of imaging using low electrons with the purity of epitaxial growth. The capabilities of this equipment make it unique as there is no other instrument able to provide information on the dynamics of the growth of III-Arsenides. A schematic representation of this equipment is displayed in Figure 3.

By adjusting the configuration of the magnetic lenses, it is possible to switch from LEEM to micro-spot Low Energy Electron Diffraction (μm-LEED). Measuring Photo-emission Electron Microscopy (PEEM) is also possible by the illumination of the surface with a source of UV light i.e. Mercury lamp. By filtering a particular diffraction spot in the back focal plane of the objective lens, phase discrimination is possible. Thorough information about discrimination of different surfaces will be provided in the next chapter.

Due to the low energies the system works at, the chromatic aberration is powerful with not so much of spherical aberration. These aberrations limit the resolution of the system.

Combining LEEM and MBE provides great advantages, but it also leads to certain limitations in the geometry of the system. The MBE growth time is limited because the deposition in the optical part of the system result critical. Long deposition times will unavoidably block the objective in the long term, leading to arcing between the sample and the objective, or even effectively blocking the path of electron beam. Having the effusion cells at a higher angle compared to a conventional MBE, might also affect in the anisotropy during growth, and it suppose a limitation for the system.

In the next section, a detailed analysis of the new instrumentation changes implemented in the system, as well as their impact, and the advantages and limitations of the system will be discussed.

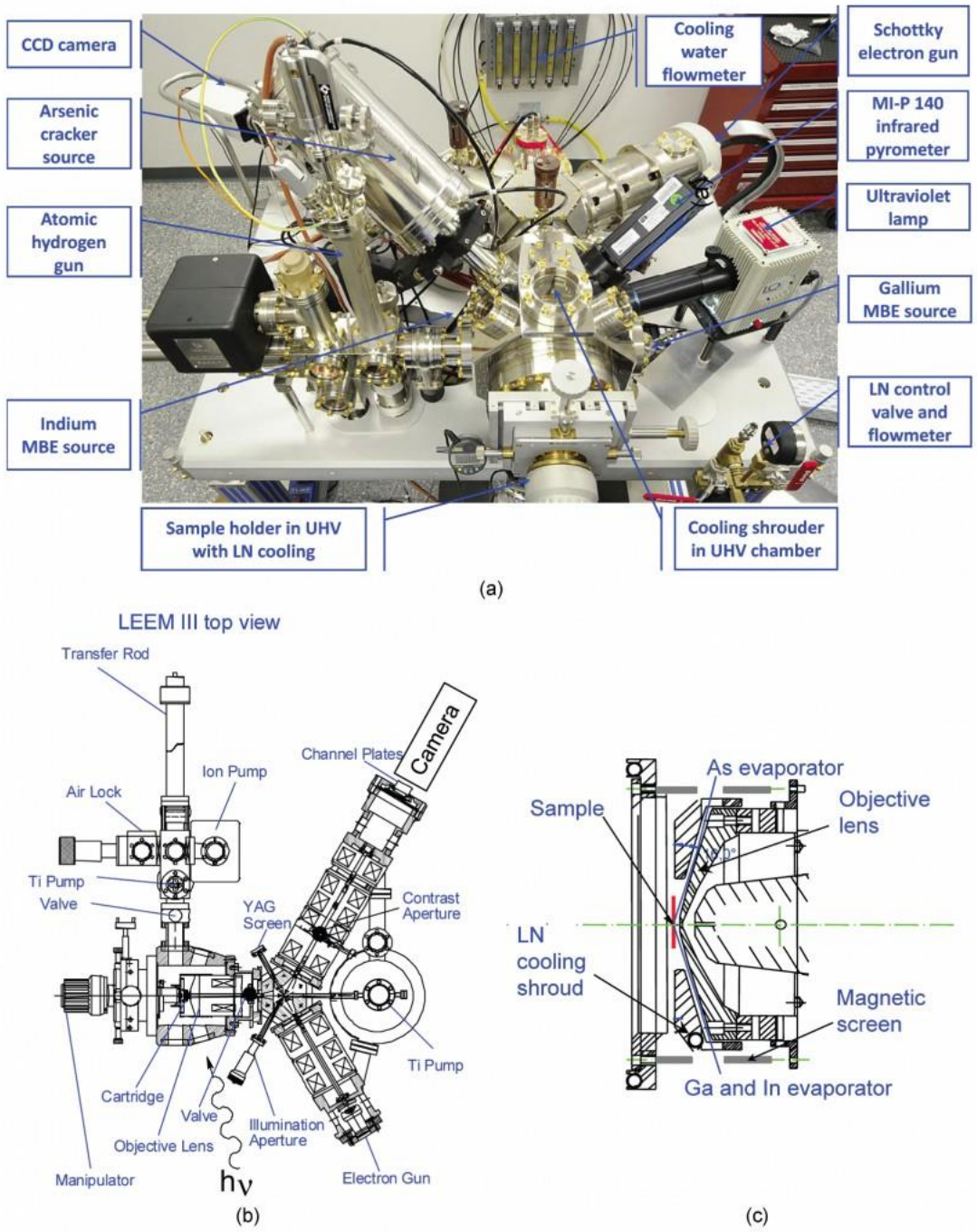

Figure 3. (a) Image of the III–V LEEM system. (b) Cross section of the III–V LEEM system. (c) Enlarged view of the objective lens area showing the location of the cooling shroud and access for the MBE sources. (CCD: charge-coupled device; YAG: yttrium–aluminium garnet). (Figure adapted from [2] with permission from publisher).

New instrumentation applied to LEEM-MBE at Cardiff University

1. Preparation chamber: A new preparation chamber has been implemented in the system. This chamber is a stainless-steel spherical structure of a diameter of 12 cm and it has 13 2.75 Conflat flanges currently hosting a mass spectrometer, an Argon ion gun, an ion pump, the turbopump vacuum line and an ion gauge. A 1.33 Conflat flange hosts a small window placed right above the sample holder manipulator enabling sample surface monitoring. The purpose of this chamber is to create an additional space to monitor different processes under UHV using different characterisation techniques, reducing the exposure time for the objective lens to be exposed to As-flux, as well as redeposition. This chamber is equipped with a power supply able to heat up the sample prior to its introduction in the main chamber. This chamber allows for e-beam heating of the sample up to 900^0C, under Ultra High Vacuum environment, and has been designed to enable desorption of a protective As capping layer, therefore enabling transfer of samples under atmospheric conditions while preventing oxidation of the samples surface. Complex samples can then be grown externally and sent to Cardiff. The chamber set-up has been designed to allow for further expansion of the MBE-LEEM. Therefore, few ports are still available for a vacuum suitcase, future connection to a STM chamber, or further developments.

2. Manipulator: A manipulator enabling sample heating and transfer within the preparation chamber has been installed in the preparation chamber. This manipulator has been mounted in a 2.75 Conflat flange located at the very bottom of the new preparation chamber. This instrument enables heating the sample through radiation (a filament is installed within the sample holder and can be used for radiation heating of the sample up to

550^0C via Joule effect) and e-beam bombardment (by applying high voltage between the sample and the filament while driving up to 3 A through the filament. A detailed description of the heating on the sample holder can be found in chapter 1. This allows us to reach temperatures over 1500°C, which we limit to 900°C to avoid overheating in windows and flanges due to the chamber geometry. The manipulator moves linearly along the Z-axis and allows 360^0 rotation in the X-Y plane to favour transfer between the old preparation chamber. This rotation in the X-Y plane provides versatility if more vacuum chambers are implemented in the future (e.g. plans to add a vacuum suitcase or to connect the system to an STM).

3. Mass spectrometer: Two mass spectrometers, a 300 a.m.u. (atomic mass units) and a 100 a.m.u. from Stanford Research have been purchased and successfully installed in the system. The 100 a.m.u. spectrometer provides line of sight measurements of sample surface in the preparation chamber. This allows us to monitor desorption of species at the surface. A very interesting application of this, is the monitoring of the As capping protective layer for As-capped samples, which allows MBE-MBE transfers of high-complexity samples preserving the surface. The 300 a.m.u. has been placed in the main chamber and it can be used to track the As flux during growth. This spectrometer enables monitoring of As_2 and As_4 molecules, of 150 and 300 a.m.u. respectively. A graphic example for the As cell calibration is hereby provided in Figure 4. Both spectrometers can also be utilised for leak detection and monitoring of different contamination species within the vacuum system. This technique is very important due to the lack of flux measurement on the system.

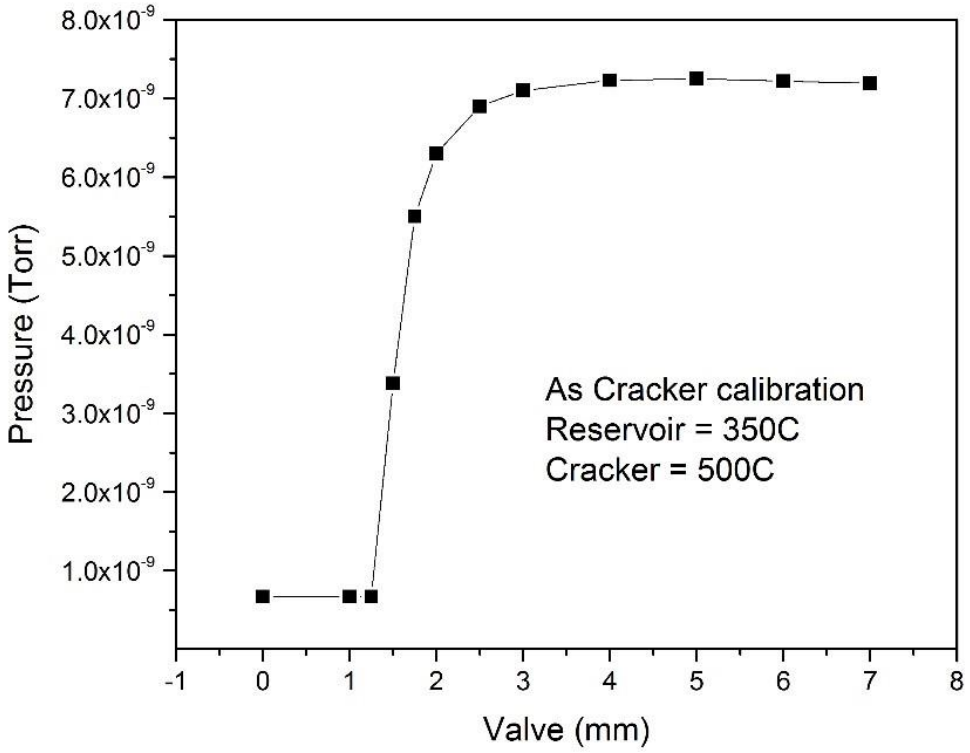

Figure 4. As source calibration in our LEEM-MBE system.

4. Vacuum system: Keeping the pressure as low as possible is a key factor in LEEM-MBE. A new ion-pump system has been purchased to be installed in the main chamber. With this replacement pump, the reliability of the vacuum level will be assured.

5. Cooling system: In order to help keeping the chamber pressure as low as possible, a cooling system is in place. The equipment possesses two liquid nitrogen cooling shrouds. One of the shrouds cools down the main chamber for pressure reduction to favour a high local pressure next to the objective lens but avoiding arcing between the sample and the objective lens. The other one is installed on a circuit that goes through the sample stage, and its purpose is to cool down the sample. Using liquid nitrogen,

the temperature could be minimised down to around 100K. Potential use of He could reduce this pressure even further up to 1 or 2 K.

6. New filament design: An additional problem related to sample heating is the temperature inhomogeneity. Experiments recording Langmuir evaporation from GaAs(001) surfaces exhibited that the edges of the sample were at a significantly higher temperature than the central area of the sample. In order to overcome this problem and increase the reproducibility and homogeneity of the temperature at the samples, a new zig-zag-shaped filament has been developed. The new filaments can be fabricated in-house, reducing costs significantly.

7. Smaller illumination aperture: The illumination aperture in LEEM, consists of a strap with a set of 3 holes (100, 30 and 10 μm) which block part of the electron beam shining only a particular area of the real space. The LEEM-MBE has incorporated a new hole of 3 μm. By reducing the size of this spot, the resolution with which different areas of the real space can be discriminated is increased to tenths of nanometres. This is particularly useful for surface phase discrimination experiments, in which diffraction patterns of a specific phase need to be obtained to study the nature of such phase reconstruction. This effect is important in situations of phase coexistence. Chapter 6 will describe this further.

8. Temperature acquisition: Temperature measurement is one of the most challenging tasks in UHV systems due to the inaccuracy and unreliability of the existing temperature acquisition techniques. In our system, a thermocouple is placed into the sample heater providing reproducibility to the experiments. Nonetheless, this technique does not provide a very accurate indication of the absolute temperature of the sample due to temperature inhomogeneity across the sample and mechanical vibrations. We have also developed a method to spot-weld the thermocouple to the

holder in order to improve reproducibly. The LEEM systems normally have installed a pyrometer which relies in the blackbody emission in one of the flanges. This measurement provides a better estimation of the real temperature. However, this instrument is subject to technical instrumentation problems such as metallization of the window or stray light (ion-gauges, heating filament, etc.).

Recently, a commercial KSA BandIt band-edge pyrometer has been installed in the system. The location of this piece of equipment is the same location the previous pyrometer was placed in. The BandIt pyrometer supplies temperature measurement using the temperature-dependent optical absorption edge of the semiconductor material. This technique is immune to changes in viewport transmission, stray light, and signal contribution from substrate or source heaters (which can all contribute sources of measurement error for pyrometers) and significantly improves the accuracy of temperature measurements. Moreover, the BandIt also provides a good estimation of the absolute temperature so extrapolation to partner MBE's temperature reading is possible. This new pyrometer also broadens the range of measurements to lower temperatures, which is particularly important for certain processes such as droplet epitaxy.

The temperature in this work has been always calibrated using the temperature of a surface transition as a reference.

9. <u>Further development:</u>

    a. A new Mn inverted source has been purchased. The source has been specially designed to work upside down so that it can be installed in one of the empty ports on the top part of the main chamber, due to port not being available at the bottom, increasing the flexibility of the system to grow new materials.

b. Incorporation of an ion-sputtering gun in the new preparation chamber is expected in the near future in order to favour planarization of metallic surfaces.
c. We are currently working on the acquisition of an STM system to be incorporated in the new preparation chamber. This system improvement would combine the accuracy and resolution of the STM measurements with the feasibility of the LEEM to observe dynamical processes at semiconductor surfaces.

For the sake of clarity, Figure 5 has been created. This picture shows the changes introduced in the LEEM system to provide state-of-the-art MBE capabilities. The new preparation chamber is shown on the bottom-left of the picture. The second Mass Spectrometer and the band-edge pyrometer are shown on the bottom-right of the picture.

The LEEM-MBE system is currently able to carry out growth studies on externally grown samples. Collaborations with Paul Drude Institute (PDI) in Germany, Sheffield University, Universidad Autónoma de Madrid (UAM) and ISOM-UPM (Madrid) have been established.

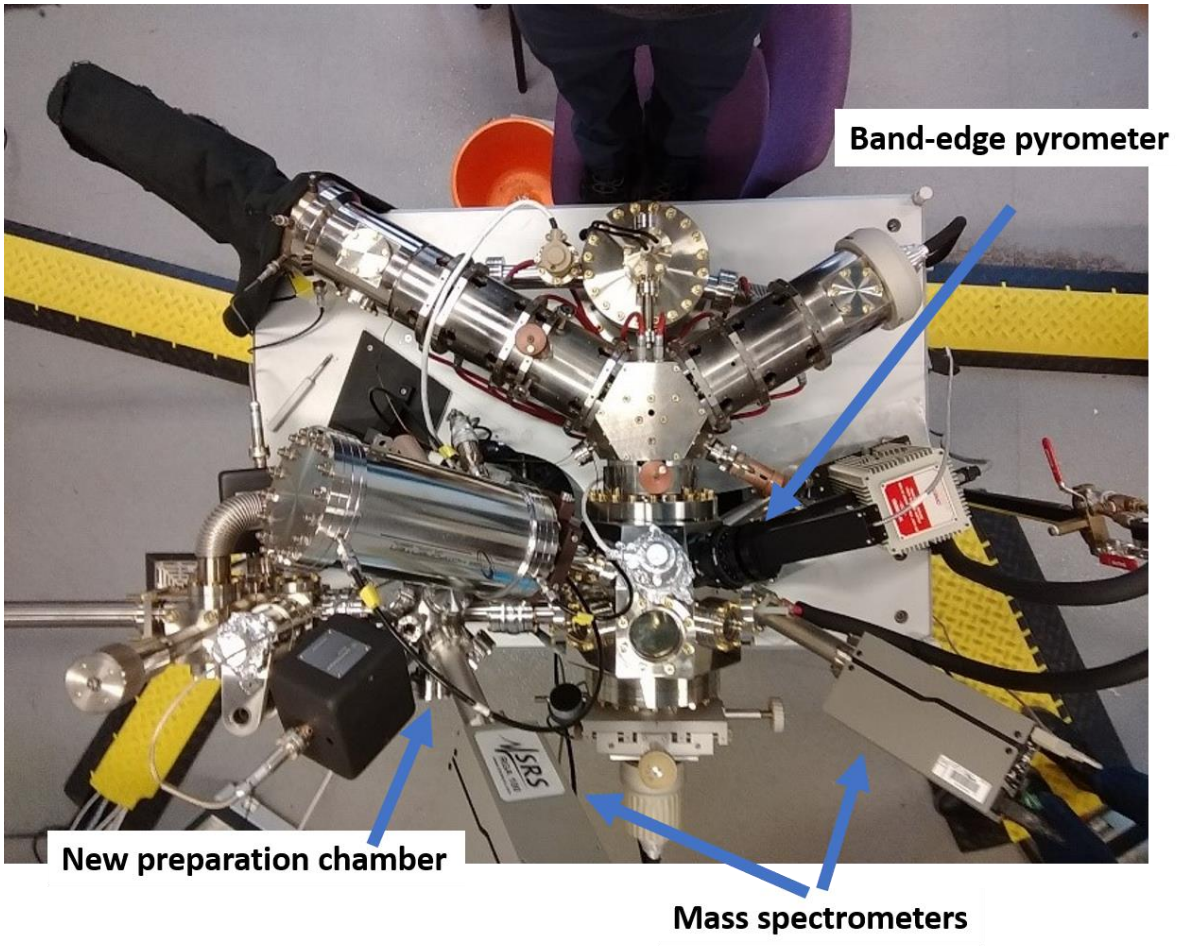

Figure 5. Images of the current LEEM system at Cardiff University. The new preparation chamber, a mass spectrometer and the new ion pump for the preparation chamber can be found on the bottom left corner of the picture. The new band-edge pyrometer and a second mass spectrometer can be found on the right side of the chamber.

Sample preparation

The procedure for sample preparation has been standard and reproducible for all our experiments. In order to introduce a sample into a UHV system, the sample needs to be cleaned and degreased. For this purpose, we make our samples to go through an ultrasonic bath for 20 minutes. The first 10 minutes the sample is submerged in acetone, and the second ten minutes, the sample is under

isopropanol (IPA). The reason for this order is because the acetone leaves an organic residue.

MBE-LEEM is highly sensitive to the material surface, therefore avoiding surface contaminants such as water or carbon is important. Once the samples have been cleaned and degreased, they are introduced in the preparation chamber. GaAs(001) wafers native oxide is removed in ultra-high vacuum (UHV) keeping the sample at 580^0C for 2 hours. The oxide removal process produces a rough and faceted surface. In conventional MBE systems, a GaAs buffer layer with a minimum thickness of 500 nm is grown in order to smooth the surface and bury interfacial defects. However, within the LEEM system, Arsenic exposure must be minimized, since over time the contamination of the objective lens can cause arcing between it and the sample. Therefore, large exposures of V-fluxes must be avoided.

In order to obtain the GaAs (001) flat surfaces for the LEEM-MBE equipment, two different approaches can be followed. The first procedure involves the smoothing of the sample surface by generation and motion of Ga droplets as reported by J. Tersoff et al [69]. For this method, the sample is heated up above the GaAs congruent temperature (around 620°C for GaAs [70]) , where the evaporation of As occurs at higher rate than the Ga evaporation. This phenomenon leaves an excess of Ga on the surface. The Ga atoms diffuse across the surface forming Ga droplets. Then, the temperature is reduced around 20°C (up to approximately 600°C) to favour droplet motion. When the droplets move across the surface, the surface gets planarized on the trail the droplet leaves behind. It has been observed certain anisotropy in the form of preferential directions the droplets move across the surface.

The other method to prepare a flat surface, is the utilisation of As-capped samples, which is derived from the capabilities of the new preparation chamber and all the associated instruments. The samples are then introduced in the LEEM system, the As capping layer is then thermally removed, while monitoring the desorption using line-of-sight-mass spectroscopy; enabling the study of growth mechanisms on the clean surface [71].

The As capping desorption is monitored via line-of-sight-spectroscopy measurements, preventing the sample to be overheated in the preparation chamber. Figure 6 shows the line-of-sight mass spectroscopy results, where a clear peak of As desorption is observed. The desorption occurs at around 150°C, at that temperature we can see the sample and the sample holder are still desorbing water from the environment, but a clear peak for As is easily observed. Preliminary results show no significant advantages capping with As_2 or As_4.

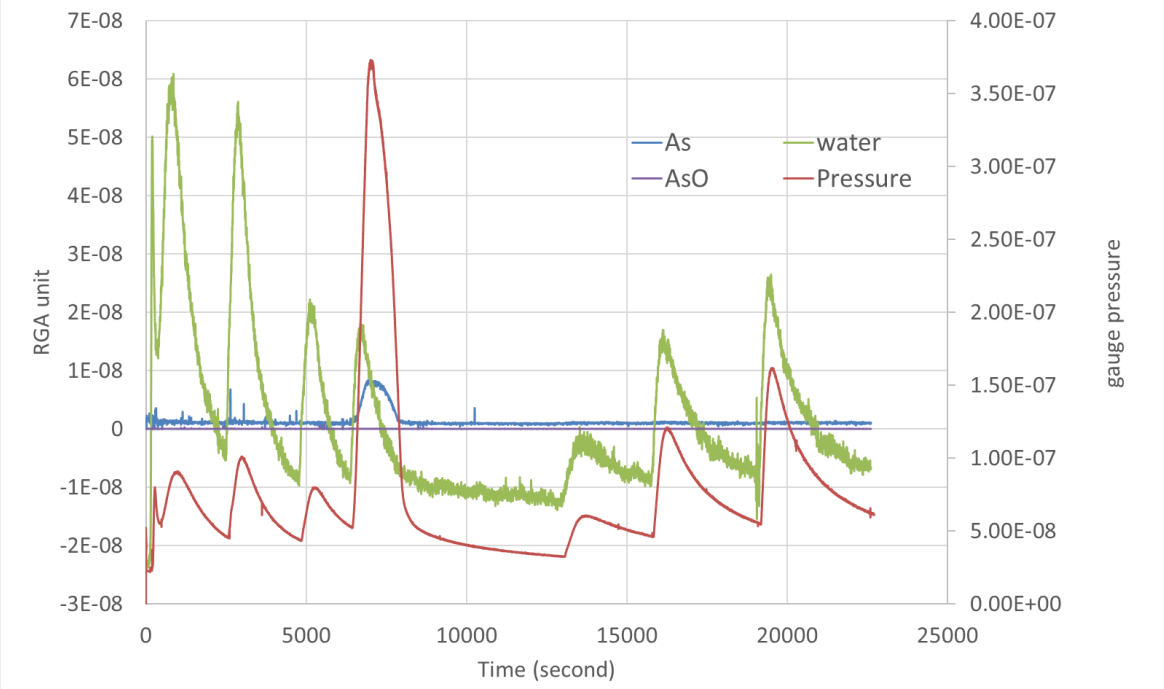

Figure 6. Line-of-Sight Mass Spectroscopy results demonstrating successful monitoring of As capping desorption of an externally grown sample.

After desorption the sample is transferred into the main chamber for further investigations. The surface reconstruction of GaAs (001) right after the observation of the desorption of the cap is a (4×4) structure, although overheating might produce a (6×6). Further annealing transforms the sample into (2×4) and (6×6) reconstructions. Initial preparation of the sample is shown to be critical for the surface phase diagram.

In general, we have observed a noticeable dependence on the heating curve of the sample. It has been found that for certain processes like the generation of droplets by congruent evaporation, the density of the droplets gets smaller with a slower heating curve.

LEEM-MBE relevance

In the consequent chapters of this thesis we will demonstrate that LEEM-MBE is a very promising technique which could complement other in-situ characterisation techniques such as TEM-MBE, RHEED, or STM-MBE, for the study of dynamical processes involved in the growth of epitaxial structures. Our unique equipment allows us to study the effect of arsenide compounds on semiconductor surfaces. The new instrumental implementations in the system that have taken place recently have driven to the successful analysis of GaAs (001) dynamics and the study of different transformations, coexistence, and metastability of different phase reconstructions.

In the next chapters the capabilities of this unique system will be revealed with illustrative examples that have led to several submissions of publications in high-impact journals.

References:

[1] R. M. Tromp, M. Mankos, M. C. Reuter, A. W. Ellis, and M. Copel, "A New Low Energy Electron Microscope," *Surf. Rev. Lett.*, vol. 05, no. 06, pp. 1189–1197, 2003.

[2] J. P. Viterbo, "LEEM lab," *Low Energy Electron Microscopy lab*, 2019. [Online]. Available: https://leemlab.cf.ac.uk/. [Accessed: 29-Jul-2019].

[3] I. Bartos, "Electronic structure of crystals via vleed," *Prog. Surf. Sci.*, vol. 59, no. 1–4, pp. 197–206, 1998.

[4] J. B. Maxson *et al.*, "Novel dark-field imaging of GaN { 0001 } surfaces with low- energy electron microscopy," vol. 464, pp. 217–222, 2000.

[5] H. A. Mckay and R. M. Feenstra, "Low energy electron microscopy of indium on Si (001) surfaces," *Surf. Sci.*, vol. 547, pp. 127–138, 2003.

[6] T. Giela, D. W.- Sl, M. Sl, and N. Spiridis, "LEEM study of high-temperature oxygen structures on W (110) and their transformations," *Appl. Surf. Sci.*, vol. 425, pp. 314–320, 2017.

[7] E. Bauer, "A brief history of PEEM," *J. Electron Spectros. Relat. Phenomena*, vol. 185, pp. 314–322, 2012.

[8] E. Bauer, *Surface microscopy with Low Energy Electrons*. Springer, 2014.

[9] J. De Figuera and K. F. Mccarty, *Low-Energy Electron Microscopy*. 2013.

[10] Elmitec, "Sample cartridge for Elmitec microscopes," 2019. [Online]. Available: https://elmitec.de/Components.php?Bereich=Cartridges. [Accessed: 31-Jul-2019].

[11] I. Stanley, G. Coleiny, and R. Venkat, "Theoretical study of in desorption and segregation kinetics in MBE growth of InGaAs and InGaN," *J. Cryst. Growth*, vol. 251, no. 1–4, pp. 23–28, 2003.

[12] O. A. Ageev, M. S. Solodovnik, S. V. Balakirev, I. A. Mikhaylin, and M. M.

Eremenko, "Monte Carlo simulation of the kinetic effects on GaAs/GaAs(001) MBE growth," *J. Cryst. Growth*, vol. 457, pp. 46–51, 2017.

[13] O. A. Ageev, M. S. Solodovnik, S. V. Balakirev, and M. M. Eremenko, "Kinetic Monte Carlo simulation of GaAs(001) MBE growth considering the V/III flux ratio effect," vol. 34, no. 4, pp. 1–4, 2016.

[14] H. Mao, W. Jing, J. Wang, J. Yu, L. Wang, and N. Dai, "Nucleation and growth mechanism of GaAs epitaxial growth," *Thin Solid Films*, vol. 515, no. 7–8, pp. 3624–3628, 2007.

[15] F. Magnus, A. S. Ingason, S. Olafsson, and J. T. Gudmundsson, "Growth and in-situ electrical characterization of ultrathin epitaxial TiN films on MgO," *Thin Solid Films*, vol. 519, no. 18, pp. 5861–5867, 2011.

[16] S. Schimmel *et al.*, "In situ X-ray monitoring of transport and chemistry of Ga-containing intermediates under ammonothermal growth conditions of GaN," *J. Cryst. Growth*, vol. 498, no. June, pp. 214–223, 2018.

[17] S. P. Svensson *et al.*, "Determination of N-/Ga-rich growth conditions, using in-situ auger electron spectroscopy," *J. Cryst. Growth*, vol. 425, pp. 2–4, 2015.

[18] I. Masakazu, M. Ohkura, and K. Hayakawa, "Micro-Probe Reflection High-Energy Electron Diffraction techique. III. Observation of polycrystalline Silicon film on crystalline Silicon substrate irradiated by continuous-wave Ar+ laser," *Japanese J. Appl. Physics, Part 1 Regul. Pap. Short Notes*, vol. 22, no. 3, pp. 527–533, 1983.

[19] M. Ichikawa, "Crystallographic analysis and observation of surfaxee micro-areas using microprobe Reflection High-Energy Electronn Diffraction," *Mater. Sci. Reports*, vol. 4, pp. 147–192, 1989.

[20] M. Ichikawa, T. Doi, M. Ichihashi, and K. Hayakawa, "Observation of Surface Micro-Structures by Micro-Probe Reflection High-Energy Electron Diffraction," *Jpn. J. Appl. Phys.*, vol. 23, no. 7R, pp. 913–920, 1984.

[21] T. Doi and M. Ichikawa, "Microscopic observation of Si MBE on Si(001)

surface using microprobe RHEED," *J. Cryst. Growth*, vol. 95, no. 1–4, pp. 468–471, 1989.

[22] D. Kishimoto, T. Ogura, A. Yamashiki, T. Nishinaga, S. Naritsuka, and H. Sakaki, "2D-nucleation on (1 1 1)B micro-facet studied by microprobe-RHEED in GaAs MBE for mesa-structure fabrication," *J. Cryst. Growth*, vol. 216, no. 1, pp. 1–5, 2000.

[23] M. Hata, T. Isu, A. Watanabe, and Y. Katayama, "Real-time observation of molecular beam epitaxy growth on mesa-etched GaAs substrates by scanning microprobe reflection high-energy electron diffraction," *Appl. Phys. Lett.*, vol. 56, no. 25, pp. 2542–2544, 1990.

[24] T. Nishinaga, A. Yamashiki, and X. Q. Shen, "Arsenic pressure dependence of inter-surface diffusion in MBE of GaAs studied by the microprobe-RHEED/SEM MBE system," *Thin Solid Films*, vol. 306, no. 2, pp. 187–191, 1997.

[25] T. Nishinaga, "Understanding of crystal growth mechanisms through experimental studies of semiconductor epitaxy," *J. Cryst. Growth*, vol. 275, no. 1–2, pp. 19–28, 2005.

[26] T. Nishinaga and X. Q. Shen, "Surface diffusion and adatom stoichiometry in GaAs MBE studied by microprobe-RHEED/SEM MBE," *Appl. Surf. Sci.*, vol. 82–83, no. C, pp. 141–148, 1994.

[27] T. Nishinaga, X. Q. Shen, and D. Kishimoto, "Surface diffusion length of cation incorporation studied by microprobe-RHEED/SEM MBE," *J. Cryst. Growth*, vol. 163, no. 1–2, pp. 60–66, 1996.

[28] T. Nishinaga and A. Yamashiki, "Recent understandings of elementary growth processes in MBE of GaAs," *Thin Solid Films*, vol. 343–344, no. 1–2, pp. 495–499, 1999.

[29] H. Yamaguchi and Y. Homma, "SEM imaging of fundamental growth processes during MBE of GaAs on (111)A substrates," *J. Cryst. Growth*, vol. 201, pp. 124–127, 1999.

[30] Y. Wu, Q. Chen, M. Takeguchi, and K. Furuya, "High-resolution transmission electron microscopy study on the anomalous structure of lead nanoparticles with UHV-MBE-TEM system," *Surf. Sci.*, vol. 462, no. 1, pp. 203–210, 2000.

[31] K. Kanisawa, "Electronic processes in adatom dynamics at epitaxial semiconductor surfaces studied using MBE-STM combined system," *J. Cryst. Growth*, vol. 401, pp. 381–387, 2014.

[32] B. Voigtländer, "Scanning tunneling microscopy studies during semiconductor growth," *Micron*, vol. 30, no. 1, pp. 33–39, 1999.

[33] P. A. Bone, J. M. Ripalda, G. R. Bell, and T. S. Jones, "Surface reconstructions of InGaAs alloys," *Surf. Sci.*, vol. 600, no. 5, pp. 973–982, 2006.

[34] I. O. Akhundov, D. M. Kazantsev, V. L. Alperovich, D. V. Sheglov, A. S. Kozhukhov, and A. V. Latyshev, "Local monitoring of atomic steps on GaAs(001) surface under oxidation, wet removal of oxides and thermal smoothing," *Appl. Surf. Sci.*, vol. 406, pp. 307–311, 2017.

[35] F. Bastiman, A. G. Cullis, and M. Hopkinson, "InAs/GaAs(001) wetting layer formation observed in situ by concurrent MBE and STM," *Surf. Sci.*, vol. 603, no. 24, pp. 3439–3444, 2009.

[36] D. D. Vvedensky, M. Itoh, G. R. Bell, T. S. Jones, and B. A. Joyce, "Island nucleation and growth during homoepitaxy on GaAs(001)-(2×4)," *J. Cryst. Growth*, vol. 201, pp. 56–61, 1999.

[37] S. Jones, "STM : Seeing is Believing," *III-Vs Rev.*, vol. 8, no. 1, pp. 37–41, 1995.

[38] N. Inoue, M. Tanimoto, K. Kanisawa, S. Hirono, J. Osaka, and Y. Homma, "In-situ microscopy of MBE growth of GaAs and related materials," *J. Cryst. Growth*, vol. 127, no. 1–4, pp. 956–961, 1993.

[39] S. Ohkouchi, I. Tanaka, and N. Ikoma, "Scanning tunneling microscopy observation of straight step-edge formation on highly misoriented GaAs (001) surfaces," *J. Cryst. Growth*, vol. 127, no. 1–4, pp. 962–965, 1993.

[40] B. A. Joyce, D. D. Vvedensky, T. S. Jones, M. Itoh, G. R. Bell, and J. G. Belk, "In situ studies of III-V semiconductor film growth by molecular beam epitaxy," *J. Cryst. Growth*, vol. 201, pp. 106–112, 1999.

[41] T. J. Krzyzewski, P. B. Joyce, G. R. Bell, and T. S. Jones, "Understanding the growth mode transition in InAs/GaAs(001) quantum dot formation," *Surf. Sci.*, vol. 532–535, pp. 822–827, 2003.

[42] T. J. Krzyzewski, P. B. Joyce, G. R. Bell, and T. S. Jones, "Surface morphology and reconstruction changes during heteroepitaxial growth of InAs on GaAs(001)-(2x4)," *Surf. Sci.*, vol. 482–485, no. PART 2, pp. 891–897, 2001.

[43] G. R. Bell, T. S. Jones, and B. A. Joyce, "Direct observation of anisotropic step activity on GaAs(001)," *Surf. Sci.*, vol. 429, no. 1, pp. 0–4, 1999.

[44] G. R. Bell, M. Itoh, T. S. Jones, and B. A. Joyce, "Nanoscale effects of arsenic kinetics on GaAs(001)-(2×4) homoepitaxy," *Surf. Sci.*, vol. 423, no. 2, pp. 5–9, 1999.

[45] T. Ide, A. Yamashita, and T. Mizutani, "STM observation of growth interruption effect of MBE growth," *Surf. Sci.*, vol. 287–288, no. PART 2, pp. 1013–1018, 1993.

[46] H. Yang, V. P. Labella, D. W. Bullock, Z. Ding, J. B. Smathers, and P. M. Thibado, "Activation energy for Ga diffusion on the GaAs(0 0 1)-(2×4) surface: An MBE-STM study," *J. Cryst. Growth*, vol. 201, pp. 88–92, 1999.

[47] Q. Xue, T. Hashizume, and T. Sakurai, "MBE-STM study of the Ga-rich 4X2 phase of the GaAs(001) surface," *Appl. Surf. Sci.*, vol. 88, pp. 364–367, 1995.

[48] Q. Xue, T. Ogino, H. Kiyama, Y. Hasegawa, and T. Sakurai, "Surface reconstruction and morphology evolution in highly strained InAs epilayer growth on GaAs(001) surface," *J. Cryst. Growth*, vol. 176, pp. 174–177, 1997.

[49] A. Popp and C. Pettenkofer, "Epitaxial growth of CuGaSe 2 thin-films by MBE—Influence of the Cu/Ga ratio," *Appl. Surf. Sci.*, vol. 416, pp. 815–823, 2017.

[50] F. Bastiman, A. G. Cullis, and M. Hopkinson, "GaAs(0 0 1) (2 × 4) to c(4 × 4) transformation observed in situ by STM during As flux irradiation," *Surf. Sci.*, vol. 603, no. 16, pp. 2398–2402, 2009.

[51] A. Ouerghi, A. Cavanna, D. Martrou, Y. Garreau, and B. Etienne, "Large scale atomic ordering on uncovered GaAs(001) after InAs monolayer capping: Atomic structure of the (12×6) reconstruction," *Surf. Sci.*, vol. 602, no. 9, pp. 1631–1635, 2008.

[52] M. Tanimoto, J. Osaka, T. Takigami, S. Hirono, and K. Kanisawa, "Scanning tunneling microscopy on molecular-beam-epitaxy-grown GaAs(001) surfaces," *Ultramicroscopy*, vol. 44, pp. 1275–1280, 1992.

[53] J. Behrend, M. Wassermeier, and K. H. Ploog, "Virtual-surfactant mediated epitaxy of InAs on GaAs(001) studied by scanning tunneling microscopy," *J. Cryst. Growth*, vol. 167, no. 3–4, pp. 440–445, 1996.

[54] A. Khatiri, J. . Ripalda, T. . Krzyzewski, G. . Bell, C. . McConville, and T. . Jones, "Atomic hydrogen cleaning of GaAs(001): a scanning tunnelling microscopy study," *Surf. Sci.*, vol. 548, no. 1–3, pp. L1–L6, 2004.

[55] S. Tsukamoto, G. R. Bell, and Y. Arakawa, "Heteroepitaxial growth of InAs on GaAs(0 0 1) by in situ STM located inside MBE growth chamber," *Microelectronics J.*, vol. 37, no. 12, pp. 1498–1504, 2006.

[56] G. R. Bell, M. Pristovsek, S. Tsukamoto, B. G. Orr, Y. Arakawa, and N. Koguchi, "In situ scanning tunneling microscopy of InAs quantum dots on GaAs(001) during molecular beam epitaxial growth," *Surf. Sci.*, vol. 544, no. 2–3, pp. 234–240, 2003.

[57] S. Tsukamoto and N. Koguchi, "Atomic-level in situ real-space observation of Ga adatoms on growth," *J. Cryst. Growth*, vol. 202, pp. 118–123, 1999.

[58] S. Tsukamoto *et al.*, "Ga-rich GaAs[001] surfaces observed by STM during high-temperature annealing in MBE chamber," *MBE 2002 - 2002 12th Int. Conf. Mol. Beam Ep.*, vol. 251, pp. 113–114, 2002.

[59] E. Bauer, "LEEM studies of the early stages of epitaxial growth," *Appl. Surf.*

Sci., vol. 92, pp. 20–29, 1996.

[60] J. B. Hannon and R. M. Tromp, "Low-energy electron microscopy of surface phase transitions," *Annu. Rev. Mater. Sci.*, vol. 33, pp. 263–288, 2003.

[61] B. Q. Li, W.Swiech, J. A. Venables, and J. M. Zuo, "A LEEM study of bamboo-like growth of Ag crystals on Si(001) surfaces," *Surf. Sci.*, vol. 569, pp. 142–148, 2004.

[62] A. Kawazu, "Recent progress in low-energy electron diffraction : and application to semiconductor surfaces theory," *Mater. Sci. Eng.*, vol. R14, pp. 255–317, 1995.

[63] P. Sutter, E. Mateeva, J. S. Sullivan, and M. G. Lagally, "Low-energy electron microscopy of nanoscale three-dimensional SiGe islands on Si (100)," *solid Film.*, vol. 336, pp. 262–270, 1998.

[64] A. Pavlovska *et al.*, "In situ real-time studies of GaN growth on 6H — SiC (0 0 0 1) by low-energy electron microscopy (LEEM)," *J. Cryst. Growth*, vol. 190, pp. 310–316, 1998.

[65] A. Pavlovska, E. Bauer, and D. J. Smith, "In situ studies of the role of excess Ga on the growth morphology of thin GaN layers," *Surf. Sci.*, vol. 496, pp. 160–178, 2002.

[66] M. Foerster and L. Mart, "Initial stages of the growth of mixed iron-cobalt oxides on Ru (0001)," *Phys. Procedia*, vol. 85, pp. 12–19, 2016.

[67] M. B. Casu, "Growth, structure, and electronic properties in organic thin films deposited on metal surfaces investigated by low energy electron microscopy and photoelectron emission microscopy," *J. Electron Spectros. Relat. Phenomena*, vol. 204, pp. 39–48, 2015.

[68] R. Wu, A. Gozar, and I. Bo, "Large-area borophene sheets on sacrificial Cu(111) films promoted by recrystallization from subsurface boron," no. July, pp. 1–6, 2019.

[69] J. Tersoff, D. E. Jesson, and W. X. Tang, "Running Droplets of Gallium from

Evaporation of Gallium Arsenide," *Science (80-.).*, vol. 324, no. 5924, pp. 236–238, 2008.

[70] Z. Y. Zhou, C. X. Zheng, W. X. Tang, D. E. Jesson, and J. Tersoff, "Congruent evaporation temperature of GaAs(001) controlled by As flux," *Appl. Phys. Lett.*, vol. 97, no. 121912, pp. 1–3, 2010.

[71] U. Resch *et al.*, "Arsenic passivation of MBE grown GaAs(100): structural and electronic properties of the decapped surfaces," *Surf. Sci.*, vol. 269–270, no. C, pp. 797–803, 1992.

Chapter 4: Selective Energy Dark Field Low Energy Electron Microscopy (SEDFLEEM)

In this chapter, a novel technique for LEEM system has been described. This technique allows for discrimination of surface phases and for identification of complex structures forming at the surface of semiconductors.

Introduction

I-V curves are highly sensitive to the crystal geometry and the shape of the potential barrier of a surface [1]. An I-V curve in LEED is a representation of the intensity of the intensity of a specific spot in the reciprocal lattice as a function of the electron energy on the surface. It is the intensities of diffracted beams rather than their directions that are affected by dynamical effects. A deep analysis on the I-V curves theory for the (0,0) spot has been developed by J. I. Flege and E. E. Krasovski, in which they utilised I-V LEEM to study the transformation from the (1×1)-O adlayer phase to RuO_2(110) during Ru(0001) oxidation on the nanometre scale, concluding that I-V LEEM characterisation of surface structure combined with theoretical calculations, can provide very useful information on geometric and electronic structure and chemical composition [2]. In an I-V curve, where the surface energy of the electrons is varied, one finds shifts in the energies at which Bragg peaks occur [3]. For I-V LEEM, the intensity of a specific point of the real space is recorded at different electron energies. This also applies to any other kinematically expected peak when the surface structure is not a simple termination of the bulk structure. Furthermore, additional peaks appear that are due entirely to multiple scattering. These peaks, contain as much structural information as the original Bragg peaks and can therefore be considered as useful data for structural determinations [4].

The Bloch waves decay exponentially even within the allowed bands, as a result of current loss [5]. Also, the inelastic effects reduce the number of electrons that are reflected and smooth its dependence on energy and incident direction, removing the sharp band-gap edges that would otherwise generate abrupt changes in the reflectivity as a function of energy [6]. More information about multiple scattering can be found in chapter 2 (LEED). Due to the complexity of modelling and calculating multiple scattering of electrons with the matter, we offer an alternative approach which uses experimental intensities to maximise the contrast and favour phase discrimination.

In order to offer a much simplistic way of visualising these effects, we can describe Angle-Resolved Photoemission (PE) Spectroscopy (ARPES), which is one of the main experimental methods to map E(k) with resolution in energy E [7], [8]. One can assume that an electron, will see a different "surface band-structure" depending on the atomic arrangement on the surface. This can be analogue to change the angle with which the electrons hit on the surface. For the sake of clarity, let us assume a surface with a certain atomic termination. This phase will have a certain I-V curve, and it can be seen as the "signature" of the phase. If we maximised the electron surface energy for a local maximum from the I-V curve, the contrast will be maximised. Now let us also imagine the same surface, with a symmetry such, that the termination of the atoms will be rotated 30°. If we rotated the angle of the incident beam to 30°, the contrast would be the same. However, if we were to shine the electron beam normal to surface again, the "surface band-structure" that the electron will see, will be totally different since the atomic arrangement at the surface, is different. The I-V curve of the phase will be different, and the maximum contrast will happen at a different energy. Thus, different atomic arrangements i.e. phase reconstructions, at the surface, will lead to different I-V curves for each point. Taking advantage of the difference in reflectivity for each surface phase reconstruction, I-V curves can be utilised for surface phase discrimination.

In optical microscopy, Dark-Field technique is a simple method for imaging unstained and transparent specimens. Dark-Field technique is regularly applied

to samples in which the feature to be analysed have refractive indices very close in value to those of their surroundings and are difficult to image with conventional Bright-Field. Dark-Field imaging blocks out of the central light rays along the optical axis of the microscope, which pass through and around the specimen. By blocking these light rays, only those oblique rays that are found at large angles strike the specimen, enhancing the contrast by the superposition of a brightly shining specimen on a dark background [9].

In contrast to optical microscopy, Dark-Field imaging in electron microscopy is slightly different. In electron microscopy, certain points of the reciprocal lattice are filtered (for further information, see chapter 1). This effect leads to a high contrast for certain phases, improving phase discrimination. Normally, DF-LEEM imaging is applied at constant incident electron beam energy and this has previously been utilised to discriminate different surface reconstructions for various different materials such as Au [10], Si [11], W [12], [13], Ru [14], NiO [15], graphene [16], [17], GaP [18] or GaN [19].

The information obtained by diffraction and dark-field images, can be potentially misleading for a certain energy. Plotting the difference in diffracted intensity against incident beam energy (also called I-V curves) has led to discriminate between (7×7) and (1×1) domains in Si (111) at constant energy for the specular (00) beam [20]. We have applied this technique to complex surfaces exhibiting varying stoichiometry like GaAs (001).

We have investigated the LEED pattern from one surface reconstructions for GaAs (001), the c(8×2), which is Ga-rich; at different incident beam energies. The first pattern displays a (4×1) periodicity at 10.6 eV. Nonetheless, at 6.6 eV the same pattern displays a c(8×2) periodicity. This is a very simple example which highlights the importance of scanning the LEED pattern across a range of incident beam energy in order to determine which is the highest periodicity for each surface phase, optimising the surface energy of the electrons for the best reflectivity. This case can be found in Figure 1. However, if instead of having only one phase at the surface, there was coexistence of different phases over a range

of temperatures or over time, the process gets more complicated as there will be a superimposition of diffraction pattern (see chapter 5).

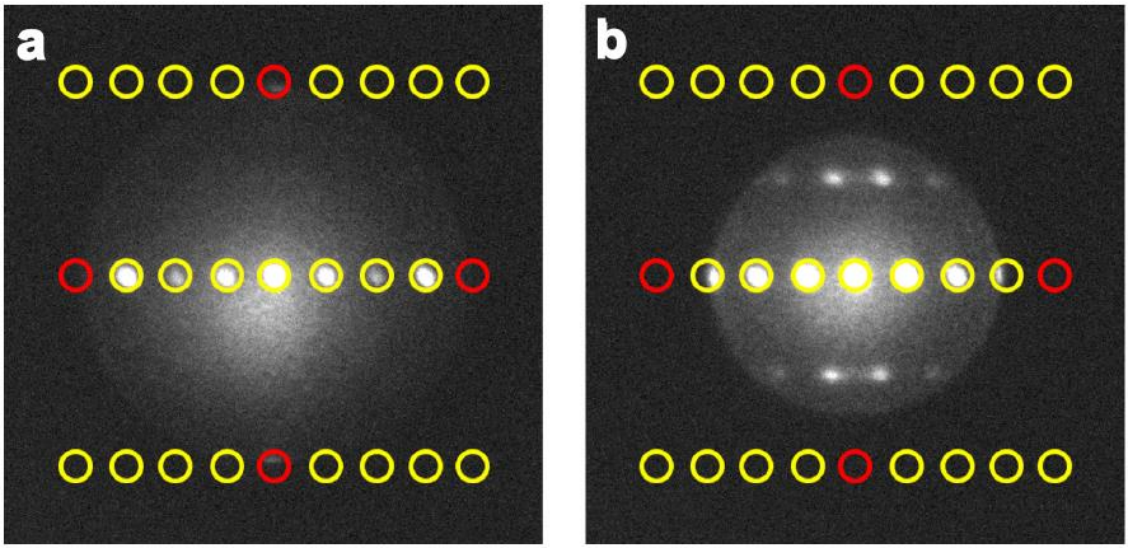

Figure 1. LEED patterns of the c(8×2) surface reconstruction for GaAs at (a) 10.6 eV and (b) 6.6 eV. The apparent (4×1) periodicity in (a) is misleading. (1,0) and (0,1) type spots are indicated by red circles. (1, n) and ($\overline{1}$, n) rows of spots lie outside the Ewald sphere and are represented by yellow circles. (Figure adapted from [21] with permission from publisher).

For GaAs (001) reconstructions in (m×n) periodicity, not all diffracted orders in the LEED pattern are visible at a single energy. Firstly, the Ewald sphere is dependent on the energy, and some points might be left out. Secondly, changes in the surface energy of the electrons alter the energy band at different points of the material, leading to changes in the diffracted intensity. An initial I-V curve scan results crucial for accurate characterisation of surface structures as it allows the optimisation of the reflectivity on the surface for each phase, improving the contrast and facilitating phase discrimination.

SEDFLEEM

We have combined the advantages of Dark Field and I-V LEED to develop an imaging technique that we have named as Selective Energy Dark Field Low Energy Electron Microscopy (SEDFLEEM). We demonstrated this technique in our LEEM-MBE equipment by the discrimination between two surface reconstructions for GaAs (001): the c(8×2) and the (6×6) phases, since these two phases are found to be heavily mixed [22], [23] and coexistence between them has been demonstrated [24] over a range of temperatures. We prepared the surface following the standard procedures described in chapter 3. After generating droplets and preparing a flat surface on the droplet trail, we cooled the sample down to reach a state of coexistence of the two phases. Figure 3a represents the superposition of the two LEED patterns for both phases.

Different reflections can be used to discriminate the two phases using DF-LEEM. In our case, we have filtered the $(\frac{1}{4}, 0)$ spot of the c (8×2) phase represented in yellow on the LEED pattern inset contained in Figure 2a. For this particular spot, the electron energy needs to be tuned for optimum intensity. The I-V curve for this spot has been represented. The optimum surface energy for the electrons for a maximum intensity occurs at 6.2 eV as indicated by the arrow in Figure 3a. The corresponding $(\frac{1}{4}, 0)$ DF-LEEM image for optimised energy is illustrated in Figure 2b.

Equivalently, for the (6×6) reconstruction, we have filtered the spot. For this point, we have also plotted the I-V curve. The I-V curve is represented in Figure 3b. As it can be appreciated by the position of the arrow, the optimum energy for this spot has been selected as 5.0 eV. A DF-LEEM image filtering the $(0,\frac{3}{6})$ spot is presented in Figure 2c.

For the sake of clarity, the DF-LEEM images in Figure 2b and 2c have been combined in single composite image by assigning different colours to the intensities from the two phases. We have assigned yellow to c(8×2) and red to

(6×6). This SEDFLEEM effect can be appreciated in Figure 2d. Applying this technique, one would be able to combine and complement the information from the two original DF-LEEM images and provides an efficient means of visualising coexisting phases on the surface.

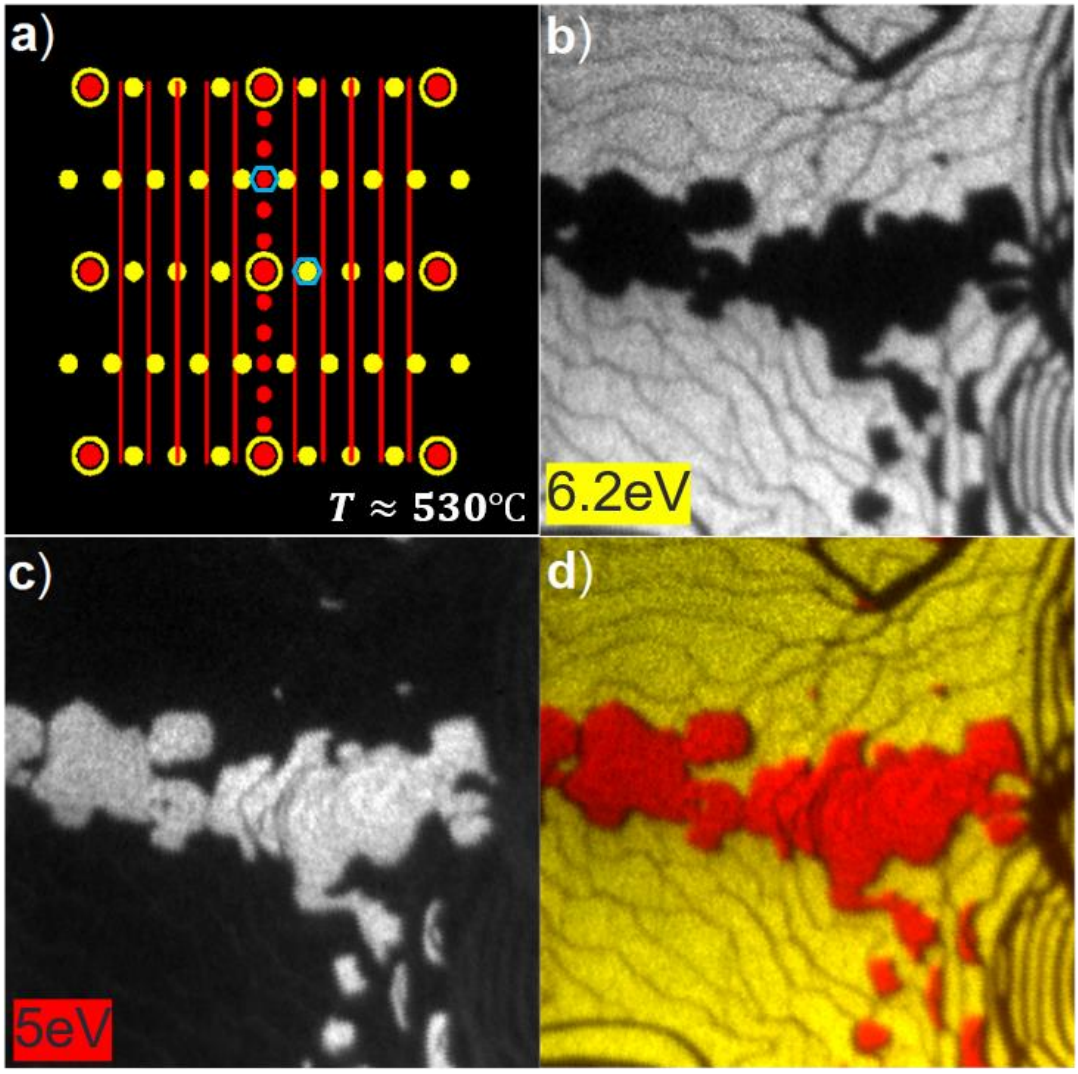

Figure 2. (a) Schematic superimposition of c(8×2) (yellow) and (6×6) (red) LEED patterns. (b) Dark-field image of the c(8×2) phase obtained with the (1/4, 0) spot at 6.2 eV (see Fig. 2(a)). (c) Dark-field image of the (6×6) phase obtained with the (0, 3/6) spot at 5.0 eV (see Fig. 2(c)). (d) Composite SEDF LEEM image obtained by assigning yellow to the dark-field c(8×2) intensity in 2(b) and red to (6×6) intensity in 2(c). (Figure adapted from [21] with permission from publisher).

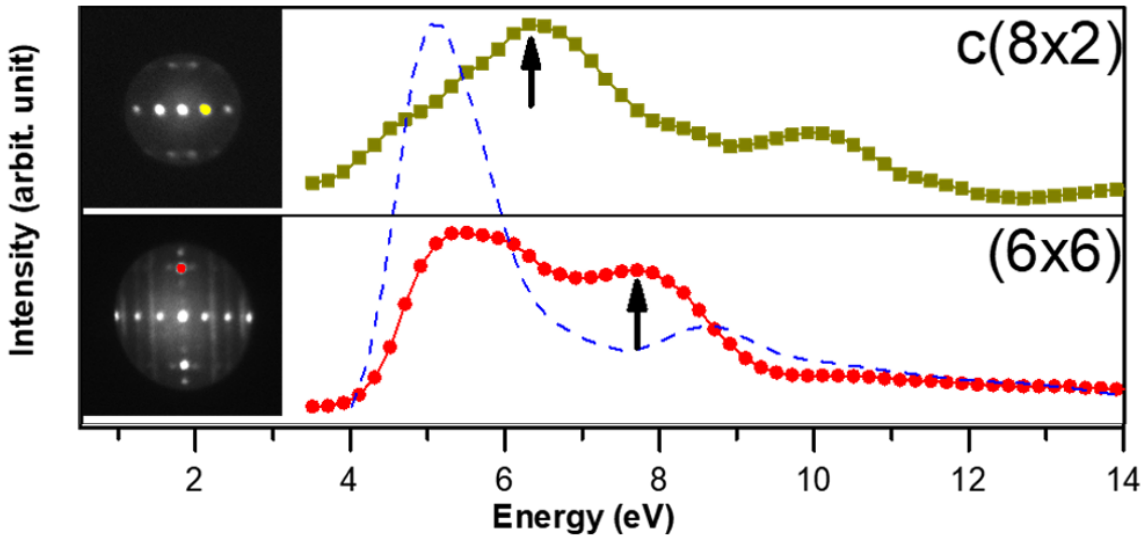

Figure 3. I(V) curves for selected diffraction spots highlighted by colours in the LEED pattern insets. (a) (1/4,0) spot of c(8×2), (b) (0, 3/6) spot of (6×6). The LEED patterns are obtained at the optimal energies indicated by the black arrows under the I(V) curves (arrow 1 in panel (b)). In (b) the blue dashed curve corresponds to the (0, 2/4) spot of β2(2×4). Since the energy is very close, this explains why the second local maximum was taken. (Figure adapted from [21] with permission from publisher).

To conclude, we have developed a powerful technique which combines the advantages of DF-LEEM imaging with the precision of the I-V curve of diffracted spots for identification of complex structures forming at the surface of GaAs (001). Thus, this technique holds substantial potential for surface phase discrimination. In the next chapters, further applications of this technique to the study of different phases GaAs (001) surfaces like c(8×2) and (6×6) coexistence between 520°C and 570°C (see chapter 6) and metastability above 570°C (see chapter 7). We have also applied this technique to study the evolution of the Ga chemical potential using the principles of droplet epitaxy (see chapter 5). This unique technique also allows for the in-situ study of dynamical processes for the nucleation of nanostructures (chapter 8).

References:

[1] C. Q. Sun, "Spectral sensitivity of the VLEED to the bonding geometry and the potential barrier of the O-Cu(001) surface," *Vacuum*, vol. 48, no. 5, pp. 491–498, 1997.

[2] J. I. Flege and E. E. Krasovskii, "Intensity-voltage low-energy electron microscopy for functional materials characterization," *Phys. Status Solidi - Rapid Res. Lett.*, vol. 8, no. 6, pp. 463–477, 2014.

[3] J. Koukal and I. Bartos, "On electron damping in VLEED," *Surf. Sci.*, vol. 251–252, no. C, pp. 508–510, 1991.

[4] M. A. Van Hove, W. H. Weinberg, and C. M. Chan, *Low-Energy Electron Diffraction Experiment, Theory and Surface Structure Determination*, vol. 53, no. 9. 2013.

[5] E. Villalon, "The inverse scattering problem for Semi-infinite crystals," *Appl. Numer. Math.*, vol. 29, pp. 520–535, 1978.

[6] I. Bartoš and J. Koukal, "On Pd(111) sharp resonances in VLEED," *Prog. Surf. Sci.*, vol. 35, no. 1–4, pp. 55–58, 1990.

[7] V. N. Strocov, "Intrinsic accuracy in 3-dimensional photoemission band mapping," *J. Electron Spectros. Relat. Phenomena*, vol. 130, no. 1–3, pp. 65–78, 2003.

[8] J. Jobst *et al.*, "Quantifying electronic band interactions in van der Waals materials using angle-resolved reflected-electron spectroscopy," *Nat. Commun.*, vol. 7, pp. 1–6, 2016.

[9] Nikon, "Darkfield Illumination," *Mycroscopy U*, 2019. [Online]. Available: https://www.microscopyu.com/techniques/stereomicroscopy/darkfield-illumination. [Accessed: 02-Aug-2019].

[10] E. Bauer, M. Mundschau, and W. Telieps, "Surface domain structure of reconstructed Au{100} observed by dark field low energy electron

microscopy," *Surf. Sci.*, vol. 225, pp. 87–96, 1990.

[11] E. Bauer, "LEEM studies of the early stages of epitaxial growth," *Appl. Surf. Sci.*, vol. 92, pp. 20–29, 1996.

[12] K. Pelhos, J. B. Hannon, G. L. Kellogg, and T. E. Madey, "LEEM investigation of the faceting of the Pt covered W (111) surface," vol. 432, pp. 115–124, 1999.

[13] T. Giela, D. W.- Sl, M. Sl, and N. Spiridis, "LEEM study of high-temperature oxygen structures on W (110) and their transformations," *Appl. Surf. Sci.*, vol. 425, pp. 314–320, 2017.

[14] T. Herranz, B. Santos, K. F. Mccarty, and J. De Figuera, "Real-space study of the growth of magnesium on ruthenium," *Surf. Sci.*, vol. 605, pp. 903–911, 2011.

[15] J. Das and K. S. R. Menon, "On the evolution of antiferromagnetic nanodomains in NiO thin films : A LEEM study," *J. Magn. Magn. Mater.*, vol. 449, pp. 415–422, 2018.

[16] H. Hibino, S. Wang, C. M. Orofeo, and H. Kageshima, "Growth and low-energy electron microscopy characterizations of graphene and hexagonal boron nitride," *Prog. Cryst. Growth Charact. Mater.*, vol. 62, no. 2, pp. 155–176, 2016.

[17] T. A. De Jong, E. E. Krasovskii, C. Ott, R. M. Tromp, S. J. Van Der Molen, and J. Jobst, "Intrinsic stacking domains in graphene on silicon carbide : A pathway for intercalation," *Phys. Rev. Mater.*, vol. 2, no. 104005, pp. 1–7, 2018.

[18] H. Döscher, B. Borkenhagen, G. Lilienkamp, W. Daum, and T. Hannappel, "III – V on silicon : Observation of gallium phosphide anti-phase disorder by low-energy electron microscopy," *Surf. Sci.*, vol. 605, pp. L38–L41, 2011.

[19] J. B. Maxson *et al.*, "Novel dark-field imaging of GaN { 0001 } surfaces with low- energy electron microscopy," vol. 464, pp. 217–222, 2000.

[20] W. Telieps and E. Bauer, "The (7x7) - (1x1) phase transition on si(111)," *Surf. Sci.*, vol. 162, pp. 163–168, 1985.

[21] Y. R. Niu, J. Pereiro, D. Gomez, and D. E. Jesson, "Selected energy dark field imaging using low energy electrons for optimal surface phase discrimination," *Ultramicroscopy*, vol. 200, no. February, pp. 79–83, 2019.

[22] K. Seino, W. G. Schmidt, and O. A., "Ga-rich GaAs(001) surface from ab initio calculations: Atomic structure of the (4x6) and (6x6) reconstructions," *Phys. Rev. B*, vol. 73, no. 035317, pp. 4–9, 2006.

[23] A. Ohtake, "Structure and composition of Ga-rich (6×6) reconstructions on GaAs(001)," *Phys. Rev. B - Condens. Matter Mater. Phys.*, vol. 75, no. 15, pp. 4–7, 2007.

[24] A. Ohtake, P. Koćan, K. Seino, W. G. Schmidt, and N. Koguchi, "Ga-rich limit of surface reconstructions on GaAs(001): Atomic structure of he (4 × 6) phase," *Phys. Rev. Lett.*, vol. 93, no. 26 I, pp. 4–7, 2004.

Chapter 5: SEDFLEEM for droplet epitaxy on GaAs (001)

In this chapter, we have mapped the GaAs (001) phase diagram around liquid Ga droplets using the approach of droplet epitaxy in just few microns at a fixed temperature. Conclusions on the stability of (3×6) and (6×6) phases will be outlined.

Introduction

One of the most common methods for the fabrication of quantum nanostructures is the growth of lattice-mismatched III-V semiconductor materials via the Stranski-Krastanov (SK) mode. This method has been described in chapter 1. The accurate control of size and shape of QDs via SK self-assembly remains problematic, limiting therefore the possibilities for tailoring electronic and optical properties of quantum structures. To overcome the SK growth limitations, Droplet Epitaxy (DE) was introduced. DE is a growth procedure fully limited by kinetics and does not rely on strain for the formation of 3D nanostructures. An initial deposition of metallic group III leads to the formation of nanometre-sized liquid droplets. Further exposure of the liquid droplets to the group V flux causes them to crystallize into quantum structures. This technique is a flexible tool for controlling the morphology of quantum structures [1-23] including double-dots [23], molecules [8], rings [20] and multi-rings [18], [21], [24], [25]. Understanding the precise mechanisms behind the formation of such structures is critical to controlling the various properties such as shape, size, and composition.

Investigations on surface phases of different structure and composition are widely used in the growth of optoelectronic materials, InGaAs/GaAs quantum devices, and dilute magnetic semiconductors by MBE; for its importance in the

morphological properties of the materials. This has led to noteworthy efforts to comprehend and control the stability of surface phases as a function of the experimental conditions. For GaAs, the conventional approach is to calculate the surface free energy (i.e. Gibbs free energy) as a function of Ga surface chemical potential μ_{Ga} (or equivalently As chemical potential μ_{As}, since the sum is fixed [26], [27]).

One of the phase diagrams accepted for GaAs was presented by Däweritz et al. [28]. This diagram, which has been illustrated in chapter 1 for further information, represents the most stable phase reconstruction for a given temperature, depending on the ratio between V-flux over III-flux. The chemical potential of Ga and As (μ_{Ga} and μ_{As}) directly depend on these parameters [29]. The fact that μ_{Ga} depends sensitively on temperature [30] and material deposition [1] makes it a parameter difficult to control experimentally. Lately, efforts have been devoted to control μ_{Ga} by slowly varying the substrate temperature in the presence of liquid droplets [31]. This technique aids the study of the phase diagram in the Ga-rich limit. Nonetheless, key questions regarding phase stability across the wider range of μ_{Ga}, extending towards and including the As-rich regime remain still unanswered.

In this chapter we have applied SEDFLEEM technique and utilise droplet epitaxy combined with low energy electron microscopy (LEEM) imaging to obtain an experimental map of surface free energy as a controlled function of chemical potential.

Droplet epitaxy using LEEM-MBE

As described in chapter 4, SEDFLEEM technique is a flexible tool developed for optimum control of the morphology of quantum structures. By observing the sequential order of phases away from the edge of the droplet we can deduce their relative stability as a function of chemical potential.

To perform this experiment, we have set off from the standard conditions for droplet epitaxy. Figure 1 shows a BF LEEM image of a Ga droplet on GaAs(001) under a 10^{-5} Torr beam effective pressure (BEP) As_4 flux of at 550°C. In this picture we can see a Ga droplet in the middle, surrounded by a dark concentric elliptical ring corresponding to a different surface reconstruction. The dark ring is enclosed by the boundaries I and II. The ellipsism of the ring is due to anisotropic surface diffusion on GaAs (001). The difference in contrast is associated to differences in the effective work functions of each phase reconstruction at the surface. This effect ultimately translate into variations in incident electron reflectivity [32]. We have defined this contrast variation as a droplet epitaxy phase pattern (DEPP). We have carried out micro-spot low energy electron diffraction (μLEED) measurements which revealed that the inner bright region corresponds to a c(8×2) phase reconstruction. The outer bright region corresponds to a β2(2×4), which is one of the most stable forms of (2×4) As-rich reconstructions [33]. The dark ring itself has been identified as a (3×6) surface reconstruction. However, as we will reveal later in this chapter, boundary I is also associated with a (6×6) phase reconstruction.

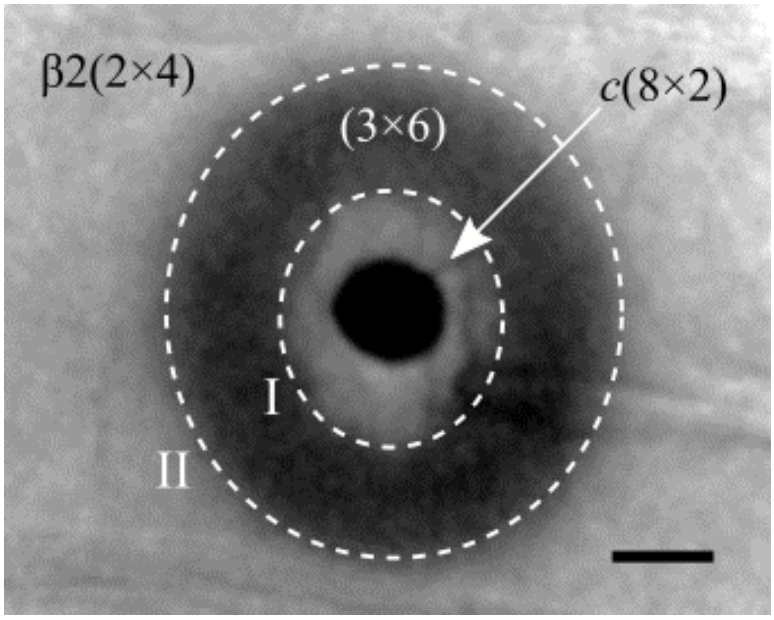

Figure 1. Droplet epitaxy phase pattern (DEPP) of GaAs(001). The BF contrast spatially separates surface phases surrounding a central Ga droplet. The scale bar corresponds to 2 µm. (Figure adapted from [34] with permission from publisher).

To explain the origin of this phase pattern and establish the link to the surface free energy, we consider a simple model for DEPP formation [35]. The Ga droplet acts as a source of Ga adatoms which interact with surface As from the evaporation source. Using the relationship between the surface adatom concentration and the chemical potential, $\mu_{Ga}(r) = E_{Ga} + k_B T \ln(C_{Ga}/\nu_{Ga})$ [36], the Ga chemical potential as a function of the radial position r and temperature T, for flux F_{As} is represented in Equation 1.

$$\mu_{Ga}(r) = E_{Ga} + k_B T \ln\left(\frac{B K_0(r/L_{Ga})}{\nu_{Ga}} + \frac{(C_{Ga}C_{As})_{eq}}{\nu_{Ga} F_{As} \tau_{As}}\right) \qquad \text{Eq. 1}$$

Where k_B is the Boltzmann's constant and we assume the Ga adatoms may sit at ν_{Ga} equivalent surface sites per unit area, of energy E_{Ga}. B is a constant for a given T and a given F_{As}, K_0 is a modified Bessel Function of the second type [37], L_{Ga} is the diffusion length for Ga, which is equal to $L_{Ga} = \sqrt{D_{Ga}\tau_{Ga}}$ where D_{Ga} is the Ga

diffusion coefficient and τ_{Ga} is the residence time for Ga atoms; and C_{Ga} and C_{As} are the adatom concentration of Ga and As respectively. The expression for the concentration of As adatoms is $C_{As} = F_{As}\tau_{As}$ [35].

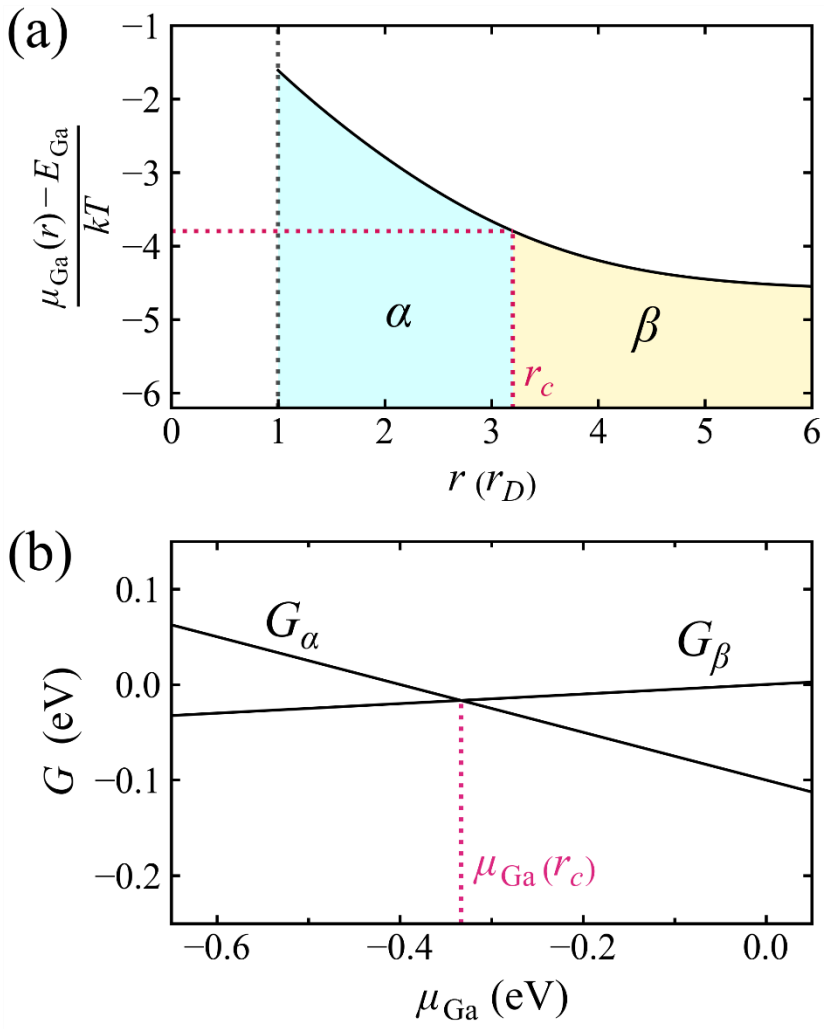

Figure 2. (a) Ga chemical potential at radial position r away from the droplet edge located at r_D. For illustration we have taken C_{Ga}^{l}/ν_{Ga}= 0.2, C_{Ga}(L)/ ν_{Ga} = 0.01 and r_D/L_{Ga} = 1. (b) Schematic representation of the free energy G (per (1×1) unit cell) of phases α and β plotted as a function of μ_{Ga}. The phases have the same free energy at $\mu_{Ga}(r_C)$ corresponding to radial position r_C in (a). (Figure adapted from [34] with permission from publisher).

The droplet acts as a source of Ga adatoms which further react with As to form GaAs. This provokes a monotonically decreasing Ga chemical potential as a

function of radial distance from the droplet edge. This effect is represented in Figure 2a.

Applying this theoretical model [35] to our case illustrated in Figure 1, we consider a radial position r_C associated with the boundary between phases α and β as represented in Figure 2a. This boundary approximates to the experimental boundaries I or II shown in Figure 1. This is associated with a chemical potential $\mu_{Ga}(r_C)$ such that the surface free energies (per (1×1) cell) of both phases are the same. This scenario is illustrated in Figure 3b and the mathematical expression is represented in Equation 2. Thus, the real-space position of phase boundaries around droplets can be used to map the surface free energies as a function of chemical potential. We have improved the resolution of the technique in μ_{Ga} by using the time dependence of DEPP formation. By generating a stationary diffusion field around the Ga droplet and using and As flux, we can use our LEEM-MBE to create a time dependent chemical potential $\mu_{Ga}(r,t)$ at video rate, identifying different phase reconstructions associated with the change in chemical potential over time.

$$G_\alpha(\mu_{Ga}(r_C)) = G_\beta(\mu_{Ga}(r_C)) \qquad \text{Eq. 2}$$

Thus, we have used SEDFLEEM (see chapter 3) for the identification of different phases on the trail of a Ga-droplet. The preparation of the surface has been carried out by surface planarization running Ga droplets [30]. The Ga droplet and its trail have been exposed to an As-flux. The Ga droplet acts again as a continuous source of Ga for the rest of the vicinal surface along the trail, generating a μ_{Ga} profile across the trail.

The substrate temperature was around 550 °C and the As shutter was initially closed. At this time, the entire trail region is composed of the c(8×2) phase. Upon opening the As shutter at t = 0, boundaries I and II move inwards towards the droplet. This interesting effect is demonstrated in Figure 3b, where the radial

position of boundaries I and II is represented as a function of time. At t = 33 s the boundaries approach their steady-state positions, at which point the As is turned off. These boundaries then move outwards along the trail as observed in Figure 3c. These results are plotted in Figure 4b, where the trajectories of phase boundaries I and II when turning the As flux on and off . The horizontal dotted line marks the position of the aperture in Figure 3a, and the dotted vertical lines represent the times at which the As shutter was opened and closed. The crosses correspond to the acquisition times of the LEED data contained in Figure 4a.

Under the action of the As flux, different phases were observed across the GaAs (001) flat trail. We found that the c(8×2), (3×6) and the β2(2×4) reconstructions. The phases have been mentioned in order from more Ga-rich to more As-rich. Figure 4a displays μLEED diffraction patterns for each of these phases (i) to (iv). The patterns were collected at corresponding times indicated by the crosses in Figure 4b. Schematic diffraction patterns are also shown, where large circles indicate the positions of (1×1) spots. Diffraction patterns (i), (iii) and (iv) correspond to the c(8×2), (3×6) and β2(2×4) phases, respectively. Nevertheless, we detected new diffraction information at time (ii), near the boundary I. The observed μLEED diffraction pattern appears to be a superposition of (6×6) and c(8×2) indicating the presence of an additional (6×6) phase in this region. More detailed information over this superposition of diffraction patterns from the c(8×2) and (6×6) will be discussed thoroughly in the next chapters. Also, a more technical information about these phases, has been described by Ohtake et al. [33].

These results provide very useful information about the kinetics at the GaAs(001) surface. SEDFLEEM-MBE is a unique in-situ technique which allows the observation of such kinetical processes i.e. Ga diffusion evolution under As flux, mapping of the chemical potential across the surface.

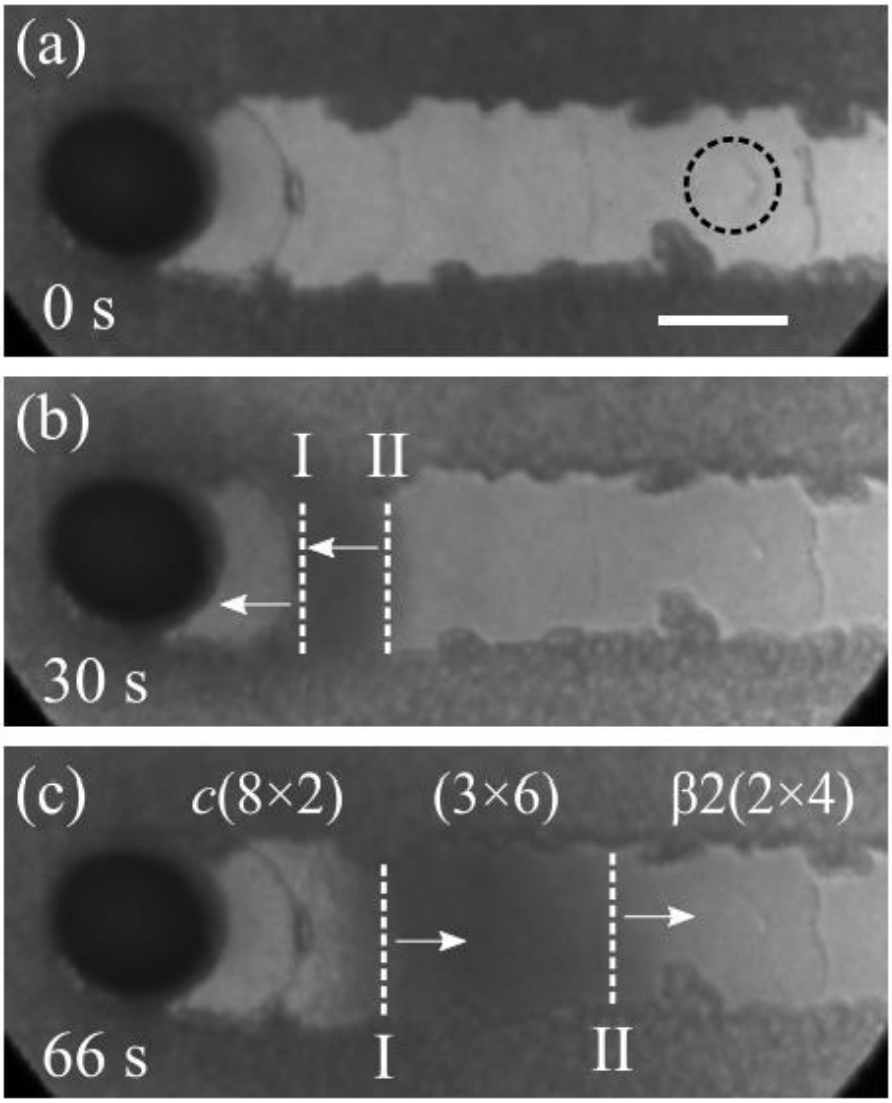

Figure 3. BF- LEEM image of a Ga droplet and smooth trail region of GaAs(001). (a) at t = 0 s before the As flux is turned on. b) 30 s after the As flux is turned on and (c)66 s after the As flux is turned off. The sample temperature is 550°C. The scale bar in (a) is 2 μm. (Figure adapted from [34] with permission from publisher).

Following the methodology described for SEDFLEEM technique described in chapter 3, it is important to know the optimum energy at which each phase needs to be filtered. For this purpose, Figure 5 is presented. In this picture, the different I-V curves for the four different phase reconstructions are plotted. The arrow in each graph indicates the local maximum of energy at which each point has been filtered. For the c(8×2), the $\left(\frac{1}{4}, 0\right)$ spot has been filtered, and the optimum energy

for this spot is 6.2 eV, as indicated in Figure 5a. For the (6×6) the $\left(0,\frac{3}{6}\right)$ spot has been filtered. The optimum energy for this spot is 5 eV, as illustrated by arrow 1 in Figure 5b. The $\left(0,\frac{1}{6}\right)$ spot has an optimum energy of 11 eV. This spot has a much smaller intensity and has not been plotted. For the (3×6) reconstruction, the spot that has been filtered for DF imaging is the $\left(\frac{1}{3},0\right)$ spot. The optimum energy for this spot is 5 eV. Finally, the $\left(0,\frac{1}{4}\right)$ spot has been used to filter the β2(2×4) phase. The optimum energy for this spot is 11.2 eV. To discriminate between the different phases, we must also observe the complication that the $\left(0,\frac{2}{4}\right)$ spot of the β2(2×4) reconstruction is at the same reciprocal space position as the $\left(0,\frac{3}{6}\right)$ spot of the (6×6) reconstruction. The LEED I-V curve of the $\left(0,\frac{2}{4}\right)$ diffraction spot is superimposed as the blue dashed line in Figure 5b. Certainly, the use of 5 eV for the$\left(0,\frac{3}{6}\right)$ reflection would also include a large contribution from β2(2×4). To avoid this effect, we use the next local maximum of the I-V curve as the optimum energy (7.7 eV) of the $\left(0,\frac{3}{6}\right)$ dark-field image of the (6×6) phase indicated by arrow 2 in Figure 6b. Here, the intensity of the $\left(0,\frac{2}{4}\right)$ spot reflection is much lower than that of $\left(0,\frac{3}{6}\right)$. Generally, we would alternatively use the $\left(0,\frac{1}{6}\right)$ to avoid overlap with $\left(0,\frac{2}{4}\right)$, but, in this case, the intensity of the $\left(0,\frac{1}{6}\right)$ is too low for imaging, even at its optimum energy. Furthermore, the position of $\left(0,\frac{1}{6}\right)$ is quite close to the $\left(0,\frac{1}{4}\right)$ spot used for imaging the β2(2×4) phase so that small misalignments of the contrast aperture on the optical path could still mix dark-field signals from the two phases. We therefore used the $\left(0,\frac{3}{6}\right)$ spot at 7.7 eV for (6×6) as presented in arrow 2 in Figure 5b and the $\left(0,\frac{1}{4}\right)$ spot at 11.2 eV for the β2(2×4) phase reconstruction, as illustrated in the arrow in Figure 5d.

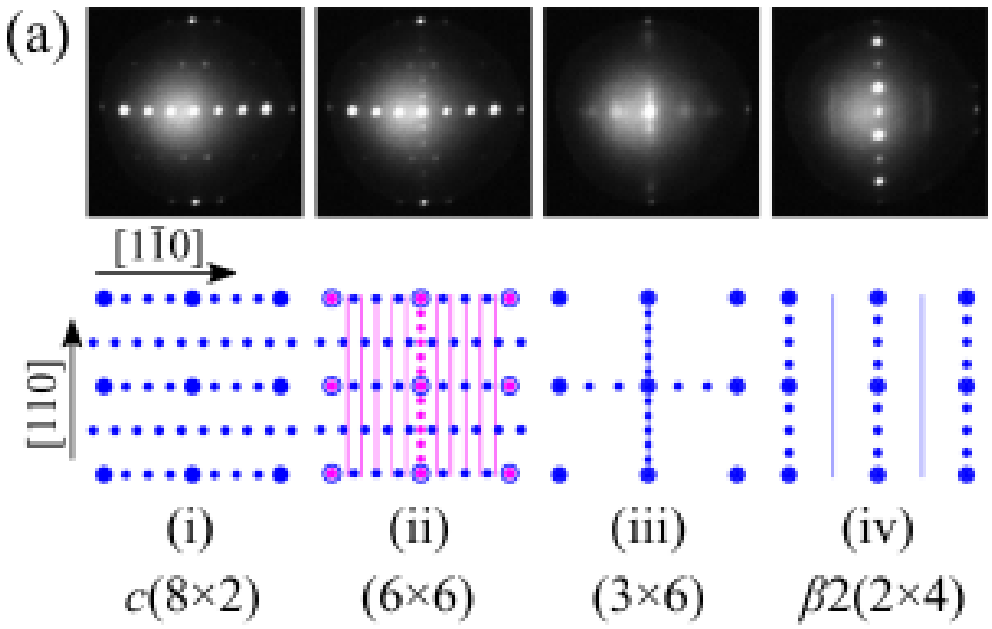
(a)
[1$\bar{1}$0]
[110]
(i)
c(8×2)
(ii)
(6×6)
(iii)
(3×6)
(iv)
β2(2×4)

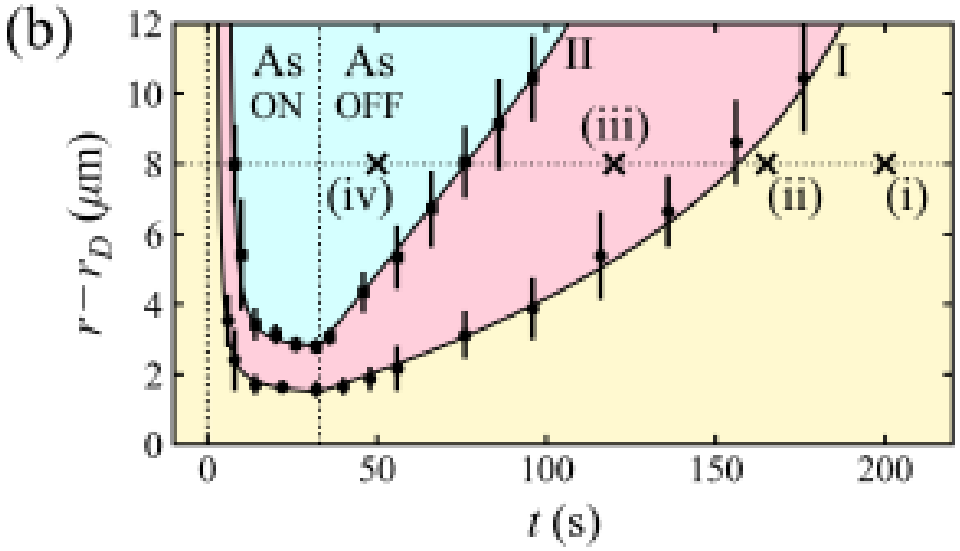
(b)
As ON
As OFF
II
I
(iii)
(iv)
(ii)
(i)
$r - r_D$ (μm)
t (s)

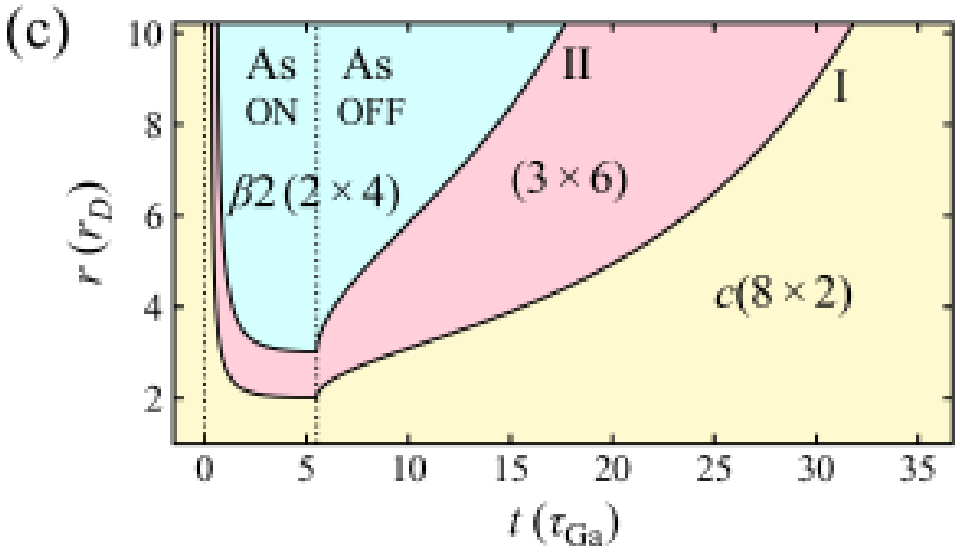
(c)
As ON
As OFF
II
I
β2 (2 × 4)
(3 × 6)
c(8 × 2)
r (r_D)
t (τ_{Ga})

Figure 4. (a) Time-resolved μLEED data collected from the illumination aperture shown in Figure 5a located 8μm away from the droplet. Schematic diffraction patterns are also shown. The large circles indicate the positions of (1×1) spots. (b)Measured r vs t trajectories of phase boundaries I and II, when turning the As flux on and off. The horizontal dotted line marks the position of the aperture in Figure 5a. The crosses corresponding to the acquisition times of the LEED data contained in (a). The dotted vertical lines represent the times at which the As shutter was opened and closed. (c) Theoretical trajectories of boundaries I and II The chemical potentials defining boundaries I and II give stationary boundary positions at $r_I/r_D = 2$ and $r_{II}/r_D = 3$, respectively. (Figure adapted from [34] with permission from publisher).

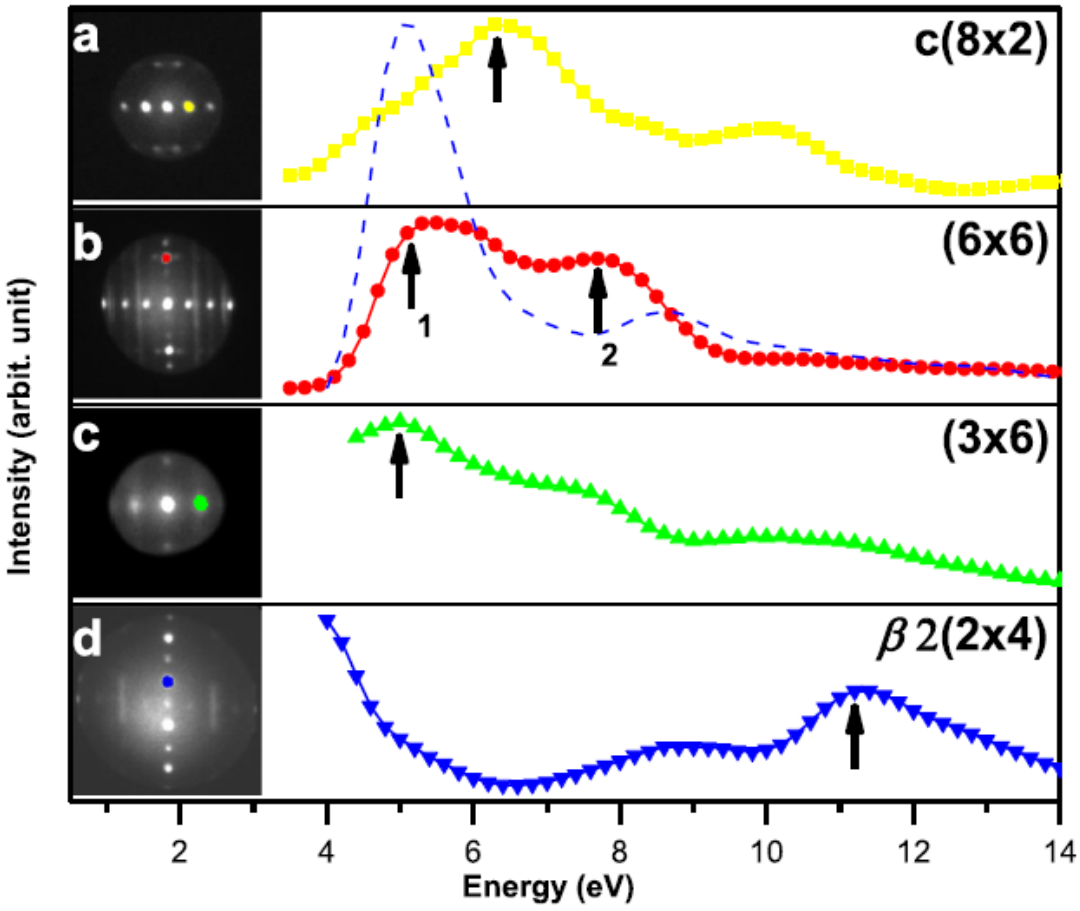

Figure 5. I-V curves for selected diffraction spots highlighted by colours in the LEED pattern insets. (a) (1/4,0) spot of c(8×2), (b) (0, 3/6) spot of (6×6), (c) (1/3, 0) spot of (3×6) and (d) (0, 1/4) spot of β2(2×4). The LEED patterns are obtained at the optimal energies indicated by the black arrows under the I-V curves (arrow

1 in panel (b)). In (b) the blue dashed curve corresponds to the (0, 2/4) spot of β2(2×4). (Figure adapted from [38] with permission from publisher).

Having implemented SEDFLEEM for the optimum discrimination of the four surface reconstructions represented in Figure 5 we programmed the microscope's control software to automatically acquire a sequence of optimal dark-field images for the four phases and a bright-field image in a loop. Figure 7 was then created from the real-time video acquired during the experiment. This image represents the four SEDFLEEM images and a SEBFLEEM image of the Ga droplet and the trail.

The phases appear in different spatial regions of the trail. The droplet under As flux is stationary, but the phase boundaries are slowly moving towards the droplet from right to left at a rate of about 0.4 μm/min. The order of the phases reflects the Ga adatom concentration profile (i.e. the μ_{Ga}) which decreases as the distance from the droplet increases. Hence, the order of the phases is consistent with existing knowledge of the GaAs phase diagram [28], [31], [33] and the Ga-rich or As-rich nature of the phases. The (6×6) phase occupies a narrow band located approximately 4 μm form the droplet edge. Interestingly, this cannot be distinguished in the SEBFLEEM image illustrated in figure 8a because the (0, 0) I-V curves of the (3×6) and (6×6) phases are very similar (not shown). In Figures 6c and 6d, we can appreciate some bright regions very close to the droplet. We believe these might have to do with a pure (4×6) reconstruction forming under very Ga-rich conditions. The x6 periodicity would explain why this phase appears bright when doing DF imaging of the (6×6) and the (3×6) phases.

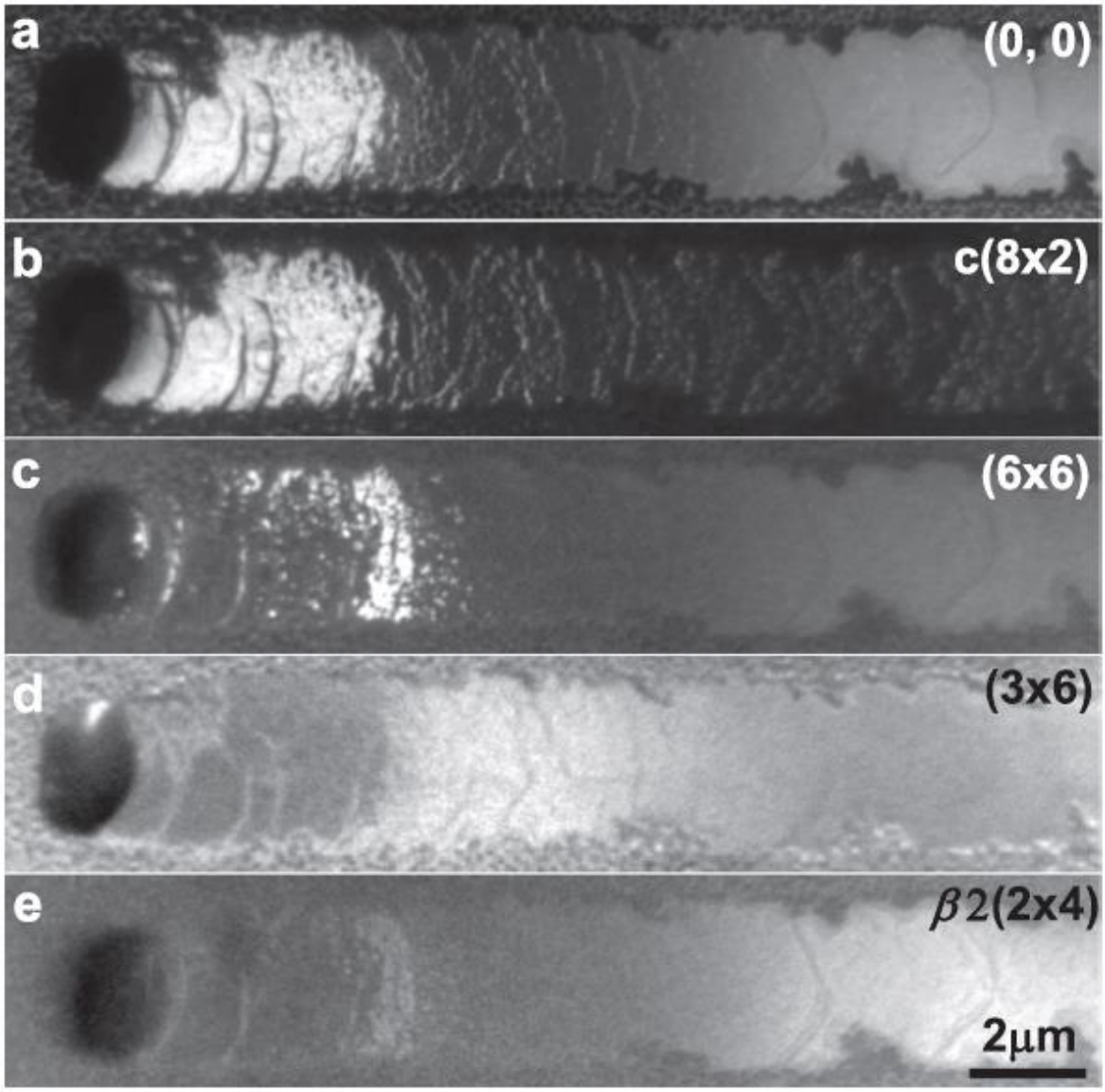

Figure 6. LEEM images of a droplet trail on GaAs (001) after exposing to As flux for 1500 s: (a) bright-field image obtained at 8.6 eV. Dark-field images obtained with (b) the (1/4, 0) spot of c(8×2), (c) the (0, 3/6) spot of (6×6), (d) the (1/4, 0) spot of (3×6) and (e) the (0, 1/4) spot of β2(2×4). The dark-field images are obtained at the optimal energies indicated by the arrows under the I(V) curves in Fig. 3 (arrow 2 in panel(b)). (Figure adapted from [38] with permission from publisher).

For the sake of clarity, we have created a composite SEDFLEEM image represented in Figure 7. We have respectively assigning the colours yellow, red, green and blue to the intensities of the c(8×2), (6×6), (3×6) and β2(2×4) phases

contained in Figure 7(b–e). The time taken to obtain the sequence of images in Figure 6 is 12.6 s. This can be considered fast compared to phase boundary motion. Therefore, Figure 8 can be regarded as an instantaneous snapshot of the surface phase distribution under As flux, surrounding the droplet. The black circle corresponds to the Ga droplet. This temporally resolved SEDFLEEM spatial phase distribution image provides a new basis for studying the surface kinetics of GaAs (001) reconstructions and related phase transformation mechanisms i.e. Ga diffusion, chemical potential evolution over time.

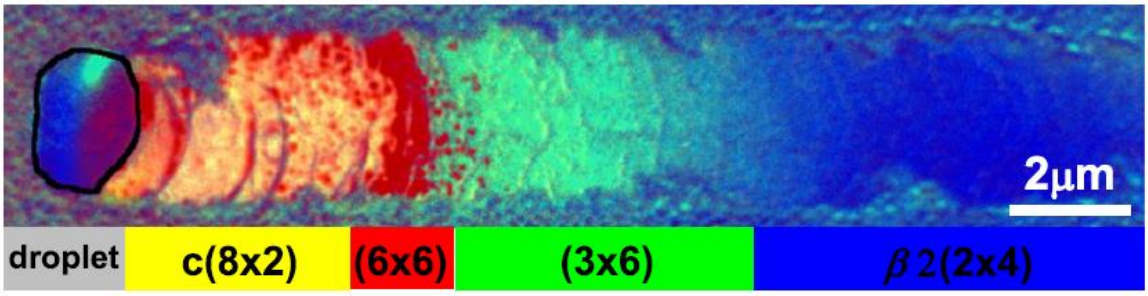

Figure 7. Composite SEDF LEEM image formed by respectively assigning the colours yellow, red, green and blue to the intensities of the c(8×2), (6×6), (3×6) and β2(2×4) darkfield images contained in Fig. 4(b)–(e). Note the irregular shape of the droplet is due to contact line pinning. (Figure adapted from [38] with permission from publisher).

In order to match the theoretical model that we have developed with the experimental results, we have created Figure 8. Figure 8a shows the radial sequence of phases observed in the DEPP Figure 1. We have directly inferred values of μ_{Ga} corresponding to phase boundaries and approximately superimpose them on DFT phase diagrams making use of Equation 2. For more information regarding the theoretical model, see Appendix (DFT model). The gradient of the free energy curve would be directly related with the stoichiometry of the reconstruction. This parameter will therefore provide a good indication of the level of Ga or As richness of a certain phase. A positive slope would indicate a more

As-rich phase while a negative slope would indicate a more Ga-rich reconstruction.

For the (3×6) reconstruction, looking at the high Ga chemical potential regime and taking into account that no (4×6) or β2(2×4) are present in this region; the free energy line for the (3×6) must be somewhere between points A and B according to Figure 8b. We have labelled this point as D. Likewise, lowering the chemical potential of Ga this phase transforms to β2(2×4), having no presence of c(4×4) or c(8×2). Thus, the (3×6) line must be found somewhere between points B and C. We have labelled this point as E. Having this on set, we can now approximate the (3×6) free energy line in Figure 8b. Similarly, the (6×6) besets between c(8×2) and (3×6), therefore it must interact with the (3×6) line between points D and E, and cross the c(8×2) line between A and D. This information allows us to plot approximately the free energy line for the (6×6) in Figure 8b. These lines have been plotted based on experimental observations, therefore their positions in the diagram might not be sufficiently accurate.

Figure 8a also reveals that (6×6) transforms to c(8×2) via a transition zone involving phase coexistence. This coexistence between the (6×6) and the c(8×2) phases will be analysed in detail in chapter 6. It is important to note that these approximate surface free energy plots are obtained directly from the DEPPs in Figures 1 and 2a. Important information is gained from the sequential order of the phases due to the monotonically decreasing chemical potential. This method is insensitive to the detailed position of the phase boundaries and provides DFT researchers with important new information to model the GaAs(001) surface phase diagram. The (6×6) had not been observed to be stable under As flux before [33]. Figure 8a conclusively proves that the (6×6) phase is stable under As flux at finite T over a narrow range of μ_{Ga}. The (6×6)⇔c(8×2) phase coexistence region in Fig. 5(a) also infers the approximate range of μ_{Ga} where coexistence is important. In addition, we have observed the (6×6) patches growing under As flux although further experiments will confirm with more detail.

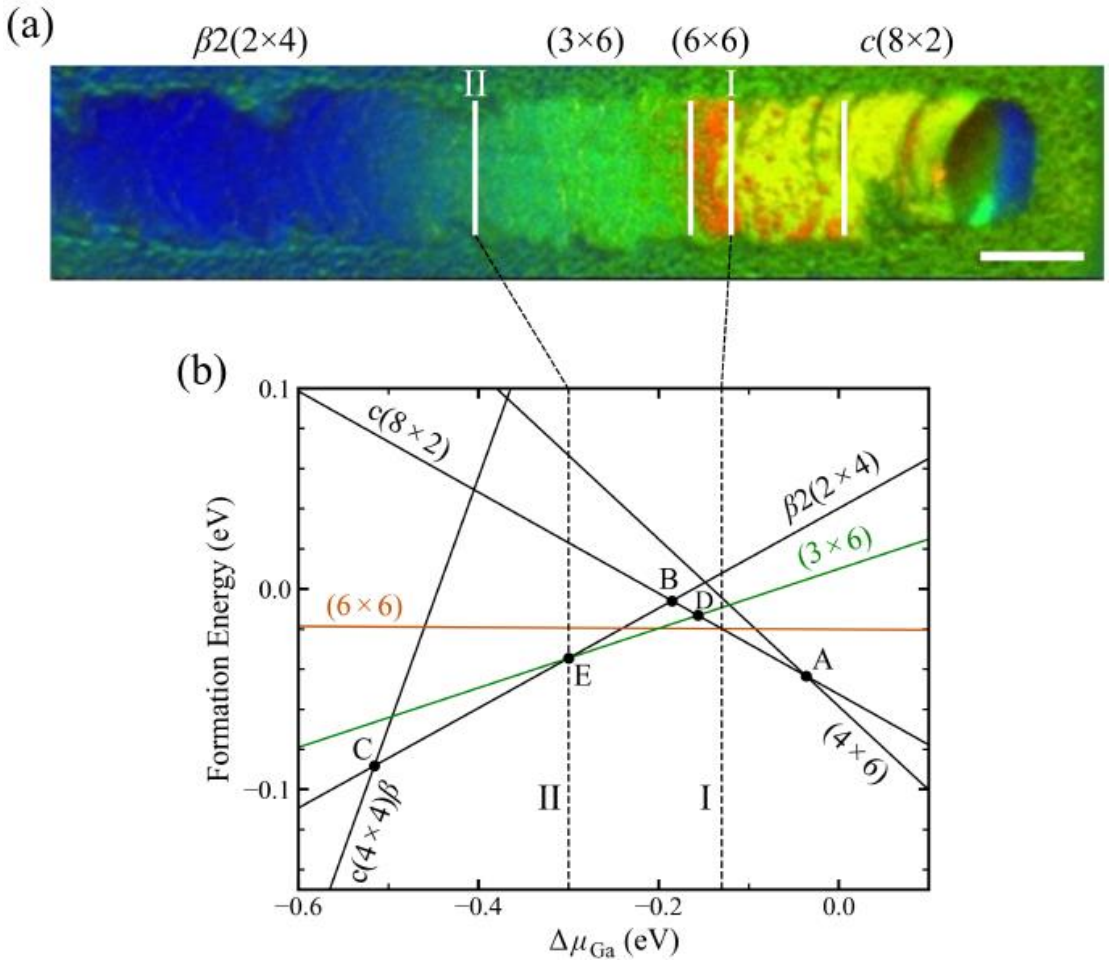

Figure 8. (a) SEDF LEEM image where blue, green, orange and yellow correspond to 2(2×4), (3×6), (6×6) and c(8×2) phases, respectively. This map clearly resolves boundary I in more detail, revealing a stable (6×6) region and phase intermixing between the (6×6) and c(8x 2) phases. (b) Existing DFT calculation of the GaAs (001) phase diagram [29], [33], plotting formation energy with respect to the β2(2×4) surface per (1×1) unit cell against relative Ga chemical potential $\Delta\mu_{Ga}$ with respect to Ga bulk at 0 K. From the image in panel (a) we can approximately superimpose the formation energy lines of the (3×6) and (6×6) phases as shown. The dashed vertical lines are the chemical potential values defining boundaries I and II. The scale bar in (a) is 2 μm. (Figure adapted from [34] with permission from publisher).

In summary, we have developed this technique with our unique LEEM-MBE equipment with which we are able to apply MBE fluxes and characterise the surface in situ using LEEM. We have combined SEDFLEEM imaging and μLEED

techniques to approximately map the GaAs(001) phase diagram around liquid Ga droplets using the approach of droplet epitaxy in just few microns at a fixed temperature. This is highly complementary to existing DFT calculations. The method reflects phase stability at finite temperature and so naturally incorporates the influence of entropy. We foresee the possibilities of DEPPs to be used for surface free energy mapping for a wide range of technologically important III-V materials, including nitrides. We have demonstrated the capabilities of SEDFLEEM for the in-situ study of kinetical processes involved in growth.

References:

[1] Z. Y. Zhou, C. X. Zheng, W. X. Tang, D. E. Jesson, and J. Tersoff, "Congruent evaporation temperature of GaAs(001) controlled by As flux," *Appl. Phys. Lett.*, vol. 97, no. 121912, pp. 1–3, 2010.

[2] J. Tersoff, D. E. Jesson, and W. X. Tang, "Decomposition controlled by surface morphology during Langmuir evaporation of GaAs," *Phys. Rev. Lett.*, vol. 105, no. 3, pp. 1–4, 2010.

[3] Z. Y. Zhou, C. X. Zheng, W. X. Tang, J. Tersoff, and D. E. Jesson, "Origin of quantum ring formation during droplet epitaxy," *Phys. Rev. Lett.*, vol. 111, no. 3, pp. 1–5, 2013.

[4] J. G. Keizer, J. Bocquel, P. M. Koenraad, T. Mano, T. Noda, and K. Sakoda, "Atomic scale analysis of self assembled GaAs/AlGaAs quantum dots grown by droplet epitaxy," *Appl. Phys. Lett.*, vol. 96, no. 062101, pp. 1–4, 2010.

[5] J. Wu *et al.*, "Self-assembly of multiple stacked nanorings by vertically correlated droplet epitaxy," *Adv. Funct. Mater.*, vol. 24, no. 4, pp. 530–535, 2014.

[6] P. Boonpeng, W. Jevasuwan, S. Panyakeow, and S. Ratanathammaphan, "Fabrication of self-assembled InGaAs squarelike nanoholes on GaAs(001) by droplet epitaxy," *Jpn. J. Appl. Phys.*, vol. 49, no. 4 PART 2, 2010.

[7] N. Ha *et al.*, "Droplet epitaxy growth of telecom InAs quantum dots on metamorphic InAlAs / GaAs (111) A," *Jpn. J. Appl. Phys.*, vol. 54, p. 04DG07, 2015.

[8] S. Huang, Z. Niu, Z. Fang, H. Ni, Z. Gong, and J. Xia, "Complex quantum ring structures formed by droplet epitaxy," *Appl. Phys. Lett.*, vol. 89, no. 3, pp. 10–13, 2006.

[9] J. Wu and Z. M. Wang, "Droplet epitaxy for advanced optoelectronic materials and devices," *J. Phys. D. Appl. Phys.*, vol. 47, no. 17, p. 173001, 2014.

[10] T. Mano, K. Watanabe, S. Tsukamoto, H. Fujioka, M. Oshima, and N. Koguchi, "New self-organized growth method for InGaAs quantum dots on GaAs(001) using droplet epitaxy," *Japanese J. Appl. Physics, Part 2 Lett.*, vol. 38, no. 9 A/B, pp. 2–5, 1999.

[11] C. Somaschini, "PhD Thesis: Development of advanced GaAs nanostructures by Droplet Epitaxy," Universitá degli Studi di Milano-Bicocca, 2010.

[12] Z. Y. Lu *et al.*, "Impact of growth parameters on the morphology and microstructure of epitaxial GaAs nanowires grown by molecular beam epitaxy," *J. Alloys Compd.*, vol. 580, pp. 82–87, 2013.

[13] S. Bietti *et al.*, "Fabrication of GaAs quantum dots by droplet epitaxy on Si/Ge virtual substrate," *IOP Conf. Ser. Mater. Sci. Eng.*, vol. 6, no. 001, p. 012009, 2009.

[14] A. W. Wood, K. Collar, J. Li, A. S. Brown, and S. E. Babcock, "Droplet-mediated formation of embedded GaAs nanowires in MBE GaAs $_{1-x}$ Bi $_{x}$ films," *Nanotechnology*, vol. 27, no. 11, p. 115704, 2016.

[15] C. Heyn and D. E. Jesson, "Congruent evaporation temperature of molecular beam epitaxy grown GaAs (001) determined by local droplet etching," *Appl. Phys. Lett.*, vol. 107, no. 16, pp. 10–14, 2015.

[16] D. P. Kumah, S. Shusterman, Y. Paltiel, Y. Yacoby, and R. Clarke, "Atomic-scale mapping of quantum dots formed by droplet epitaxy.," *Nat. Nanotechnol.*, vol. 4, no. 12, pp. 835–838, 2009.

[17] J. Bocquel, A. D. Giddings, T. Mano, T. J. Prosa, D. J. Larson, and P. M. Koenraad, "Composition profiling of GaAs/AlGaAs quantum dots grown by droplet epitaxy," *Appl. Phys. Lett.*, vol. 105, no. 153102, pp. 1–4, 2014.

[18] Z. Gong, Z. C. Niu, S. S. Huang, Z. D. Fang, B. Q. Sun, and J. B. Xia, "Formation of GaAs / AlGaAs and InGaAs / GaAs nanorings by droplet molecular-beam epitaxy," *Appl. Phys. Lett.*, vol. 87, no. 093116, 2005.

[19] C. X. Zheng *et al.*, "Mapping Surface Free Energy of GaAs(001) during Droplet Epitaxy," *Phys. Rev. Mater.*, vol. 3, no. 124603, pp. 1–9, 2019.

[20] T. Mano and N. Koguchi, "Nanometer-scale GaAs ring structure grown by droplet epitaxy," *J. Cryst. Growth*, vol. 278, pp. 108–112, 2005.

[21] C. Somaschini, S. Bietti, N. Koguchi, and S. Sanguinetti, "Shape control via surface reconstruction kinetics of droplet epitaxy nanostructures," *Appl. Phys. Lett.*, vol. 97, no. 203109, pp. 3–5, 2010.

[22] S. Huang, Z. Niu, Z. Fang, H. Ni, and Z. Gong, "Complex quantum ring structures formed by droplet epitaxy," *Appl. Phys. Lett.*, vol. 89, no. 031921, 2006.

[23] M. Yamagiwa *et al.*, "Self-assembly of laterally aligned GaAs quantum dot pairs," *Appl. Phys. Lett.*, vol. 89, no. 113115, 2006.

[24] T. Mano *et al.*, "Self-Assembly of Concentric Quantum Double Rings," *Nano Lett.*, vol. 5, no. 3, pp. 425–428, 2005.

[25] C. Somaschini, S. Bietti, N. Koguchi, and S. Sanguinetti, "Fabrication of Multiple Concentric Nanoring Structures," *Nano Lett.*, vol. 9, no. 10, pp. 3419–3424, 2009.

[26] J. Grotendorst, N. Attig, S. Bl, and A. Simulation, *Multiscale Simulation Methods in Molecular Sciences*. 2009.

[27] J. Y. Tsao, *Materials Fundamentals of Molecular Beam Epitaxy*. 1993.

[28] L. Daweritz, "Surface characterization by RHEED techniques during MBE growth of GaAs and AlxGa1-xAs," *Superlattices Microstruct.*, vol. 9, no. 2, pp. 141–145, 1997.

[29] A. Ohtake, P. Koćan, K. Seino, W. G. Schmidt, and N. Koguchi, "Ga-rich limit of surface reconstructions on GaAs(001): Atomic structure of he (4 × 6) phase," *Phys. Rev. Lett.*, vol. 93, no. 26 I, pp. 4–7, 2004.

[30] J. Tersoff, D. E. Jesson, and W. X. Tang, "Running Droplets of Gallium from Evaporation of Gallium Arsenide," *Science (80-.).*, vol. 324, no. 5924, pp. 236–238, 2008.

[31] C. X. Zheng, J. Tersoff, W. X. Tang, A. Morreau, and D. E. Jesson, "Novel GaAs

surface phases via direct control of chemical potential," *Phys. Rev. B*, vol. 93, no. 19, p. 195314, 2016.

[32] E. Bauer, *Surface microscopy with Low Energy Electrons*. Springer, 2014.

[33] A. Ohtake, "Surface reconstructions on GaAs(001)," *Surf. Sci. Rep.*, vol. 63, pp. 295–327, 2008.

[34] C. X. Zheng *et al.*, "Mapping the Surface Phase Diagram of GaAs(001) using Droplet Epitaxy," *Phys. Rev. X*, vol. 3, no. 124603, pp. 1–9, 2019.

[35] "The theoretical model has been developed by Kennet Rodriguez Hannikainen." .

[36] J. Tersoff, M. D. Johnson, and B. G. Orr, "Adatom Densities on GaAs : Evidence for Near-Equilibrium Growth," *Phys. Rev. Lett.*, vol. 78, no. 2, pp. 282–285, 1997.

[37] F. W. J. Olver, D. W. Lozier, R. F. Boisvert, and C. W. Clark, *NIST Handbook of Mathematical Functions*. 2010.

[38] Y. R. Niu, J. Pereiro, D. Gomez, and D. E. Jesson, "Selected energy dark field imaging using low energy electrons for optimal surface phase discrimination," *Ultramicroscopy*, vol. 200, no. February, pp. 79–83, 2019.

Chapter 6: Phase coexistence in GaAs (001)

In this chapter, we have analysed the phase coexistence of the (6×6) phase and the c(8×2) for GaAs (001) and compared the results with a pre-existing theory for first order transitions used in Si. The results indicate that the theory used for Si can be used to describe more complex systems like GaAs.

Introduction to phase coexistence for GaAs

The study of surface phase transitions in semiconductors has been a matter of study during the past years for its relevance for setting the thermodynamic boundaries during growth. In the literature, several articles can be found regarding first order surface phase transformations in Si [1]–[6] and for GaAs [7]–[9]. For two phases coexisting on the surface the concept of thermodynamic stability plays an important role for determining the phase that will dominate at each temperature, as well as the boundaries for the phase transition between the phases. As a rule, the most thermodynamically stable phase will be the one with the smallest surface free energy.

Phase transitions can be mainly classified as first-order transitions (also referred as discontinuous transitions) and second-order transitions (also known as continuous transitions).

A first order phase transition involves a discontinuous jump in some variable. This transition occurs when the thermodynamic properties of a substance change abruptly. Transitions have discontinuities in the first derivatives of G, these discontinuities are expressed in Eq. 1. In this case, a completely specified amount of heat, is released or absorbed per unit mass. This change in entropy corresponds to the latent heat $L = T\Delta S$ [10]. The discontinuous first-order phase transitions depend on the microscopic details of the system. First-order phase transitions include evaporation and condensation, melting and solidification, sublimation

and condensation to the solid phase, and certain structural transformations in solids. The discontinuous property is called the order parameter. The order parameter increases on moving deeper into the ordered phase and measures the degree of order as the phase transition advances. The order parameter is physically observable, and it is often related to a first derivative of G. Each phase transition has its own order parameter [11].

$$\left(\frac{\partial G}{\partial T}\right)_P = -S \qquad \left(\frac{\partial G}{\partial P}\right)_T = V \qquad \text{Eq. 1}$$

In a second-order phase transition, different variables change continuously, and heat is neither released nor absorbed. Continuous transitions are those in which some changes occur more gently than a discontinuous jump in the basic variables. The positions in phase diagrams at which we see continuous transitions are referred to as critical points.

The phenomenon of phase coexistence has been reported for the Si (111) for the (7×7) to (1×1) transition [12] and for Si (100) for the (1×2) to (2×1) transition [13]. In both cases strain was reported to be the cause of the coexistence. Hannon et al. developed a study of the (7×7) to (1×1) transition in Si(111) and they concluded that phase coexistence was due to long-range elastic and electrostatic domain interactions. GaAs is, in principle, a more complex system than Si as it is a bi-atomic system. For GaAs, phase coexistence between phases has also been reported by several groups [14], [15]. These studies have led to significant efforts to understand and control the stability of surface phases as a function of the experimental conditions.

In our case, we have dedicated our work to investigate the transition between c(8×2) and (6×6) for GaAs (001) comparing the results with those applicable to Si. Some studies have been devoted to the study of the mechanisms behind this particular transition [16], [17], and some of these reports, have analysed the coexistence of the (6×6) and the c(8×2) [18]–[21]. Some of these reports agree

on the necessity to take these studies further to unravel the relative importance of elastic and electrostatic effects, or strain to phase coexistence of (6×6) and c(8×2). The range of temperatures for this transition have been represented by Zheng et al. in Figure 1.

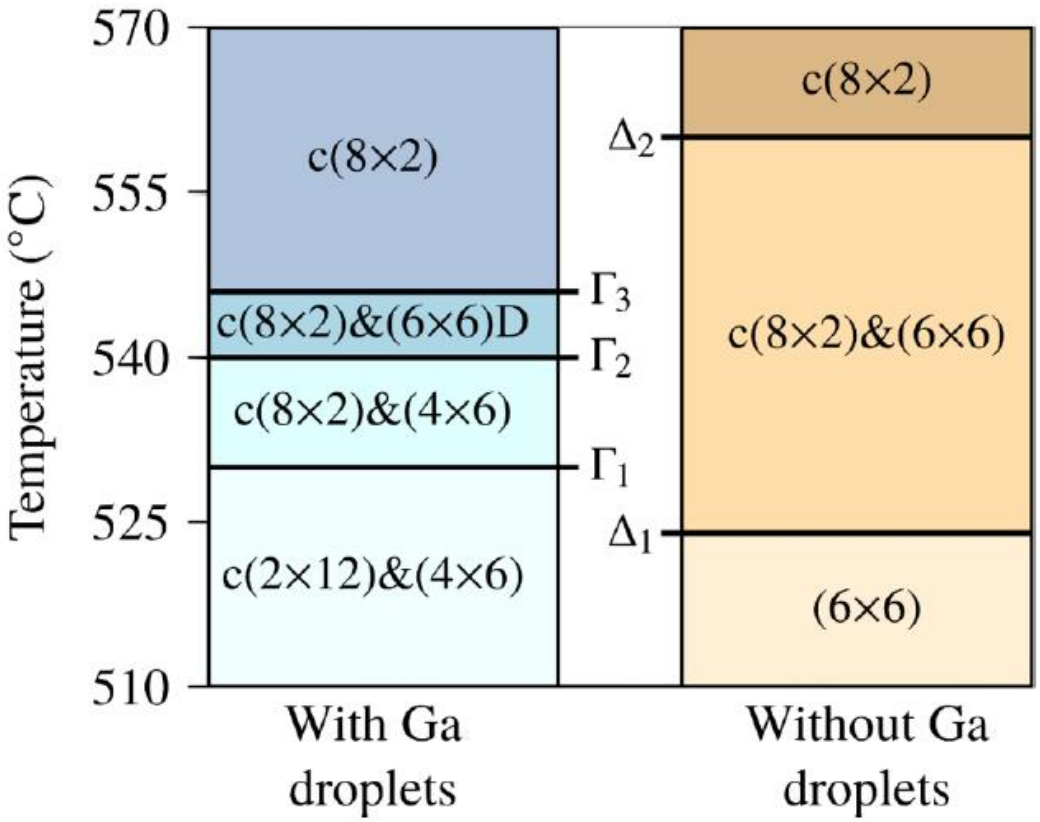

Figure 1. Phase diagram with and without droplets deduced from LEEM imaging and μLEED as a function of temperature. (Figure adapted from [21] with permission from publisher).

Following the job carried out by Zheng et al., we have analysed quantitatively the coexistence regime between the (6×6) and the c(8×2) using our unique technique of LEEM-MBE. We set off trying to mimic the conditions that led to D. Jesson et al. to the conclusions they presented in their work, to analyse the mechanisms behind coexistence between these two phases. We have compared these results in GaAs to the work carried out in Si by Hanon et al. [22] concluding that the

mechanisms behind phase coexistence for a GaAs bi-atomic system are very similar to the ones described for the mono-atomic system of Si.

(6×6) and c(8×2) coexistence vs temperature

Firstly, we prepared a GaAs (001) following the procedure and we generated Ga droplets to planarize the surface as described in "sample preparation" in chapter 3. After creating an atomically flat surface, we commenced to investigate the c(8×2) to (6×6) transition. We cooled down the sample from the c(8×2) regime up to ~560°C which is the transition temperature between the two phases [21]. The pattern appears to be thermodynamically stable as we checked that its shape remains constant during a period of time of 3-4 hours. The phase coexistence between c(8×2) and the (6×6) can be observed in Figure 2. The black region corresponds to a (6×6) reconstruction while the rest of the surface corresponds to a c(8×2). The rest of the ununiform lines correspond to the atomically-high step edges.

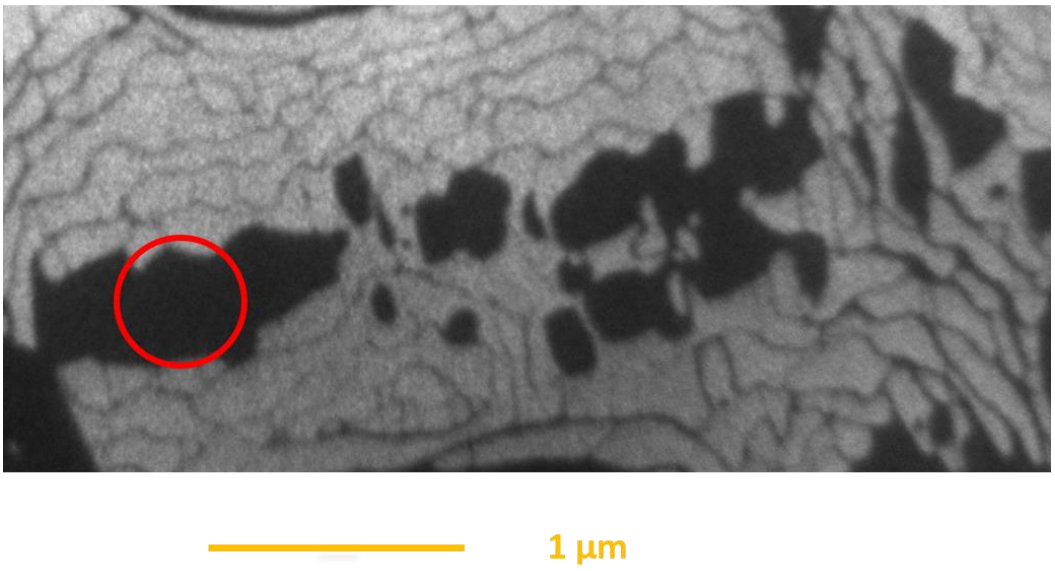

Figure 2. LEEM image in BF at around 560°C. The black areas correspond to the (6×6) and the bright areas are c(8×2). The surface energy was around 8.5 eV.

Diffraction measurements at the surface were carried out in order to study the nature of the two phases. To do this, undertook μLEED measurements. The red circle in Figure 2, indicates the position where the illumination aperture was placed. The diffraction pattern that we obtained is a mixture between c(8×2) and (6×6). A representation of this mixed pattern is displayed in Figure 3.

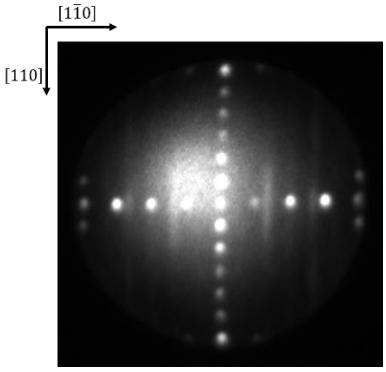

Figure 3. Diffraction pattern for c(8×2) and the (6×6) at 12 eV.

In the pattern, a (4×6) pattern is illustrated. This pattern arises from the superimposition of the c(8×2) and the (6×6). The 4x periodicity characteristic of the c(8×2) can be seen in the 4 dots on the horizontal orientation. This appearance of a (4×1) reconstruction for the c(8×2), seems to be given by a one-dimensional disorder [19]. The 6x periodicity is shown in the form of vertical stripes. These stripes in the diffraction pattern also seem to indicate a slight disorder in the crystalline structure. In the vertical orientation, the x6 periodicity is represented by 6 dots. The (0,1) point is shared between both phases. The (1,0) has the two x4 spots in $(1, \frac{1}{4})$ and $(1, -\frac{1}{4})$ characteristics of the c(8×2).

In order to allow phase discrimination, SEDFLEEM technique was utilised. We run an I-V scan in diffraction using μLEED. We varied the surface energy of the electrons by tuning the Start Voltage (See Chapter 3) in diffraction mode. Figure 4 was then created. It can be observed how, at high energies, the c(8×2) dominates the pattern, whereas at lower energies, the (6×6) shines brighter. The small circle in red in Figure 4 a), indicates the point of the reciprocal lattice that

was filtered for the identification of the (6×6). The energy selected for the (6×6) is around 5 eV, where this phase has its peak of intensity.

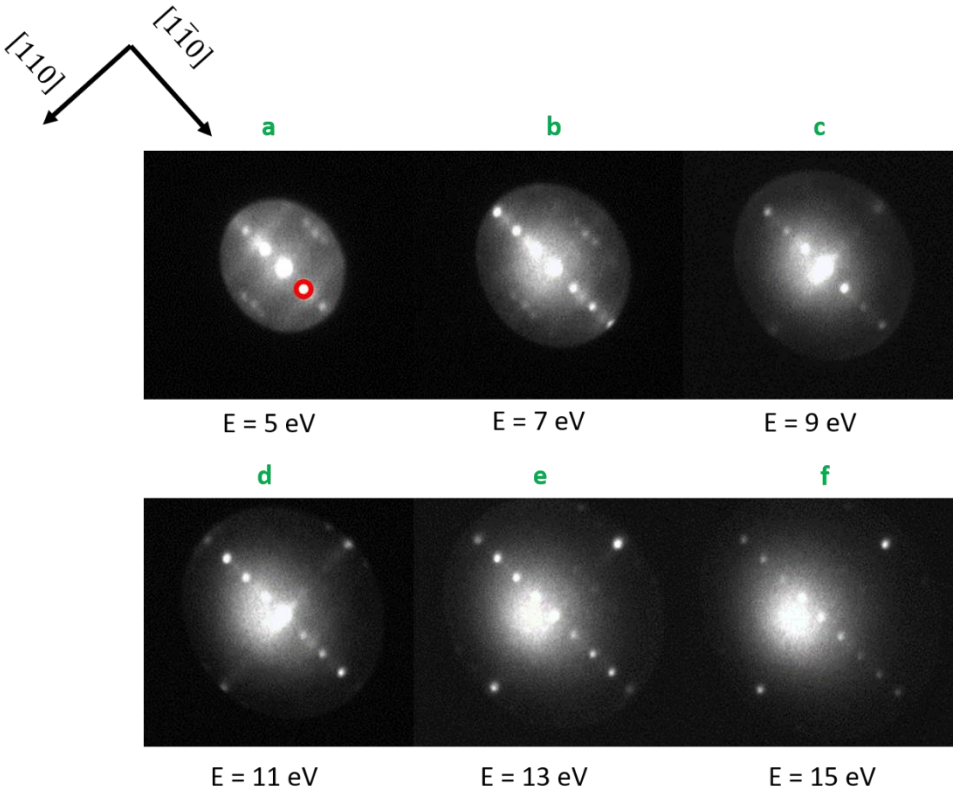

Figure 4. Different diffraction patterns for the c(8×2) to (6×6) coexistence regime at different energies.

The coverage ratio of these phases is different at different temperatures. We investigated the transition varying the temperature slightly, within the range presented in the literature [21]. In Figure 5, a representation of the phase coexistence of the c(8×2) and (6×6) at different temperatures is shown. In these images we can regard how the diffraction pattern is much closer to a pure (6×6) pattern at lower temperatures, and closer to a pure c(8×2) pattern at higher temperatures. We can also observe how the coverage of the (6×6) on the c(8×2) phase changes noticeably with temperature. For all the cases, we assume a stable coexistence between phases since the coverage is not affected by time.

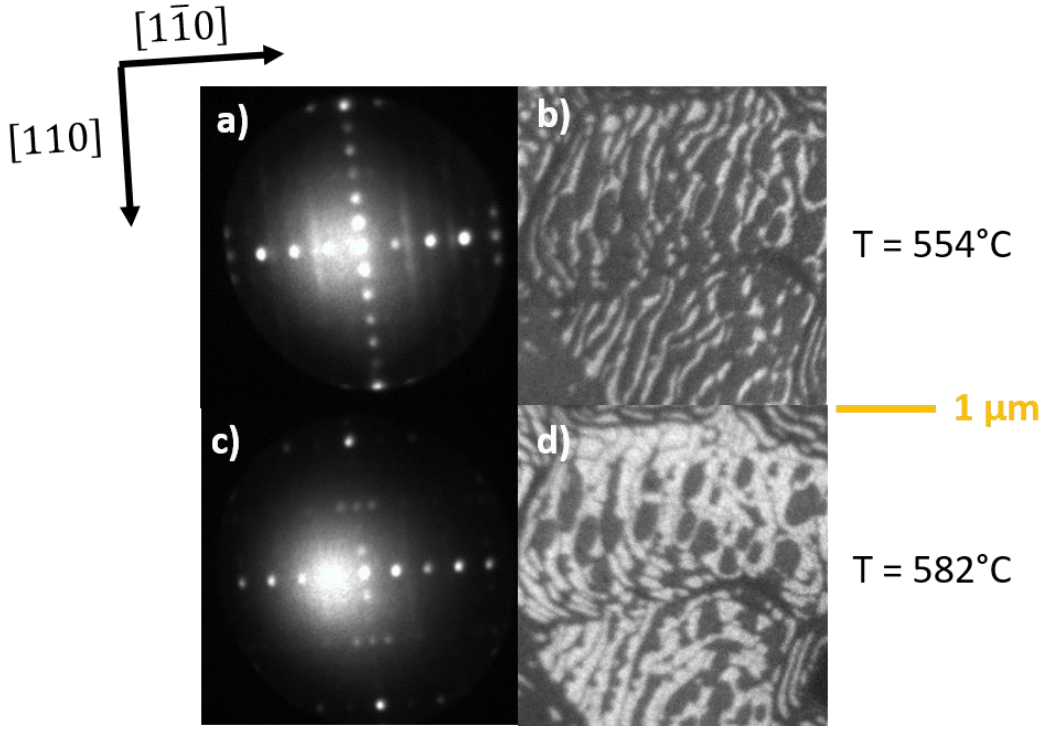

Figure 5. Set of different diffraction patterns at different temperatures with different coverages of c(8×2) and (6×6).

For further investigations, we alternated LEEM mode (SEBFLEEM and SEDFLEEM) and µLEED to monitor the c(8×2) to (6×6) transition over a certain range of temperatures. The energy of the electrons at the surface was optimised for the best contrast. Figure 6 shows this transition over different temperatures combining LEEM and µLEED. It was noticed that the coverage of (6×6) in c(8×2) was changing conspicuously over temperature.

We then decided to quantify the coverage during the transition. We wanted to know what percentage of (6×6) on the c(8×2) was present in the surface for each temperature. In order to achieve this, we varied the temperature of the surface in very little steps to allow more data points to be obtained. The process was very slow since we needed to make sure the phase was always stable. This is of high importance for the thermodynamics of the transition. Under these conditions, Figure 7 was then created.

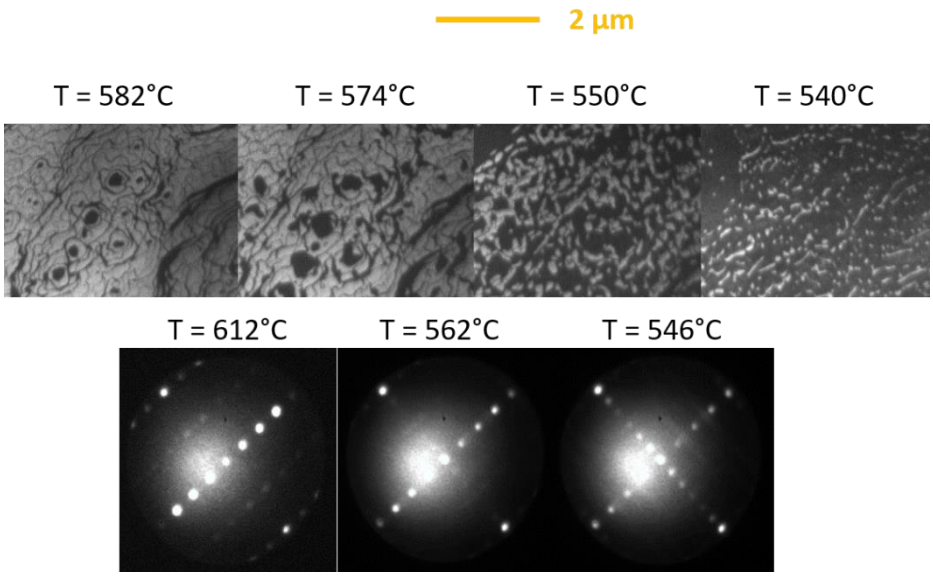

Figure 6. c(8×2) to (6×6) transition combining µLEED and LEEM.

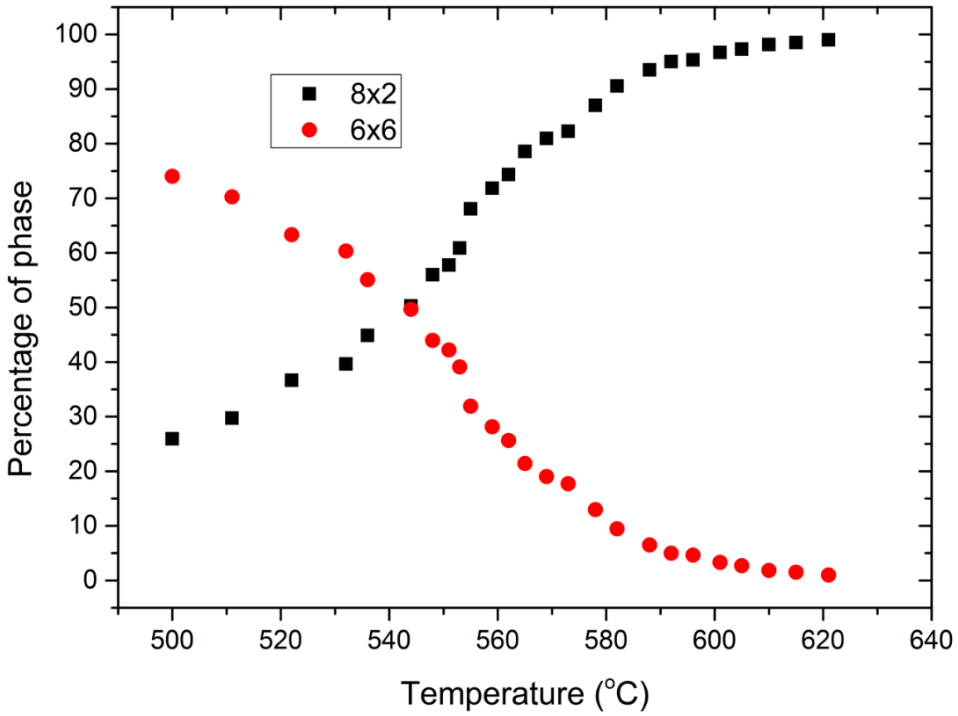

Figure 7. Analysis of coverage of c(8×2) and (6×6) on GaAs (001) surface at different temperatures.

The analysis of the coverage over temperature indicated that the (6×6) to c(8×2) is a wide range transition. T_0 was then defined as the temperature where the coverage is 50% for both phases. This parameter was taken as 550°C. Above 570°C, we noticed that the (6×6) was not stable anymore. This metastability of the (6×6) patches over the surface was detected for all the temperatures above 570°C. This mechanism is developed with detail in chapter 7. Below 570°C, we observed that the (6×6) patches were stable and there was a phase coexistence between the two phases over a wide range of temperatures.

In order to check the stability of the phases, we demonstrated reproducibility and reversibility of the process. We run two sets of experiments and we observed how the transition was roughly the same when heating up the material or when cooling it down. However, some hysteresis effect when cooling down was detected, which may be due to the (6×6) pinning to the steps. Examples of this reversibility can be seen in Figure 8.

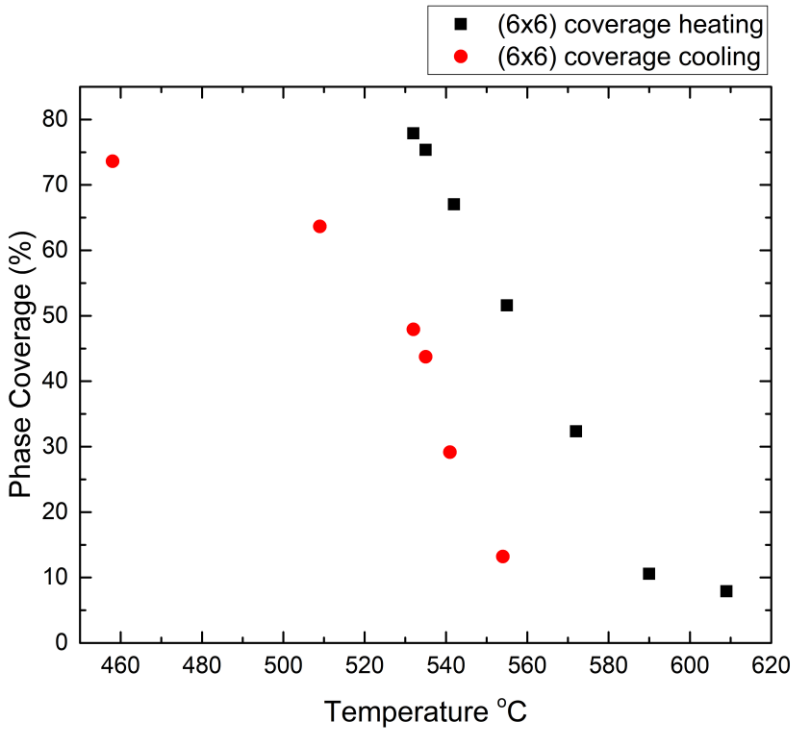

Figure 8. Hysteresis process for (6×6) coverage on GaAs (001).

We then intended to match up this theory with other theories developed regarding phases coexistence and phases interactions. According to David Vanderbilt, two different types of long-range interactions have been defined for two surface phases: **elastic interactions (C_λ),** derived from difference in the surface stress for each phase; and **electrostatic interactions (C_φ),** derived from the difference in work functions for each phase. The result for the total interaction between two surface phases (C_T) is expressed in Eq. 2. [23]

$$C_T = C_\varphi + C_\lambda \qquad \text{Eq. 2}$$

Where C_φ is defined as $C_\varphi = \frac{\Delta\varphi^2}{8\pi^2}$ in electrostatic units. $\Delta\varphi$ is the difference in work function. C_λ is determined as $C_\lambda = \left({\lambda_m}^2\right)\frac{(1-\nu^2)}{\pi Y}$, where λ_m is the difference in surface stress between the two phases, ν is the Poisson's ratio, and Y is Young's modulus.

Hanon et al. followed this theory and applied it to the analysis of a phase coexistence on Si (111) [22]. They concluded that the elastic interactions C_λ dominate the boundary interaction, and the parameters needed for its calculation were much easier to obtain neglecting electrostatic interactions. Electrostatic interactions can be neglected when the difference in work function for the two phases is small enough. For large work function differences, the electrostatic term plays an important role. They approximated the electrostatic interactions using the formulas derived for metals, and presented the energy per unit area as a function of the asymmetry parameter p. This parameter gives an idea of the coverage of each phase, and for the case of Si (111) it corresponds to $p = \left(\frac{2w}{L} - 1\right)$. Where w is defined as the width of the 7x7 reconstruction domain and L is the length of the terrace. For $p = 1$, the 7x7 would cover the whole surface whereas for $p = -1$, the 1x1 reconstruction would completely dominate. The energy per unit are as a function of p given by Hanon et al is described on Eq. 3.

$$E = \frac{C_0}{L} + \frac{\Delta S(T - T_0)p}{2} - \frac{2C_T}{L}\ln\left[\frac{L}{\pi a}\cos\left(\frac{p\pi}{2}\right)\right] + \frac{C_d}{L^2}\tan\left(\frac{p\pi}{2}\right) - \frac{8C_r}{L^3}\left[\frac{1}{(1+p)^2} + \frac{1}{(1-p)^2}\right] \quad \text{Eq. 3}$$

C_0 includes the formation energies of the steps and phase boundaries. $\Delta S(T - T_0)$, corresponds to the difference in surface free energy between the two phases. ΔS is taken as the difference in entropy. Long-range interactions are defined by three different terms. C_T represents the interaction at the phase boundaries between elastic and/or electrostatic monopoles. C_d serves as the long-range interaction between the monopoles and the force dipoles at both step and terrace phase boundaries. The C_r term represents a short-range repulsion between the phase boundaries [22].

Following Eq. 3, if we calculate $\frac{dE}{dp} = 0$ we obtain an expression for p as a function of T. Hanon et al. highlighted how for wide terraces near T_0, C_r and C_d have a small contribution. This leads to Eq. 4. In this model described by Hanon et al. for Si (111), the parameter p is an indirect quantification of the coverage of each phase [22].

$$\tan\left(\frac{p\pi}{2}\right) \approx -\frac{L\Delta S}{2\pi C_T}(T - T_0) \quad \text{Eq.4}$$

Following this theory for Si (111), we have tried to reproduce the same theory for our binary system of GaAs (001). In our case, we have taken p as the coverage ratio between the two phases (6×6) and c(8×2). We have reproduced this theory and compare the two systems. The result is represented in Figure 9. Figure 9a, corresponds to the results presented by Hanon et al. for Si (111). Figure 9b typifies our case for GaAs (001). For GaAs, the range of temperatures seems to be slightly higher than for Si. Other than that, we observe that the theory for GaAs follows a similar behaviour than the one for Si (111).

These results indicate that phase coexistence for a complex system like GaAs can be treated as a first-order phase transition and that elastic interactions can be used to model the mechanisms behind this transition. The similarities in the trends for both systems represented in Figure 9 demonstrate that GaAs phase transitions behave similarly to Si phase transitions, making the bi-atomic system much easier to model.

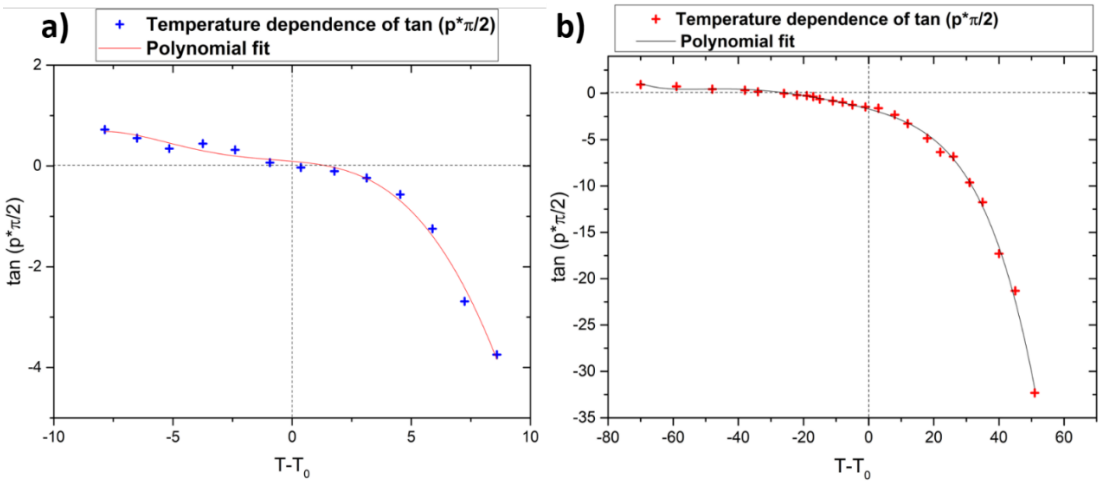

Figure 9. a) Adaptation from Hanon et al. [22] of the representation of the $tan\left(\frac{p\pi}{2}\right)$ as a function of the temperature for the (7×7) and (1×1) coexistence for Si (111). b) Representation of $tan\left(\frac{p\pi}{2}\right)$ as a function of temperature for the (6×6) and c(8×2) coexistence in GaAs (001).

(6×6) and c(8×2) coexistence vs μ_{Ga}

The chemical potential at the surface limits what is the stable phase for given conditions. Ultimately, varying the temperature implies a variation of the μ_{Ga} on the surface. Until now, different coverage ratios of c(8×2) and (6×6) have been observed at different temperatures. In order to investigate further the phenomenon of coexistence of the (6×6) and the c(8×2), we used the approach of droplet epitaxy to demonstrate that we can also achieve coexistence of the two

phases just by using a Ga-droplet as a source of Gallium and a planar trail. As it has been described in chapter 3, having a gradient of μ_{Ga} across the trail allows us to have different values of μ_{Ga} in few microns. This could be equivalent to temperature variation, except that we can have a wide range of values for μ_{Ga} in a small surface.

Figure 10 shows a (6×6) SEDFLEEM image of a Ga droplet with a planar trail. Along the trail, the value of μ_{Ga} changes as a function of the distance to the droplet. The bright phase corresponds to the (6×6) phase while the dark phase corresponds to the c(8×2).

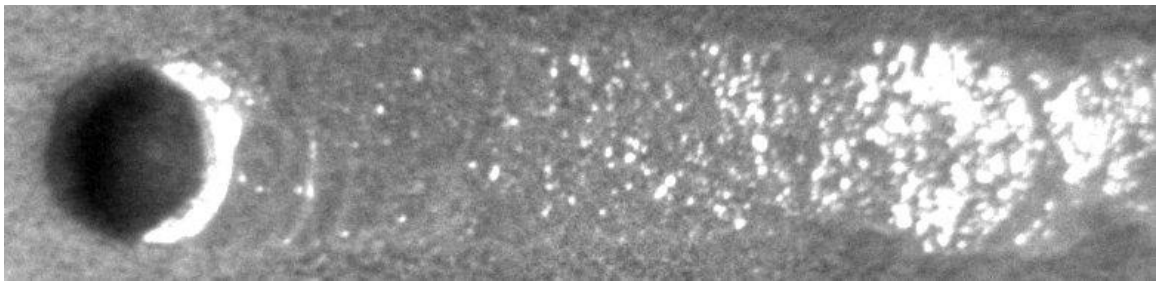

Figure 10. (6×6) SEDFLEEM image of Ga droplet with a planar trail on a GaAs (001) surface.

Using this approach, we have quantified the variation of the (6×6) coverage as a function of the distance to the droplet. At different points of the trail, the chemical potential of Ga will vary with respect to the droplet. The Ga droplet provides a constant profile of Ga to the trail, and the distance to the droplet is directly related with the μ_{Ga}. For this purpose, Figure 11 has been generated by measuring the coverage of different sections along the trail.

The chemical potential of Ga varies as a function to the distance to the droplet, which will be equivalent to changes in temperature. In Figure 10 it can be noticed how the (6×6) coverage decreases nearer to the droplet. At further distance to the droplet, the value of the Ga chemical potential is less, and so the coverage of

(6×6) will this is equivalent to increasing the temperature. Both actions are equivalent, and conclusively suppose a change in μ_{Ga}.

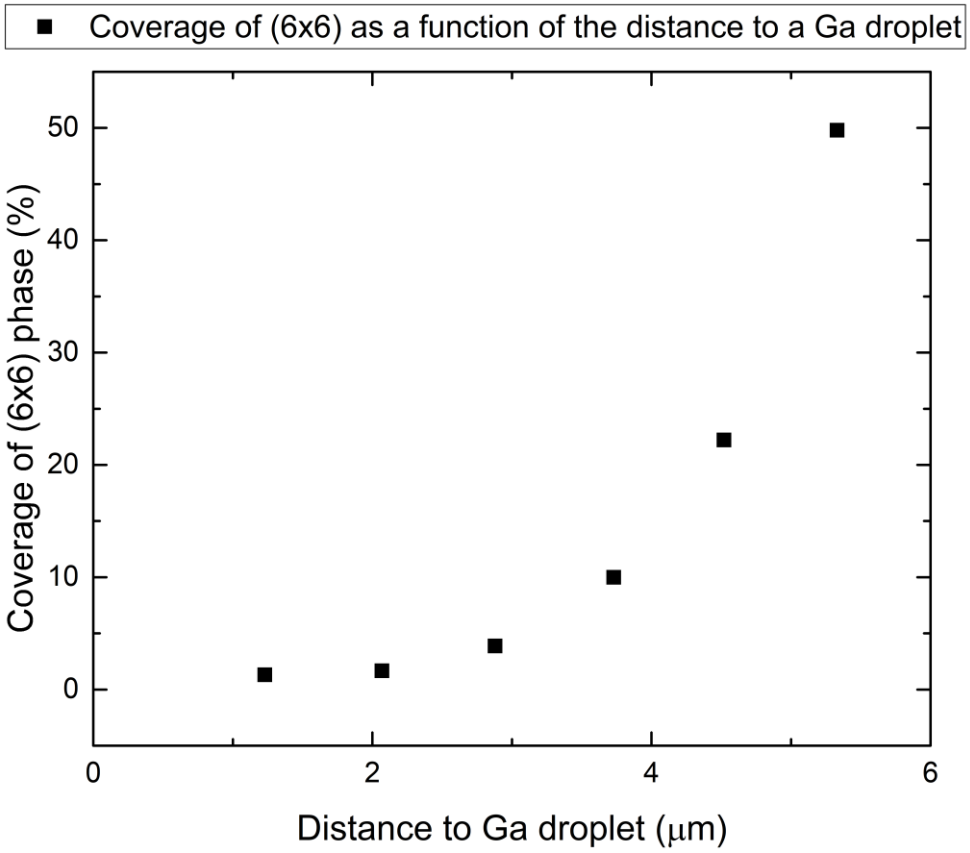

Figure 11. Variation of (6×6) coverage as a function of the distance to the droplet.

Finally, Figure 12 has been generated. In this picture, the same parameter of the $\tan\left(\frac{p\pi}{2}\right)$ has been presented, in this case, as a function of the distance to the droplet. It can be observed how the graph follows once again the tendency shown by Hanon et al. for Si, reaffirming that the phase transitions at both systems can be treated with the same theory as they both seem to be first-order transitions. This behaviour simplifies the GaAs system bi-atomic system for the studies of phase transformations. We expect similar behaviours to occur for other III-V systems of technological interest such as GaN or GaP.

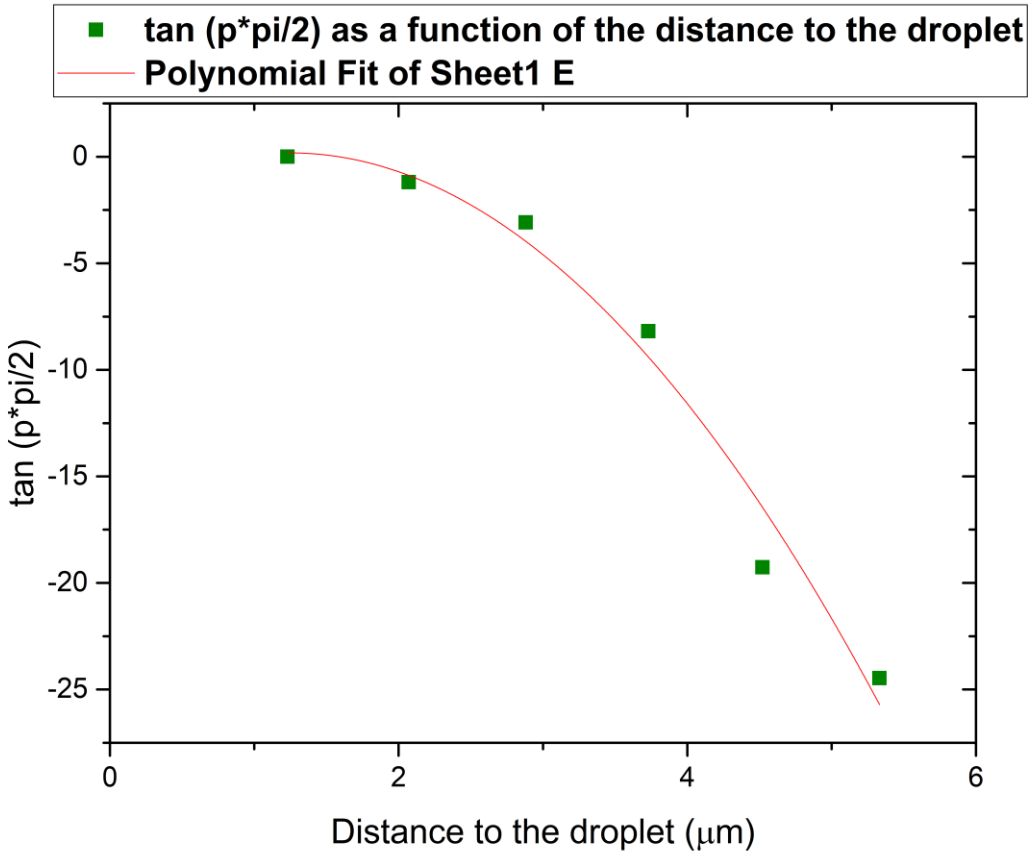

Figure 12. tan (p*pi/2) as a function of the distance to the droplet.

To sum up, we have analysed the phase coexistence of the (6×6) phase and the c(8×2) for GaAs (001). We have demonstrated that the two phases are thermodynamically stable over a period of time of 4 hours for a range of temperatures, and we have quantified the coverage of each phase as a function of temperature. We have also demonstrated the reversibility of the transition. We have also quantified this phenomenon using droplet epitaxy and we have compared this theory to the one developed by Hanon et al. for (7×7) and (1×1) phases for Si (111). We have demonstrated that the theory developed for Si is applicable to GaAs.

References:

[1] R. M. Tromp, M. Mankos, M. C. Reuter, A. W. Ellis, and M. Copel, "A New Low Energy Electron Microscope," *Surf. Rev. Lett.*, vol. 05, no. 06, pp. 1189–1197, 2003.

[2] K. T. and K. Y. Yasumasa TANISHIRO, "On the phase transition between the (7 x 7) AND (1 x 1) structures of Silicon (111) surface studied by Reflection Electron Microscopy," *Ultramicroscopy*, vol. 11, pp. 95–102, 1983.

[3] Y. Asaoka, T. Kanebishi, N. Sano, and T. Kaneko, "In situ control of the desorption process of GaAs surface native oxide by direct Ga beam irradiation," *Molecular Beam Epitaxy, 2002 International Conference on*. pp. 111–112, 2002.

[4] N. Osakabe, K. Yagi, and G. Honjo, "Reflection electron microscope observations of dislocations and surface structure phase transition on clean (111) silicon surfaces," *Jpn. J. Appl. Phys.*, vol. 19, no. 6, pp. L309–L312, 1980.

[5] W. Telieps and E. Bauer, "The (7x7) - (1x1) phase transition on si(111)," *Surf. Sci.*, vol. 162, pp. 163–168, 1985.

[6] P. A. Bennett and M. W. Webb, "The Si(111) 7 × 7 TO '1 × 1' transition," *Surf. Sci.*, vol. 104, no. 1, pp. 74–104, 1981.

[7] W. G. Schmidt, F. Bechstedt, and J. Bernholc, "GaAs(001) surface reconstructions: geometries, chemical bonding and optical properties," *Appl. Surf. Sci.*, vol. 190, no. 1, pp. 264–268, 2002.

[8] V. V Preobrazhenskii, M. A. Putyato, O. P. Pchelyakov, and B. R. Semyagin, "Surface structure transitions on (001)GaAs during MBE," *J. Cryst. Growth*, vol. 202, pp. 166–169, 1999.

[9] L. Daweritz, "Surface characterization by RHEED techniques during MBE growth of GaAs and AlxGa1-xAs," *Superlattices Microstruct.*, vol. 9, no. 2, pp. 141–145, 1997.

[10] A. Schekochihin, "Phase transitions," 2011. [Online]. Available: https://www-thphys.physics.ox.ac.uk/people/AlexanderSchekochihin/A1/2011/handout13.pdf . [Accessed: 05-Aug-2019].

[11] L. P. Kadanoff, "More is the same; phase transitions and mean field theories," *J. Stat. Phys.*, vol. 137, no. 5, pp. 777–797, 2009.

[12] J. Chevrier, L. T. Vinh, and A. Cruz, "Phase transition on the Si(111) surface: a first order phase transition under strain?," *Surf. Sci.*, vol. 268, no. 1–3, 1992.

[13] E. Pehlke and J. Tersoff, "Nature of the Step-Height Transition on Vicinal Si(001) Surfaces," *Phys. Rev. Lett.*, vol. 67, no. 4, pp. 2193–2196, 1990.

[14] M. Pristovsek, T. Trepk, M. Klein, J.-T. Zettler, and W. Richter, "Dynamic study of the surfaces of (001) gallium arsenide in metal-organic vapor-phase epitaxy during arsenic desorption," *J. Appl. Phys.*, vol. 87, no. 3, p. 1245, 2000.

[15] S. Tsukamoto *et al.*, "Ga-rich GaAs[001] surfaces observed by STM during high-temperature annealing in MBE chamber," *MBE 2002 - 2002 12th Int. Conf. Mol. Beam Ep.*, vol. 251, pp. 113–114, 2002.

[16] M. Pristovsek *et al.*, "Gallium-rich reconstructions on GaAs(001)," *Phys. Status Solidi Basic Res.*, vol. 240, no. 1, pp. 91–98, 2003.

[17] M. Kuball, D. T. Wang, N. Esser, M. Cardona, J. Zegenhagen, and B. O. Fimland, "Microscopic structure of the GaAs(001)-(6 x 6) surface derived from scanning tunneling microscopy," *Phys Rev B Condens Matter*, vol. 51, no. 19, pp. 13880–13882, 1995.

[18] A. Ohtake, P. Koćan, K. Seino, W. G. Schmidt, and N. Koguchi, "Ga-rich limit of surface reconstructions on GaAs(001): Atomic structure of he (4 × 6) phase," *Phys. Rev. Lett.*, vol. 93, no. 26 I, pp. 4–7, 2004.

[19] A. Ohtake, "Surface reconstructions on GaAs(001)," *Surf. Sci. Rep.*, vol. 63, pp. 295–327, 2008.

[20] U. Resch-Esser *et al.*, "Surface quality and atomic structure of MBE-grown GaAs(100) prepared by the desorption of a protective arsenic layer," *Surf. Sci.*, vol. 352–354, pp. 71–76, May 1996.

[21] C. X. Zheng, J. Tersoff, W. X. Tang, A. Morreau, and D. E. Jesson, "Novel GaAs surface phases via direct control of chemical potential," *Phys. Rev. B*, vol. 93, no. 19, p. 195314, 2016.

[22] J. B. Hannon, F. J. Meyer zu Heringdorf, J. Tersoff, and R. M. Tromp, "Phase coexistence during surface phase transitions," *Phys. Rev. Lett.*, vol. 86, no. 21, pp. 4871–4874, 2001.

[23] D. Vanderbilt, "Phase segregation and work-function variations on metal surfaces: spontaneous formation of periodic domain structures," *Surf. Sci.*, vol. 268, pp. L300–L304, 1992.

Chapter 7: Surface phase metastability on GaAs (001)

In this chapter we have applied SEDFLEEM to analyse a metastable (6×6) present at any temperature at which Langmuir evaporation takes place, including the thermodynamically stable c(8×2) regime. The (6×6) reconstruction is observed to be associated with the generation of new terraces.

Introduction

Molecular Beam Epitaxy (MBE) is a technique for semiconductor growth (see chapter 1) that requires good control of physical parameters i.e. temperature and flux of impinging atoms. Ruling these parameters, leads to control in the atomic arrangement at the surface. A deep understanding of the way the atoms are organized at the surface during growth, is crucial for the thorough control of the interfaces and ultimately to optimise the growth of highly pure and defect-free structures.

It is well stablished then, that the phase reconstructions at the surface is a key factor that affects growth. In the literature, we can find many examples where different GaAs surface reconstructions have been investigated with detail [1]–[5]. Special attention deserves the work presented by Akihiro Ohtake in which he reviewed with exquisite detail a big number of the surface phase reconstructions on GaAs [6]. In this work, Ohtake used STM characterisation technique to reveal the atomic structure of different surface phases from Ga-rich to As-rich.

Prior to MBE growth, the atomic arrangement at the surface needs to be scrutinised, as this has a high influence in the quality of the grown material [7]–[11]. Along the years, many examples can be found in the literature in which the surface phase reconstructions are inspected prior to growth [12], via RHEED

commonly [13]–[19], but also using LEED [20], STM [21], [22], or even combining STM with RAS (Reflectance Anisotropy Spectrum) [23]. The phase reconstruction in which GaAs is usually grown is the As-rich (2×4) due to the fact that the material to grow on top of is the highest quality [24], and growers always provide evidences of such phase prior to growth. A much deeper discussion on the (2×4) phase reconstruction and its use for GaAs (001) growth has been already provided by Akihiro Ohtake [25]. Normally, when growing GaAs, the conditions for growth are always As-rich due to the low sticking coefficient of As.

Pashley and Haberen developed STM measurements of the (2×4) reconstruction highlighting that the understanding of this and other surface reconstructions is crucial to understand the atomic growth mechanisms. In this work, it is concluded that the study of the phase reconstructions is crucial as they play a critical role in both growth and the electronic properties of the GaAs(001) surface and how this will be ultimately useful in the fabrication of new device structures [26].

Akihiro Ohtake et al. provided a very good insight on the effects of the surface reconstructions on the formation of Ga-droplets on different surface reconstructions at a GaAs (001) surface [27]. They investigated this effect over three different phase reconstructions: (2×4), c(4×4)β, and the Ga-rich (4×6). They concluded that the atomic arrangement on the surface and the residual As pressures on MBE, have important effects on the diffusion of Ga atoms at the surface and this was impacting at a great level on the size and density of Ga droplets generated at the surface. They also confirmed that the initial deposition of Ga was modifying the As-rich surface reconstructions of (2×4) and c(4×4)β before the formation of Ga droplets, whereas Ga droplets were formed straightforwardly on the Ga-rich (4×6) surface.

In MBE-growth, during the nucleation of new structures, an impinging beam of atoms arrive at the surface. Atoms then diffuse across the surface until they create a nucleus (also known as seed). Further atoms will then be incorporated to that nucleus carrying out the epitaxial growth laterally i.e. layer-by-layer growth, or vertically i.e. NWs, Volmer-Weber. An example of the different stages of the nucleation phenomenon for GaN is illustrated in Figure 1.

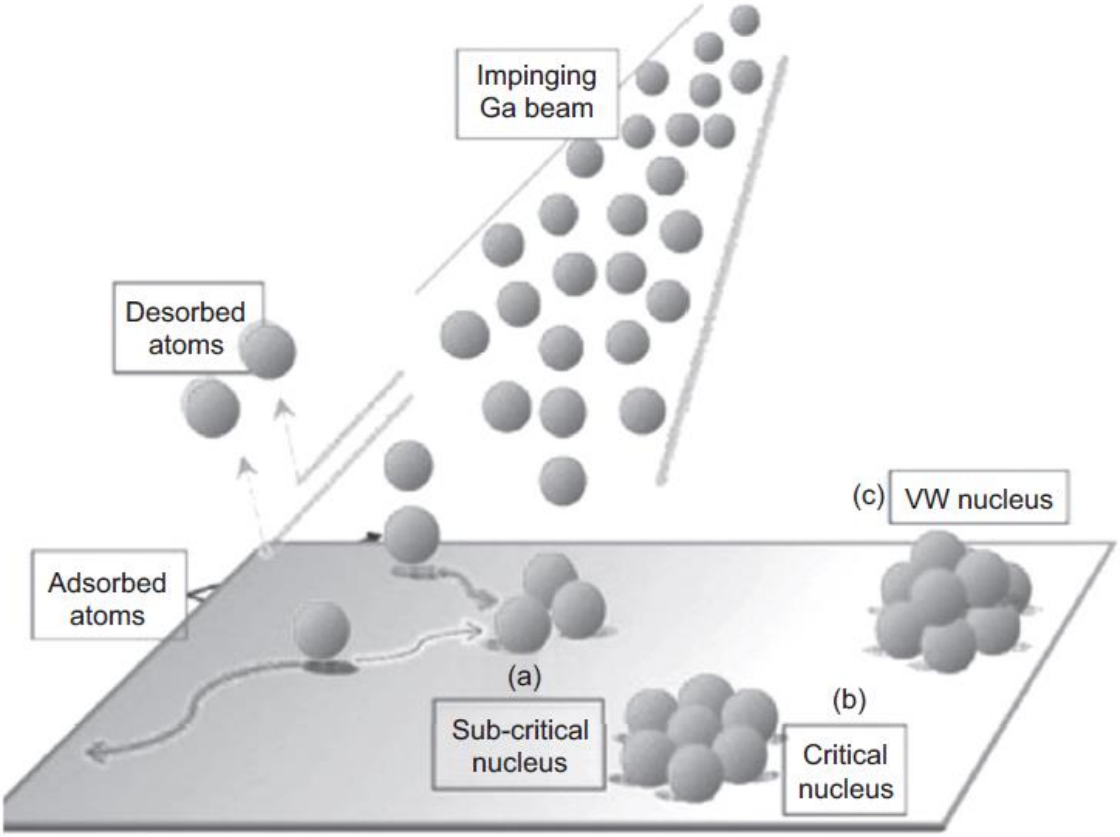

Figure 1. Schematic diagram of MBE nucleation for GaN Nanowires. VW stands for Volmer-Weber. (Figure adapted from [15] with permission from publisher).

While studying different surface phases, various physical phenomena come into play. Two phase reconstructions can be stable and coexist on the surface of different materials under the right conditions. A good example of this phase coexistence has been deeply analysed in chapter 6. Also, under certain conditions some phases are found to be metastable due to strain or other external conditions [28]–[38]. Metastability happens when a different phase reconstruction from the one expected thermodynamically, is present over certain time. For GaAs, metastability for different surface phases has already been reported by different groups [39]–[45]. However, none of the aforementioned in-situ characterization techniques are able to detect small changes prior to growth. RHEED patterns are

representations of the reciprocal space averaged over the surface, and so with this technique is not possible to detect local processes happening over a small period of time. Given the importance of the atomic arrangement of the surface and its influence in epitaxial growth, an in-situ characterisation technique able to resolve dynamic processes i.e. metastable phases, that affect the nucleation processes and therefore, the ultimate properties of the grown materials; was needed.

Langmuir evaporation is a model for adsorption of species at the surface which assumes a perfectly homogeneous surface and no interactions between adsorbate molecules on adjacent sites. Our unique LEEM-MBE equipment allowed us to discover that within the pure c(8×2) regime [46], there is a small percentage of metastable (6×6). This metastable phase can affect the diffusion on the surface and therefore plays an important role on the epitaxial growth of structures for GaAs. The observation of surface phase metastability during Langmuir evaporation for GaAs (001) is surprising but the phenomenon should, in fact, occur quite widely. An unstable subsurface layer, suddenly exposed by evaporation, does not necessarily have to transform directly into the most thermodynamically stable state. Instead, the unstable surface can transform into a metastable intermediate state, as empirically described by Ostwald [47].

In order to understand the difference between kinetical processes and thermodynamic processes one can think of the conversion of diamond to graphite, which is thermodynamically favourable for the reason that the free energy of graphite is lower, nevertheless, this conversion does not take place under ordinary conditions because the kinetics of the reaction i.e. immense activation energy required, are extremely unfavourable. In principle, every chemical reaction is on the continuum between pure kinetic control and pure thermodynamic control. These terms are with respect to a given temperature and time scale. A process approaches pure kinetic control at low temperature and short reaction time. For a sufficiently long-time scale, every reaction approaches pure thermodynamic control. A necessary condition for thermodynamic control is reversibility or a mechanism permitting the equilibration between products.

The phase metastability that we observe for the (6×6) in the c(8×2) regime for GaAs, is a result of kinetics, not thermodynamics, and it is distinct from coexistence resulting from long-range electrostatic and elastic interactions between surface domains as discussed in chapter 6.

Metastable (6×6)

C. X. Zheng et al. presented a phase diagram for the c(8×2) and the (6×6) on GaAs (001) [46]. In this diagram (presented in chapter 6), a transition temperature between c(8×2) phase and (6×6) is set around 560°C. According to this publication, above 560°C, in no presence of Ga-droplets, the surface phase is c(8×2). We have observed surface phase metastability of the (6×6) during Langmuir evaporation of GaAs(001) using SEDFLEEM technique and therefore updated the phase diagram proposed by C. X. Zheng, et al [46]. The new phase diagram we propose is illustrated in Figure 2, and includes the metastability regime observed at temperatures higher than 570°C. This gives rise to a dynamic phase coexistence which has previously gone unnoticed, possibly due to a lack of real time imaging of this surface. Normally, at growth of structures, a single surface phase is assumed. Since surface phase metastability is likely to occur across a wide range of materials systems, it might therefore have broad technological relevance for the growth and processing of thin films under vacuum.

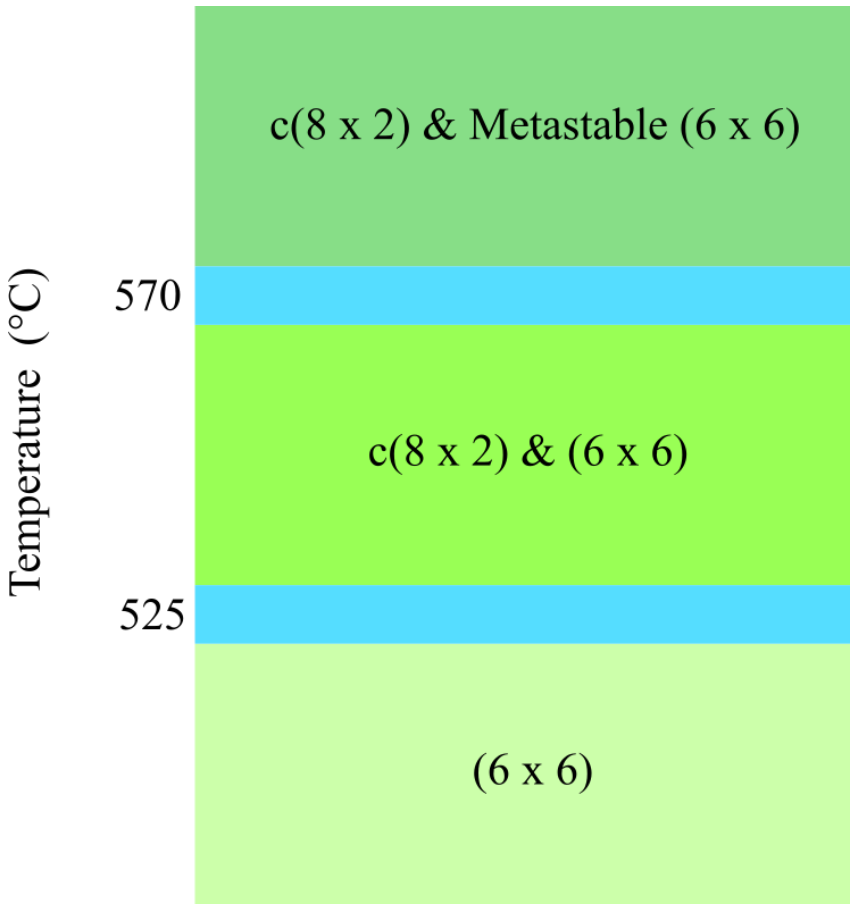

Figure 2. Updated phase diagram including the metastable (6×6) in the stable c(8×2) regime.

We have performed several experiments in which a commercial GaAs substrate was heated up following the standard procedure described in Chapter 3. The GaAs was further annealed over 560°C. Inspection of the surface revealed how instead of having a pure c(8×2) all across the surface, we observed the uniform generation of small patches of (6×6) phase with a different contrast in the whole the surface. The effect of metastable (6×6) patches was observed homogeneously randomly across the whole surface for temperatures greater than 570°C.

In order to confirm the nature of the (6×6) patches, we used the SEDFLEEM technique described thoroughly in chapter 4. This leads to Figure 3. This figure evidences the nature of the (6×6) from the black patches. Figure 3b contains a SEDFLEEM image in which the first point $\left(0,\frac{1}{6}\right)$ from the (6×6) reconstruction

(displayed in Figure 3d at the optimum energy) was filtered. The BF image from Figure 3a and the DF image from Figure 3b were taken almost simultaneously so that they correspond to each other. Figure 3c contains a combined micro-diffraction pattern (the smallest illumination aperture was utilised), as a result of the superposition of the (6×6) and the c(8×2). The points in the reciprocal lattice of the (6×6) pattern, appear to be slightly streaky. This effect could be due to a small disorder [48].

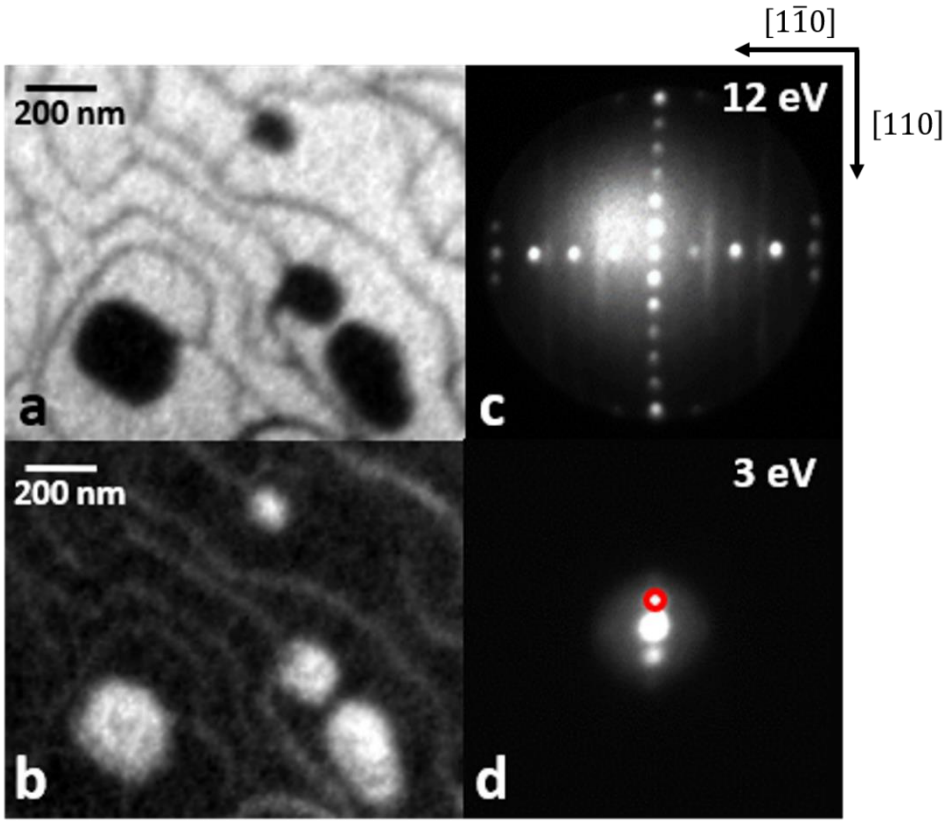

Figure 3. a) BF image at 6.8 eV showing a c(8×2) surface in bright, with some (6×6) patches in dark. b) DF image at 3.5 eV. The (0,1/6) of the (6×6) was filtered. The image was taken almost simultaneously with the Bf from a). c) Diffraction pattern corresponding to the superposition of a c(8×2) and a (6×6). d) Diffraction pattern of the (6×6) using the illumination aperture at the energy optimised for intensity.

To understand the appearance of the (6×6) patches, we must consider the mechanisms of Langmuir evaporation [49], [50]. The nucleation and growth of surface macro-vacancies (Lochkeim formation) is well known to be a key mechanism in the evaporation of surfaces [51]–[53]. Surface defects such as vacancies often form a stable monolayer-height clusters in a terrace, and the resulting step loop expands as the atoms evaporate from the surface, inducing the macro-vacancy to grow, generating a new terrace. This mechanism seems to be consistent with our inspections represented in Figure 4.

The process of generation of macro-vacancies has similarities with the nucleation processes observed during growth (Figure 1). In this case, instead of atoms diffusing across the surface to form a cluster from which the growth will start, vacancies diffuse across the surface until a macro-vacancy cluster is formed. We observe how the nucleation of new macro-vacancies is not associated with the generation of a c(8×2), which would be the most thermodynamically stable phase. Rather, the effect of generation of new macro-vacancies, is associated with the growth of a metastable (6×6) as shown in Figure 3b. These (6×6) patches were generated on different spots and they were growing for some time, after transforming again into c(8×2). An example of this phenomenon is illustrated in Figure 5. It looks plausible that this mechanism being generated on a metastable (6×6) phase is influenced by the generation of surface strain from the small step loop. Eventually, the metastable (6×6) phase will transform to a stable c(8×2) as demonstrated in Figure 5c-e. The stable c(8×2) phase then grows fast and leaves behind a bilayer-height step loop on pure c(8×2) as illustrated in Figure 5f.

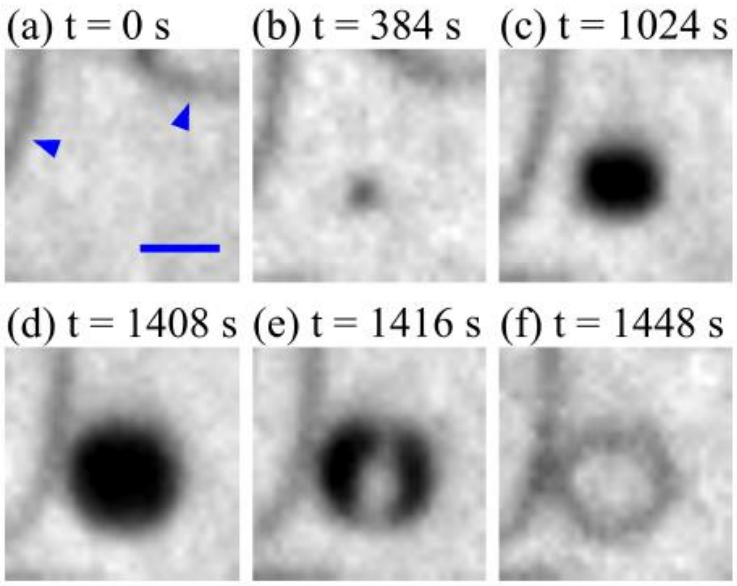

Figure 4. LEEM images showing black patches over a c(8×2) surface revealing the fundamental mechanism of surface phase metastability. The c(8×2) phase appears bright, whilst (6×6) and steps (indicated with arrows in (a)) appear dark. The scale bar in (a) is 0.1 μm and the sample temperature is 598°C. (Figure adapted from [54] with permission from publisher).

The Lochkeime effect and the generation of new terraces is represented in Figure 4. By the time Figure 5c was taken, the black patch is already gone and has let way for new terraces to nucleate again (Figure 5e). The circular lines observed in Figures 3, 4, and 5, correspond to the edge of the terrace. The fact that the patches were generated in random positions indicate that the generation of (6×6) therefore, is not associated with the generation of defects from the bulk. Even though we observe "inverted wedding-cake" structures (a concentric generation of terraces), the new terraces do not generate at the same point.

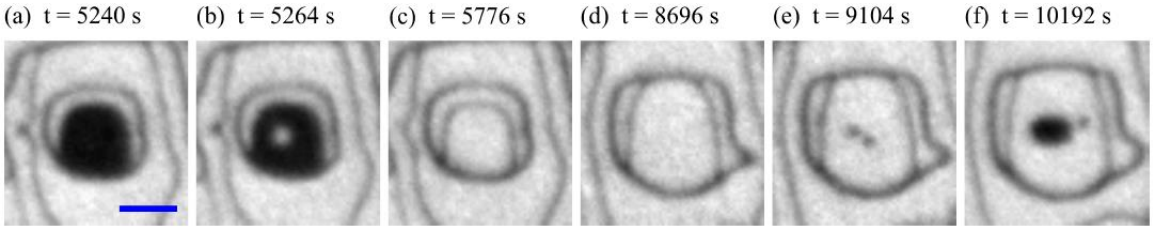

Figure 5. Sequence of LEEM images taken from a movie of a (6×6) terrace transforming to c(8×2). This initiates in panel c) and continues through panels d) and e) until the transformation completes in f), revealing a lower central (6×6) terrace. This indicates that multiple layers of (6×6) exist as inverted wedding-cake structures and that Lochkeime form more readily on (6×6) than on c(8×2). Furthermore, we find it is always the outermost (uppermost) (6×6) terrace that transforms to c(8×2) first. The sample temperature is T = 586°C, and the scale bar is 0.2 µm (obtained from supplementary material of [54] with permission from publisher).

We investigated further the process of transformation of the (6×6) patches to c(8×2) and we observed that for a fixed temperature, there was a critical size of the patches at which the (6×6) patches were transforming to c(8×2). This statistical study is illustrated in Figure 6. The fact that there is a critical size for the transformation of the patches might indicate that the process is governed by a surface mechanism such as strain.

Taking this idea further, we then decided to investigate upon different surface mechanisms that could influence the surface coverage by the (6×6) patches. We performed calculations of the evolution of the step velocity over temperature based on experimental observations from the LEEM movies. During this investigation, we assume based on observations that the velocity is the same across the perimeter of the terrace. The results of these calculations have been displayed in Figure 7. The analysis of the velocity of the step at different temperatures revealed an Arrhenius-type dependence with the temperature. Detailed examination of this dependence led to the calculation of an activation energy of 3.38 eV.

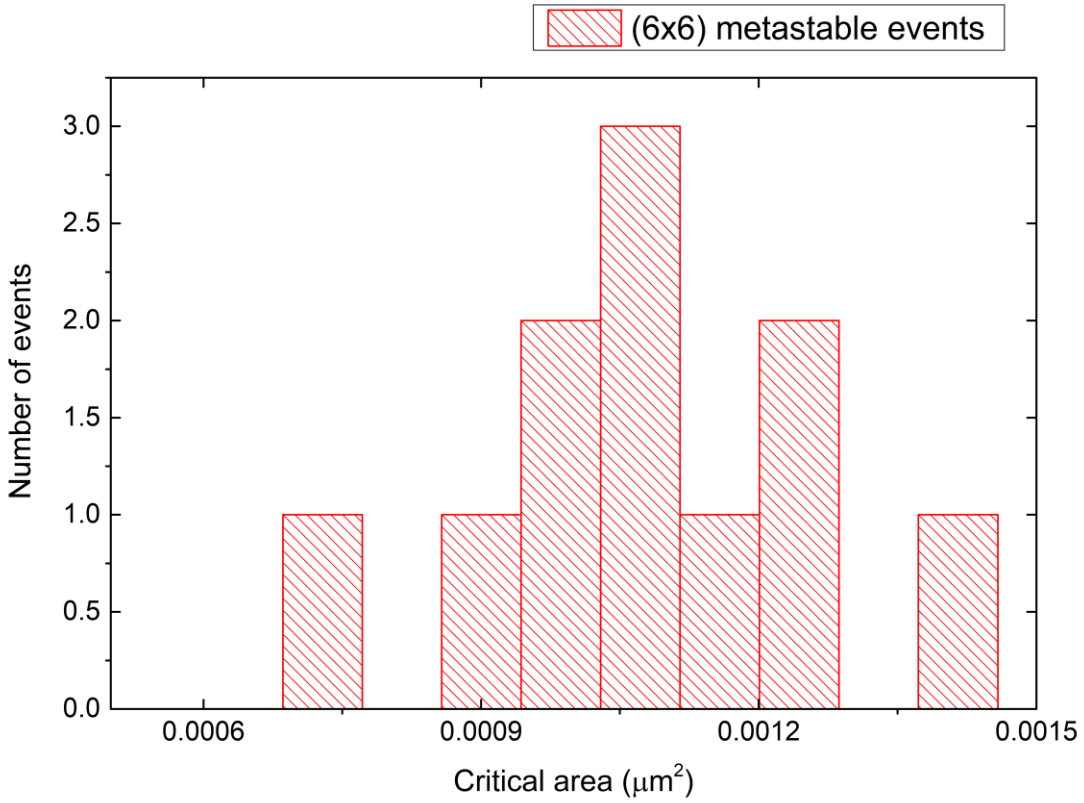

Figure 6. Evolution of metastable (6×6) patches over time at 630°C. The critical size is defined as the size by which the (6×6) patches start their transformation to c(8×2).

Moreover, we have analysed the frequency of generation of new terraces over temperature. The observations reveal that all the new terraces generate in a metastable (6×6) and that we observe a higher density of terraces being generated at higher temperatures. This effect has been quantified and plotted in Figure 8. This graph shows another Arrhenius-type dependence, and so therefore we measured the activation energy for this process, giving us a value of 4.75 eV.

Comparing these two activation energies (3.38 eV and 4.75 eV) with other similar processes on the literature, we hypothesise that the values that we obtain are reasonable and correspond to thermally activated processes. Values in the literature show activation energies of 2.3 eV for one-dimensional diffusion on the (2×4) reconstruction for GaAs [55], 1.2 eV for α and β cross-slip misfit

dislocations on InGaAs/GaAs (001) systems [56], or 3.6 eV for GaAs/AlGaAs interdiffusion [57]. However, since various processes may be interplaying at the same time contributing to the value of the activation energy, we believe that these values only provide a qualitative indication for the sake of reference.

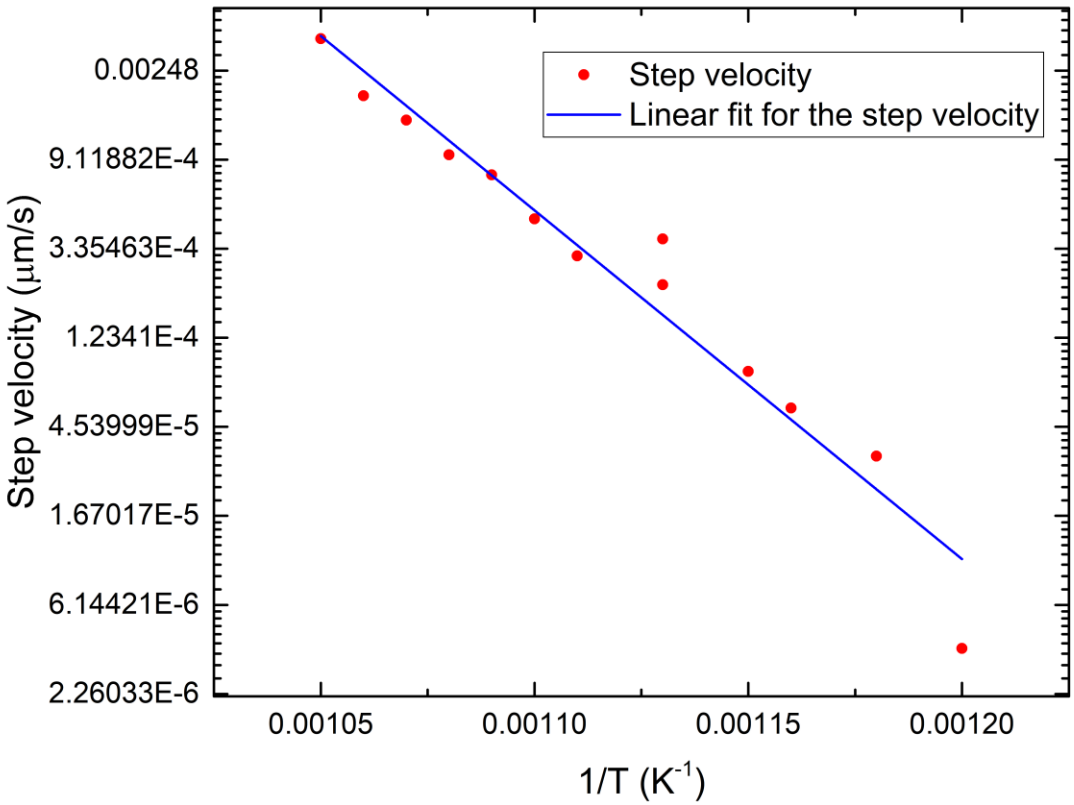

Figure 7. Logarithmic plot of the step velocity for GaAs (001) surfaces.

We checked upon the possibility of this phenomenon being caused by impurities coming from the bulk. This idea was soon dismissed. The temperature behaviour shows an increase of the density of events as the temperature increases, which indicates it must be intrinsic to the sample, as impurity density due to background pressure must be roughly constant. If this phenomenon was due to a build-up of impurities during the setting up of the experiment or during the experiment, the coverage would not be reversible. Once we increase temperature most impurities

would have reacted or being desorbed, so when we decrease the temperature, we would not observe the same density of events (i.e. coverage). The specifications of our GaAs wafers say that the density of impurities is less than 2000 per cm^2. Therefore, a lot lower density than the density of wedding cakes (pinned Lochkeime) we observe.

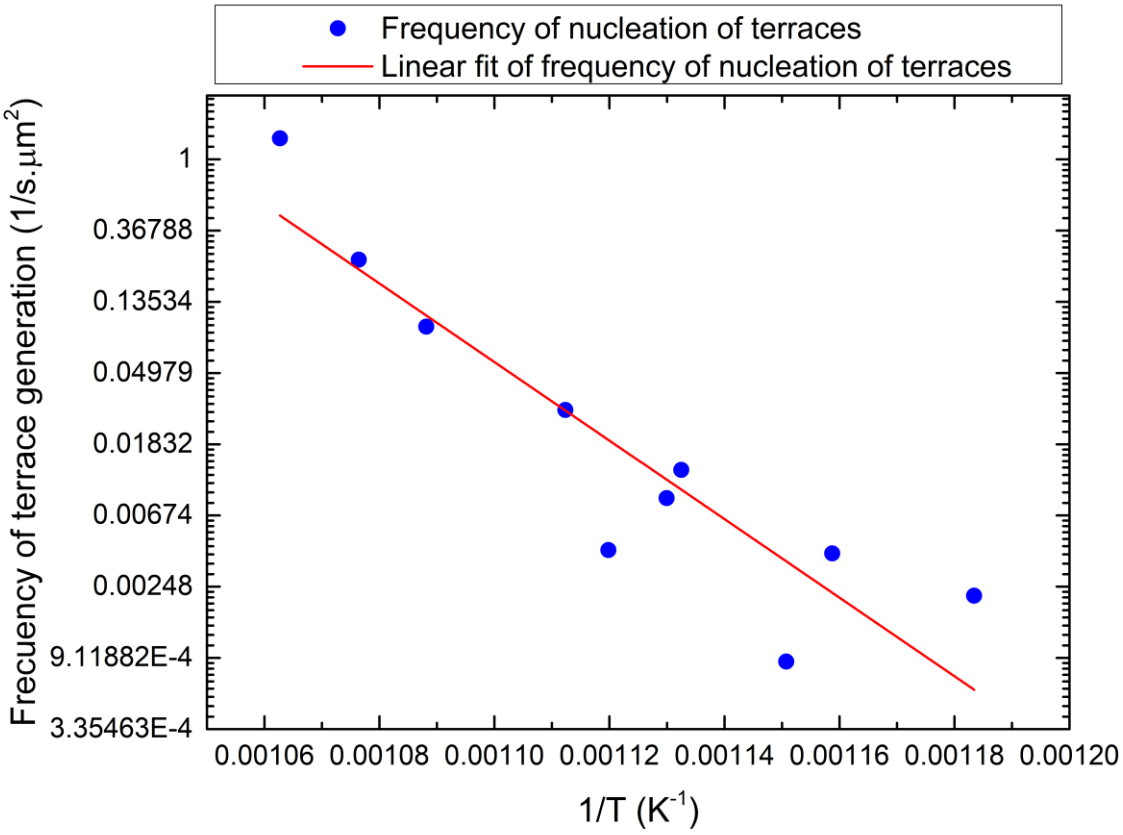

Figure 8. Logarithmic representation of the frequency of generation of new terraces for GaAs (001) surfaces.

In addition, in order to deride the idea of this phenomenon to be caused by impurities coming from the sample, we have carried out a small calculation of what would be the incorporation of atoms coming from the chamber. For this purpose, we have taken into consideration incorporation of As_4 (atomic mass = 300 a.m.u.). The base pressure on the chamber during the experiments was

around $P_{BASE} = 5 \cdot 10^{-10}$ Torr. The volume in our chamber is estimated to be of 12.5 L, and the temperature in the chamber was assumed to be 20°C. Knowing these parameters, we calculated the flux of As species being incorporated in the chamber per unit area using Eq. 1. Where K_B, is the Boltzmann constant in the corresponding units.

$$\varphi_{effusion} = \frac{P_{BASE}}{\sqrt{2\pi M_{species} K_B T}} \qquad \text{Eq. 1}$$

In our case, we obtain a flux of As species of $\varphi_{effusion} = 5.93 \cdot 10^{10} \frac{atoms}{cm^2 s}$. We then compared this result with the number of atoms on the (6×6) reconstruction using our experimental data. In this set of data, the coverage of (6×6) was 5%. The area analysed was $1.767 \cdot 10^{-6}$ cm^2. Taking the lattice parameter of GaAs to be 5.653 Å. Assuming 1 atom of As per unit cell at the surface, we get a surface density of $3.129 \cdot 10^{14} \frac{atoms}{cm^2 s}$. To particularise for the (6×6) reconstruction, we need to divide by 6, and apply that to only 5% of the surface. We therefore get a density of (6×6) atoms at the surface of about $2.608 \cdot 10^{12} \frac{atoms}{cm^2 s}$. This value is about 50 times larger than the density of atoms incorporated by residual pressure, reaffirming on the idea that this phenomenon in an intrinsic property from the material.

Additionally, a theoretical Monte Carlo (MC) model based on kinetics mechanisms for the phenomenon of metastability has been developed (see Appendix Monte Carlo simulation). The method is governed by a set of simple rules derived from our experimental observations in LEEM movies [58]. The MC model matches the effects that we observe experimentally. An example of this can be found in Figure 9. In this sequence of LEEM images, it can be noticed how increasing the temperature provokes that the size of the metastable (6×6) patches gets reduced. Figure 9a, 9b and 9c illustrate real LEEM images while Figure 9d, 9e and 9f show screenshots of the MC simulation taken at the same temperature at the LEEM images. Agreement between the model and the real experiment can be easily appreciated.

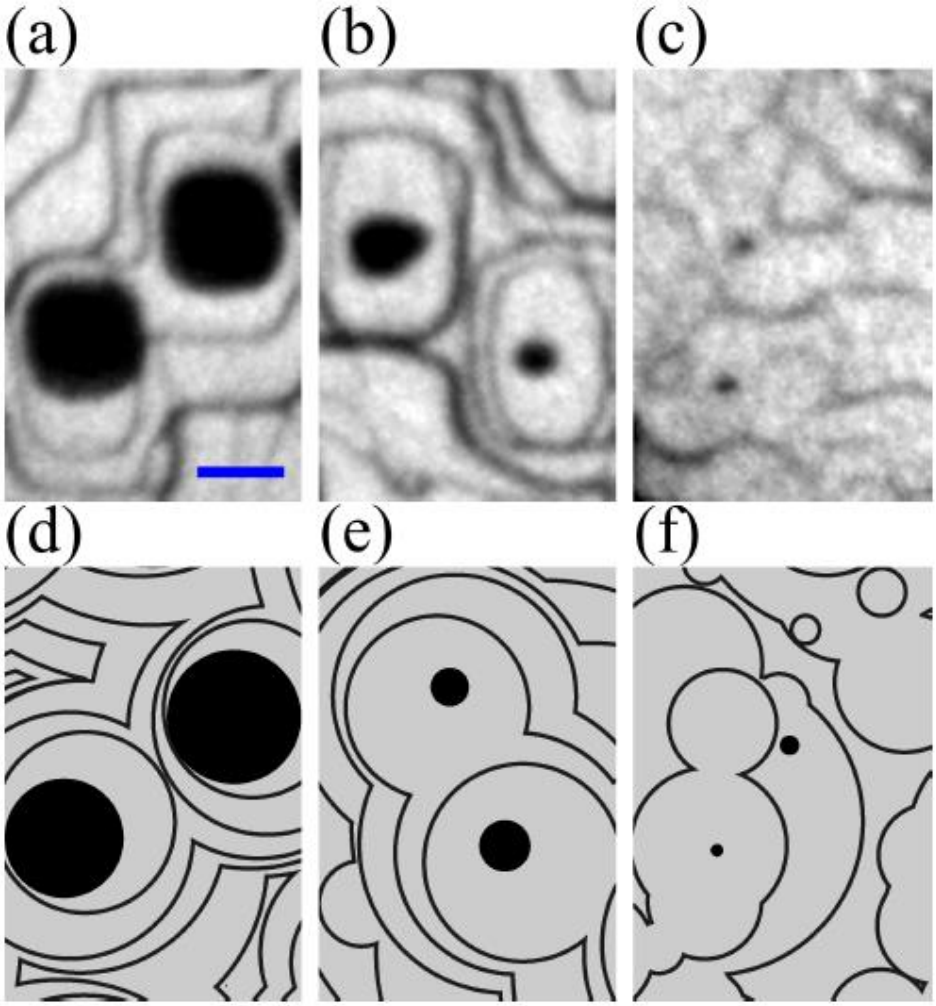

Figure 9. Snapshots of evolving surface morphology taken from LEEM movies at a) 581°C, b) 598°C and c) 639°C and Monte Carlo simulation movies at d) 581°C , e) 598°C and f) 639°C. Dark areas correspond to (6×6) terraces. The scale bar in a) is 0.2 µm. (Figure adapted from [54] with permission from publisher).

As observed in Figure 9, dynamics of nucleation, growth and annihilation gives rise to a time-averaged coverage of (6×6). At different temperatures, this coverage changes, as the transformation of the patches from metastable (6×6) to c(8×2) happens earlier at higher temperatures. To evidence quantitatively this phenomenon, Figure 10 was created. In this graph, the time-averaged coverage at different temperatures is represented. The experimental results for the time-averaged coverage have been compared with the values obtained from the MC

model. Figure 10 shows the agreement between the model and the experimental data. The small plot contained in the main graph, shows the stability of the metastable phases over time in the MC model. The initial peak appears because the model sets off from a clean defect-free surface, so the (6×6) metastable patches have no terraces to merge with, therefore, the initial coverage in the model has a peak of coverage.

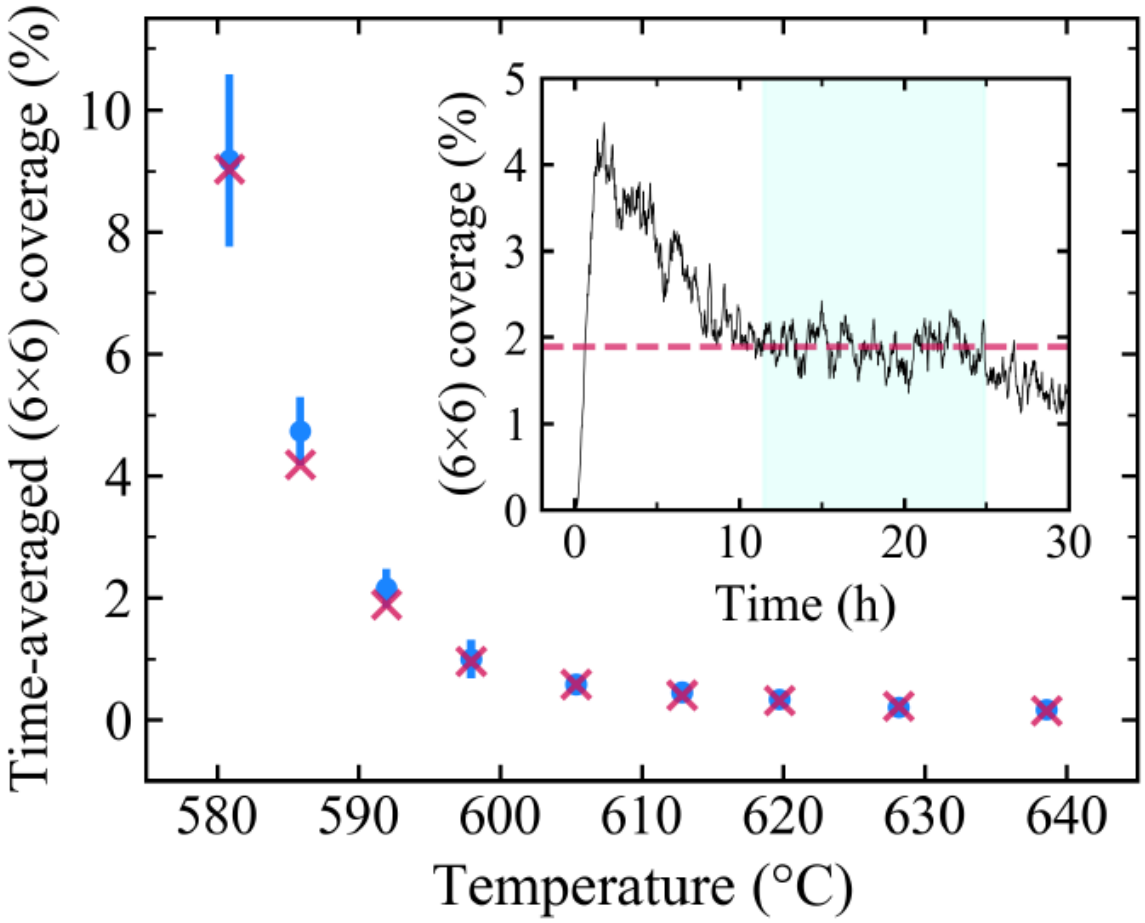

Figure 10. Time-averaged (6×6) coverage as a function of temperature. The circles are experimental values and the crosses were calculated from the Monte Carlo simulation. The inset shows the time evolution of the (6×6) coverage produced by the Monte Carlo simulation at 592°C. The dashed line shows the time-averaged coverage obtained from the shaded region (see text). Error bars are computed as standard deviations from the mean. (Figure adapted from [54] with permission from publisher).

For the MC model, different physical events from the experimental observations have had to be taken into consideration. One of the processes that helped developing the model, was the detailed study of the generation of new terraces and the interaction between patches. For the sake of clarity, Figure 11 was created. In this sequence, we demonstrate that two terraces generated simultaneously in two different positions near to each other on the surface (Figure 11a and 11b), when they grow until they touch each other, both patches coalesce (Figure 11c) given place to only one (6×6) patch (Figure 11d). After the big patch transforms to c(8×2), a one-layer-height terrace is left behind, as represented in Figure 11f. This indicates that the two initial patches were generated at the same atomic level, which is in agreement with the rest of the observations. This effect is also observed in Figure 10, where a point of nucleation is generated next to a terrace edge (Figure 12b) grows until its coalescence with the terrace edge (Figure 12d), causing the patch to die (Figure 12e), leaving the surface where the black patch was nucleated at the same atomic level the pre-existing terrace was at (Figure 12f).

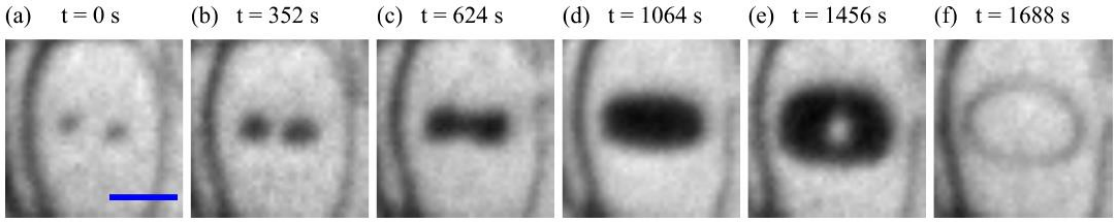

Figure 11. Sequence of LEEM images taken from a movie showing the coalescence of two (6×6) terraces, forming a larger (6×6) terrace. The combined (6×6) terrace transforms to c(8×2) as a single domain like shown in e), and f). The sample temperature is T = 592 C, and the scale bar displayed in a) is 0.15 μm (Obtained from supplementary material of [54] with permission from publisher).

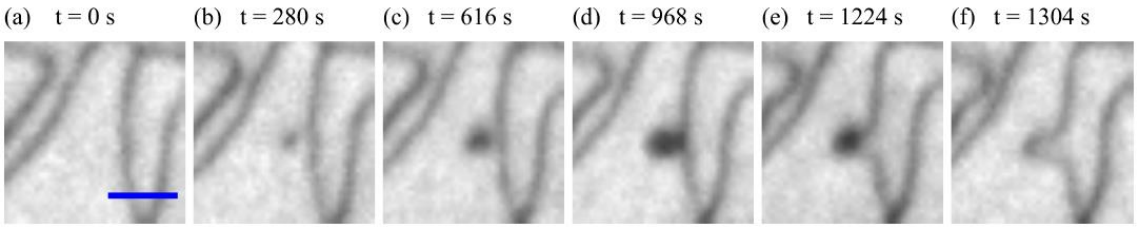

Figure 12. Sequence of LEEM images obtained from a movie showing that a (6×6) terrace transforms to c(8×2) on coalescing with a c(8×2) terrace. The sample temperature is T = 586°C, and the scale bar is 0.15 μm (Obtained from supplementary material of [54] with permission from publisher).

We conclude that there is a metastable (6×6) present during the whole range of what was thought to be a pure c(8×2) regime. These patches nucleate in a metastable (6×6) surface reconstruction, and lead to the generation of new terraces. After some time, they reach a critical size and transform to c(8×2). The generation of the metastable phase are governed by kinetics since the (6×6) is not the most thermodynamically stable phase above 570°C. The processes are not related to incorporation of impurities since a random nucleation of new terraces is observed across the surface. This mechanism of metastability may be present in other systems and the investigation of metastability and other dynamical processes possesses a critical impact on the quality of the grown material and ultimately in the device structures. Our unique SEDFLEEM technique allows to observe metastable mechanisms in-situ during growth.

References:

[1] A. Ohtake and T. A. T. Ito, "As-rich (2 × 2) surface reconstruction on GaAs(111)A," *Surf. Sci.*, vol. 606, no. 23–24, pp. 1864–1870, 2012.

[2] J. Northrup and S. Froyen, "Energetics of GaAs (100)-(2× 4) and-(4× 2) reconstructions," *Phys. Rev. Lett.*, vol. 71, no. 14, pp. 2276–2279, 1993.

[3] I. Chizhov, G. S. Lee, R. F. Willis, D. Lubyshev, and D. L. Miller, "Evolution of the GaAs(001) surface structure during the transition from the As-rich (2x4) to the Ga-rich (4x2) reconstruction," *Surf. Sci.*, vol. 419, no. 1, pp. 1–11, 1998.

[4] M. Pristovsek *et al.*, "Gallium-rich reconstructions on GaAs(001)," *Phys. Status Solidi Basic Res.*, vol. 240, no. 1, pp. 91–98, 2003.

[5] K. Seino, W. G. Schmidt, and O. A., "Ga-rich GaAs(001) surface from ab initio calculations: Atomic structure of the (4x6) and (6x6) reconstructions," *Phys. Rev. B*, vol. 73, no. 035317, pp. 4–9, 2006.

[6] A. Ohtake, "Surface reconstructions on GaAs(001)," *Surf. Sci. Rep.*, vol. 63, pp. 295–327, 2008.

[7] J. S. Kim, "Ga-migration on a Ga-rich and As-stabilized surfaces: Ga-droplet and GaAs- nanostructure formation," *Mater. Sci. Semicond. Process.*, vol. 57, no. April 2016, pp. 70–76, 2017.

[8] S. Bietti *et al.*, "Ga metal nanoparticle-GaAs quantum molecule complexes for terahertz generation," *Nanotechnology*, vol. 29, no. 36, 2018.

[9] A. Ohtake, A. Hagiwara, K. Okukita, K. Funatsuki, and J. Nakamura, "Mn-Induced Surface Reconstructions on GaAs(001)," *J. Phys. Chem. C*, vol. 120, no. 11, pp. 6050–6062, 2016.

[10] A. Ohtake, A. Hagiwara, and J. Nakamura, "Controlled incorporation of Mn in GaAs: Role of surface reconstructions," *Phys. Rev. B - Condens. Matter Mater. Phys.*, vol. 87, no. 16, pp. 1–5, 2013.

[11] O. A. Ageev, M. S. Solodovnik, S. V. Balakirev, I. A. Mikhaylin, and M. M. Eremenko, "Monte Carlo simulation of the kinetic effects on GaAs/GaAs(001) MBE growth," *J. Cryst. Growth*, vol. 457, pp. 46–51, 2017.

[12] J. Puustinen, J. Hilska, and M. Guina, "Analysis of GaAsBi growth regimes in high resolution with respect to As/Ga ratio using stationary MBE growth," *J. Cryst. Growth*, vol. 511, no. January, pp. 33–41, 2019.

[13] L. Goswami, R. Pandey, and G. Gupta, "Epitaxial growth of GaN nanostructure by PA-MBE for UV detection application," *Appl. Surf. Sci.*, vol. 449, pp. 186–192, 2018.

[14] P. Maiti, P. Guha, H. Hussain, R. Singh, C. Nicklin, and P. V. Satyam, "Microscopy and spectroscopy study of nanostructural phase transformation from β-MoO 3 to Mo under UHV – MBE conditions," *Surf. Sci.*, vol. 682, no. September 2018, pp. 64–74, 2019.

[15] Q. Zhuang, *Molecular beam epitaxy (MBE) growth of nitride semiconductors*. Woodhead Publishing Limited, 2014.

[16] S. Dewan, M. Tomar, R. P. Tandon, and V. Gupta, "In-situ and post deposition analysis of laser MBE deposited GaN films at varying nitrogen gas flow," *Vacuum*, vol. 164, no. March, pp. 72–76, 2019.

[17] A. Ohtake, T. Yasuda, and N. Miyata, "Anisotropic kinetics on growing Ge (001) surfaces," *Surf. Sci.*, vol. 603, no. 5, pp. 826–830, 2009.

[18] K. Tobari, M. Ohtake, K. Nagano, and M. Futamoto, "Structure characterization of Pd/Co/Pd tri-layer films epitaxially grown on MgO single-crystal substrates," *Thin Solid Films*, vol. 519, no. 23, pp. 8384–8387, 2011.

[19] A. Ohtake, "Structure and composition of Ga-rich (6×6) reconstructions on GaAs(001)," *Phys. Rev. B - Condens. Matter Mater. Phys.*, vol. 75, no. 15, pp. 4–7, 2007.

[20] A. Popp and C. Pettenkofer, "Epitaxial growth of CuGaSe 2 thin-films by MBE—Influence of the Cu/Ga ratio," *Appl. Surf. Sci.*, vol. 416, pp. 815–823,

2017.

[21] A. Ohtake and N. Koguchi, "Self-assembled growth of ordered GaAs nanostructures," *Appl. Phys. Lett.*, vol. 89, no. 8, pp. 23–25, 2006.

[22] A. Ohtake, P. Kocán, J. Nakamura, A. Natori, and N. Koguchi, "Kinetics in surface reconstructions on GaAs(001)," *Phys. Rev. Lett.*, vol. 92, no. 23, pp. 2–5, 2004.

[23] S. Tsukamoto *et al.*, "Ga-rich GaAs[001] surfaces observed by STM during high-temperature annealing in MBE chamber," *MBE 2002 - 2002 12th Int. Conf. Mol. Beam Ep.*, vol. 251, pp. 113–114, 2002.

[24] H. H. Farrell, J. P. Harbison, L. D. Peterson, H. H. Farrell, J. P. Harbison, and L. D. Peterson, "Molecular - beam epitaxy growth mechanisms on GaAs (100) surfaces," *J. Vac. Sci. Technol. B*, vol. 5, no. 1482, 1987.

[25] A. Ohtake, "Structures of the As-deficient phase on GaAs(001)-(2×4)," *Phys. Rev. B - Condens. Matter Mater. Phys.*, vol. 74, no. 16, pp. 2–5, 2006.

[26] M. Pashley, KW. Haberen, "The role of surface reconstrutions in MBE growth of GaAs," in *Semiconductor Interfaces at the Sub-Nanometer Scale, 243*, 1993.

[27] A. Ohtake, T. Mano, A. Hagiwara, and J. Nakamura, "Self-assembled growth of ga droplets on GaAs(001): Role of surface reconstructions," *Cryst. Growth Des.*, vol. 14, no. 6, pp. 3110–3115, 2014.

[28] N. Nepal, D. Scott Katzer, and D. J. Meyer, *MBE growth and characterization of gallium oxide*. Elsevier Inc., 2019.

[29] N. Mavridi, N. M. Eldose, K. A. Prior, and R. T. Moug, "Optimization of the MBE growth of metastable zinc blende MnS on GaAs (1 0 0) substrates using ZnS as sulphur source," *J. Cryst. Growth*, vol. 511, no. January, pp. 61–64, 2019.

[30] H. T. Yuan *et al.*, "Formation of metastable MgO structures on type-III oxide surfaces : Effect of periodic out-of-plane electric dipole moment of

substrates," *J. Cryst. Growth*, vol. 311, pp. 425–428, 2009.

[31] K. A. Prior, C. Bradford, L. David, X. Tang, and B. C. Cavenett, "Metastable group II sulphides grown by MBE : surface morphology and crystal structure," *J. Cryst. Growth*, vol. 275, pp. 141–149, 2005.

[32] X. Zhu *et al.*, "Growth of the metastable zinc-blende MnTe fi lms on highly dissimilar perovskite SrTiO 3 (001) substrates by molecular beam epitaxy," *J. Alloys Compd.*, vol. 729, pp. 95–99, 2017.

[33] S. V Ivanov, T. V Shubina, T. A. Komissarova, and V. N. Jmerik, "Metastable nature of InN and In-rich InGaN alloys," *J. Cryst. Growth*, vol. 403, pp. 83–89, 2014.

[34] K. A. Prior, C. Bradford, I. A. Davidson, and R. T. Moug, "Metastable II – VI sulphides : Growth , characterization and stability," *J. Cryst. Growth*, vol. 323, no. 1, pp. 114–121, 2011.

[35] K. Inaba *et al.*, "Heteroepitaxial growth of metastable ErF3 on CaF2(1 1 1) by molecular beam epitaxy a novel material for optical upconversion," *J. Cryst. Growth*, vol. 179, pp. 488–494, 1997.

[36] M. D. L. Ã, S. Mita, R. Collazo, Z. Sitar, and J. Maria, "Epitaxial growth of the metastable phase ytterbium monoxide on gallium nitride surfaces," *J. Cryst. Growth*, vol. 310, pp. 51–56, 2008.

[37] J. Dekoster, A. Vantomme, and M. Caymax, "Stable and metastable iron silicide phases on Si (1 0 0)," *Surf. Sci.*, vol. 599, pp. 122–127, 2005.

[38] J.-Y. N. Pierre Stocker, Jean-Marc Gay, "Metastable α-FeSi2 films grown on Si(1 1 1) at low temperature," *Phys. B*, vol. 198, pp. 240–242, 1994.

[39] A. Beyer, W. Stolz, and K. Volz, "Metastable cubic zinc-blende III / V semiconductors : Growth and structural characteristics," *Prog. Cryst. Growth Charact. Mater.*, vol. 61, no. 2–4, pp. 46–62, 2015.

[40] J. P. Harbison, T. Sands, R. Ramesh, L. T. Florez, B. J. Wilkens, and V. G. Keramidas, "MBE growth of ferromagnetic metastable epitaxial MnA1 thin

films on AlAs/GaAs heterostructures," *J. Cryst. Growth*, vol. 111, pp. 978–983, 1991.

[41] A. V Vasev, S. I. Chikichev, and B. R. Semyagin, "Ellipsometric detection of transitional surface structures on decapped GaAs," *Surf. Sci.*, vol. 588, pp. 149–159, 2005.

[42] M. Ohtake, J. Higuchi, O. Yabuhara, F. Kirino, and M. Futamoto, "Preparation of metastable bcc permalloy epitaxial thin fi lms on GaAs (011) B 3 single-crystal substrates," *Thin Solid Films*, vol. 519, no. 23, pp. 8367–8370, 2011.

[43] M. A. Vidal, M. E. Constantino, R. Asomoza, and A. Merkulov, "Structural study of metastable (GaAs) (Ge) thin films grown by RF magnetron sputtering," *J. Cryst. Growth*, vol. 197, pp. 783–788, 1999.

[44] A. C. Redfield, M. A. Bowent, K. E. Newman, and J. D. Dow, "Surface states of metastable (GaAs)1-x Ge2x alloys," *Solid State Commun.*, vol. 46, no. 5, pp. 371–373, 1983.

[45] E. Gastellóu *et al.*, "Influence of the GaAs crystals diffusion in the shift towards low energies in the photoluminescence emission band of the GaN / GaN buffer / GaAs structure," *Opt. Mater. (Amst).*, vol. 88, pp. 277–281, 2019.

[46] C. X. Zheng, J. Tersoff, W. X. Tang, A. Morreau, and D. E. Jesson, "Novel GaAs surface phases via direct control of chemical potential," *Phys. Rev. B*, vol. 93, no. 19, p. 195314, 2016.

[47] W. Ostwald, "Studies of the formation and transformation of solid substances," *Phys. Chem.*, vol. 22, no. 289, 1897.

[48] M. A. Van Hove, W. H. Weinberg, and C. M. Chan, *Low-Energy Electron Diffraction Experiment, Theory and Surface Structure Determination*, vol. 53, no. 9. 2013.

[49] A. A. Spirina, N. L. Shwartz, and M. Carlo, "Metal droplet formation and motion during the III-V semiconductor evaporation," *Mater. Sci. Semicond. Process.*, vol. 100, no. May, pp. 319–325, 2019.

[50] B. Goldstein, D. J. Szostak, and V. S. Ban, "Langmuir evaporation from the (l00), (111 A), AND (111 B) faces of GaAs," *Surf. Sci.*, vol. 57, pp. 733–740, 1976.

[51] E. Bauer, M. Mundschau, and W. Telieps, "Atomic steps on Si(001) and steps dynamics during sublimation studied by Low Energy Electron Microscopy," *Surf. Sci.*, vol. 223, pp. 413–423, 1989.

[52] J.-J. Pimpinelli, Alberto and Métois, "Macrovacancy Nucleation on Evaporating Si(001)," *Phys. Rev. Lett.*, vol. 72, no. 22, 1994.

[53] J. J. Metois and D. E. Wolf, "Kinetic surface roughening of Si(001) during sublimation," *Surface Science*, vol. 298, no. 1. pp. 71–78, 1993.

[54] K. Hannikainen, D. Gomez, J. Pereiro, Y. R. Niu, and D. E. Jesson, "Surface Phase Metastability during Langmuir Evaporation," *Phys. Rev. Lett.*, vol. 123, no. 186102, pp. 1–5, 2019.

[55] H. Yang, V. P. Labella, D. W. Bullock, Z. Ding, J. B. Smathers, and P. M. Thibado, "Activation energy for Ga diffusion on the GaAs(0 0 1)-(2×4) surface: An MBE-STM study," *J. Cryst. Growth*, vol. 201, pp. 88–92, 1999.

[56] G. Lacey *et al.*, "In-situ direct measurement of activation energies for the generation of misfit dislocations in the InGaAs/GaAs (001) system," *Appl. Surf. Sci.*, vol. 123–124, pp. 718–724, 1998.

[57] S. F. Wee, M. K. Chai, K. P. Homewood, and W. P. Gillin, "The activation energy for GaAs/AlGaAs interdiffusion," *J. Appl. Phys.*, vol. 82, no. 10, pp. 4842–4846, 1997.

[58] "The theoretical model has been developed by Kennet Rodriguez Hannikainen." .

Chapter 8: Nucleation of nanostructures in LEEM-MBE

In this chapter, a review on the work carried out associated to the nucleation of nanostructures by LEEM-MBE will be presented. Different approaches will be described highlighting the potential that our system holds for the real-time observation of nucleation of quantum structures.

Introduction

Quantum-structure-based optoelectronic devices have been subject of interest all around the world due to their high efficiency and their potential application for novel quantum information technologies e.g. single photon emission for quantum computing [1], [2], quantum cryptography [3], high-efficiency quantum-dot based lasers [4]–[7] or even for biological applications [8], [9]. Nevertheless, significant limitations in the understanding of the underlying mechanisms behind the nucleation of quantum structures i.e. role of strain in the wetting layer for QD formation or In diffusion for the QD nucleation [10], [11].

In order to optimise the growth parameters to improve the fabrication techniques of quantum-structure-based devices, deep understanding on the growth mechanisms and the dynamical processes of the physics behind the formation of quantum structures like Nanowires (NWs) [12]–[15] or Quantum Dots (QDs) [16]–[22], is required. Numerous studies have been reported regarding various phenomena involved in the QD formation, such as the influence of strain [23], the influence of the growth pauses [24], the role of dislocations for preferential nucleation [25], or the nucleation mechanisms of QDs within the wetting-layer [26]–[28]. Different techniques such as AFM [29]–[33], TEM [34]–[41] or STM [42] have been utilised for nucleation studies of quantum structures. Our arsenide

LEEM-MBE at Cardiff University allows the obtention of in-situ movies of how advanced compound semiconductor quantum structures form under high arsenic molecular flux. Arsenic flux has previously limited the use of conventional imaging techniques (see Chapter 3) and so this objective will revolutionise the real-time study of technologically important III-V quantum structure fabrication. The new insights gained from these movies will assist the optimisation of the growth of advanced nanostructures. This knowledge will ultimately pave the way for advance semiconductor applications such as the practical integration of single QDs into photonic integrated circuits for applications in quantum computing.

In this Chapter, on-going and future projects on quantum structures nucleation will be discussed, with special attention to the capabilities of our LEEM-MBE equipment as a unique technique for the analysis of dynamical processes behind growth [43].

Quantum Dots nucleation studies

Quantum Dots are nanostructures where electrons are confined in the three dimensions of the space. This localisation of carriers, favour the electron-hole pair recombination, increasing the efficiency of light emission and detection. The most common growth method for QDs is the so-called Stranski-Krastanov (SK) method [44]. This method is defined as layer + islands growth model. It consists of an initial layer of atoms epitaxially grown on a previously prepared surface. When the layer acquires a critical thickness, a transition from 2D to 3D growth occurs so that the self-assembled quantum dots are generated [45]. Then, by the effect of the strain, the QDs formation takes place. The nucleation mechanisms affect the morphology of the quantum structure. In addition, the confinement properties of the QDs depend on their detailed chemical composition profile, i.e. their local stoichiometry [46]. Thus, the comprehension of the mechanisms involved in quantum structures nucleation is of great importance for quantum applications. However, key questions regarding quantum dot (QD) formation remain unanswered. Whether nanostructures form via nucleation or instability, the role

of the wetting layer in QDs nucleation, the process of crystallization of the QDs or atomic diffusion within the wetting layer; are processes which remain not fully understood. These issues are key to control size distribution, morphology and location of quantum structures.

The growth of III-Vs QDs is highly influenced by different parameters such as the orientation of the crystal's surface [47]–[49] or the flux of III-V species (In, Ga, As in our case [50]–[53] an so it has been proven in many scientific reports. Zhou et al. have investigated the effect that the dislocations have on the nucleation of quantum dots, showing that the pure edge dislocations are preferentially nucleate at the base centre of the quantum dots, whereas 60° mixed dislocations, nucleate preferentially at positions near to the edge of the quantum dot base [54], [55]. Another example of the importance of the growth parameters for the QD formation was given by Schuh et al. where the demonstrated the generation of QD arrays using cleaved surfaces [56]. Fortina et al. provided evidences that for a given coverage, the density of QDs varies with the crystal orientation [57]. Weir et al. showed for InGaAs QDs, that a higher V/III ratio increases the wavelength and reduces the FWHM for photoluminescence [58]. Fournier et al. demonstrated that In incorporation is enhanced by a higher V/III ratio and by the use of As_2 [59]. A higher V/III ratio for InSb/GaSb QDs have been proved to reduce the QD density [60]. Kammiya et al. demonstrated that a higher In flux as well as a higher As flux, both resulted in an increase of InGaAs QDs density [61].

Up to now, MBE QD growth involves mostly ex-situ characterization techniques i.e. AFM, STM or TEM measurements, to characterise the morphology of the epitaxially grown QDs. However, there is a necessity of in-situ real time measurements to study thin film growth, as it has already been reported by G.J. Whaley and P.I. Cohen, where they concluded that the relaxation for films with high In mole fractions was rapid [62]. The dislocation velocity in the InGaAs/GaAs system may stop during growth pauses, even if the sample is kept at growth temperature. In 1993, E. A. Stach et al. reported that the dislocations in SiGe/Si(100) slow down by a factor of three if the sample is removed from ultra-high vacuum [63]. A similar situation could as well be expected for quantum

nanostructures, where the results from in-situ characterization and the results from ex-situ characterization will differ, due to strain, cooling, mechanical vibrations, growth pauses, post-growth processes or simply sample exposure to air.

The III-V LEEM system at Cardiff is ideally suited to study the key dynamic mechanisms of QD self-assembly as it allows real-time observation during the growth of quantum structures.

Currently, the group have carried out significant work for the observation of QD nucleation. We reproduced the conditions for the observation of self-assembled QDs nucleation by direct observation of the x3 periodicity characteristic from the InGaAs WL formation [64]. However, we are finding some troubles with the DF contrast on the real-time imaging, which we will need to overcome. Figure 1 shows an AFM image of QDs grown by LEEM-MBE. Future work on this, will be able to optimise the imaging conditions in LEEM for the nucleation of these structures. Preliminary observations show that on the presence of a Ga-trail (see chapter 3), the QDs tend to nucleate on the edges.

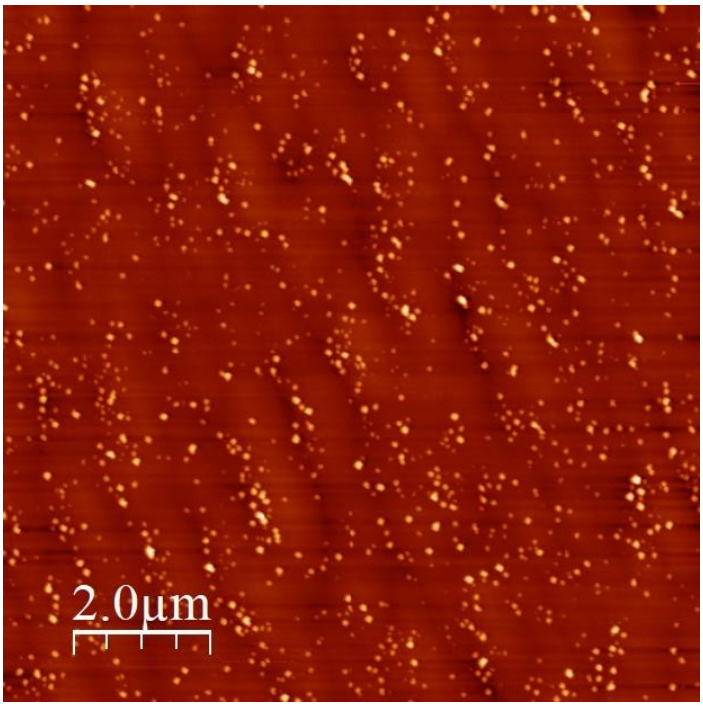

Figure 1. AFM image of Quantum Dots grown by LEEM-MBE at Cardiff.

Droplet Epitaxy approach

An alternative to the Stranski-Krastanov method for site-controlled QD growth is Droplet Epitaxy (DE) [65].

With this method, QDs are grown on a crystallised metal droplet. The study of the mechanisms behind the formation of crystallised Ga droplets is therefore crucial for the further application of DE-based site-controlled QDs [66], [67]. J. Tersoff et al. carried out studies on the surface morphology during Langmuir evaporation in GaAs [68]. They concluded that the evaporation of As is controlled by step density, while evaporation of Ga is not, highlighting the importance of close observation of surface mechanisms for the optimisation of growth parameters. Analysis of these surface effects suggests a new approach for the self-assembly and positioning of quantum structures via droplet epitaxy.

In the literature we can find different examples of the growth of quantum structures such as Quantum Dots [69]–[83] and Quantum Rings [84]–[87] using Droplet Epitaxy. Zhou et al, demonstrated the formation of double Quantum Ring structures using the unique capabilities of III-V LEEM-MBE [88].

We desire to take these studies further and analyse in detail the processes behind the formation of site-controlled QDs using Droplet Epitaxy. Recently, we have performed several experiments following Zhou's approach and we have achieved the generation of Quantum Rings in LEEM-MBE. AFM images are shown in Figure 2 evidencing the effectiveness of our III-V LEEM-MBE system. Further work will take these studies to consecutive next steps improving the imaging conditions and making the growth of QD structures using Droplet Epitaxy.

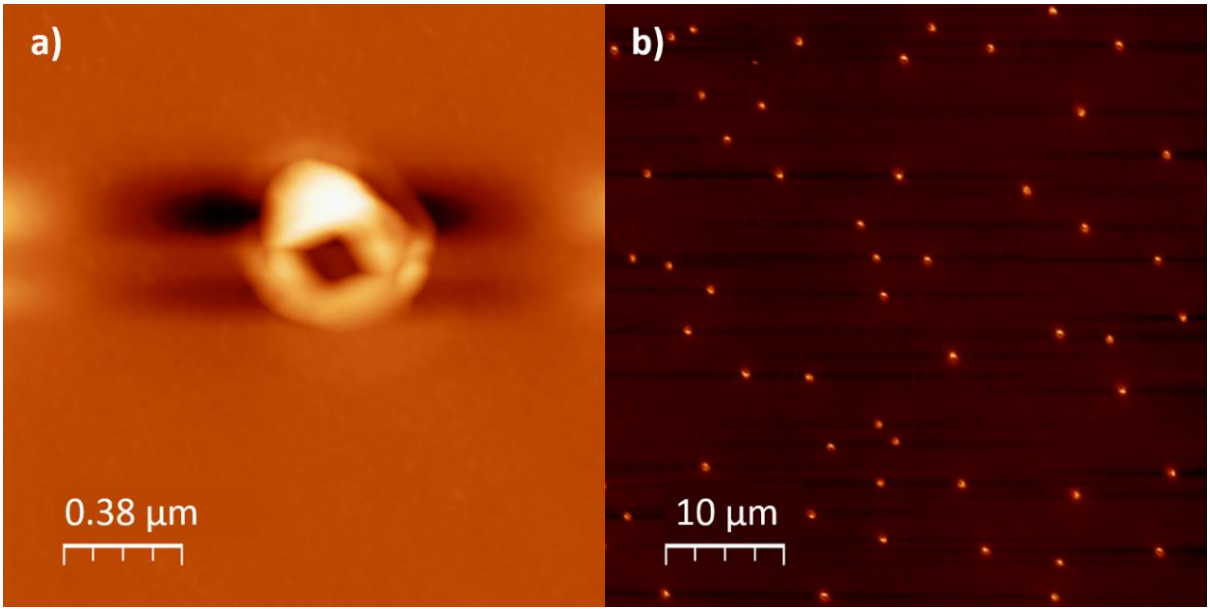

Figure 2. Droplet epitaxy results. Growth of GaAs rings by LEEM-MBE.

Droplet etching approach

This technique sets off from the same principles of droplet epitaxy. A higher temperature and a higher V-flux, favours the drilling of Ga droplets at the surface, generating nanoholes [89]–[97]. These nanohole propitiate a good candidate for quantum structures nucleation sites such as NWs [98], QRs [99], or QDs [100]–[104]. High optical quality of Local Droplet Etched (LDE) QDs have been demonstrated [105]. The generation of nanoholes, also depends on the growth parameters such as As flux [106], crystal orientation [107], or temperature. Kerbst et al. studied how increasing the temperature (up to 620°C), the density of nanoholes in AlAs gets reduced [108]. The understanding of the Langmuir evaporation at the surface and the mechanisms behind the metal droplet nano-drilling is critical for the implementation of LDE for preferential QD nucleation on surface nanoholes. Heyn et al. have used the principles of droplet etching to estimate 680°C as the congruent temperature for GaAs [109]. Stemmann et al. observed how In droplets generated remain on the surface only for etching with low In concentration indicates a preferred desorption of In from the liquid droplets [110].

We have investigated the effect of using different As background pressures to perform the Local Droplet Etching (LDE), looking for the boundary conditions between droplet epitaxy and droplet etching and the role of As flux during droplet etching/epitaxy. The process dynamics is unknown, as investigations are usually carried out using only AFM ex-situ after the growth. Understanding the dynamics and being able to manipulate them by using the appropriate conditions would be key to design nanostructures and grow them using this method. Figure 3 shows an example of LDE on our LEEM-MBE equipment. We started off from mimicking the conditions reported by D. Fuster et al. [111]. This group investigated the role of As in the metal drilling at 500°C and they observed a preferential drilling towards certain crystallographic orientations as well as a crystallization in the vicinity of the nanohole due to DE conditions being intermixed with LDE . In our measurements we have also been able to observe such anisotropic effect as shown in Figure 3b. We have also observed, that the temperature (500°C) and Ga-flux (0.04 ML/s) and the As-flux (0.08 ML/s) used in this work, is too low for nano-drilling of the surface, leaving a mixture of DE and LDE.

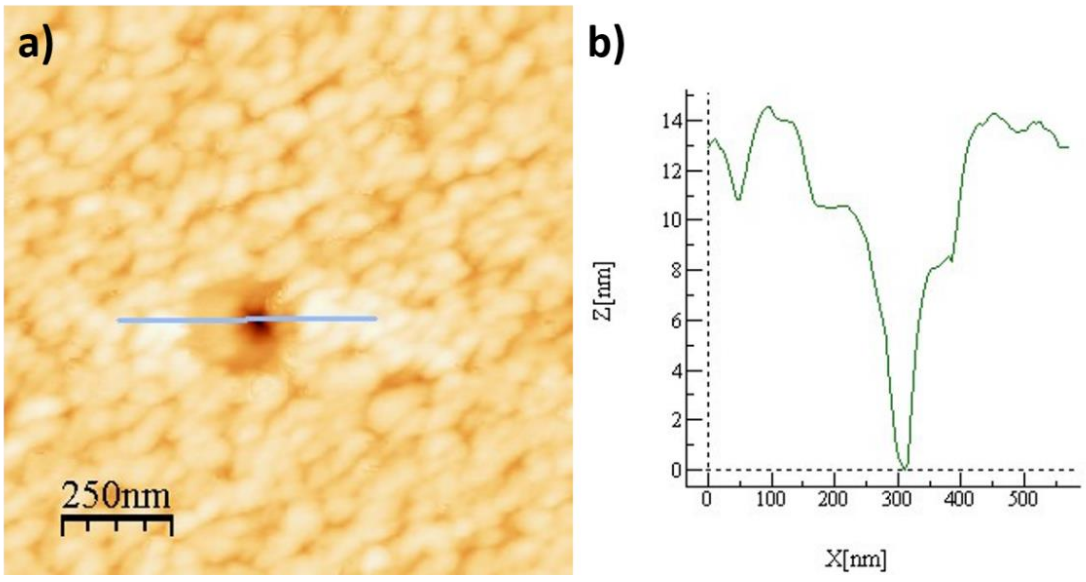

Figure 3. a) Nanohole in GaAs (001) by Droplet Etching generated in LEEM-MBE. b) Vertical profile corresponding to the blue line in a).

Currently, we are trying to increase the temperature to (600°C) and the Ga flux to 0.8 ML/s as presented by Heyn et al. [112], [113]. These conditions implicate a flux which might be too high and problematic with our LEEM-MBE limitations, since our system does not allow for long-range flux deposition (see chapter 3). Future work will develop this experiment further and will try to perform nano-drilling of surfaces under Heyn's conditions and give answers to the underlying mechanisms behind LDE for generation of site-controlled quantum structures.

Alumina mask for site-controlled quantum structures using anodisation cell

Anodisation is an electrochemical mechanism in which a metal surface is oxidised. This process modifies the properties of the metal at the surface, improving their resistance to corrosion, or their mechanical resistance. To be able to use the oxide layer generated on the surface of a metal for technical processes, the oxide structure must be stable and attain mechanical properties that would make the flesh of the material resistant to corrosion.

Pilling-Bedworth rule has been used as an indication of the quality of the oxide material for different metals. This rule, as shown in Eq. 2, stablish a ratio (PBR) between the volume of the elementary cell of the metal oxide to the volume of the elementary cell of the corresponding metal.

$$PBR = \frac{V_{oxide}}{V_{metal}} \qquad \text{Eq. 2}$$

Aluminium (Al), has a PBR of 1.29 [114], what makes its oxide a good candidate for different technological applications. Since the 1930's, anodised Al has been a popular material to use for a wide range of industries, due to its strength,

durability, conductivity and decorative finish. The applications for anodised Al include external architectural components, automotive parts and sports equipment.

The process of anodisation uses electrolysis in which, a metal sheet is submerged in an acidic solution between an anode and a cathode inside an acidic electrolyte and applying a voltage to favour a Reduction-Oxidation (Redox) reaction. A Redox reaction is a type of chemical reaction that involves a transfer of electrons between two species. When a direct current is applied, hydrogen is released at the cathode and oxygen is produced at the anode. For aluminium electrolysis, usually a sulphuric or oxalic solution is used. The oxidation of the surface in the case of aluminium (Al), provokes the formation of a hard-ceramic compound, Aluminium Oxide (Al_2O_3), also referred to as alumina [115].

Aluminium anodisation enables the production of an ordered network of nanometric pores. Alumina pores are usually 40 -150 nm in diameter, depending on the anodisation conditions and chemical treatments used [116]–[122]. The porous membranes can be used as an etching mask in order to create a pattern of holes on the surface of the chosen substrate. This masks with nano-holes can be applied in the growth of selective-area nano-structures [93], [123]–[125] or for optical applications [126]

We have developed an in-house Al anodisation cell that allows us to generate alumina porous membranes for MBE-selective growth. The cell was fabricated in Teflon and 2 O-rings isolate the copper anode from the electrolyte while still exposing the surface of the aluminium sheet placed in electrical contact with the copper anode. The Teflon cell is connected to a titanium cathode and immersed in oxalic acid [127] that is kept at 7°C. The whole set-up consists of a chiller that works with a solution of water and alcohol to keep the low temperature of the solution and a voltage source/meter that enable us to apply a voltage difference between the anode and the cathode and monitor the current between them. A simple sketch of this anodising cell is presented in Figure 4 for the sake of clarity. A detailed CAD file of the Teflon Anode Shell is illustrated in Figure 5.

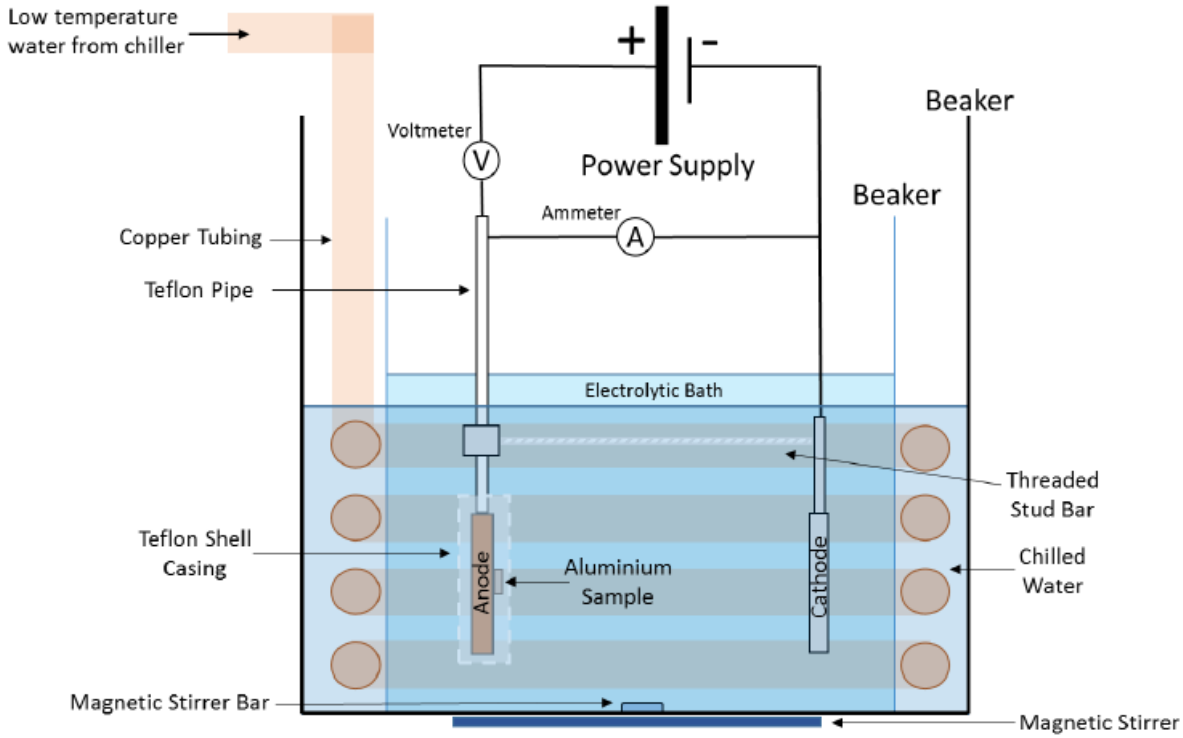

Figure 4. Sketch of an in-house electrolytic cell for aluminium oxidation. (Figure adapted from [128] with permission from publisher).

The anode and the cathode are kept at a constant potential and the current is monitored, which ensures reproducibility of the process and permits us to calculate the total current circulated which can be related to the oxide layer thickness. The control of the current allows us for detection of electrolyte leakages into the anode.

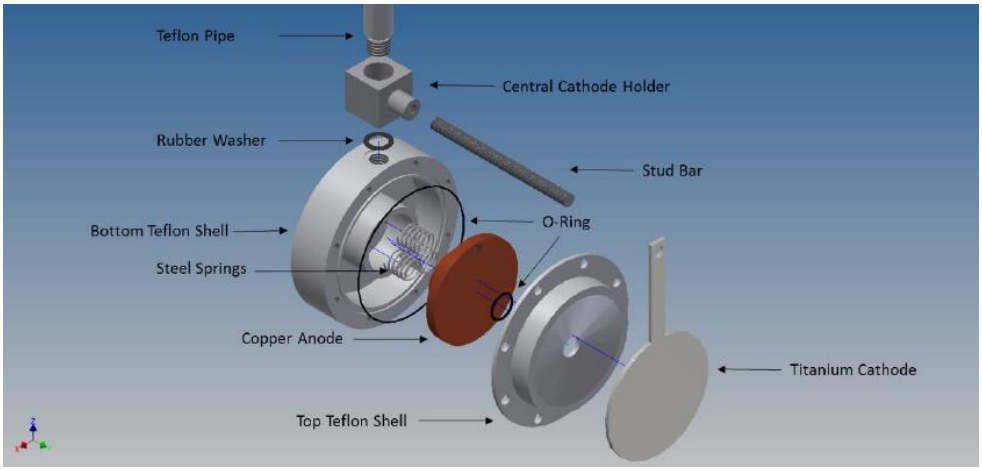

Figure 5. CAD file of the Teflon Casing Shell System in the Al-anodisation cell. (Figure adapted from [128] with permission from publisher).

For the anodisation process, we use a two-step anodisation process. The first anodisation generates a porous alumina layer. This layer tends to be inhomogeneous, so it is removed and re-anodised. The pores from the first anodisation act as nucleation sites for the new pores. This provides better ordering of pores [129], [130]. A visual example of this process is exposed in Figure 6.

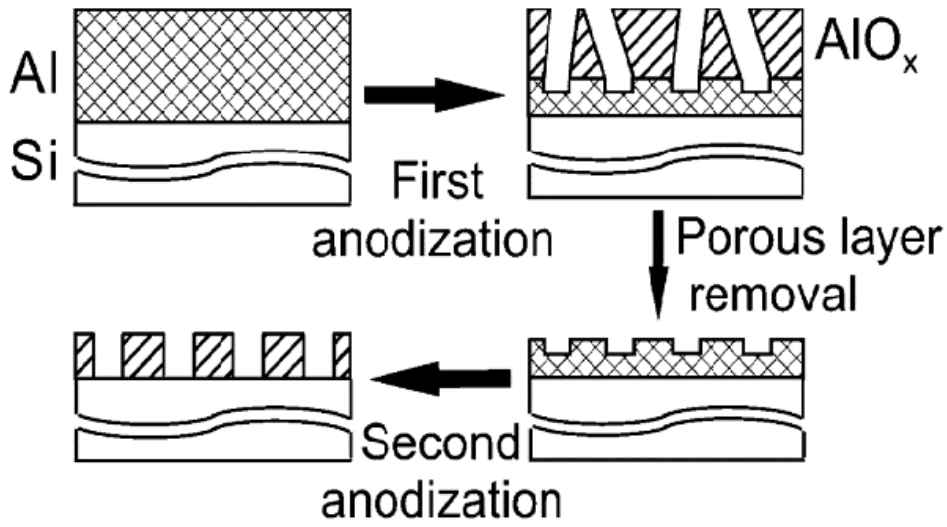

Figure 6. Two-step anodisation process for porous alumina masks. (Figure adapted from [129] with permission from publisher).

The most common approach for site-controlled QD growth approach is to grow on a pre-patterned substrate with an array of small holes that act as nucleation sites for QDs. The patterned substrate is usually prepared prior to growth [131]–[144]. One of the most popular methods for the pre-patterning of the surface is e-beam lithography [145]–[153]. e-beam lithography is a very precise type of lithography in which a beam of electrons is shone onto a light-sensitive photo-resist. The wavelength of the electrons is smaller than other type of radiation like UV light, which improves the spatial resolution. After the pattern is generated, the photo-resist is etched away, generating the desired pattern in the surface.

Despite of being one of the most prevailing methods, e-beam lithography, however, is a very slow process which makes difficult its implementation for large-scale industrial processes. Different cheaper alternatives have been proposed i.e. colloidal quantum dots [154]. However, this technique has clear limitations associated with weak surface bonding, carrier-carrier interactions, or blinking. We propose an alternative approach for pre-patterning substrates which would combine a reduced cost and a potentially high-efficiency and that could be easily implemented in the mass-production chain of site-controlled quantum-structure-based optoelectronic devices.

Aluminium anodization enables the production of an ordered network of nanometric pores. The pores are usually 40 -150 nm in diameter, depending on the oxidation conditions and chemical treatments used. The porous membranes can be used as a template for the fabrication of NWs or as a pre-patterned mask for the creation of site-controlled QDs.

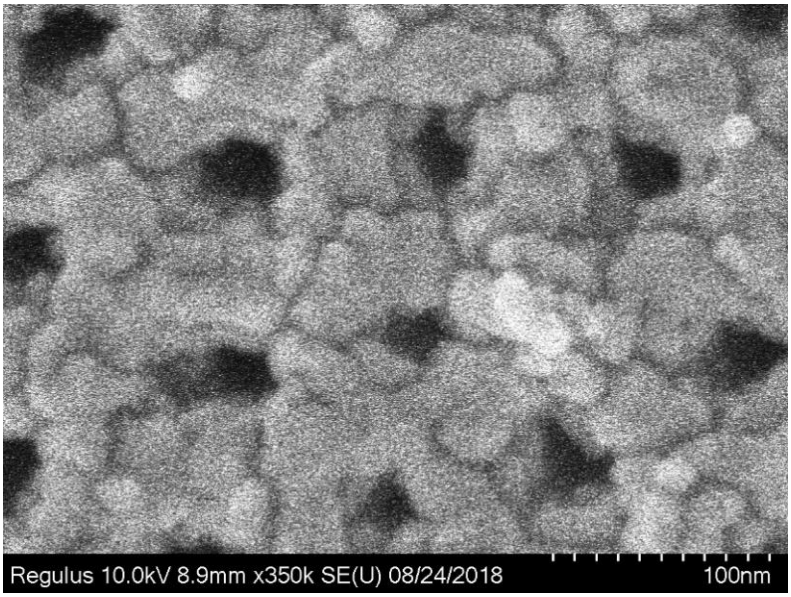

Figure 7. SEM micrograph of porous alumina before pore opening fabricated in Cardiff University.

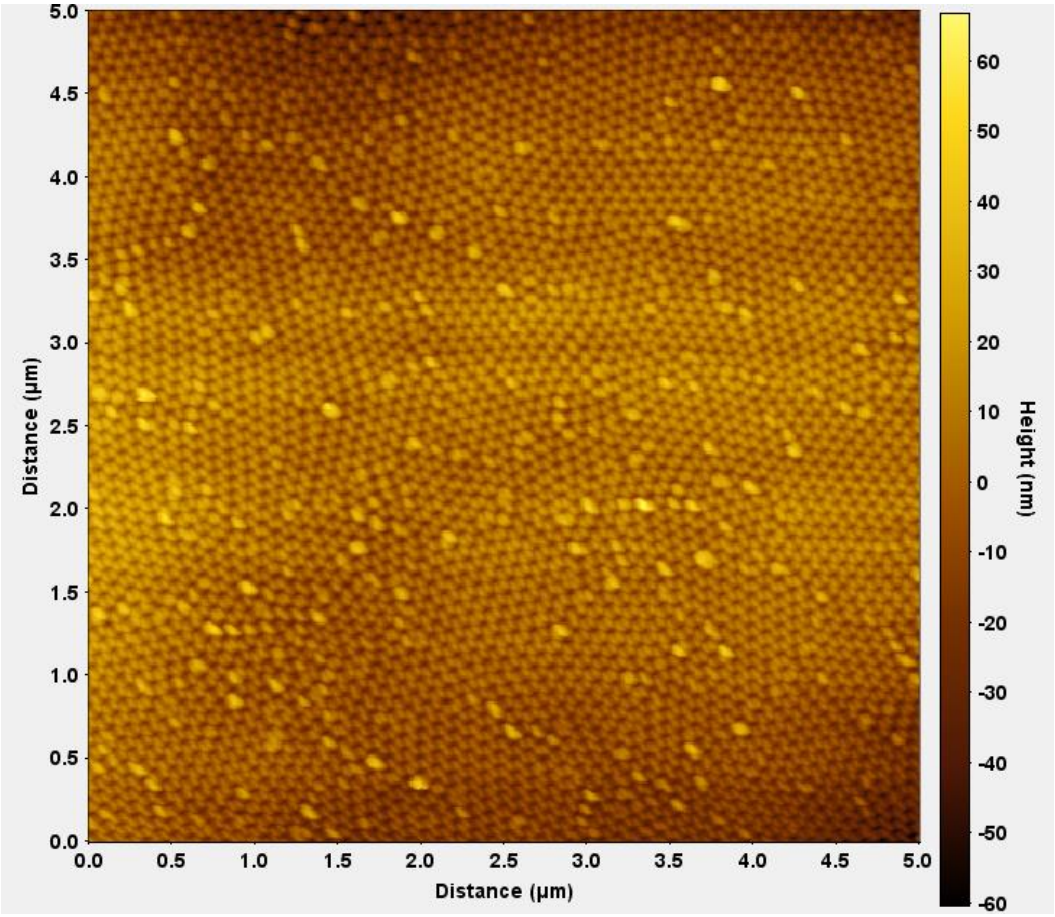

Figure 8. AFM images of homogeneously distributed nanopores generation by anodization of Al.

Anodic oxidation is an electrochemical process in which the surface of a metal, such as aluminium (Al), titanium (Ti) or niobium (Nb) is oxidised. The anodizing process modifies the crystal structure of the metal near the surface and improves the corrosive resistance of the metal surface as well as preparing the surface for further treatments or coatings [155]. Since the 1930's, anodized Al has been a popular material to use for a wide range of industries, due to its strength, durability, conductivity and decorative finish. The applications for anodized Al include external architectural components, automotive parts and sports equipment.

We have successfully developed and put to work the set-up for fabrication and transfer of alumina (Al_2O_3 or aluminium oxide) membranes. An example of porous aluminium oxide fabricated in Cardiff University is exhibited in Figure 7. Our experimental set-up enables us to anodize thick aluminium sheets, creating well-ordered networks of pores. A representation of the homogeneity and the distribution of these pores across the surface can be found in Figure 8.

Future work on this project will consist of alumina mask direct transfer to semiconductor substrates for the nucleation of nanostructures.

Our III-V LEEM-MBE system holds potential for the direct in-situ analysis of nucleation mechanisms of nanostructures. Future work carried out in any of the aforementioned approaches will lead to deep understanding of nucleation mechanisms which will ultimately assist the implementation of these techniques to the mass-production of quantum-structure-based optoelectronic devices.

References:

[1] P. P. Chougule, B. Sen, and T. D. Dongale, "Realization of processing In-memory computing architecture using Quantum Dot Cellular Automata," *Microprocess. Microsyst.*, vol. 52, pp. 49–58, 2017.

[2] A. Ajagekar and F. You, "Quantum computing for energy systems optimization: Challenges and opportunities," *Energy*, vol. 179, pp. 76–89, 2019.

[3] J. P. Aumasson, "The impact of quantum computing on cryptography," *Comput. Fraud Secur.*, vol. 2017, no. 6, pp. 8–11, 2017.

[4] P. Poole, "InP-Based Quantum Dot Lasers," in *Semiconductors and Semimetals*, 1st ed., vol. 86, Elsevier Inc., 2012.

[5] P. Bhattacharya and A. Arbor, "High-Performance Quantum-Dot Lasers," in *Comprehensive Semiconductor Science and Technology*, no. July 2015, 2016.

[6] S. G. Li *et al.*, "The developments of InP-based quantum dot lasers," *Infrared Phys. Technol.*, vol. 60, pp. 216–224, 2013.

[7] J. Wu, M. Tang, and H. Liu, "III–V quantum dot lasers epitaxially grown on Si substrates," in *Nanoscale Semiconductor Lasers*, Elsevier Inc., 2019.

[8] A. S. Karakoti, R. Shukla, R. Shanker, and S. Singh, "Surface functionalization of quantum dots for biological applications," *Adv. Colloid Interface Sci.*, vol. 215, pp. 28–45, 2015.

[9] A. M. Wagner, J. M. Knipe, G. Orive, and N. A. Peppas, "Quantum dots in biomedical applications," *Acta Biomater.*, vol. 94, pp. 44–63, 2019.

[10] N. Motta *et al.*, "Controlling the quantum dot nucleation site," *Mater. Sci. Eng. B Solid-State Mater. Adv. Technol.*, vol. 101, no. 1–3, pp. 77–88, 2003.

[11] H. Lan and Y. Ding, "Ordering, positioning and uniformity of quantum dot arrays," *Nano Today*, vol. 7, no. 2, pp. 94–123, 2012.

[12] A. W. Wood, K. Collar, J. Li, A. S. Brown, and S. E. Babcock, "Droplet-mediated formation of embedded GaAs nanowires in MBE GaAs $_{1-x}$ Bi $_{x}$ films," *Nanotechnology*, vol. 27, no. 11, p. 115704, 2016.

[13] Z. Gačević, D. Gómez Sánchez, and E. Calleja, "Formation mechanisms of gan nanowires grown by selective area growth homoepitaxy," *Nano Lett.*, vol. 15, no. 2, pp. 1117–1121, 2015.

[14] K. W. Schwarz and J. Tersoff, "From droplets to nanowires: Dynamics of vapor-liquid-solid growth," *Phys. Rev. Lett.*, vol. 102, no. 20, pp. 1–4, 2009.

[15] Y. J. Chang, P. J. Simmonds, B. Beekley, M. S. Goorsky, and J. C. S. Woo, "Selective-area growth of heavily n-doped GaAs nanostubs on Si(001) by molecular beam epitaxy," *Appl. Phys. Lett.*, vol. 108, no. 163106, pp. 1–5, 2016.

[16] K. Makihara, H. Deki, H. Murakami, S. Higashi, and S. Miyazaki, "Control of the nucleation density of Si quantum dots by remote hydrogen plasma treatment," *Appl. Surf. Sci.*, vol. 244, no. 1–4, pp. 75–78, 2005.

[17] K. A. Lozovoy, A. P. Kokhanenko, and A. V. Voitsekhovskii, "Critical thickness of transition from 2D to 3D growth and peculiarities of quantum dots formation in GexSi1-x/Sn/Si and Ge1-ySny/Si systems," *Surf. Sci.*, vol. 669, no. September 2017, pp. 45–49, 2018.

[18] D. Panda, A. Ahmad, H. Ghadi, S. Adhikary, B. Tongbram, and S. Chakrabarti, "Evidence of quantum dot size uniformity in strain-coupled multilayered In(Ga)As/GaAs QDs grown with constant overgrowth percentage," *J. Lumin.*, vol. 192, no. September 2016, pp. 562–566, 2017.

[19] P. Offermans, P. M. Koenraad, J. H. Wolter, K. Pierz, M. Roy, and P. A. Maksym, "Formation of InAs quantum dots and wetting layers in GaAs and AlAs analyzed by cross-sectional scanning tunneling microscopy," *Phys. E Low-Dimensional Syst. Nanostructures*, vol. 26, no. 1–4, pp. 236–240, 2005.

[20] O. Leifeld, A. Beyer, E. Müller, D. Grützmacher, and K. Kern, "Nucleation of Ge quantum dots on the C-alloyed Si(001) surface," *Thin Solid Films*, vol.

380, no. 1–2, pp. 176–179, 2000.

[21] D. Dorfs, R. Krahne, A. Falqui, L. Manna, C. Giannini, and D. Zanchet, *Quantum Dots: Synthesis and Characterization*, vol. 1–5, no. Ic. Elsevier Ltd., 2010.

[22] H. Zhang, Y. Chen, G. Zhou, C. Tang, and Z. Wang, "Wetting layer evolution and its temperature dependence during self-assembly of InAs/GaAs quantum dots.," *Nanoscale Res. Lett.*, vol. 7, no. 1, p. 600, 2012.

[23] A. Löffler *et al.*, "Influence of the strain on the formation of GaInAs/GaAs quantum structures," *J. Cryst. Growth*, vol. 286, no. 1, pp. 6–10, 2006.

[24] S. Sengupta, N. Halder, S. Chakrabarti, M. Herrera, M. Bonds, and N. D. Browning, "Investigation of the effect of varying growth pauses on the structural and optical properties of InAs/GaAs quantum dot heterostructures," *Superlattices Microstruct.*, vol. 46, no. 4, pp. 611–617, 2009.

[25] C. Shin, H. Jin, J. Chang, H. Kim, and W. W. Kim, "Computation of the preferential nucleation sites for Ge quantum dots on a relaxed SiGe layer," *Acta Mater.*, vol. 55, no. 1, pp. 225–231, 2007.

[26] T. Konishi and S. Tsukamoto, "Spatial point analysis of quantum dot nucleation sites on InAs wetting layer," *Surf. Sci.*, vol. 605, no. 5–6, pp. L1–L5, 2011.

[27] J. E. Prieto and I. Markov, "Stranski–Krastanov mechanism of growth and the effect of misfit sign on quantum dots nucleation," *Surf. Sci.*, vol. 664, no. February, pp. 172–184, 2017.

[28] M. Gutiérrez *et al.*, "Critical barrier thickness for the formation of InGaAs/GaAs quantum dots," *Mater. Sci. Eng. C*, vol. 25, no. 5–8, pp. 798–803, 2005.

[29] Q. Gong, R. Nötzel, and J. H. Wolter, "Strain-driven (In,Ga)As growth instability on GaAs [311]A and [311]B: Self-organization of template for InAs quantum dot nucleation control," *MBE 2002 - 2002 12th Int. Conf. Mol.*

Beam Ep., vol. 251, pp. 321–322, 2002.

[30] P. Howe, B. Abbey, E. C. Le Ru, R. Murray, and T. S. Jones, "Strain-interactions between InAs/GaAs quantum dot layers," *Thin Solid Films*, vol. 464–465, pp. 225–228, 2004.

[31] F. Patella *et al.*, "Structural study of the InAs quantum-dot nucleation on GaAs(001)," *Microelectronics J.*, vol. 34, no. 5–8, pp. 419–422, 2003.

[32] V. H. Méndez-García, A. Pérez-Centeno, and M. López-López, "Synthesis of GaAs quantum dots on Si-layers on AlGaAs films grown on GaAs(100)," *Thin Solid Films*, vol. 433, no. 1-2 SPEC., pp. 63–67, 2003.

[33] B. D. Gerardot, I. Shtrichman, D. Hebert, and P. M. Petroff, "Tuning of the electronic levels in vertically stacked InAs/GaAs quantum dots using crystal growth kinetics," *J. Cryst. Growth*, vol. 252, no. 1–3, pp. 44–50, 2003.

[34] Q. Zhuang, H. Li, L. Pan, J. Li, M. Kong, and L. Lin, "Self-organization of the InGaAs/GaAs quantum dots superlattice," *J. Cryst. Growth*, vol. 201, pp. 1161–1163, 1999.

[35] Y. Zhang, K. G. Eyink, L. Grazulis, M. Hill, J. Peoples, and K. Mahalingam, "Stacking InAs quantum dots over ErAs semimetal nanoparticles on GaAs (0 0 1) using molecular beam epitaxy," *J. Cryst. Growth*, vol. 477, pp. 19–24, 2017.

[36] X. Liu *et al.*, "Synthesis of high quality and stability CdS quantum dots with overlapped nucleation-growth process in large scale," *J. Colloid Interface Sci.*, vol. 354, no. 1, pp. 15–22, 2011.

[37] E. Müller, E. Ribeiro, T. Heinzel, K. Ensslin, G. Medeiros-Ribeiro, and P. M. Petroff, "TEM study of InAs self-assembled quantum dots in GaAs," *Thin Solid Films*, vol. 336, no. 1–2, pp. 38–41, 1998.

[38] D. Hernández-Maldonado *et al.*, "Transmission electron microscopy study of vertical quantum dots molecules grown by droplet epitaxy," *Appl. Surf. Sci.*, vol. 256, no. 18, pp. 5659–5661, 2010.

[39] X. D. Wang, Z. C. Niu, H. Wang, and S. L. Feng, "Formation of InAs quantum dots on low-temperature GaAs epi-layer," *J. Cryst. Growth*, vol. 218, no. 2, pp. 209–213, 2000.

[40] S. Kadkhodazadeh, "High resolution STEM of quantum dots and quantum wires," *Micron*, vol. 44, no. 1, pp. 75–92, 2013.

[41] G. Nicotra, S. Lombardo, R. Puglisi, C. Spinella, G. Ammendola, and C. Gerardi, "Observation of the nucleation kinetics of Si quantum dots on SiO2 by EFTEM," *Microsc. Semicond. Mater. 2003*, vol. 205, pp. 119–122, 2018.

[42] M. C. Xu, Y. Temko, T. Suzuki, and K. Jacobi, "On the location of InAs quantum dots on GaAs(0 0 1)," *Surf. Sci.*, vol. 589, no. 1–3, pp. 91–97, 2005.

[43] S. M. Kennedy *et al.*, "Characterizing the geometry of InAs nanowires using mirror electron microscopy," *Nanotechnology*, vol. 23, no. 12, p. 125703, 2012.

[44] L. Bányai and S. W. Koch, "Semiconductor quantum dots," *World Sci. Ser. At. Mol. Opt. physics,* vol. 20, pp. 352–360, 1993.

[45] I. N. Stranski and L. Krastanow, "Zur Theorie der orientierten Ausscheidung von Ionenkristallen aufeinander.," *Akad. der Wissenschaften und der Lit.*, vol. 72, no. 1, pp. 76–76, 1939.

[46] G. Biasiol and S. Heun, "Compositional mapping of semiconductor quantum dots and rings," *Phys. Rep.*, vol. 500, no. 4–5, pp. 117–173, 2011.

[47] K. Jacobi, "Atomic structure of InAs quantum dots on GaAs," *Prog. Surf. Sci.*, vol. 71, pp. 185–215, 2003.

[48] E. Eugenio-López *et al.*, "InAs quantum dots nucleation on (100) and anisotropic (631)-oriented GaAs substrates," *Phys. E Low-Dimensional Syst. Nanostructures*, vol. 95, no. August 2017, pp. 22–26, 2018.

[49] S. Sanguinetti *et al.*, "Self-aggregation of InAs quantum dots on (N11) GaAs substrates," *Thin Solid Films*, vol. 336, no. 1–2, pp. 9–12, 1998.

[50] L. Höglund, E. Petrini, C. Asplund, H. Malm, J. Y. Andersson, and P. O. Holtz,

"Optimising uniformity of InAs/(InGaAs)/GaAs quantum dots grown by metal organic vapor phase epitaxy," *Appl. Surf. Sci.*, vol. 252, no. 15, pp. 5525–5529, 2006.

[51] Z. H. Tian, Y. J. Wang, J. H. Xu, and G. S. Luo, "Intensification of nucleation stage for synthesizing high quality CdSe quantum dots by using preheated precursors in microfluidic devices," *Chem. Eng. J.*, vol. 302, pp. 498–502, 2016.

[52] F. Mazen, T. Baron, J. M. Hartmann, G. Brémond, and M. N. Séméria, "Influence of carrier and doping gases on silicon quantum dots nucleation," *J. Cryst. Growth*, vol. 255, no. 3–4, pp. 250–257, 2003.

[53] T. Ishihara, S. Lee, M. Akabori, J. Motohisa, and T. Fukui, "Dependence on In content of InxGa1-xAs quantum dots grown along GaAs multiatomic steps by MOVPE," *J. Cryst. Growth*, vol. 237–239, no. 1-4 II, pp. 1476–1480, 2002.

[54] S. Zhou, Y. Liu, H. Ye, D. Wang, P. Lu, and Z. Yu, "Calculation of critical size of coherent InAs quantum dot on GaAs substrate," *Phys. E Low-Dimensional Syst. Nanostructures*, vol. 46, pp. 52–56, 2012.

[55] S. Zhou *et al.*, "The preferential formation site of dislocations in InAs/GaAs quantum dots," *Superlattices Microstruct.*, vol. 51, no. 1, pp. 53–61, 2012.

[56] D. Schuh *et al.*, "Controlled positioning of self-assembled InAs quantum dots on (1 1 0) GaAs," *Phys. E Low-Dimensional Syst. Nanostructures*, vol. 26, no. 1–4, pp. 72–76, 2005.

[57] S. C. Fortina *et al.*, "InAs quantum dots grown on nonconventionally oriented GaAs substrates," *J. Cryst. Growth*, vol. 187, no. 1, pp. 126–132, 1998.

[58] N. Weir, R. Yao, C.-S. Lee, and W. Guo., "Growth of InAs quantum dots on vicinal GaAs substrates by molecular beam epitaxy," *J. Cryst. Growth*, vol. 251, no. 1–4, pp. 201–207, 2003.

[59] F. Fournier *et al.*, "Growth dynamics of InGaAsGaAs by MBE," *J. Cryst. Growth*, vol. 175–176, P, pp. 203–210, 1997.

[60] C. C. Ahia, N. Tile, and J. R. Botha, "Dependence of optimum V/III ratio on substrate orientation, and influence of buffer layer on MOVPE grown InSb/GaSb quantum dots," *J. Cryst. Growth*, vol. 507, no. October 2018, pp. 157–162, 2019.

[61] I. Kamiya, T. Shirasaka, K. Shimomura, and D. M. Tex, "Influence of in and As fluxes on growth of self-assembled InAs quantum dots on GaAs(0 0 1)," *J. Cryst. Growth*, vol. 323, no. 1, pp. 219–222, 2011.

[62] G. J. Whaley and P. I. Cohen, "Relaxation of strained InGaAs during molecular beam epitaxy," *Appl. Phys. Lett.*, vol. 57, no. 2, pp. 144–146, 1990.

[63] E. A. Stach *et al.*, "Effect of the surface upon misfit dislocation velocities during the growth and annealing of SiGe/Si (001) heterostructures," *J. Appl. Phys.*, vol. 83, no. 4, pp. 1931–1937, 1998.

[64] B. A. Joyce, P. C. Kelires, A. G. Naumovets, and D. D. Vvedensky, *Quantum Dots: Fundamentals, Applications, and Frontiers*. 2003.

[65] S. Sanguinetti and N. Koguchi, "Droplet epitaxy of nanostructures," in *Molecular Beam Epitaxy*, Elsevier Inc., 2013.

[66] M. Y. Li *et al.*, "Formation of Ga droplets on patterned GaAs (100) by molecular beam epitaxy," *Nanoscale Res. Lett.*, vol. 7, no. 1, pp. 1–9, 2012.

[67] L. Gao *et al.*, "Observation of Ga metal droplet formation on photolithographically patterned GaAs (100) surface by droplet epitaxy," *IEEE Trans. Nanotechnol.*, vol. 11, no. 5, pp. 985–991, 2012.

[68] J. Tersoff, D. E. Jesson, and W. X. Tang, "Decomposition controlled by surface morphology during Langmuir evaporation of GaAs," *Phys. Rev. Lett.*, vol. 105, no. 3, pp. 1–4, 2010.

[69] J. G. Keizer, J. Bocquel, P. M. Koenraad, T. Mano, T. Noda, and K. Sakoda, "Atomic scale analysis of self assembled GaAs/AlGaAs quantum dots grown by droplet epitaxy," *Appl. Phys. Lett.*, vol. 96, no. 062101, pp. 1–4, 2010.

[70] D. P. Kumah, S. Shusterman, Y. Paltiel, Y. Yacoby, and R. Clarke, "Atomic-

scale mapping of quantum dots formed by droplet epitaxy.," *Nat. Nanotechnol.*, vol. 4, no. 12, pp. 835–838, 2009.

[71] Z. B. Chen *et al.*, "Preferential nucleation and growth of InAs/GaAs(0 0 1) quantum dots on defected sites by droplet epitaxy," *Scr. Mater.*, vol. 69, no. 8, pp. 638–641, 2013.

[72] A. Nemcsics, "Quantum Dots Prepared by Droplet Epitaxial Method," in *Quantum Dots - Theory and Application*, 2015.

[73] M. Elborg, T. Noda, T. Mano, M. Jo, Y. Sakuma, and K. Sakoda, "Self-assembly of Ga droplets attached to GaAs quantum dots," *J. Cryst. Growth*, vol. 378, pp. 53–56, 2013.

[74] M. Y. Li *et al.*, "Sharp contrast of the density and size of Ga metal droplets on photolithographically patterned GaAs (100) by droplet epitaxy under an identical growth environment," *Phys. Status Solidi Appl. Mater. Sci.*, vol. 209, no. 6, pp. 1075–1079, 2012.

[75] C. Frigeri, S. Bietti, G. Isella, and S. Sanguinetti, "Structural characterization of GaAs self-assembled quantum dots grown by Droplet Epitaxy on Ge virtual substrates on Si," *Appl. Surf. Sci.*, vol. 267, pp. 86–89, 2013.

[76] J. Bocquel, A. D. Giddings, T. Mano, T. J. Prosa, D. J. Larson, and P. M. Koenraad, "Composition profiling of GaAs/AlGaAs quantum dots grown by droplet epitaxy," *Appl. Phys. Lett.*, vol. 105, no. 153102, pp. 1–4, 2014.

[77] J. Wu and Z. M. Wang, "Droplet epitaxy for advanced optoelectronic materials and devices," *J. Phys. D. Appl. Phys.*, vol. 47, no. 17, p. 173001, 2014.

[78] N. Ha *et al.*, "Droplet epitaxy growth of telecom InAs quantum dots on metamorphic InAlAs / GaAs (111) A," *Jpn. J. Appl. Phys.*, vol. 54, p. 04DG07, 2015.

[79] S. Bietti *et al.*, "Fabrication of GaAs quantum dots by droplet epitaxy on Si/Ge virtual substrate," *IOP Conf. Ser. Mater. Sci. Eng.*, vol. 6, no. 001, p. 012009, 2009.

[80] M. A. Vasilenko, I. G. Neizvestny, and N. L. Shwartz, "Formation of GaAs nanostructures by droplet epitaxy - Monte Carlo simulation," *Comput. Mater. Sci.*, vol. 102, pp. 286–292, 2015.

[81] T. Mano, K. Watanabe, S. Tsukamoto, H. Fujioka, M. Oshima, and N. Koguchi, "New self-organized growth method for InGaAs quantum dots on GaAs(001) using droplet epitaxy," *Japanese J. Appl. Physics, Part 2 Lett.*, vol. 38, no. 9 A/B, pp. 2–5, 1999.

[82] Á. Nemcsics, "On the shape formation of the droplet epitaxial quantum dots," *Microelectron. Reliab.*, vol. 56, pp. 73–77, 2016.

[83] C. Somaschini, "PhD Thesis: Development of advanced GaAs nanostructures by Droplet Epitaxy," Universitá degli Studi di Milano-Bicocca, 2010.

[84] S. Bietti *et al.*, "Complex quantum ring structures formed by droplet epitaxy," *Appl. Phys. Lett.*, vol. 97, no. 3, pp. 1–4, 2010.

[85] M. Kunrugsa, K. H. P. Tung, A. J. Danner, S. Panyakeow, and S. Ratanathammaphan, "Fabrication of GaSb quantum rings on GaAs(0 0 1) by droplet epitaxy," *J. Cryst. Growth*, vol. 425, pp. 287–290, 2015.

[86] J. Wu *et al.*, "Self-assembly of multiple stacked nanorings by vertically correlated droplet epitaxy," *Adv. Funct. Mater.*, vol. 24, no. 4, pp. 530–535, 2014.

[87] M. Elborg *et al.*, "Self-assembly of vertically aligned quantum ring-dot structure by Multiple Droplet Epitaxy," *J. Cryst. Growth*, vol. 477, pp. 239–242, 2017.

[88] Z. Y. Zhou, C. X. Zheng, W. X. Tang, J. Tersoff, and D. E. Jesson, "Origin of quantum ring formation during droplet epitaxy," *Phys. Rev. Lett.*, vol. 111, no. 3, pp. 1–5, 2013.

[89] Z. M. Wang, B. L. Liang, K. A. Sablon, and G. J. Salamo, "Nanoholes fabricated by self-assembled gallium nanodrill on GaAs(100)," *Appl. Phys. Lett.*, vol. 90, no. 11, 2007.

[90] X. Li *et al.*, "Origin of nanohole formation by etching based on droplet epitaxy," *Nanoscale*, vol. 6, no. 5, pp. 2675–2681, 2014.

[91] S. Li *et al.*, "Thermal etching process of microscale pits on the GaAs(001) surface," *Phys. Status Solidi - Rapid Res. Lett.*, vol. 6, no. 1, pp. 25–27, 2012.

[92] C. Heyn, A. Stemmann, and W. Hansen, "Dynamics of self-assembled droplet etching," *Appl. Phys. Lett.*, vol. 95, no. 17, 2009.

[93] R. P. Sugavaneshwar, T. Nagao, and K. K. Nanda, "Fabrication of highly dense nanoholes by self-assembled gallium droplet on silicon surface," *Mater. Express*, vol. 2, no. 3, pp. 245–250, 2012.

[94] P. Boonpeng, W. Jevasuwan, S. Panyakeow, and S. Ratanathammaphan, "Fabrication of self-assembled InGaAs squarelike nanoholes on GaAs(001) by droplet epitaxy," *Jpn. J. Appl. Phys.*, vol. 49, no. 4 PART 2, 2010.

[95] C. Heyn, "Kinetic model of local droplet etching," *Phys. Rev. B - Condens. Matter Mater. Phys.*, vol. 83, no. 16, pp. 1–5, 2011.

[96] C. Heyn, D. Sonnenberg, A. Graf, J. Kerbst, A. Stemmann, and W. Hansen, "Local droplet etching-Nanoholes, quantum dots, and air-gap heterostructures," *AIP Conf. Proc.*, vol. 1598, pp. 91–94, 2014.

[97] A. Stemmann, C. Heyn, T. Köppen, T. Kipp, and W. Hansen, "Local droplet etching of nanoholes and rings on GaAs and AlGaAs surfaces," *Appl. Phys. Lett.*, vol. 93, no. 12, pp. 1–4, 2008.

[98] C. Heyn, D. Sonnenberg, T. Bartsch, A. Wetzel, J. Kerbst, and W. Hansen, "GaAs nanopillars by self-assembled droplet etching," *J. Cryst. Growth*, vol. 378, pp. 446–449, 2013.

[99] C. Heyn *et al.*, "Self-assembly of semiconductor quantum rings by local droplet etching," *J. Nanoelectron. Optoelectron.*, vol. 6, no. 1, pp. 62–67, 2011.

[100] E. Zallo, P. Atkinson, A. Rastelli, and O. G. Schmidt, "Controlling the formation of quantum dot pairs using nanohole templates," *J. Cryst. Growth*,

vol. 338, no. 1, pp. 232–238, 2012.

[101] J. Wu, Z. M. Wang, X. Li, Y. I. Mazur, and G. J. Salamo, "Fabrication of ultralow-density quantum dots by droplet etching epitaxy," *J. Mater. Res.*, vol. 32, no. 21, pp. 4095–4101, 2017.

[102] C. Heyn, A. Küster, A. Gräfenstein, A. Ungeheuer, A. Graf, and W. Hansen, "GaAs quantum dot molecules filled into droplet etched nanoholes," *J. Cryst. Growth*, vol. 477, pp. 235–238, 2017.

[103] Y. Nakamura, N. Ikeda, S. Ohkouchi, Y. Sugimoto, H. Nakamura, and K. Asakawa, "Regular array of InGaAs quantum dots with 100-nm-periodicity formed on patterned GaAs substrates," *Phys. E Low-Dimensional Syst. Nanostructures*, vol. 21, no. 2–4, pp. 551–554, 2004.

[104] L. Jihoon *et al.*, "Low-Density Quantum Dot Molecules by Selective Etching Using in Droplet as a Mask," *IEEE Trans. Nanotechnol.*, vol. 10, no. 3, pp. 600–605, 2011.

[105] C. Heyn *et al.*, "Mechanism and applications of local droplet etching," *J. Cryst. Growth*, vol. 323, no. 1, pp. 263–266, 2011.

[106] C. Heyn, M. Zocher, S. Schnüll, and W. Hansen, "Role of Arsenic During Aluminum Droplet Etching of Nanoholes in AlGaAs," *Nanoscale Res. Lett.*, vol. 11, no. 1, pp. 5–11, 2016.

[107] D.- Berlin, "Thermal etching of GaAs (1 1 3) surfaces," *Powder Technol.*, vol. 9, pp. 115–119, 1998.

[108] J. Kerbst, C. Heyn, T. Slobodskyy, and W. Hansen, "Density limits of high temperature and multiple local droplet etching on AlAs," *J. Cryst. Growth*, vol. 389, pp. 18–22, 2014.

[109] C. Heyn and D. E. Jesson, "Congruent evaporation temperature of molecular beam epitaxy grown GaAs (001) determined by local droplet etching," *Appl. Phys. Lett.*, vol. 107, no. 16, pp. 10–14, 2015.

[110] A. Stemmann *et al.*, "Local etching of nanoholes and quantum rings with Inx

Ga1-x droplets," *J. Appl. Phys.*, vol. 106, no. 6, pp. 5–8, 2009.

[111] D. Fuster, Y. González, and L. González, "Fundamental role of arsenic flux in nanohole formation by Ga droplet etching on GaAs(001)," *Nanoscale Res. Lett.*, vol. 9, no. 1, pp. 1–6, 2014.

[112] C. Heyn, T. Bartsch, S. Sanguinetti, D. Jesson, and W. Hansen, "Dynamics of mass transport during nanohole drilling by local droplet etching.," *Nanoscale Res. Lett.*, vol. 10, p. 67, 2015.

[113] C. Heyn, S. Schnüll, D. E. Jesson, and W. Hansen, "Thermally controlled widening of droplet etched nanoholes," *Nanoscale Res. Lett.*, vol. 9, no. 1, p. 285, 2014.

[114] C. Xu and W. Gao, "Pilling-Bedworth ratio for oxidation of alloys Pilling-Bedworth ratio for oxidation of alloys," *Mater. Res. Innov.*, vol. 3, pp. 231–235, 2000.

[115] M. Network, "Processes in the spotlight," *What types of Anodising are there, and which materials can you Anodise?*, 2019. [Online]. Available: https://www.manufacturingnetwork.com/knowledgebase/view/40#. [Accessed: 11-Aug-2019].

[116] Ł. S. Małgorzata Norek, "Anodic alumina growth on Al substrates after multi-variant mechanical and heat treatment," *Surf. Coat. Technol.*, vol. 357, no. October 2018, pp. 802–810, 2019.

[117] L. Zaraska, G. D. Sulka, and M. Jasku, "Anodic alumina membranes with defined pore diameters and thicknesses obtained by adjusting the anodizing duration and pore opening / widening time," *J. Solid State Electrochem*, vol. 15, pp. 2427–2436, 2011.

[118] M. Michalska-doma, W. Jerzy, and M. Salerno, "Effect of inter-electrode separation in the fabrication of nanoporous alumina by anodization," *J. Electroanal. Chem.*, vol. 823, no. April, pp. 47–53, 2018.

[119] F. Casanova, C. Chiang, A. M. Ruminski, L. Berkeley, I. K. Schuller, and S. Diego, "Effect of surface interactions on the hysteresis of capillary

condensation in nanopores," *Europhys. Lett.*, vol. 81, no. 26003, pp. 1–5, 2008.

[120] K. M. Chahrour, N. M. Ahmed, M. R. Hashim, N. G. Elfadill, A. M. Al-diabat, and M. Bououdina, "Influence of wet etching time cycles on morphology features of thin porous Anodic Aluminum oxide (AAO) template for nanostructure's synthesis," *J. Phys. Chem. Solids*, vol. 87, pp. 1–8, 2015.

[121] W. J. St and Z. Bojar, "Synthesis of anodic aluminum oxide (AAO) at relatively high temperatures . Study of the in fl uence of anodization conditions on the alumina structural features," *Surf. Coat. Technol.*, vol. 206, pp. 265–272, 2011.

[122] L. Cantelli and J. S. Santos, "The effect of anodization temperature on optical properties of nanoporous anodic alumina (NAA) fi lms," *J. Electroanal. Chem.*, vol. 780, pp. 386–390, 2016.

[123] L. A. Meier, A. E. Alvarez, D. R. Salinas, and M. C. Barrio, "Formation of dense alumina nanowires from anodic alumina membranes," *Mater. Lett.*, vol. 85, pp. 146–148, 2012.

[124] C. E. Chiang, C. Li, I. V Roshchin, A. M. Ruminski, M. J. Sailor, and I. K. Schuller, "Gas adsorption and capillary condensation in nanoporous alumina films," *Nanotechnology*, vol. 19, no. 315709, pp. 1–6, 2008.

[125] T. Ohgai, "Magnetoresistance of Nanowires Electrodeposited into Anodized Aluminum Oxide Nanochannels," in *Nanowires - Recent Advances*, 2012, pp. 101–125.

[126] W. A. El-said, M. Abdel-shakour, and A. M. Abd-elnaiem, "An efficient and low-cost photoanode for backside illuminated dye-sensitized solar cell using 3D porous alumina," *Mater. Lett.*, vol. 222, pp. 126–130, 2018.

[127] M. K. Kushwaha, "A comparative Study of Different Electrolytes for Obtaining Thick and Well-ordered nano-porous Anodic Aluminium Oxide (AAO) films," *Procedia Mater. Sci.*, vol. 5, pp. 1266–1273, 2014.

[128] J. Grant, "Year 3 Project Report: Crystal Surface Optimization," 2017.

[129] C. Li, I. V Roshchin, X. Batlle, M. Viret, and I. K. Schuller, "Fabrication and structural characterization of highly ordered sub-100-nm planar magnetic nanodot arrays over 1 cm 2 coverage area," *J. Appl. Phys.*, vol. 100, no. 074318, pp. 1–7, 2006.

[130] S. Ate, E. Baran, and B. Yaz, "The nanoporous anodic alumina oxide formed by two-step anodization," *Thin Solid Films*, vol. 648, pp. 94–102, 2018.

[131] P. Atkinson, O. G. Schmidt, S. P. Bremner, and D. A. Ritchie, "Formation and ordering of epitaxial quantum dots," *Comptes Rendus Phys.*, vol. 9, no. 8, pp. 788–803, 2008.

[132] J. N. Aqua and X. Xu, "Growth of quantum dots on pit-patterns," *Surf. Sci.*, vol. 639, pp. 20–24, 2015.

[133] S. Birudavolu *et al.*, "Selective area growth of InAs quantum dots formed on a patterned GaAs substrate," *Appl. Phys. Lett.*, vol. 85, no. 12, pp. 2337–2339, 2004.

[134] M. Schramboeck, W. Schrenk, T. Roch, A. M. Andrews, M. Austerer, and G. Strasser, "Self organized InAs quantum dots grown on patterned GaAs substrates," *Microelectron. Eng.*, vol. 83, no. 4-9 SPEC. ISS., pp. 1573–1576, 2006.

[135] B. D. Gerardot *et al.*, "Self-assembling quantum dot lattices through nucleation site engineering," *J. Cryst. Growth*, vol. 236, no. 4, pp. 647–654, 2002.

[136] M. Mehta, D. Reuter, A. Melnikov, A. D. Wieck, and A. Remhof, "Site-selective growth of self-assembled InAs quantum dots on focused ion beam patterned GaAs," *Phys. E Low-Dimensional Syst. Nanostructures*, vol. 40, no. 6, pp. 2034–2036, 2008.

[137] S. Hussain, A. Pozzato, M. Tormen, V. Zannier, and G. Biasiol, "III-V site-controlled quantum dots on Si patterned by nanoimprint lithography," *J. Cryst. Growth*, vol. 437, pp. 59–62, 2016.

[138] S. Ohkouchi, Y. Nakamura, H. Nakamura, and K. Asakawa, "Indium nano-dot

arrays formed by field-induced deposition with a Nano-Jet Probe for site-controlled InAs/GaAs quantum dots," *Thin Solid Films*, vol. 464–465, pp. 233–236, 2004.

[139] J. Lee *et al.*, "InGaAs quantum dot molecules during selective etching using an in droplet mask," *J. Phys. D. Appl. Phys.*, vol. 44, no. 2, pp. 2–7, 2011.

[140] J. Tommila *et al.*, "Nanoimprint lithography patterned GaAs templates for site-controlled InAs quantum dots," *J. Cryst. Growth*, vol. 323, no. 1, pp. 183–186, 2011.

[141] M. Schramboeck, A. M. Andrews, T. Roch, W. Schrenk, A. Lugstein, and G. Strasser, "Nano-patterning and growth of self-assembled quantum dots," *Microelectronics J.*, vol. 37, no. 12, pp. 1532–1534, 2006.

[142] J. Martín-Sánchez *et al.*, "Ordered InAs quantum dots on pre-patterned GaAs (0 0 1) by local oxidation nanolithography," *J. Cryst. Growth*, vol. 284, no. 3–4, pp. 313–318, 2005.

[143] X. Xu and J. N. Aqua, "Quantum dot growth on a stripe-pattern," *Thin Solid Films*, vol. 543, pp. 7–10, 2013.

[144] M. Zander, J. Nishinaga, and Y. Horikoshi, "Selective area growth of InAs nanostructures on faceted GaAs microstructures by migration enhanced epitaxy," *J. Cryst. Growth*, vol. 378, pp. 480–484, 2013.

[145] G. Biasiol *et al.*, "Composition uniformity of site-controlled InAs/GaAs quantum dots," *J. Cryst. Growth*, vol. 323, no. 1, pp. 176–179, 2011.

[146] M. Helfrich, B. Terhalle, Y. Ekinci, and D. M. Schaadt, "Controlling structural properties of positioned quantum dots," *J. Cryst. Growth*, vol. 371, pp. 39–44, 2013.

[147] T. Umeda, K. Kumakura, J. Motohisa, and T. Fukui, "InAs quantum dot formation on GaAs pyramids by selective area MOVPE," *Phys. E Low-Dimensional Syst. Nanostructures*, vol. 2, no. 1–4, pp. 714–719, 1998.

[148] P. Atkinson, S. P. Bremner, D. Anderson, G. A. C. Jones, and D. A. Ritchie,

"Molecular beam epitaxial growth of site-controlled InAs quantum dots on pre-patterned GaAs substrates," *Microelectronics J.*, vol. 37, no. 12, pp. 1436–1439, 2006.

[149] P. Atkinson *et al.*, "Site control of InAs quantum dot nucleation by ex situ electron-beam lithographic patterning of GaAs substrates," *Phys. E Low-Dimensional Syst. Nanostructures*, vol. 32, no. 1-2 SPEC. ISS., pp. 21–24, 2006.

[150] S. Kohmoto, H. Nakamura, T. Ishikawa, S. Nishikawa, T. Nishimura, and K. Asakawa, "Site-controlled self-organization of InAs quantum dots," *Mater. Sci. Eng. B Solid-State Mater. Adv. Technol.*, vol. 88, no. 2–3, pp. 292–297, 2002.

[151] A. Huggenberger *et al.*, "Site-controlled In(Ga)As/GaAs quantum dots for integration into optically and electrically operated devices," *J. Cryst. Growth*, vol. 323, no. 1, pp. 194–197, 2011.

[152] C. X. Cui *et al.*, "Study of nucleation positions of InAs islands on stripe-patterned GaAs (1 0 0) substrate," *Phys. E Low-Dimensional Syst. Nanostructures*, vol. 31, no. 1, pp. 43–47, 2006.

[153] J. C. Lin *et al.*, "The control of size and areal density of InAs self-assembled quantum dots in selective area molecular beam epitaxy on GaAs (0 0 1) surface," *Microelectronics J.*, vol. 37, no. 12, pp. 1505–1510, 2006.

[154] P. Guyot-Sionnest, "Colloidal quantum dots," *Comptes Rendus Phys.*, vol. 9, no. 8, pp. 777–787, 2008.

[155] C. J. Donahue and J. A. Exline, "Anodizing and Coloring Aluminum Alloys," *J. Chem. Educ.*, vol. 91, pp. 711–715, 2014.

Conclusions

The fabrication of high-quality optoelectronic devices relies on the optimum control of the interfaces. In order to optimise the growth parameters for the fabrication of high-quality materials, a deep understanding on the physical processes involved in growth is required. Up to now, there exist various in-situ characterisation. SEM-MBE, TEM-MBE or STM-MBE are powerful techniques that allow imaging of the surface of different semiconductors under growth conditions. are able to investigate dynamical processes at the surface. Our III-Vs LEEM-MBE at Cardiff allows the study of dynamical processes on of complex structures i.e. Gallium Arsenide under MBE conditions i.e. nucleation of nanostructures, with atomic resolution in the vertical axis and 5 nm in the XY plane at video rate. A novel technique has been invented: Selective Energy Dark-Field Low Energy Electron Microscopy (SEDFLEEM). This technique combines the advantages of Dark-Field LEEM with the accuracy of the I-V curve of diffracted spots for identification of complex structures and provides a very useful tool for the investigation of atomic arrangements and nanostructures nucleation.

Firstly, a study on the c(8×2) and the (6×6) phase reconstructions for GaAs(001) using SEDFLEEM revealed a metastable (6×6) within the stable c(8×2) regime that is present in the surface at temperatures above 570°C.

Secondly, we have utilised the principles of droplet epitaxy, generating a Gallium droplet and creating a monotonically decreasing Gallium chemical potential (μ_{Ga}) profile along a flat trail. We have used SEDFLEEM to map qualitatively different phase reconstructions around liquid gallium droplets at a fixed temperature. We have demonstrated the stability of the (6×6) under As flux.

Moreover, we have analysed the coexistence of the c(8×2) and the (6×6) for GaAs(001) between 520°C and 570°C using SEDFLEEM. Comparing these studies with similar studies on Silicon have revealed that this transition is a first order

transition and that theory on transitions for monoatomic systems can be applied to complex binary systems.

We have investigated the kinetic processes behind droplet epitaxy and droplet etching. Future work will improve imaging conditions for a better understanding of the surface kinetics of droplet epitaxy and droplet etching. Studying these mechanisms will benefit site-controlled quantum structures nucleation. We have also developed an anodisation system for generation of porous alumina. The pores from the alumina can be used as nucleation for quantum structures. The thorough understanding on these surface processes is a key factor for the control of the growth parameters leading to optimum control of the interfaces. The implementation of this knowledge to industrial growth processes results crucial for the growth of high-purity crystalline structures and will pave the way for the development of high-technology optoelectronic devices.

Appendices

DFT model

Density Functional Theory (DFT) is a computational method used in physics, chemistry and materials science to examine the electronic structure of different systems such as atoms, molecules or condensed phases and that has the potential of yielding the exact electronic energy of such systems [1]. Setting off these principles, the total energy of the GaAs system, can be compared with the free energy of each atomic reconstruction considering two different atomic arrangements at the surface following Eq. 1.

$$\Delta G = \Delta G_{\,reconstruction} - \Delta N_{As} G_{GaAs}^{bulk} + (\Delta N_{As} - \Delta N_{Ga})\mu_{Ga} \qquad \text{Eq. 1}$$

Where $\Delta G_{\,reconstruction}$ is the relative formation energy of one reconstruction with respect to another, ΔN_{As} and ΔN_{Ga} correspond to the number of atoms of each species that are needed to go from one reconstruction to another (related to stoichiometry), G_{GaAs}^{bulk} is the free formation energy of the bulk. This function can be approximated to a linear function, in which the gradient would be directly related with the stoichiometry.

Using atomistic models, the slope and the intercept for each reconstruction can be calculated and further compared with other phase reconstructions.

Monte Carlo simulation

Monte Carlo (MC) simulation is basically the generation of random objects or processes by means of a computer. The idea behind MC models is to repeat the experiment many times or use a sufficiently long simulation run to acquire many

quantities of interest using the Law of Large Numbers and other methods of statistical inference [2]. By assigning different probabilities for different processes to occur, one can simulate complex physical surface processes.

In our case, the MC model has been applied for the calculation of a metastable (6×6) phase within the c(8×2) for GaAs (001) (see chapter 7 for further details). In this theoretical model developed by Kennet Hannikainen [3], several probabilities have been assigned to different physical events based on experimental observations with the LEEM-MBE equipment. For example, in the simulation, the probability of a c(8×2) phase to nucleate within a (6×6) patch on a differential time ∂t, is $\rho A \partial t$, where ρ is the probability of nucleation per unit area and time of nucleation, and A is the area of the patch. Therefore, for a certain instant of the simulation, the probability $\rho A \partial t$ is calculated; and a random number is generated. This random number will determine if there will be nucleation or not. The process repeats likewise for the other probabilities J_b and J_w rate of Lochkeime formation per unit area of (6×6), and rate of formation of point-like Lochkeime per unit area respectively. The parameter ν is taking as the step velocity. The steps advance in ∂t a distance of $\nu \partial t$.

References

[1] T. Van Mourik and R. J. Gdanitz, "A critical note on density functional theory studies on rare-gas dimers," *J. Chem. Phys.*, vol. 116, no. 22, pp. 9620–9623, 2002.

[2] D. P. Kroese, T. Brereton, T. Taimre, and Z. I. Botev, "Why the Monte Carlo method is so important today," *Wiley Interdiscip. Rev. Comput. Stat.*, vol. 6, no. 6, pp. 386–392, 2014.

[3] "The theoretical model has been developed by Kennet Rodriguez Hannikainen." .